Neuromodulation Strategies for Controlling Brain Network Plasticity Dynamics

Presented in Partial Fulfillment of
the Requirements for the Degree of

Doctor of Philosophy

with a Major in

Chemical Engineering

in the

College of Graduate Studies

University of Idaho

by

Joseph T. Schmalz

Major Professor
Gautam Kumar, Ph.D.

Committee
Ben Richardson, Ph.D.
D. Eric Aston, Ph.D.
Fuchang Gao, Ph.D.
James Moberly, Ph.D.

Department Administrator
Dev Shrestha, Ph.D.

August 2021

Authorization to Submit Dissertation

This dissertation of Joseph T. Schmalz, submitted for the degree of Doctor of Philosophy with a Major in Chemical Engineering and titled "Neuromodulation Strategies for Controlling Brain Network Plasticity Dynamics," has been reviewed in final form. Permission, as indicated by the signatures and dates below, is now granted to submit final copies to the College of Graduate Studies for approval.

Major Professor:	Gautam Kumar, Ph.D.	Date
Committee Members:	Ben Richardson, Ph.D.	Date
	D. Eric Aston, Ph.D.	Date
	Fuchang Gao, Ph.D.	Date
	James Moberly, Ph.D.	Date
Department Administrator:	Dev Shrestha, Ph.D.	Date

Abstract

Neuromodulation refers to a broad term for perturbing the brain states using either external electrical stimulation, optical stimulation, a drug, or a combination of all. In recent years, neurostimulation, a paradigm for perturbing the brain states electrically or optically, has emerged as a promising approach for investigating basic neuroscience questions and developing therapies for various brain disorders such as Parkinson's disease, epilepsy, major depressive disorders, and Alzheimer's disease. However, most of the existing neurostimulation-based therapies for brain disorders focus on suppressing symptoms and ignore the dynamical aspects of the underlying network that create the pathological symptoms. As a result, the symptoms of specific disorders reemerge once the external stimulation turns off. Based on the evidence of the plastic nature of brain circuits in many areas of the brain, this dissertation investigates novel neuromodulation strategies to achieve long-term changes in the brain states by harnessing brain network's plasticity. In the first part of this dissertation, a unified multi-timescale computational modeling framework is developed to investigate drug-based neuromodulation strategies for modulating synaptic plasticity dynamics in the hippocampus and basal ganglia circuits for potential applications in developing therapies for stress-mediated brain disorders and Parkinson's disease. The second part of the dissertation focuses on developing electrical stimulation strategies for controlling synchronization of neuronal activity in large-scale brain networks by harnessing synaptic plasticity for potential applications in suppressing epileptic seizures and pathological synchronization in Parkinson's disease.

Table of Contents

List of Tables

List of Figures

Acknowledgements

Throughout my journey as a Ph.D. student at the University of Idaho and during the process of writing this dissertation, I have received an abundance of support, assistance, and guidance. For whom, I would like to take a moment to thank.

First of all I would like to extend my deepest gratitude to my supervisor Dr. Gautam Kumar for without his suggestion and encouragement I would never have completed a PhD. I will always be grateful for his continued guidance, feedback, and patience during the course of my doctorate that has helped me grow as a researcher, and thank you for the trips to Starbucks for coffee, which fueled my research.

I am extremely grateful to my committee members Dr. Richardson, Dr. Aston, Dr. Moberly, and Dr. Gao for their guidance and support through the course of my Ph.D. (and undergraduate) journey at the University of Idaho.

Thanks also to the other lab members Ben, Niko, and especially Andrew for allowing me to bounce ideas off of him and always being up for a good conversation. I would like to thank Sebastian for tolerating my German over these last four years.

I would like to thank my parents, my brother, and my friends for their support.

Last but not least, I would like to give a special thanks to my wife Liz, who is always up for an adventure, for her love and support.

meiner Frau, meinen Eltern, meinem Bruder und meinen Freunden

CHAPTER 1

Introduction

Neuromodulation is defined as changes in the activity of a neuron or neuronal population due to either the internal release of neurochemicals or hormones, or the external electrical or chemical stimulation of the nervous system (Kaczmarek and Levitan, 1987; Krames *et al.*, 2009). This allows people to learn new skills and react to their ever changing environment. Currently, pharmaceutical neuromodulation is used to treat symptoms of Parkinson's disease, depression, and epilepsy. In some cases, patients are resistant to the pharmaceutical management of the symptoms. These patients are eligible for direct electrical stimulation of the brain to suppress the symptoms. Constant electrical stimulation is required to suppress the pathological brain dynamics thought to produce the symptoms, such as the strong oscillatory neural activity in Parkinson's disease patients. One major challenge to the current approaches to treat neurological diseases, such as Parkinson's disease, is that they purely focus on suppressing the symptoms in place of fixing the underlying brain structure that is producing the symptoms. Harnessing the brain plasticity by developing pharmacological or electrical neuromodulation strategies could lead to the development of next-generation therapies for various neurological and psychiatric disorders. The focus of this dissertation is to develop novel pharmacological and electrical neuromodulation strategies to harness brain plasticity in order to develop therapies for various brain disorders. Although in this dissertation I have focused on the applicability of designed strategies in treating Parkinson's disease, stress-mediated brain disorders, and epilepsy, the ideas developed in this dissertation may find applicability in various other brain disorders.

1.1 BACKGROUND

1.1.1 *Neuron Anatomy and Function*

I begin my dissertation with the fundamental building block of the brain, the neuron. The neurons in our brain are responsible for encoding our thoughts, impulses, and nonconscious actions, such as breathing, through electrical signals. These electrical signals travel through the three main parts: the cell body, the dendrites, and the axon (Purves *et al.*), which are depicted and labeled in the diagram in Figure 1.1A. The dendrites of each neuron receive input from other neurons due to the release of chemicals called neurotransmitters, which bind to receptors on dendrite in the synaptic cleft. When neurotransmitters bind to their corresponding receptor in the synaptic cleft, they can either depolarize (increase) or hyperpolarize (decrease) the synaptic potential, which travels down the dendrite to the cell-body. Each synaptic potential from all of the dendrites of the neuron integrate together in the cell-body. If the membrane potential of the cell-body is depolarized past a threshold, the membrane potential rapidly depolarizes further. This is followed by the membrane potential rapidly repolarizing back to the resting membrane potential. The rapid depolarization-repolarization is called an action potential, and an example of an action potential is shown in Figure 1.1B. At this point, the depolarized membrane potential travels down the axon of the neuron to the axon terminal where it terminates and releases a neurotransmitter to the dendritic cleft of another neuron.

The ion channels, which are located on the membrane of neurons, are responsible for creating the action potential and propagating any changes in the membrane potentials from the dendrite, to the cell-body, and down the axon. The membrane potential is created by an imbalance in the concentration of various ions, such as the sodium, potassium, calcium, and chloride ions, on either side of the membrane, which are tightly regulated by the neuron (Purves *et al.*; Hodgkin and Huxley, 1952). The imbalance of ions creates an electricochemical gradient. This consists of an electrical gradient, due to the charge imbalance, and a chemical concentration gradient, due to the different concentrations of each ion on either side of the membrane. Therefore, each ion has an equilibrium potential, which is responsible for creating the driving

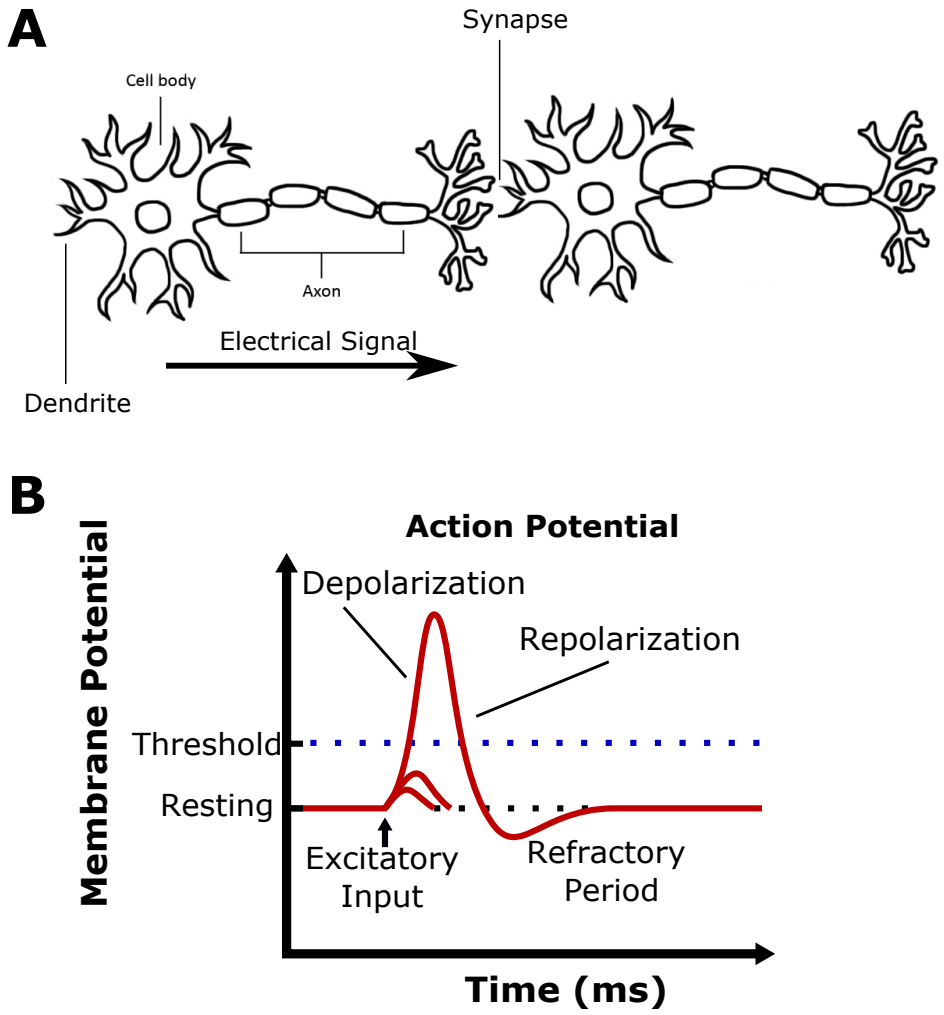

FIGURE 1.1: Neuron fundamentals. **(A)** shows a simple schematic of two neurons taken from *www.brainfact.org*. **(B)** shows a diagram of an action potential.

force of the generation and propagation of the action potential. The equilibrium potential for each ion can be calculated by the Nernst equation,

$$E_X = \frac{RT}{zF} \ln \frac{[X]_{out}}{[X]_{in}}, \tag{1.1}$$

where E_X is the equilibrium potential for ion X, R is the gas constant, T is the temperature, z is the valence of the ion, and F is Faraday's constant. The concentration of the ion on the outside and inside of the membrane are $[X]_{out}$ and $[X]_{in}$, respectively.

The two main ions that contribute the most to the resting membrane potential and the action potential are the sodium and potassium ions (Purves *et al.*). The resting membrane potential is largely determined by the large potassium concentration

gradient maintained across the membrane with a high concentration of potassium on the inside of the membrane compared to outside of the membrane, while the initialization of the action potential is largely due to the permeability of the neuron's membrane to sodium ions. There exists voltage dependent sodium ion channels that become permeable to the sodium ions when the membrane potential is depolarized. Furthermore, there exists a large sodium gradient across the membrane potential with a higher concentration of sodium ions on the outside of the membrane compared to the inside of the neuron's membrane. When the voltage-gated sodium ion channels open, there is a large influx of sodium ions as the membrane becomes more permeable to sodium ions. This leads to a rapid depolarization of the membrane potential to create the action potential. The permeability of the membrane to sodium is short lived and the sodium voltage-gated ion channels close. At this point, the membrane becomes more permeable to potassium and a large efflux of potassium occurs to repolarize the membrane potential. The flow of potassium ions cause the membrane potential to overshoot the resting potential. The membrane slowly returns back to the resting membrane potential as the initial balance of sodium and potassium ions is restored. This overshooting phase is called the refractory period. During this time, the neuron is not responsive to excitatory input from other neurons. Figure 1.2 shows a schematic of the flow of sodium and potassium ions during each part of the action potential. After generation, the action potential travels down the axon of the neuron to the axon terminal to release neurotransmitters or neuromodulators to the dendrite of another neuron.

The synaptic cleft is the point where the axon terminal meets the dendrite of another neuron, and it is how neurons communicate with each other over long distances (Purves *et al.*). When the action potential reaches the axon terminal, it releases neurotransmitters or neuromodulators to the next neuron. Each neuron is responsible for releasing one neurotransmitter or neuromodulator, and it is typically defined by the neurochemical it releases. Here, the neuron releasing neurotransmitters is defined as the pre-synaptic neuron and the neuron receiving the neurotransmitters is defined as the post-synaptic neuron. There exists excitatory and inhibitory neurotransmitters, such as glutamate and γ-aminobutyric acid

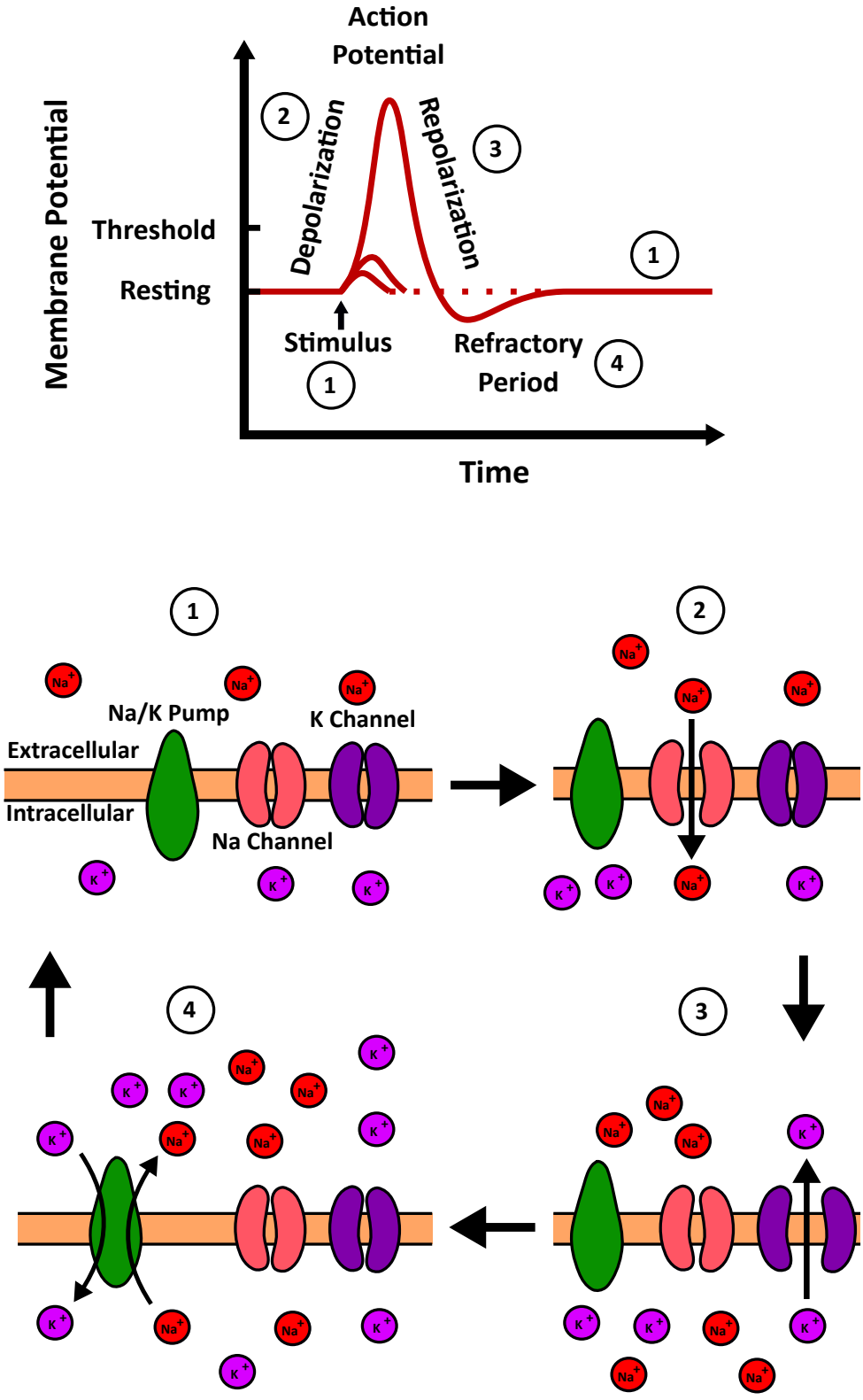

FIGURE 1.2: The basis of the action potential. Here, I show a schematic of the flow of sodium and potassium ions in relation to the evolution of the action potential.

(GABA). Glutamate binds to α-amino-3-hydroxy-5-methyl-4-isoxazolepropionic acid receptor (AMPAR) and ionotropic N-Methyl-d-aspartic acid receptor (NMDAR). When glutamate binds to the AMPAR, the ionotropic channel opens and allows the flow of sodium ions into the neuron, which depolarizes the membrane potential. The NMDAR receptor requires both glutamate to bind to the receptor and the ejection of a Mg^{2+} ion from the channel by the depolarization of the membrane potential in order for sodium ions to flow through the channel. The inhibitory neurotransmitter GABA binds to its corresponding GABA receptor (GABAR). The activation of the GABAR allows chloride ions to flow into the neuron and produces a hyperpolarization of the membrane potential, which inhibits the generation of action potentials. Since AMPAR, NMDAR, and GABAR result in the influx of ions, they are classified as ionotropic receptors.

1.1.2 *Neural Plasticity*

Synaptic plasticity is the change in the response of the postsynaptic neuron to neurotransmitters released from the presynaptic neuron. The inherent synaptic plasticity of our brain allows college students to learn a new language, children to learn a new sport, or teachers to remember the names of an incoming class. One of the most well-know definitions of plasticity was postulated by the Canadian physiologist Donald Hebb, and the definition was named Hebbian plasticity after him (Hebb, 1949). Hebbian plasticity states that the synaptic strength between a presynaptic and postsynaptic neuron increases due to the persistent stimulation of a post-synaptic neuron by a presynaptic neuron. Neuroscientists define an increase in the synaptic strength as potentiation, while a decrease in the synaptic strength as depotentiation. Based on Hebbian plasticity, a spike-time dependent plasticity (STDP) (Song *et al.*, 2000; Abbott and Nelson, 2000) rule has been proposed that states the synaptic strength increases when a presynaptic neuron fires before a postsynaptic neuron, while the synaptic strength decreases when a postsynaptic neuron fires before a presynaptic neuron. Additionally, researchers found that the high frequency stimulation (HFS) of the axon of a presynaptic neurons in the hippocampus induced a sustained increase in the synaptic strength between the two neuron called long-

term potentiation (LTP) (Lomo, 1966; Bliss and Lømo, 1973; Collingridge *et al.*, 1983). In contrast to LTP, researchers found that low frequency stimulation (LFS) of the axon of a presynaptic neuron decreased the synaptic strength and is called long-term depression (LTD) (Dudek and Bear, 1992). The release of neuromodulators, such as dopamine, can modify the effect of these different stimulation protocol's induction of potentiation or depotentiation. For example, the binding of dopamine to the D1 receptor results in further potentiation in the hippocampus and the basal ganglia (Huang and Kandel, 1995; Sajikumar and Frey, 2004; Otmakhova and Lisman, 1996; Mockett *et al.*, 2007; Shen *et al.*, 2008, 2015).

1.1.3 *Neuromodulators and their signaling cascades*

Another class of neurochemicals released by neurons are neuromodulators, which bind to metabotropic receptors on post-synaptic neuron. Unlike ionotropic receptors, metabotropic receptors don't allow ions to pass into the membrane immediately upon a neuromodulator binding to it. Metabotropic receptors initiate a cascade of biochemical reactions inside of the neuron that modulates the neural plasticity by phosphorylating voltage-gated ion channel, ionotropic receptors, and proteins involved in gene expression. A metabotropic receptor is coupled to heterotrimeric G-coupled-protein (Neves *et al.*, 2002; Gilman, 1987). Therefore, when a neuromodulator binds to the receptor, the α subunit separates from the $\beta\gamma$ dimer. Then, the free α subunit controls the activation of an effector protein that initiates a biochemical signaling cascade. There exists three subtypes of G-protein-coupled receptors, which are G_s, G_i, and G_q (Pitcher *et al.*, 1998). The G_s-protein-coupled and G_i-protein-coupled receptors directly oppose each other. The activation of the G_s protein activates the effector protein adenylyl cylcase (AC) (Glatt and Snyder, 1993), while the activation of the G_i protein inhibits AC (Gerfen and Surmeier, 2011). The activation of AC amplifies the biochemical signal by catalyzing the conversion of adenosine triphosphate (ATP) to cyclic adenosine monophosphate (cAMP), which activates protein kinase A (PKA) (Frey *et al.*, 1993). A schematic diagram of the G_s-protein-coupled and G_i-protein-coupled receptor biochemical pathways are shown in Figure 1.3A. The activation of the G_q-protein-coupled receptor activates

the effector protein phospholipase C (PLC) (Kostenis *et al.*, 2020), which is shown in the schematic diagram in Figure 1.3B. The activation of PLC catalyzes the splitting of phosphatidylinositol biphosphate (P_2P) into diacylglycerol (DAG) and inositol triphosphate (IP_3). DAG is responsible for activating protein kinase C (PKC), which phosphorylate various membrane proteins, and IP_3 binds to the IP_3 receptor, which releases internal storage of calcium. The internal release and inward flow of calcium through voltage-gated calcium channels or permeable NMDAR also activates post-synaptic biochemical signaling cascades.

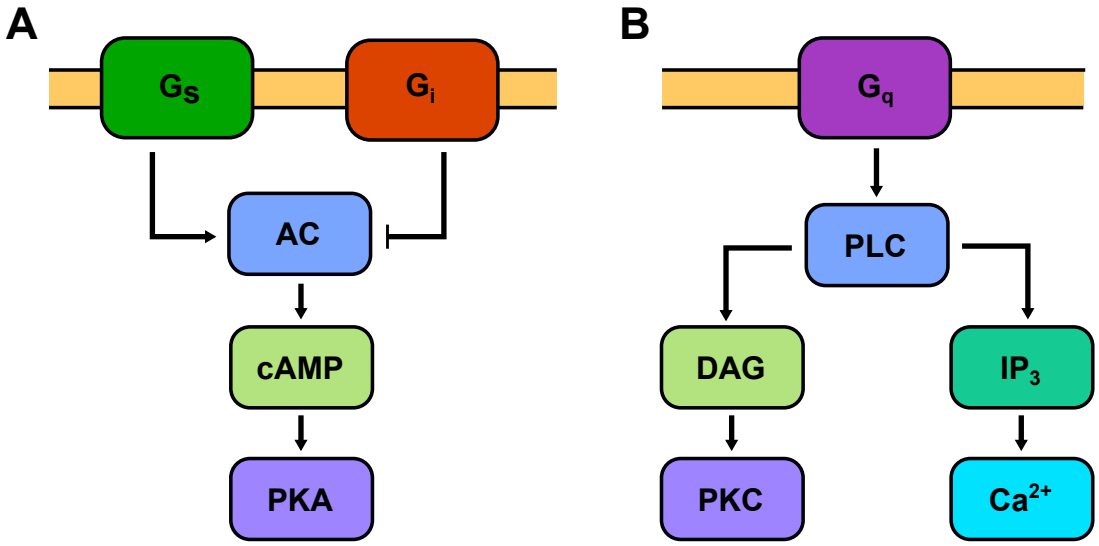

FIGURE 1.3: A schematic diagram of the pathways activated by G-protein-coupled receptors. **(A)** shows the opposing action of the G_s- and G_i-protein-coupled receptors on the activation of AC. The arrow represents an excitatory effect, while a T represents an inhibitory effect. **(B)** shows biochemical pathway induced by activating the G_q-protein-coupled receptor.

The release of Ca^{2+} ions into the neuron, due to the neuron firing or the internal release, activates two well-known Ca^{2+}-activated kinases, which are Ca^{2+}/calmodulin-dependent protein kinase II (CaMKII) and PKC (Lisman *et al.*, 2012). CaMKII is a critical post-synaptic protein that consists of 12 subunits and plays a critical role in long-term potentiation (LTP). CaMKII contributes to LTP by directly phosphorylating AMPARs so that more AMPARs open when glutamate is released by the presynaptic neuron. Additionally, CaMKII phosphorylates other protein kinases involved in transcription and translation of more AMPARs and NMDARs, which

also increases the post-synaptic neuron's response to glutamate release from the presynaptic neuron.

1.2 BROADER PROBLEM

As I have just discussed, the plasticity dynamics of neurons or populations of neurons is modulated by the release of multiple neuromodulators and the inherent electrical activity of the membrane potential. The combination, duration, and timing of the release of different neuromodulators can have a profound effect on the dynamics of neurons by initiating different biochemical signaling cascades at different times and strengths. Therefore, how would one design an experiment to efficiently investigate the interaction of multiple neuromodulators as well as the temporal interaction between the different neuromodulators? Furthermore, changes in the membrane potential dictate the release of neuromodulators and neurotransmitters as well as the open-state of voltage-gated ion channels. The opening of voltage-gated calcium channels can initiate intracellular signaling pathways that interact with those activated by neuromodulators. As a result, another question arise. How does one efficiently explore the temporal interaction of the electrical signal of the membrane potential and the biochemical signals of the neuromodulators? The number of experiments required to sufficiently analyze the temporal interaction of just one neuromodulator at different concentrations, durations, and timings with the electrical dynamics of the membrane potential alone would cost the experimentalist too much time and money to conduct the experiments. As a result, computational models that capture the electrical and biochemical dynamics of neurons have arisen to cheaply and quickly study potential experimental conditions.

1.2.1 *Computational models of neuron dynamics*

Single Neuron Membrane Potential Models — In order to more easily study the complex dynamics of our brain, researchers have developed reduced mathematical models of the neurons that make up our brain. The first electrical mathematical models of a neuron's membrane dynamics began to emerge at the

beginning of the 20^{th} century. The development of the first phenomenological mathematical model of a neuron is credited to Lapicque in 1907 (Brunel and Van Rossum, 2007). Lapicque's mathematical formulation of a neuron's dynamics were modeled after a leaky capacitor, which was coined and formalized as the leaky integrate-and-fire neuron model in the 1970s (Knight, 1972). The leaky integrate-and-fire neuron dynamics is shown in Equation 1.2

$$\tau_m \frac{dV}{dt} = -(V - V_{rest}) + RI_{app}, \tag{1.2}$$

where τ_m is the time-constant of the membrane dynamics, V is membrane potential, V_{rest} is the resting potential, R is the membrane resistance, and I_{app} is the applied current. The simplified model attempts to capture the subthreshold membrane potential dynamics. The action potentials are captured in this model by an event, which is triggered by the membrane potential crossing a defined membrane potential threshold value. Once the modeled membrane potential hits the threshold value, the potential is reset to the resting potential value. While this model is able to computationally efficiently capture the subthreshold dynamics and the action potential events, it doesn't capture the biophysical dynamics of the action potential.

The first biophysical mathematical neuron model was developed in the 1950's by two British scientist Hodgkin and Huxley (Schwiening, 2012). The pair collected squid and successfully obtained the first intracellular recording of an action potential from the squid's giant axon. Later, they invented the voltage-clamp that allowed the pair to investigate the sensitivity and kinetics of ion channels on the giant axon. Based on these measurements, they developed a mathematical model of the fast dynamics of an action potential that bears their name today: the Hodgkin-Huxley model (Hodgkin and Huxley, 1952). Figure 1.4A shows that the model accurately captures the dynamics of an action potential in a squid giant axon shown in Figure 1.4C. Amazingly, the pair did all this with a mechanical calculator similar to the one shown in Figure 1.4B (Schwiening, 2012).

The Hodgkin-Huxley model incorporated physical properties that later elegantly predicted the gating structure of the sodium and potassium ion channels. The model

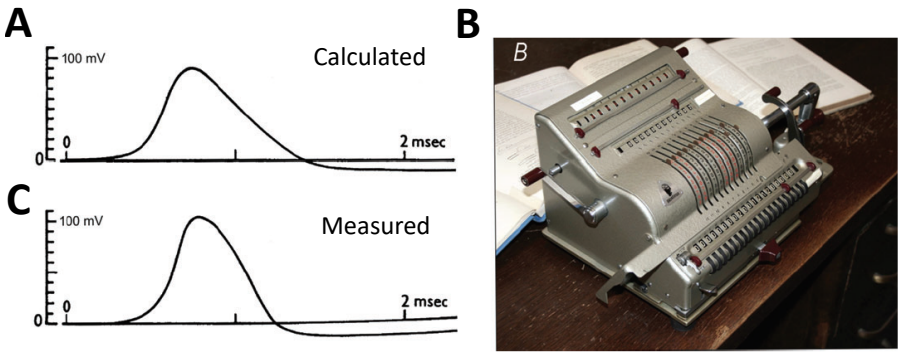

FIGURE 1.4: Mathematical solution to Hodgkin-Huxley neuron model. **(A)** shows the action potential calculated using the mechanical calculator shown in **(B)**. **(C)** shows the measured action potential in a squid giant axon. The images were taken from (Schwiening, 2012).

sums the different ion currents to predict the membrane dynamics. Equation 1.3 shows the membrane dynamics in terms of the applied (I_{app}), leaky ($\bar{g}_l(V - V_l)$), sodium ion ($\bar{g}_{Na}m^3h(V - V_{Na})$), and potassium ($\bar{g}_K n^4(V - V_K)$) currents. Here, the membrane conductance for each channel are $\bar{g}_l$, $\bar{g}_K$, and $\bar{g}_{Na}$, and the reversal potentials are V_l, V_K, and V_{Na}. The voltage-dependent gating variables n, m, and h were later found to mimic the opening and closing of the potassium and sodium ion channels in experiment.

$$C_m \frac{dV}{dt} = I_{app} - \bar{g}_l(V - V_l) - \bar{g}_K n^4(V - V_K) - \bar{g}_{Na}m^3h(V - V_{Na}) \tag{1.3}$$

While these electrical models of a neuron's membrane potential captured the fast changes in the dynamics of the membrane potential, they ignored the slower biochemical dynamics, such as the biochemical signaling cascades initiated by G-coupled protein receptors shown in Figure 1.3.

Biochemical Kinetic Models — Biochemical kinetic mathematical models of a neuron attempt to capture the dynamics of key signaling proteins involved in modulating the excitability of the neuron (Kotaleski and Blackwell, 2010; Nair *et al.*, 2014). These models provide mechanistic insight into how a neuron's plasticity and excitability is modulated by different neuromodulators. Many of the of the neuromodulators bind to a seven-membrane spanning G-protein coupled receptors. There exist dopamine, muscarinic, nicotinic, and adenosine G-protein coupled receptors. As previously stated, upon the neuromodulator binding to its corresponding receptor, the Gα subunit dissociates from the G$\beta\gamma$ dimer. Both of these G protein subunits control the initiation of a biochemical cascade through an effector enzymes, such as adenylyl cyclase (AC) or phospholipase C (PLC). The effector enzyme activate secondary messengers that amplify the response in order to control the intrinsic excitability of the neuron by phosphorylating voltage-dependent ion channels, the response to excitatory or inhibitory input from other neurons by phosphorylating ligand-gated ion channels, or controlling the translation of plasticity dependent proteins.

Over the last two decades, with the advances in high performance computers, detailed biochemical computational models of the biochemical kinetics of plasticity have been develop in parts of the brain such as the Hippocampus (Mergenthal *et al.*, 2020), Basal Ganglia (Nair *et al.*, 2014, 2016, 2015; Blackwell *et al.*, 2019; Lindroos *et al.*, 2018; Mattioni and Le Novère, 2013), and cortex (Mäki-Marttunen *et al.*, 2020). Computational models of the biochemical cascades initiated by the binding of dopamine, acetylcholine, or adenosine to their corresponding receptors have been developed to study their individual and combined effect on key signaling proteins involved in corticostriatal plasticity, such as cAMP dependent protein kinase A (PKA) and Ca^{2+}-Calmodulin-dependent kinase II (CaMKII). The low cost of creating these biochemical models from the already existing experimental data allows scientist to quickly and cheaply test their hypotheses and experimental set-up before spending money and time on a project. These models have provided mechanistic insight and have proposed potential new experiments in order to expand our understanding of the signaling pathways involved in neural plasticity.

Typically, researchers model the biochemical cascades of neural plasticity with simple kinetic dynamics. Simple biochemical dynamic models describe the reaction of one or more substrate molecules or proteins, which produce one or more product molecules or proteins. For example, the generic biochemical reaction

$$A \quad + B \underset{k_b}{\overset{k_f}{\rightleftharpoons}} C + D, \tag{1.4}$$

describes the interaction of substrates A and B to form C and D. The rate of the forward and backward reaction are described by k_f and k_b. Additionally, the biochemical reactions include enzyme kinetics due to the presence of multiple kinases. The dynamics

$$A \quad + E \underset{k_b}{\overset{k_f}{\rightleftharpoons}} AE \overset{k_{cat}}{\rightarrow} E + B, \tag{1.5}$$

describe the conversion of substrate A into B catalyzed by enzyme E, which is neither created or destroyed in the process. Both of these biochemical kinetics can be written

as deterministic rate equations. Due to the high number of proteins known and not known to be involved in synaptic plasticity, these biochemical kinetic models are quite large.

1.2.2 *Need for a biochemical and electrical modeling framework*

In order to efficiently fill the gaps of our understanding and design novel therapies to treat various brain disorders, I require a computational model that can quickly and cheaply explore the interaction of various neuromodulators with each other at different concentration, durations, and times as well as with the electrical dynamics of the membrane potential of neurons. This computational model could quickly and cheaply explore the rules of neuromodulators temporal interacting with each other and with the membrane potential. These results would highlight the most important experiments. Most of the previous computational models either only capture the fast electrical dynamics of the membrane potential (Hodgkin and Huxley, 1952; Knight, 1972; Golomb *et al.*, 2006) or the slow biochemical dynamics of the intracellular signaling pathways of neurons (Triesch *et al.*, 2018; Bhalla and Iyengar, 1999; Kotaleski and Blackwell, 2010; Blackwell and Jedrzejewska-Szmek, 2013; Blackwell and Miningou, 2020; Mäki-Marttunen *et al.*, 2020; Foncelle *et al.*, 2018; Brzosko *et al.*, 2017). While there exists unified multi-scale models that combine detailed biochemical molecular level dynamics with electrical dynamics in medium spiny neurons (Mattioni and Le Novère, 2013) and CA1 hippocampal neurons (Bhalla, 2011) to explain published biochemical data from several experimental protocols of LTP induction, these models do not integrate the initiation of biochemical signaling cascades by neuromodulator with the electrical dynamics. Therefore, a unified modeling framework is required that integrates the biochemical and electrophysiology dynamics in order to systematically investigate the interaction of different timings, concentrations, and duration of various neuromodulator with each other and with the electrical membrane dynamics.

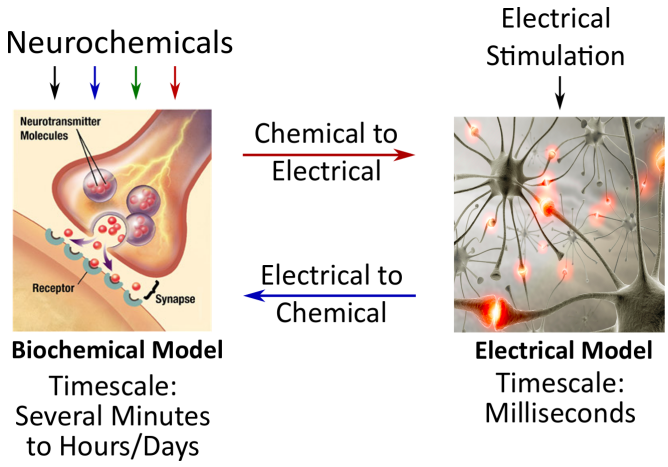

FIGURE 1.5: A unified model of the biochemical and electrical dynamics.

1.3 DISSERTATION OVERVIEW

My dissertation is organized as follows: In Chapter 2, I discuss my investigation into the changes of corticostriatal biochemical signaling pathways as dopamine is depleted in order to mimic the death of dopamine neurons in Parkinson's diseases. Based on this model, I will suggest new targets for therapies to treat the symptoms of Parkinson's disease. In Chapter 3, I develop a set of phenomenological models to describe the temporal dose-dependent effect of the dopamine D1/D5 receptors agonists SKF 38393, 6-bromo-APB, and dopamine, on the Schaffer-collateral CA1 (SC-CA1) pyramidal neuron synaptic conductance using published electrophysiological data from hippocampal CA1 slice experiments on the % change in field excitatory postsynaptic potential (fEPSP) slope. In Chapter 4, I develop a novel neurostimulation strategy called "Forced Temporal Spike-Time Stimulation (FTSTS)" that I show is able to efficiently desynchronize large excitatory-inhibitory (E-I) spiking neuron networks and keep the network desynchronized without any further input by harnessing the synaptic weight of the network. In Chapter 5, I expand upon the novel FTSTS strategy developed in Chapter 4 by applying the stimulation protocol to a biophysically constrained neocortical-onset seizure model and explore the parameter space of the FTSTS protocol. Here, I determine the optimal parameters to efficiently control the average synaptic weight. In the final Chapter, I summarize the work presented in my dissertation and propose future directions of the various research topics.

CHAPTER 2

Restoration of Biochemical Signaling Pathway in Dopamine Deficient Parkinson's State

2.1 INTRODUCTION

One of the most well-known neuromodulators is dopamine. It plays a critical role in regulating our actions by modulating the dynamics of neuron structures located in the middle of our brain called the basal ganglia (Davie, 2008; Kordower *et al.*, 2013; Damier *et al.*, 1999; Rajput *et al.*, 2008). Input enters the basal ganglia through the striatum from the cortex (KEMP and Powell, 1970). The traditional view of the basal ganglia is that there exists two pathways, the direct and indirect pathways, that diverge in the striatum (Kravitz *et al.*, 2012; Calabresi *et al.*, 2014). The direct pathway is classified by the expression of D1 dopamine G_s-protein-coupled receptors on the inhibitory medium spiny neurons (MSNs), and the indirect pathway is classified by the expression of D2 G_i-protein-coupled receptors on MSNs (Nagai *et al.*, 2016). The activation of the D1 receptors on direct MSNs increases the excitability of the direct MSNs, while the activation of D2 receptors on indirect MSNs decreases or inhibits the excitability of the MSNs (Shen *et al.*, 2008, 2015). Direct pathway MSNs have inhibitory GABAergic projections to the globus pallidus interna (GPi), which project out of the basal ganglia and inhibit the thalamus (TH) (Utter and Basso, 2008; Smith *et al.*, 2004). Indirect pathway MSNs have inhibitory projections to the globus pallidus externa (GPe), which inhibit the subthalamic nucleus (STN). Then, the STN excites the GPi, which outputs to the thalamus. A schematic of the direct and indirect pathways of the basal ganglia is shown in Figure 2.1. Dopamine is released by projections from the substantia nigra pars compacta (SN) (Schultz, 1999, 1998). Both dopamine receptors exert their influence on the excitability of MSNs through the activation of G-coupled protein receptors that initiate biochemical signaling pathways that control the level of PKA, which is responsible for phosphorylating AMPAR and NMDAR

directly, voltage-gated ion channels that control neuron's inherent excitability, and proteins involved in the translation of plasticity related proteins.

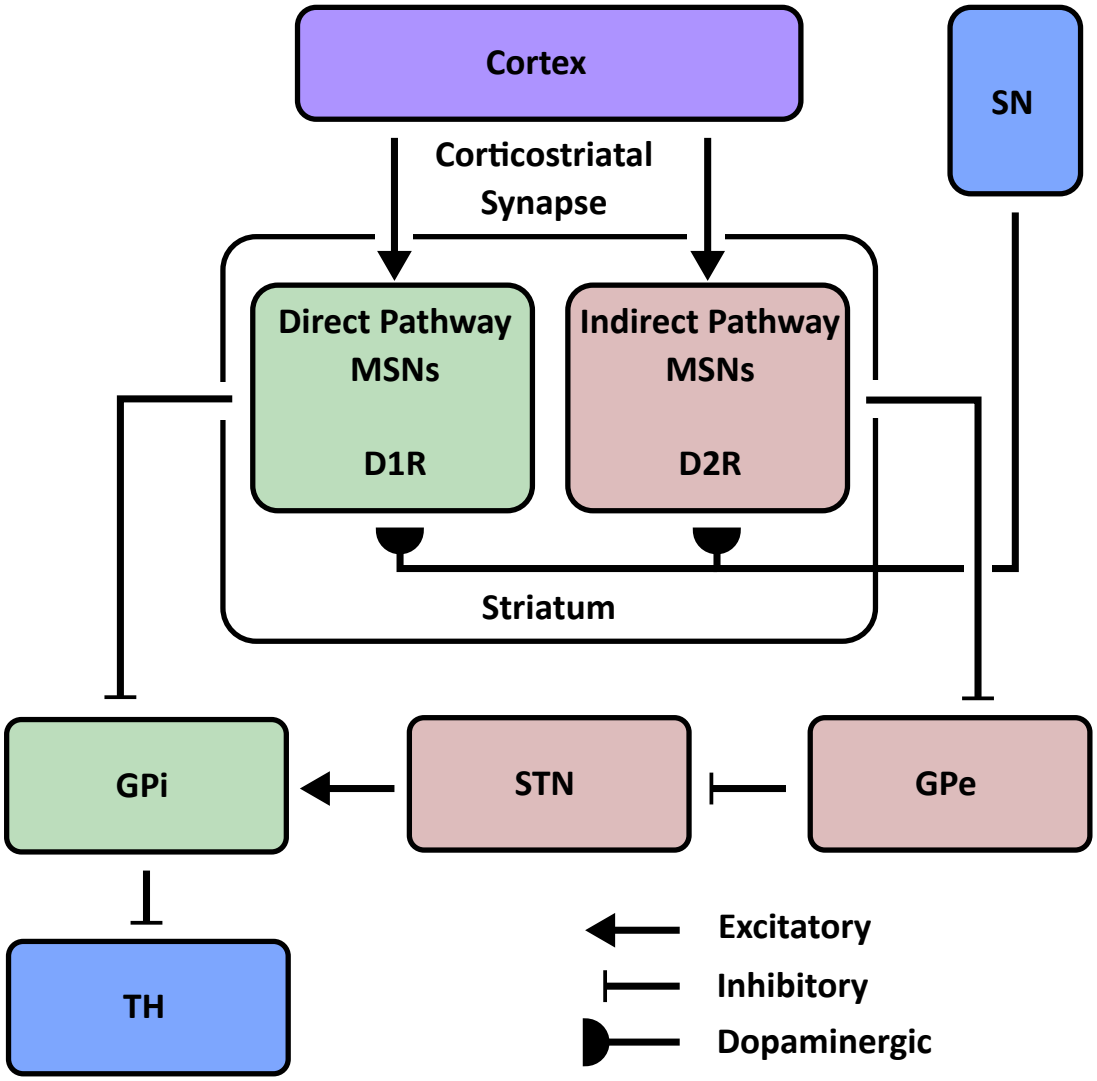

FIGURE 2.1: A schematic diagram of the direct and indirect pathways of the basal ganglia.

In addition to dopamine receptors, there exist other G-protein coupled receptors that oppose the action by the dopamine receptors expressed on the direct and indirect MSNs (Nagai *et al.*, 2016). M4 muscarinic receptors are highly localized to direct MSNs. Acetylcholine released from tonically active cholinergic interneurons binds to the M4 receptor (Shen *et al.*, 2015; Bolam *et al.*, 1984; Kemp and Powell, 1971). These receptors are G_i-coupled receptors and directly opposes the excitatory action of the dopamine binding to the D1 G_s-coupled receptor by inhibiting AC. Furthermore, the

A2a adenosine receptor is a G_s-coupled protein receptor that is expressed on indirect MSNs. When adenosine binds to the A2aR, it activates AC in order to oppose the inhibitory action on AC from dopamine binding to the D2 G_i-coupled receptor. The selectivity of the dopamine, muscarinic, and adenosine receptor to specific MSNs of the direct or indirect pathway makes them ideal targets for therapies to treat neurological disorders of the basal ganglia, such as Parkinson's disease.

Parkinson's Disease (PD) is a neurodegenerative disease characterized by the progressive loss of motor skills and the death of dopamine neurons as the disease progresses (Dauer and Przedborski, 2003; Poewe *et al.*, 2017). The lost mid-brain dopamine neurons of the substantia nigra (SN) project to the striatum of the basal ganglia in order to modulate cortical striatal synaptic plasticity (Davie, 2008; Kordower *et al.*, 2013; Damier *et al.*, 1999; Rajput *et al.*, 2008). Researchers have demonstrated that the dopamine is required to maintain normal bidirectional corticostriatal plasticity (Shen *et al.*, 2008; Garcia-Munoz *et al.*, 1992). Therefore, one hypothesis about the disease progression of PD is that the loss of dopamine neurons disrupt the balance of activity of the direct and indirect pathways, such that the activity of the indirect pathway dominates the direct pathway to prevent actions. Since PD is characterized by the death of dopamine neurons, one approach for treating symptoms of PD is to increase the concentration of dopamine in the brain (Connolly and Lang, 2014; Ferreira *et al.*, 2013; Lang and Lees, 2002). Currently, the gold-standard treatment of PD symptoms, L-DOPA, uses this approach (Connolly and Lang, 2014). L-DOPA works well at early stages of the disease but as the disease progresses higher doses are required that produce unwanted side effects, such as L-DOPA induced dyskinesia (LID) that manifests as chorea, ballism, dystonia, myoclonus, or some combination of symptoms (Pandey and Srivanitchapoom, 2017; Calabresi *et al.*, 2010). When patients become resistant to L-DOPA and the side effects become unmanageable, they become eligible for surgical implantation of electrical stimulating electrodes that attempt to disrupt the pathological dynamics to treat the symptoms of PD (Krauss *et al.*, 2020; Benabid *et al.*, 1987; for Parkinson's Disease Study Group, 2001). Recently, another less invasive approach has been suggested, which is to target the M4R on direct MSNs to oppose the potential over stimulation

of the D1R (Bernard *et al.*, 1992; Hersch *et al.*, 1994; Ztaou *et al.*, 2016; Tanimura *et al.*, 2018). In (Shen *et al.*, 2015), the M4Rs were targeted by a positive allostaric modulators (PAMs) that elevated the response of M4R to acetylcholine, in order to inhibit the over activation of the D1R by high doses of L-DOPA. While this approach has proven effective in experiment, the high levels of dopamine from the high doses of L-DOPA may still produce unwanted side effects. Additional therapies strategies are needed to effectively suppress PD symptoms with minimal unwanted side effects (Connolly and Lang, 2014). Therefore, a more effective approach would be to directly lower the activation of the M4R such that lower doses of L-DOPA are more effective at treating symptoms of PD with fewer side effects, due to the higher selectivity for the direct pathway MSNs.

Similarly, in order to investigate potential new therapies to treat PD symptoms, many experiments would be required to explore the parameter space of activating/deactivating the M4R relative to various lower activation levels of the D1R, due to the death of dopamine neurons. Again, an initial computational investigation would quickly and cheaply explore potential therapy strategies before conducting any time-consuming and expensive *in vitro* slice experiments. There exists many computational models that study the effect of neuromodulators, such as dopamine, acetylcholine, adenosine, and glutamate (Nair *et al.*, 2015, 2016, 2019; Yapo *et al.*, 2017, 2018; Mäki-Marttunen *et al.*, 2020; Kim *et al.*, 2013; Blackwell *et al.*, 2019; Nakano *et al.*, 2010), at different concentrations on corticostriatal plasticity and plasticity in other parts of the brain. Typically, these models are biochemical computational models of the known biochemical mechanisms initiated by the neuromodulator binding to its corresponding receptor, such as the dopamine receptors (D1 and D2R), the muscarinic receptors (M1 and M4R), adenosine receptor (A2aR), and glutamate receptos (mGlurR), in the striatum, neocortex, and cerebellum (Blackwell, 2013; Bhalla, 2014; Mäki-Marttunen *et al.*, 2020; Nair *et al.*, 2015; Mergenthal *et al.*, 2020; Nair *et al.*, 2016, 2019; Blackwell *et al.*, 2019; Yapo *et al.*, 2017; Nakano *et al.*, 2010). The activation of these receptors in combination with Ca^{2+} influx controls the dynamics of key synaptic plasticity kinases, such as PKA, CAMKII, and PP1, and ultimately the excitability of each neuron (Yagishita *et al.*, 2014; Nagai *et al.*, 2016). While these models have

provided key insights into the mechanism of plasticity and predictions that can be validated in experiment, thus far no computational model has investigated inhibiting M4R to offset symptoms of PD.

In this chapter, I developed a biochemical computational model of corticostriatal plasticity in the direct medium spiny neuron in order to study how the loss of dopamine effects key plasticity proteins and how targeting the M4R can restore the levels of these key plasticity protein. I do so by studying the temporal interaction of DA, ACh, and Ca^{2+} on the corticostriatal plasticity under physiological and nonphysiological conditions. My corticostriatal plasticity computational model is a biochemical single-compartment model of the direct MSN with three inputs dopamine, acetylcholine, and calcium. In order to build the model, I have integrated previously existing models and reparameterized the new model using experimental data obtained from the literature. Here, I have used my model to explore the effect of depletion of DA on key corticostriatal plasticity signaling proteins. Additionally, I explored how the reduction of key corticostriatal plasticity proteins, due to dopamine depletion, can be restored by targeting acetylcholine and calcium inputs.

2.2 MODEL SYSTEM

2.2.1 *Biochemical Pathways*

The direct medium spiny neuron (dMSN) AC5/cAMP/PKA signaling pathway is governed by the activation of the D1 dopamine (D1) and the M4 muscarinic (M4) G-coupled protein receptors (GCPR) (Nagai *et al.*, 2016; Castro *et al.*, 2013). The D1 receptor is a $G_{s/olf}$ coupled receptor that increases the level of adenylyl cylcase 5 (AC5) in D1-MSN in the striatum when DA binds to it (Glatt and Snyder, 1993). On the other hand, the M4R is a $G_{i/o}$ coupled receptor that decreases the level of AC5 with the binding of ACh (Gerfen and Surmeier, 2011). Due to the tonic firing of cholinergic interneurons, which release ACh, there is a basal tonic inhibition of AC5 (Aosaki *et al.*, 1995). This tonic inhibition is overcome by a synchronous firing pattern of dopaminergic neurons in the substantia nigra (SN), which releases a high concentration of DA in a pulse that binds to the D1 receptor. In addition to DA

binding to the D1 receptor on MSNs, it also binds to D2 receptors on cholinergic interneurons to produce a pause in the tonic release of ACh (Goldberg and Reynolds, 2011). Therefore, a pulse of dopamine is accompanied by a pause in the release of acetylcholine. Together these two signals causes an increase in the level of the effector enzyme AC5 which amplifies the input dopaminergic and acetylcholine signals by catalyzing the conversion of ATP to the intracellular secondary-messenger cyclic AMP (cAMP). Then, cAMP elevates the level of cAMP dependent protein kinase (PKA).

The PKA signaling pathway modulates the excitability of MSNs by phosphorylating targets, such as voltage-gated ion channels (Surmeier *et al.*, 1995), transcription factors (Dong *et al.*, 2006), and glutamate ionotropic receptors (Nagai *et al.*, 2016; Cepeda *et al.*, 1993). The corticostriatal synaptic plasticity is directly modulated by the direct phosphorylation of glutamate ionotropic receptors by PKA. Furthermore, PKA indirectly controls the corticostriatal synaptic plasticity by phosphorylating other intracellular signaling proteins highly enriched in the striatum, such as dopamine- and cAMP-regulated neuronal phosphoprotein (DARPP-32) (Calabresi *et al.*, 2000) and cyclic AMP-regulated phosphoprotein (ARPP-21) (Ouimet *et al.*, 1989; Rakhilin *et al.*, 2004). Phosphorylation of the threonine 34 (Thr-34) residue of DARPP-32 converts DARPP-32 into a potent protein phosphatase-1 (PP1) inhibitor, which dephosphorylates glutamate ionotropic receptors. Furthermore, the PKA signaling pathway is inhibited by the phosphorylation of the threonine 75 (Thr-75) residue of DARPP-32 by cyclin-dependent kinase (CDK5) (Bibb *et al.*, 1999). Therefore, DARPP-32 acts as a biochemical switches that, depending on the inputs, controls the PKA signaling pathways. The other highly enriched intracellular protein found in the striatum is ARPP-21, which is phosphorylated at the threonine 55 (Thr-55) residue and competes for Ca^{2+}/calmodulin (CaM) (Rakhilin *et al.*, 2004). ARPP-21 acts as a competive inhibitor for other CAM dependent proteins such as the calcium-dependent activation of CaM-dependent kinase II (CAMKII).

Additionally, the corticostriatal plasticity is govern by the level of Ca^{2+} in the dMSN. The Ca^{2+} that enters the dMSN binds to calmodulin to form a Ca^{2+}/calmodulin (CaM) complex (Stemmer and Klee, 1994). These complexes activate CAMKII, which phosphorylates AMPARs and increase the strength of the

corticostriatal synapse (Yagishita *et al.*, 2014). CAMKII phosphorylation is directly opposed by the activation of PP1 by low levels of intracellular Ca^{2+} (Yagishita *et al.*, 2014). In my model, I captured the competition of CAMKII and PP1 phosphorylating or dephosphorylating corticostriatal plasticity substrates as one variable *Substrate*.

2.2.2 *Biochemical Signaling Kinetics*

The biochemical reactions involved in corticostriatal plasticity are modeled using a simple well-mixed reversible chemical reaction model,

$$A + B \underset{k_b}{\overset{k_f}{\rightleftharpoons}} C. \tag{2.1a}$$

Using this model, a series of ordinary differential equations are written to describe the individual species dynamics, shown in Eqs 2.1b-2.1d. Here, A and B represents two generic biochemical signaling species that reversibly combine to form C with a forward k_f and backward k_b rate constants. If the reaction is irreversible, then the backward reaction k_b is set to zero. In order to investigate the temporal window of DA and ACh release on the corticostriatal plasticity, I combined two previously developed models on the corticostriatal synaptic plasticity (Nair *et al.*, 2015, 2016). The modeled reactions of DA or ACh binding to their corresponding receptor to activate the G_s- and G_i-protein-coupled receptor, respectively, are shown in Tables 2.1, 2.3, and 2.2. Then, the reversible biochemical reactions describing the amplification of cAMP by AC5 and the activation of PKA are shown in Table 2.4. The last reversible reactions are shown in Table 2.5 of the the CAMKII and PP1 dynamics. The irreversible biochemical reactions are listed in Table 2.6.

$$\frac{dC_A}{dt} = k_b C_C - k_f C_A C_B, \tag{2.1b}$$

$$\frac{dC_B}{dt} = k_b C_C - k_f C_A C_B, \tag{2.1c}$$

$$\frac{dC_C}{dt} = k_f C_A C_B - k_b C_C. \tag{2.1d}$$

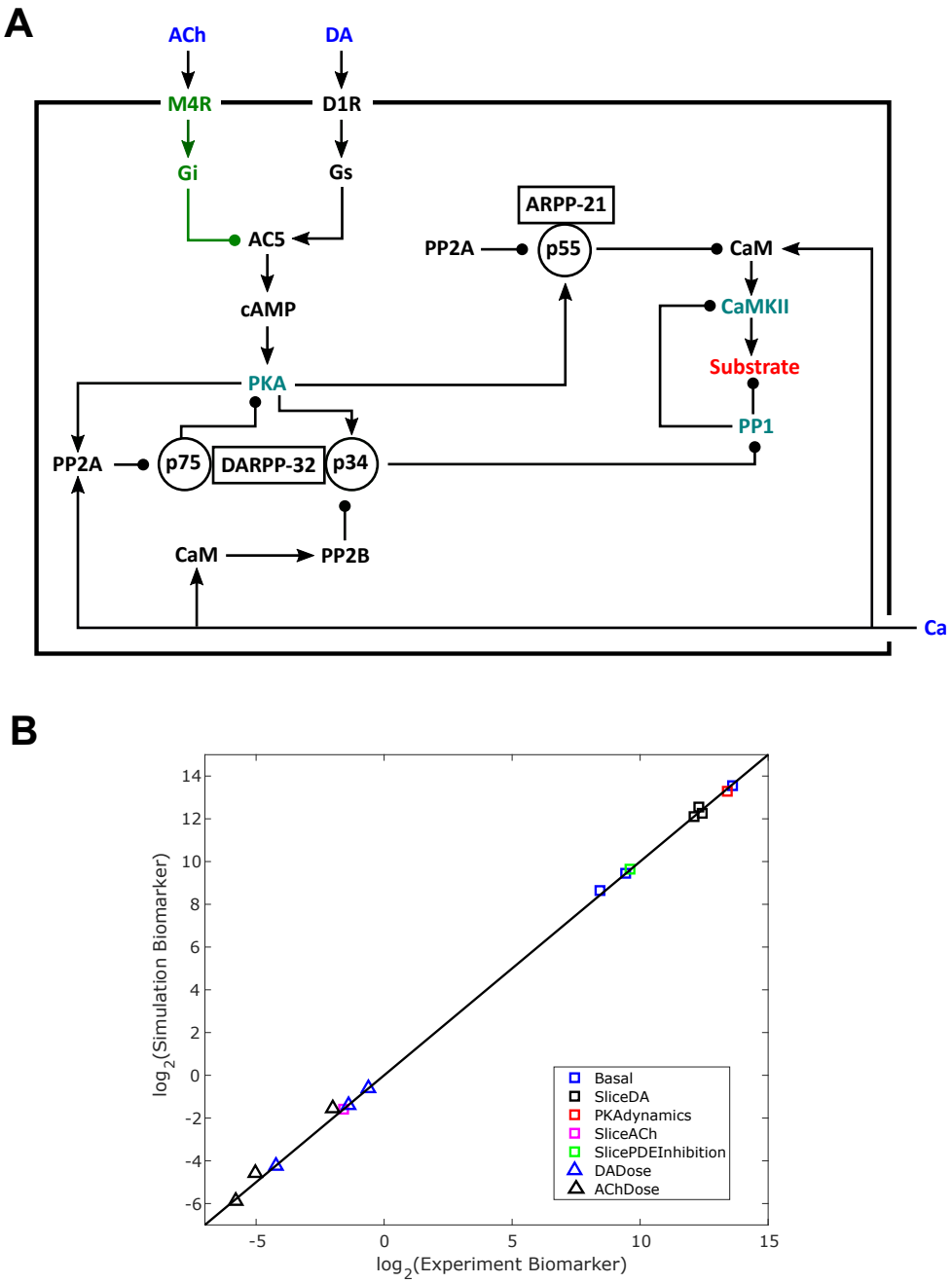

FIGURE 2.2: Validation of biochemical model of the direct MSN. (A) The biochemical signaling pathways in direct MSNs activated by Ca, DA, and ACh, which integrate together to phosphorylate the substrate (pSubstrate). (B) The model parameters were fitted using experimental data from the literature and validated using physiological experimental protocols.

TABLE 2.1: Reversible biochemical dynamics of G-protein-coupled receptors.

Biochemical Reaction
$D1RGolf + DA \underset{k_b}{\overset{k_f}{\rightleftharpoons}} D1RDAGolf$
$D1RDA + Golf \underset{k_b}{\overset{k_f}{\rightleftharpoons}} D1RDAGolf$
$D1R + Golf \underset{k_b}{\overset{k_f}{\rightleftharpoons}} D1RGolf$
$D1R + DA \underset{k_b}{\overset{k_f}{\rightleftharpoons}} D1RDA$
$M4R + Gi \underset{k_b}{\overset{k_f}{\rightleftharpoons}} M4RGi$
$M4RACh + Gi \underset{k_b}{\overset{k_f}{\rightleftharpoons}} M4RAChGi$
$ACh + M4RGi \underset{k_b}{\overset{k_f}{\rightleftharpoons}} M4RAChGi$
$ACh + M4R \underset{k_b}{\overset{k_f}{\rightleftharpoons}} M4RACh$

The corticostriatal plasticity biochemical reaction parameters were constrained by the observable biomarkers reported in the literature. I used the same biomarkers used to fit the previous versions of the D1R-M4R MSN (Nair *et al.*, 2015) and the temporal window D1R MSN (Nair *et al.*, 2016) models. The previous observable biomarkers are reported in Table 2.11. To fit the my new corticostriatal plasticity biochemical model, I used two new observable biomarkers, which were slice acetylcholine and dopamine dose-dependent data on the activation of the cAMP from *in vitro* slice experimental data. The new biomarkers are shown in Table 2.12. The concentration of the observable biomarker in my model was taken at the steady-state condition or I matched the activation dynamics parameter in my model to the the observable biomarker from the experiment. The activation of the G-protein coupled receptors were fit using this approach. The G-protein activation dynamics were fit to a monoexponential function $100\%(1 - \exp\{-kt\})$ and the parameter k was fit to a range. Here, t is the time in seconds. I hand-tuned the parameters of the combined model to match the reported observable biomarkers, and the parameters are presented in Tables 2.8, 2.9, and 2.10. Figure 2.2B shows the one-to-one comparison of the

TABLE 2.2: Reversible biochemical dynamics of G*i*-protein activation.

Biochemical Reaction
$AC5 + G_{\alpha,olf}GTP \underset{k_b}{\overset{k_f}{\rightleftharpoons}} AC5G_{\alpha,olf}GTP$
$AC5 + Ca \underset{k_b}{\overset{k_f}{\rightleftharpoons}} AC5Ca$
$AC5Ca + G_{\alpha,olf}GTP \underset{k_b}{\overset{k_f}{\rightleftharpoons}} AC5CaG_{\alpha,olf}GTP$
$G_{\alpha,i}GTP + AC5Ca \underset{k_b}{\overset{k_f}{\rightleftharpoons}} AC5CaG_{\alpha,i}GTP$
$G_{\alpha,i}GTP + AC5 \underset{k_b}{\overset{k_f}{\rightleftharpoons}} AC5G_{\alpha,i}GTP$
$G_{\alpha,i}GTP + AC5 * G_{\alpha,olf}GTP \underset{k_b}{\overset{k_f}{\rightleftharpoons}} AC5G_{\alpha,olf}GTPG_{\alpha,i}GTP$
$G_{\alpha,i}GTP + AC5 * G_{\alpha,olf}GTP \underset{k_b}{\overset{k_f}{\rightleftharpoons}} AC5CaG_{\alpha,olf}GTPG_{\alpha,i}GTP$
$AC5G_{\alpha,i}GTP + G_{\alpha,olf}GTP \underset{k_b}{\overset{k_f}{\rightleftharpoons}} AC5G_{\alpha,olf}GTPG_{\alpha,i}GTP$
$AC5CaG_{\alpha,i}GTP + G_{\alpha,olf}GTP \underset{k_b}{\overset{k_f}{\rightleftharpoons}} AC5CaG_{\alpha,olf}GTPG_{\alpha,i}GTP$
$AC5G_{\alpha,olf}GTPG_{\alpha,i}GTP + ATP \underset{k_b}{\overset{k_f}{\rightleftharpoons}} AC5G_{\alpha,olf}GTPG_{\alpha,i}GTPATP$
$ATP + AC5G_{\alpha,i}GTP \underset{k_b}{\overset{k_f}{\rightleftharpoons}} AC5G_{\alpha,i}GTPATP$

TABLE 2.3: Reversible biochemical dynamics of G_s-protein activation.

Biochemical Reaction
$AC5G_{\alpha,olf}GTP + ATP \underset{k_b}{\overset{k_f}{\rightleftharpoons}} AC5G_{\alpha,olf}GTP * ATP$
$AC5 + ATP \underset{k_b}{\overset{k_f}{\rightleftharpoons}} AC5 * ATP$
$AC5Ca + ATP \underset{k_b}{\overset{k_f}{\rightleftharpoons}} AC5Ca * ATP$
$AC5CaG_{\alpha,olf}GTP + ATP \underset{k_b}{\overset{k_f}{\rightleftharpoons}} AC5CaG_{\alpha,olf}GTP * ATP$
$AC5CaG_{\alpha,i}GTP + ATP \underset{k_b}{\overset{k_f}{\rightleftharpoons}} AC5CaG_{\alpha,i}GTP * ATP$
$AC5CaG_{\alpha,olf}GTPG_{\alpha,i}GTP + ATP \underset{k_b}{\overset{k_f}{\rightleftharpoons}} AC5CaG_{\alpha,olf}GTPG_{\alpha,i}GTP * ATP$
$G_{\alpha,olf}GTP + AC5G_{\alpha,i}GTP * ATP \underset{k_b}{\overset{k_f}{\rightleftharpoons}} AC5G_{\alpha,olf}GTPG_{\alpha,i}GTP * ATP$
$G_{\alpha,olf}GTP + AC5CaG_{\alpha,i}GTP * ATP \underset{k_b}{\overset{k_f}{\rightleftharpoons}} AC5CaG_{\alpha,olf}GTPG_{\alpha,i}GTP * ATP$
$G_{\alpha,olf}GTP + AC5 * ATP \underset{k_b}{\overset{k_f}{\rightleftharpoons}} AC5G_{\alpha,olf}GTP * ATP$
$G_{\alpha,olf}GTP + AC5Ca * ATP \underset{k_b}{\overset{k_f}{\rightleftharpoons}} AC5CaG_{\alpha,olf}GTP * ATP$

TABLE 2.4: Reversible biochemical dynamics of cAMP and PKA.

Biochemical Reaction
$Ca + AC5 * ATP \underset{k_b}{\overset{k_f}{\rightleftharpoons}} AC5Ca * ATP$
$AC5 * ATP + G_{\alpha,i}GTP \underset{k_b}{\overset{k_f}{\rightleftharpoons}} AC5G_{\alpha,i}GTP * ATP$
$G_{\alpha,i}GTP + AC5G_{\alpha,olf}GTP * ATP \underset{k_b}{\overset{k_f}{\rightleftharpoons}} AC5G_{\alpha,olf}GTPG_{\alpha,i}GTP * ATP$
$AC5Ca * ATP + G_{\alpha,i}GTP \underset{k_b}{\overset{k_f}{\rightleftharpoons}} AC5CaG_{\alpha,i}GTP * ATP$
$G_{\alpha,i}GTP + AC5CaG_{\alpha,olf}GTP * ATP \underset{k_b}{\overset{k_f}{\rightleftharpoons}} AC5CaG_{\alpha,olf}GTPG_{\alpha,i}GTP * ATP$
$cAMP + PKA \underset{k_b}{\overset{k_f}{\rightleftharpoons}} PKAcAMP2$
$cAMP + PKAcAMP2 \underset{k_b}{\overset{k_f}{\rightleftharpoons}} PKAcAMP4$
$PKAcAMP4 \underset{k_b}{\overset{k_f}{\rightleftharpoons}} PKAc + PKAreg$
$cAMP + PDE4 \underset{k_b}{\overset{k_f}{\rightleftharpoons}} PDE4 * cAMP$
$PDE10 + 2 * cAMP \underset{k_b}{\overset{k_f}{\rightleftharpoons}} PDE10c$
$cAMP + PDE10 \underset{k_b}{\overset{k_f}{\rightleftharpoons}} PDE10 * cAMP$
$cAMP + PDE10c \underset{k_b}{\overset{k_f}{\rightleftharpoons}} PDE10c * cAMP$

TABLE 2.5: Reversible biochemical dynamics of CAMKII and PP1.

Biochemical Reaction
$CaM + Ca \underset{k_b}{\overset{k_f}{\rightleftharpoons}} CaMCa2$
$Ca + CaMCa2 \underset{k_b}{\overset{k_f}{\rightleftharpoons}} CaMCa4$
$PP2B + CaM \underset{k_b}{\overset{k_f}{\rightleftharpoons}} PP2BCaM$
$PP2B + CaMCa4 \underset{k_b}{\overset{k_f}{\rightleftharpoons}} PP2Bc$
$PKAc + DARPP32 \underset{k_b}{\overset{k_f}{\rightleftharpoons}} PKAc * D32$
$PKAc + B56PP2A \underset{k_b}{\overset{k_f}{\rightleftharpoons}} PKAc * B56PP2A$
$D32p34 + PP1 \underset{k_b}{\overset{k_f}{\rightleftharpoons}} PP1D32p34$
$CDK5 + DARPP32 \underset{k_b}{\overset{k_f}{\rightleftharpoons}} CDK5 * D32$
$D32p75 + PKAc \underset{k_b}{\overset{k_f}{\rightleftharpoons}} PKAcD32p75$
$B72PP2A + Ca \underset{k_b}{\overset{k_f}{\rightleftharpoons}} B72PPA2Ca$
$B56PP2Ap + D32p75 \underset{k_b}{\overset{k_f}{\rightleftharpoons}} B56PP2Ap * D32p75$
$B72PP2A + D32p75 \underset{k_b}{\overset{k_f}{\rightleftharpoons}} B72PP2A * D32p75$
$D32p75 + B72PPA2Ca \underset{k_b}{\overset{k_f}{\rightleftharpoons}} B72PP2ACa * D32p75$
$D32p34 + PP2Bc \underset{k_b}{\overset{k_f}{\rightleftharpoons}} PP2Bc * D32p34$
$PP2BCaM + Ca \underset{k_b}{\overset{k_f}{\rightleftharpoons}} PP2BCaMCa2$
$PP2BCaMCa2 + Ca \underset{k_b}{\overset{k_f}{\rightleftharpoons}} PP2Bc$
$PP2B + CaMCa2 \underset{k_b}{\overset{k_f}{\rightleftharpoons}} PP2BCaMCa2$
$D32p75 + B56PP2A \underset{k_b}{\overset{k_f}{\rightleftharpoons}} B56PP2A * D32p75$
$D32p34 + B72PPA2Ca \underset{k_b}{\overset{k_f}{\rightleftharpoons}} B72PP2ACa * D32p34$
$D32p34 + B72PP2A \underset{k_b}{\overset{k_f}{\rightleftharpoons}} B72PP2A * D32p34$

TABLE 2.6: Irreversible Biochemical Reactions (1 of 2).

Biochemical Reaction
$G_{\alpha,olf}GTP \overset{k_{cat}}{\rightarrow} G_{\alpha,olf}GDP$
$D1RDAGolf \overset{k_{cat}}{\rightarrow} G_{\beta\gamma,olf} + D1RDA + G_{\alpha,olf}GTP$
$G_{\alpha,olf}GDP + G_{\beta\gamma,olf} \overset{k_{cat}}{\rightarrow} Golf$
$G_{\alpha,i}GTP \overset{k_{cat}}{\rightarrow} G_{\alpha,i}GDP$
$G_{\beta\gamma,i} + G_{\alpha,i}GDP \overset{k_{cat}}{\rightarrow} Gi$
$M4RAChGi \overset{k_{cat}}{\rightarrow} G_{\alpha,i}GTP + M4RACh + G_{\beta\gamma,i}$
$AC5G_{\alpha,olf}GTP * ATP \overset{k_{cat}}{\rightarrow} cAMP + AC5G_{\alpha,olf}GTP$
$cAMP + AC5G_{\alpha,olf}GTP \overset{k_{cat}}{\rightarrow} AC5G_{\alpha,olf}GTP * ATP$
$AC5 * ATP \overset{k_{cat}}{\rightarrow} cAMP + AC5$
$cAMP + AC5 \overset{k_{cat}}{\rightarrow} AC5 * ATP$
$AC5G_{\alpha,i}GTP * ATP \overset{k_{cat}}{\rightarrow} cAMP + AC5G_{\alpha,i}GTP$
$cAMP + AC5G_{\alpha,i}GTP \overset{k_{cat}}{\rightarrow} AC5G_{\alpha,i}GTP * ATP$
$AC5G_{\alpha,olf}GTPG_{\alpha,i}GTP * ATP \overset{k_{cat}}{\rightarrow} cAMP + AC5G_{\alpha,olf}GTPG_{\alpha,i}GTP$
$cAMP + AC5G_{\alpha,olf}GTPG_{\alpha,i}GTP \overset{k_{cat}}{\rightarrow} AC5G_{\alpha,olf}GTPG_{\alpha,i}GTP * ATP$
$AC5CaG_{\alpha,olf}GTPG_{\alpha,i}GTP * ATP \overset{k_{cat}}{\rightarrow} cAMP + AC5CaG_{\alpha,olf}GTPG_{\alpha,i}GTP$
$cAMP + AC5CaG_{\alpha,olf}GTPG_{\alpha,i}GTP \overset{k_{cat}}{\rightarrow} AC5CaG_{\alpha,olf}GTPG_{\alpha,i}GTP * ATP$
$AC5CaG_{\alpha,i}GTP * ATP \overset{k_{cat}}{\rightarrow} cAMP + AC5CaG_{\alpha,i}GTP$
$cAMP + AC5CaG_{\alpha,i}GTP \overset{k_{cat}}{\rightarrow} AC5CaG_{\alpha,i}GTP * ATP$

TABLE 2.7: Irreversible Biochemical Reactions (2 of 2).

Biochemical Reaction
$AC5Ca * ATP \overset{k_{cat}}{\rightarrow} cAMP + AC5Ca$
$cAMP + AC5Ca \overset{k_{cat}}{\rightarrow} AC5Ca * ATP$
$AC5CaG_{\alpha,olf}GTP * ATP \overset{k_{cat}}{\rightarrow} cAMP + AC5CaG_{\alpha,olf}GTP$
$cAMP + AC5CaG_{\alpha,olf}GTP \overset{k_{cat}}{\rightarrow} AC5CaG_{\alpha,olf}GTP * ATP$
$AC5G_{\alpha,olf}GTP \overset{k_{cat}}{\rightarrow} AC5 + G_{\alpha,olf}GDP$
$AC5CaG_{\alpha,olf}GTP \overset{k_{cat}}{\rightarrow} AC5Ca + G_{\alpha,olf}GDP$
$AC5CaG_{\alpha,i}GTP \overset{k_{cat}}{\rightarrow} AC5Ca + G_{\alpha,i}GDP$
$AC5G_{\alpha,i}GTP \overset{k_{cat}}{\rightarrow} AC5 + G_{\alpha,i}GDP$
$AC5G_{\alpha,olf}GTPG_{\alpha,i}GTP \overset{k_{cat}}{\rightarrow} AC5G_{\alpha,i}GTP + G_{\alpha,olf}GDP$
$AC5G_{\alpha,olf}GTPG_{\alpha,i}GTP \overset{k_{cat}}{\rightarrow} AC5G_{\alpha,olf}GTP + G_{\alpha,i}GDP$
$AC5CaG_{\alpha,olf}GTPG_{\alpha,i}GTP \overset{k_{cat}}{\rightarrow} AC5CaG_{\alpha,i}GTP + G_{\alpha,olf}GDP$
$AC5CaG_{\alpha,olf}GTPG_{\alpha,i}GTP \overset{k_{cat}}{\rightarrow} AC5CaG_{\alpha,olf}GTP + G_{\alpha,i}GDP$
$AC5G_{\alpha,olf}GTPG_{\alpha,i}GTP * ATP \overset{k_{cat}}{\rightarrow} G_{\alpha,i}GDP + AC5G_{\alpha,olf}GTP * ATP$
$AC5G_{\alpha,i}GTP * ATP \overset{k_{cat}}{\rightarrow} AC5 * ATP + G_{\alpha,i}GDP$
$AC5G_{\alpha,olf}GTPG_{\alpha,i}GTP * ATP \overset{k_{cat}}{\rightarrow} AC5G_{\alpha,i}GTP * ATP + G_{\alpha,olf}GDP$
$AC5G_{\alpha,olf}GTP * ATP \overset{k_{cat}}{\rightarrow} AC5 * ATP + G_{\alpha,olf}GDP$
$AC5CaG_{\alpha,olf}GTP * ATP \overset{k_{cat}}{\rightarrow} AC5Ca * ATP + G_{\alpha,olf}GDP$
$AC5CaG_{\alpha,olf}GTPG_{\alpha,i}GTP * ATP \overset{k_{cat}}{\rightarrow} AC5CaG_{\alpha,olf}GTP * ATP + G_{\alpha,i}GDP$
$AC5CaG_{\alpha,i}GTP * ATP \overset{k_{cat}}{\rightarrow} AC5Ca * ATP + G_{\alpha,i}GDP$
$AC5CaG_{\alpha,olf}GTPG_{\alpha,i}GTP * ATP \overset{k_{cat}}{\rightarrow} AC5CaG_{\alpha,i}GTP * ATP + G_{\alpha,olf}GDP$
$PDE4 * cAMP \overset{k_{cat}}{\rightarrow} PDE4 + AMP$

TABLE 2.8: Corticostriatal Biochemical Model Parameters (1 of 3). The bold parameters were hand-tuned, and the remaining parameters were taken from Nair *et al*. (2016).

Rate Constant	Value $[s^{-1}nM^{-1}]$	Rate Constant	Value $[s^{-1}nM^{-1}]$
krM4R*Gi	90	kfB72PP2ACa*D32p75	0.015
kfM4R*Gi	0.012	krB72PP2ACa*D32p75	100
krPP2B*CaMCa2	0.03	kcatPP2Bc*D32p34	1.2
kfPP2B*CaMCa2	0.1	kcatCDK5*D32	10
krPP2BCaMCa2*2Ca	100	**kactGi**	60
kfPP2BCaMCa2*2Ca	0.1	**kGiGTPase**	30
krPP2BCaM*2Ca	0.0002	**kGiback**	100
kfPP2BCaM*2Ca	0.006	**kfM4RACh*Gi**	1.2
kfPP1*D32p34	1	**krM4RACh*Gi**	90
krPP1*D32p34	1.5	kfPKA*2cAMP	0.026
kfPP2B*CaMCa4	0.1	krPKA*2cAMP	350
krPP2B*CaMCa4	0.003	krPKAc*PKAr	50
kfB72PP2A*Ca	0.01	kfPKAc*PKAr	0.03
krB72PP2A*Ca	10	kfPKA2cAMP*2cAMP	0.0346
kfPP2B*CaM	0.1	krPKA2cAMP*2cAMP	50
krPP2B*CaM	3000	kfCDK5*D32	0.001
kcatPKAc*D32	10	krCDK5*D32	100
$kG_{\alpha,olf}$GTPase	30	kactGolf	15
kfPP2Bc*D32p34	1.3	kcatPDE4*cAMP	2.5
krPP2Bc*D32p34	0.1	kfPKAc*D32	0.01
kfB56PP2A*D32p75	0.008	krPKAc*D32	200
krB56PP2A*D32p75	100	kfPDE4*cAMP	0.03
kfB56PP2Ap*D32p75	0.015	krPDE4*cAMP	1
krB56PP2Ap*D32p75	100	krPDE10*cAMP	1
kcatB56PP2Ap*D32p75	8	kcatPDE10c*cAMP	10
kcatB56PP2A*D32p75	1.5	kfPDE10*cAMP	1.00E-06
kcatB72PP2ACa*D32p75	8	kfcAMP*PDE10	0.1
kcatB72PP2A*D32p75	1.5	krcAMP*PDE10	2
kfB72PP2A*D32p75	0.008	kcatcAMP*PDE10	3
krB72PP2A*D32p75	100	kcatAC5$G_{\alpha,olf}$GTP*ATP	20

biomarkers measured in my model compared to the biomarkers measured in the various experiments that I used to fit my model.

2.3 RESULTS

2.3.1 *Precise temporal pattern and timing between Ca, DA, and ACh are required to maximize corticostriatal synaptic plasticity in direct MSNs*

I began by examining the temporal interaction between the calcium (Ca^{2+}) signal with the dopamine (DA) and acetylcholine (ACh) signals on the corticostriatal synaptic

TABLE 2.9: Corticostriatal Biochemical Model Parameters (2 of 3). The bold parameters were hand-tuned, and the remaining parameter values were taken from Nair *et al*. (2016).

Rate Constant	**Value** $[s^{-1}nM^{-1}]$	**Rate Constant**	**Value** $[s^{-1}nM^{-1}]$
kicatAC5G$_{\alpha,olf}$GTP*ATP	0.084	krPKAc*B56PP2A	0.3
kcatAC5*ATP	1	kfCaMCa2*2Ca	0.1
kicatAC5*ATP	0.0004	kcatPKAc*B56PP2A	0.2
kcatAC5G$_{\alpha,i}$GTP*ATP	0.25	kfPKAc*D32p75	0.1
kicatAC5G$_{\alpha,i}$GTP*ATP	0.00105	kfAC5G$_{\alpha,olf}$GTP*ATP	0.00105
kcatAC5CaG$_{\alpha,i}$GTP*ATP	0.125	kfAC5G$_{\alpha,i}$GTP*ATP	6.25E-05
kicatAC5CaG$_{\alpha,i}$GTP*ATP	2.81E-05	kfAC5G$_{\alpha,olf}$GTPG$_{\alpha,i}$GTP*ATP	0.0003
kcatAC5Ca*ATP	0.5	kfAC5Ca*ATP	7.50E-05
kicatAC5Ca*ATP	0.00015	kfD1R*Golf	0.003
kcatAC5CaG$_{\alpha,olf}$GTP*ATP	10	krD1R*Golf	5
kicatAC5CaG$_{\alpha,olf}$GTP*ATP	0.022	kfD1RDA*Golf	0.003
kfM4R*ACh	0.01	krD1RDA*Golf	5
kfM4RGi*ACh	1	kfB72PP2A*D32p34	0.0005
krM4RGi*ACh	90	krB72PP2A*D32p34	1
krM4R*ACh	90	krAC5X*ATP	1
kcatAC5G$_{\alpha,olf}$GTPG$_{\alpha,i}$GTP*ATP	5	kcatB72PP2A*D32p34	3
kicatAC5G$_{\alpha,olf}$GTPG$_{\alpha,i}$GTP*ATP	0.006	**kfAC5XG$_{\alpha,olf}$GTP**	0.2
kicatAC5CaG$_{\alpha,olf}$GTPG$_{\alpha,i}$GTP*ATP	0.00175	kfAC5Ca	0.001
kcatAC5CaG$_{\alpha,olf}$GTPG$_{\alpha,i}$GTP*ATP	2.5	**kfAC5XG$_{\alpha,i}$GTP**	50
kfAC5*ATP	0.0001	**kfAC5XNCG$_{\alpha,i}$GTP**	0.01
kfAC5CaG$_{\alpha,olf}$GTP*ATP	0.00055	**kfAC5XNCG$_{\alpha,olf}$GTP**	0.002
kfAC5CaG$_{\alpha,i}$GTP*ATP	5.63E-05	**krAC5XG$_{\alpha,olf}$GTP**	0.1
kfAC5CaG$_{\alpha,olf}$GTPG$_{\alpha,i}$GTP*ATP	0.000175	krAC5Ca	10
kfCaM*2Ca	0.006	**krAC5XG$_{\alpha,i}$GTP**	5
kGolfback	100	**krAC5XNCG$_{\alpha,i}$GTP**	0.01
krCaM*2Ca	20	**krAC5XNCG$_{\alpha,olf}$GTP**	0.01
kdpB56PP2Ap	0.008	krgso	0.2
krCaMCa2*2Ca	1000	krgsi	30
krPKAc*D32p75	100	kcatPP1*AKAR3p	1.2
kfPKAc*B56PP2A	0.001	kfPP1*AKAR3p	0

TABLE 2.10: Corticostriatal Biochemical Model Parameters (3 of 3). The parameter values were taken from Nair *et al*. (2016).

Rate Constant	**Value** $[s^{-1}nM^{-1}]$	**Rate Constant**	**Value** $[s^{-1}nM^{-1}]$
krPP1*AKAR3p	10	kpCaMKIIc	0.07
kcatPKAc*AKAR3	3	kfPP2A*pARPP21	0.004
kfPKAc*AKAR3	0	krPP2A*pARPP21	100
krPKAc*AKAR3	1	kcatPP2A*pARPP21	1
kfPDE10c*cAMP	0.1	kfPP2Ac*pARPP21	0.007
krPDE10c*cAMP	2	krPP2Ac*pARPP21	100
kfD1R*DA	0.005	kcatPP2Ac*pARPP21	10
kfD1RGolf*DA	0.005	kcatPP1*pSubstrate	10
krD1R*DA	5	kfPP1*pSubstrate	0.0005
krD1RGolf*DA	5	krPP1*pSubstrate	1
kfCaMKII*CaMCa4	0.1	kfPKAc*ARPP21	0.045
krCaMKII*CaMCa4	40	krPKAc*ARPP21	200
kfCaMKII*CaMCa2	0.1	kcatPKAc*ARPP21	10
krCaMKII*CaMCa2	400	kfCaMCa4*pARPP21	0.5
kfCaMKII*CaM	0.1	krCaMCa4*pARPP21	10
krCaMKII*CaM	4000	kdppCaMKII	0.1
kfCaMKIICaM*2Ca	0.006	kfpCaMKII*Substrate	0.0005
krCaMKIICaM*2Ca	2	krpCaMKII*Substrate	10
kfCaMKIICaMCa2*2Ca	0.1	kcatpCaMKII*Substrate	10
krCaMKIICaMCa2*2Ca	100	kftranspCaMKII	0.5
kfpCaMKII*CaM	0.1	krtranspCaMKII	0.001
krpCaMKII*CaM	400	kfPP1*pCaMKIIpsd	0.0008
kfpCaMKII*CaMCa2	0.1	krPP1*pCaMKIIpsd	1
krpCaMKII*CaMCa2	40	ktransCaMKII	0.5
kfpCaMKII*CaMCa4	0.1	kftransCaMKII	0.5
krpCaMKII*CaMCa4	0.4	krtransCaMKII	0.5
kfpCaMKIICaM*2Ca	0.006	kcatPP1*pCaMKIIpsd	1
krpCaMKIICaM*2Ca	2		
kfpCaMKIICaMCa2*2Ca	0.1		
krpCaMKIICaMCa2*2Ca	10		

TABLE 2.11: Previously used observable biomarkers.

Experiment	Protein	$\mathbf{x}_{bio}$	References
G-protein Activation *Saturation Dynamics*	Monoexponential $k = 10 - 100\ ms$ $B_{max} = 100$		Chuhma *et al*. (2014); Marcott *et al*. (2014)
Basal	cAMP	$30 - 90$ nM	Bacskai *et al*. (1993); Mironov *et al*. (2009)
No input	D32p34	400 nM	Nishi *et al*. (1997); Bateup *et al*. (2008)
	D32p75	1,200 nM	Bateup *et al*. (2008)
	ARPP21p	700 nM	Caporaso *et al*. (2000); Girault *et al*. (1990)
Slice Dopamine	D32p34	4,400 nM	Nishi *et al*. (2000); Bateup *et al*. (2008)
10 uM of D1R agonist	D32p75	6,000 nM	Nishi *et al*. (2000); Bateup *et al*. (2008)
	ARPP21p	4,900 nM	Girault *et al*. (1990)
Slice Calcium	D32p34	200 nM	Nishi *et al*. (2005, 2002)
100 uM of Ca	D32p75	6,000 nM	Nishi *et al*. (2005, 2002)
Slice PKA Dynamics *10 uM of D1R agonist*	cAMP	10,000 nM	Polito *et al*. (2013)
Slice PDE Dynamics *PDE Inhibitor*	D32p34	800 nM	Nishi *et al*. (2008)

TABLE 2.12: Additional observable biomarkers.

Experiment	Protein	$\mathbf{x}_{bio}$	References
Slice Acetylcholine *No dip in tonic ACh*	cAMP	0.33× (cAMP level w/ DA + ACh)	Nair *et al*. (2019)
10 nM	cAMP	1 × cAMP @ 10 nM	Nair *et al*. (2019)
100 nM	cAMP	0.2 × cAMP @ 10 nM	Nair *et al*. (2019)
500 nM	cAMP	0.03 × cAMP @ 10 nM	Nair *et al*. (2019)
1000 nM	cAMP	0.01 × cAMP @ 10 nM	Nair *et al*. (2019)
10000 nM	cAMP	0 × cAMP @ 10 nM	Nair *et al*. (2019)
Slice Dopamine			
10 nM	cAMP	0 × cAMP @ 10 nM	Yapo *et al*. (2017)
100 nM	cAMP	0.0.05 × cAMP @ 10 nM	Yapo *et al*. (2017)
500 nM	cAMP	0.4 × cAMP @ 10 nM	Yapo *et al*. (2017)
1000 nM	cAMP	0.65 × cAMP @ 10 nM	Yapo *et al*. (2017)
10000 nM	cAMP	1 × cAMP @ 10 nM	Yapo *et al*. (2017)

plasticity. The effect of the three signals on synaptic plasticity was measured through the level of phosphorylation of a generic substrate. The generic substrate stood in for the phosphorylation of voltage-gated ion channels, ionotropic receptors, and proteins involved in translation of plasticity related proteins. In order to measure the effect of the DA and ACh signals on the corticostriatal synaptic plasticity, I first applied the Ca^{2+} pulse at 2 seconds for a duration of 1 second. The calcium pulse represents the calcium that enters the neuron due to the repeated pairing of glutamate released by presynaptic neurons firing and the firing of the postsynaptic neuron (Yagishita *et al.*, 2014). The calcium signal induces an increase in the level substrate phosphorylation as shown in Figure 2.3. All of the substrate phosphorylation profiles are normalized to the maximum level of substrate phosphorylation induced by the calcium signal including the substrate phosphorylation profile induced by the the calcium signal. Therefore the pSubstrate profile induced by the calcium signal only has a maximum of one. Then, the DA and ACh signals were applied one second after the calcium signal. The DA signal consisted of a pulse of DA for one second from the basal DA level of 10 nM to 1500 nM, which is shown in Figure 2.3D, and the ACh signal consisted of a dip in the 100 nM basal level of ACh to 0 nM as shown in 2.3E. The ACh was assumed to go to zero, due to the quick dynamics of acetylcholine esterase that quickly cleaves ACh molecules. When the DA and ACh signals arrive one second after the Ca^{2+} pulse, I observed a dramatic increase in the level of pSubstrate. The increase in the level pSubstrate due to the timing of the three signals is shown in Figure 2.3A. This highlights a clear increase in the level pSubstrate due to the DA and ACh signals with the Ca^{2+} signal.

I then explored the effect of the DA and ACh signals arriving at different times relative to the Ca^{2+} signal. Figure 2.3B shows the pSubstrate profile when the DA and ACh signals arrive one second before the Ca^{2+} signal, at the same time as the Ca^{2+} signal, and one second after the Ca^{2+} signal. The arrival of the DA and the ACh signals one second before the Ca^{2+} signal resulted in no significant increase in the level pSubstrate. When the DA and ACh signals arrived at the same time and one second after the Ca^{2+} signal, there I observed a large increase in the pSubstrate level, with a larger increase observed when the DA and ACh signals arrived one second

after the Ca^{2+} signal. The dramatic effect of the DA and ACh signals arriving before and after the Ca^{2+} signal establishes a clear temporal interaction between the three signals. Therefore, additional timing between the three signals was considered. In order to compare the effect of different timings of the DA and ACh signals compared to the Ca^{2+} signal, the area on the pSubstrate curve was calculated and normalized relative to the Ca^{2+} only pSubstrate curve shown in Figure 2.3A. Then, I considered seven different timings ($\Delta t = -2\ s$, $\Delta t = -1\ s$, $\Delta t = 0\ s$, $\Delta t = 1\ s$, $\Delta t = 2\ s$, $\Delta t = 3\ s$, $\Delta t = 4\ s$) between the arrival of the Ca^{2+} signal (t_{Ca}) and the arrival of the dual DA and ACh signals ($t_{DA,ACh}$). Here, the time difference Δt is defined as $t_{Ca} - t_{DA,ACh}$. A similar trend was observed where the negative timings ($\Delta t < 0$) resulted in minimal substrate phosphorylation, while the positive timings ($\Delta t \geq 0$) resulted in a large enhancement of the total substrate phosphorylated. The optimal timing occurred when the DA and ACh signals arrived one second after the Ca^{2+} signal and the level of substrate phosphorylation gradually decayed as the timing increased. Figure 2.3F shows the total amount of substrate phosphorylation at the seven different timings.

2.3.2 *Changes in synaptic plasticity are highly sensitive to changes in DA concentrations in low dopamine regime compared to high dopamine regime.*

Next, I examined the sensitivity of the substrate phosphorylation level to non-physiological reductions in the DA levels. This mimics the loss of DA that is typically associated with PD. As the DA concentration is reduced, I observed an expected decreases in the amount of substrate phosphorylation. Figure 2.4A shows the decrease the total level of substrate phosphorylation at different timings as the dopamine amplitude concentration is decreased from 1500 nM to 187.5 nM. This decrease is due to less DA binding to the D1R to increase PKA, which influences the substrate phosphorylation level by phosphorylating DARPP-32 at the Thr-34 residue. Phosphorylation of the Thr-34 residue inhibits PP1, which is responsible for dephosphorylating the generic substrate. Therefore, a reduction in the activation of the D1R by dopamine leads to less inhibition of PP1, which lowers the level of the phosphorylated substrate. Interestingly, the decrease in the level of substrate phosphorylation at all timings decreased non-linearly with the dopamine

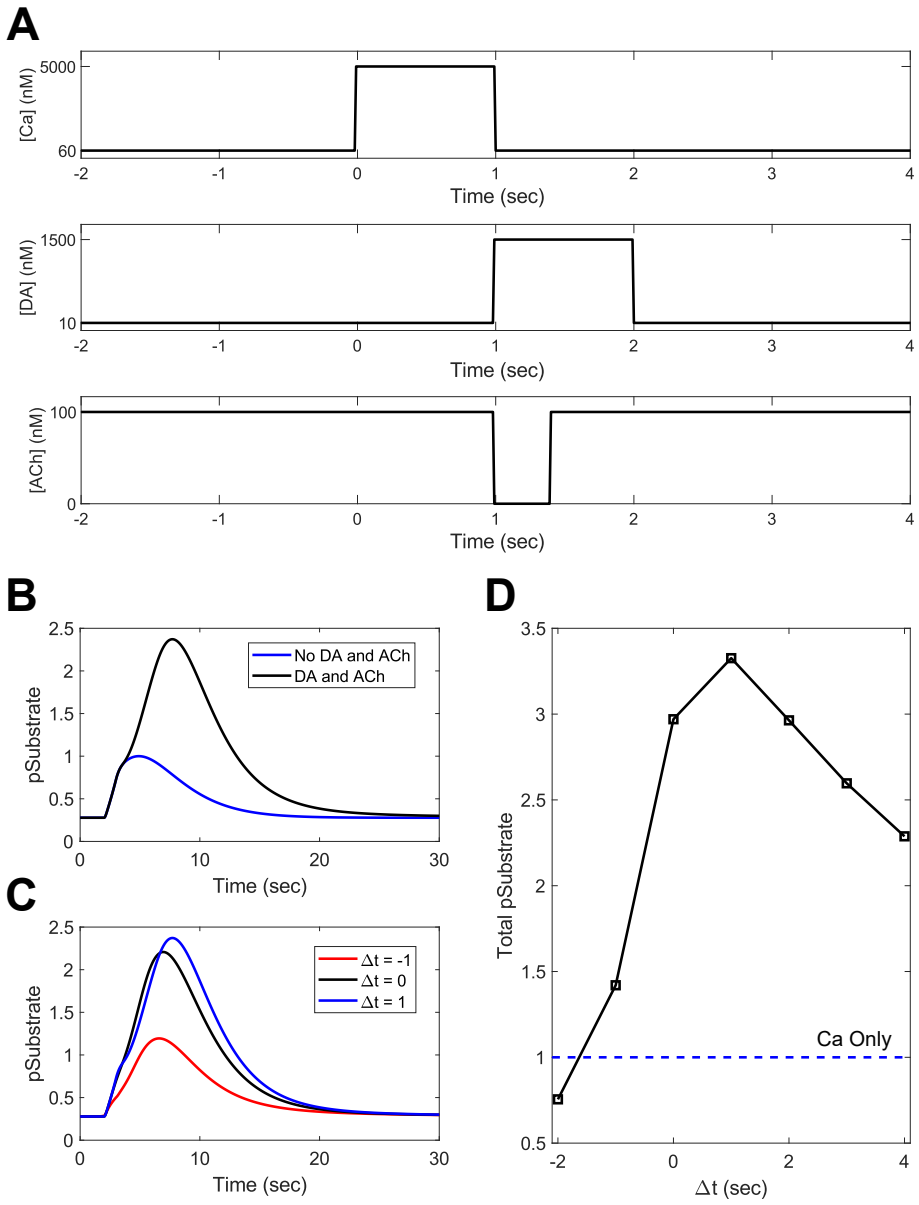

FIGURE 2.3: The temporal interactions of Ca^{2+}, DA, and ACh signals. An example of the calcium, dopamine, and acetylcholine signals are shown in **(A)**. **(B)** A comparison of the amount of substrate phosphorylated when the DA and ACh signals arrive one second after the Ca^{2+} pulse (black line) and when they are absent (blue line). Each of the profiles are normalized to the maximum of the Ca^{2+} pulse only profile. **(C)** shows the profile of the phosphorylated substrate when the DA and ACh signals arriving one second before the calcium signal ($\Delta t = -1$), at the same time as the calcium signal ($\Delta t = 0$), and one second after the calcium signal ($\Delta t = 1$). **(D)** shows the total amount of substrate phosphorylated for different arrival times of the DA and ACh signals relative to the Ca^{2+} pulse (Δt). The time difference between the two signals was calculated by subtracting the time of the DA pulse and ACh dip arriving ($t_{DA,ACh}$) from the time that the calcium pulse arrived (t_{Ca}) in other words $\Delta t = t_{DA,ACh} - t_{Ca}$. The total amount of phosphorylated substrate was calculated by taking the area under the curve of the pSubstrate curves for each timing and was normalized to the level of phosphorylation due to only the calcium signal. The blue-line represents the level of phosphorylation due to only the calcium signal arriving.

concentration amplitude. At high concentrations of DA, a relatively large reduction in the DA level only produces a small decrease in the total substrate phosphorylation level. This is shown in Figure 3A, where a 50 % reduction in the DA pulse amplitude from 1500 nM to 750 nM produced only a relatively small reduction in the substrate phosphorylation level. At low levels of dopamine, such as when the DA pulse amplitude dropped from 750 nM to 375 nM, there was a large drop in total substrate phosphorylation. This shows that the system is robust to changes in the DA concentration at high concentrations of DA but highly sensitive to changes in the DA concentration at low concentrations. This may explain why symptoms of PD typically emerge with the death of approximately 70 % of dopamine neurons. A similar trend was observed in the profiles of the key plasticity proteins PKA, pSubstrate, CaMKII, and PP1 as shown in Figures 2.4B, 2.4C, 2.4D, and 2.4E, respectively.

Dopamine is not the only neuromodulator that controls the activity of PKA and subsequently the substrate phosphorylation level. Acetylcholine also influences the substrate phosphorylation level via the G_i-coupled M4 receptor. In order to understand the role of the acetylcholine dip paired with the DA pulse, I held to the acetylcholine concentration constant and observed the changes in the plasticity time window as the amplitude of the dopamine pulse was reduced. Figure 2.5 shows the total phosphorylation plasticity time window as the dopamine amplitude concentration was decreased. Once again there was an overall reduction in the total amount of substrate phosphorylation that had a nonlinear relationship to the decrease in the concentration of dopamine. This is due to more ACh binding to the M4R, which inhibited PKA production. Since PKA influence PP1 inhibition, the reduction in PKA resulted in more dephosphorylation of the generic substrate. In addition to the overall reduction in the total substrate phosphorylation level, there was a shift in the optimal timing of the Ca^{2+} pulse and the DA pulse (Δt). Previously the optimal timing (Δt) of the Ca, DA, and ACh signals was 1 sec but the model showed that the removal of the ACh dip moved the optimal timing to $\Delta t = 0$ sec. This loss of the physiological ACh signal forced the DA and Ca^{2+} signals to arrive at the same time to achieve maximal enhancement of substrate phosphorylation. These results highlight the importance of the acetylcholine dip for healthy corticostriatal plasticity dynamics.

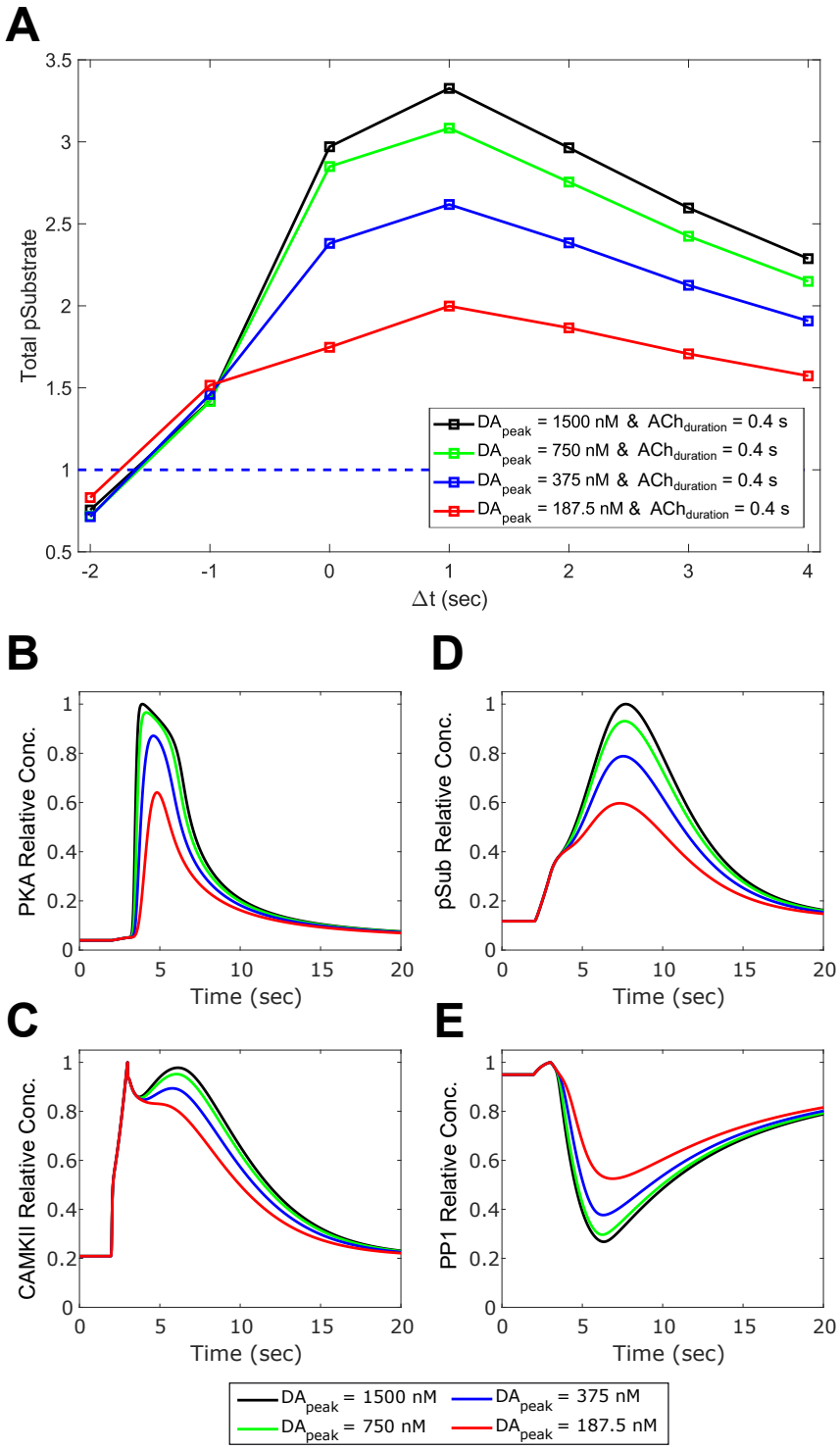

FIGURE 2.4: Changes in corticostriatal plasticity signaling due to a reduction in high amplitude dopamine pulses. **(A)** shows the decrease in the total amount of substrate phosphorylation at different timings as the amplitude of the dopamine pulse decreases. The corresponding changes in the profiles of key plasticity proteins such as PKA, CaMKII, pSubstrate, and PP1 are shown in **(B)**, **(C)**, **(D)**, and, **(E)**, respectively. In all of the figures, the level of substrate phosphorylation and the amplitude of the plasticity proteins decreases with the concentration of the dopamine amplitude.

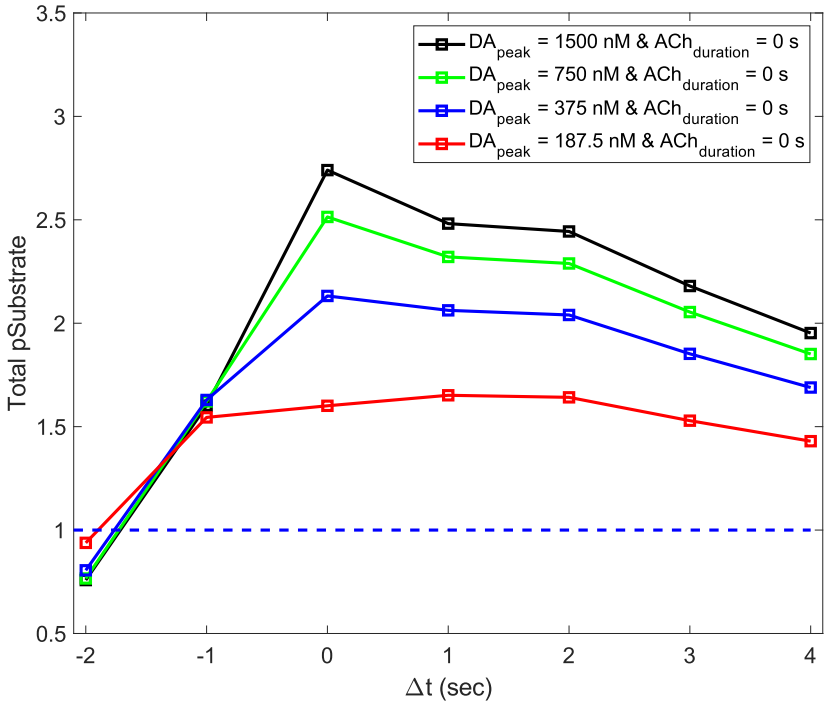

FIGURE 2.5: Effect of acetylcholine dip on corticostriatal plasticity window. The amount of substrate phosphorylation at different timings of the Ca^{2+} signal arriving and the dual DA and ACh signals. The phosphorylation time window decreases as the dopamine amplitude concentration decreases.

2.3.3 *Acetylcholine dip duration could restore the changes in corticostriatal synaptic plasticity due to the loss of dopaminergic neurons*

Next, I investigated if enhancing the acetylcholine dip duration could be used to offset the negative effect of DA depletion. I considered the case where the DA pulse amplitude is decreased by 70 % from 1500 nM to 450 nM, which is the percentage of DA neuron lost where PD motor symptoms typically begin to emerge. Figure 2.6 shows that this decrease the level of PKA, pSubstrate, CaMKII, and PP1. Then, I determined if the healthy profiles of these plasticity signaling proteins could be restored by extending the ACh dip duration. First, I showed that reducing the ACh dip duration from 0.4 *sec* to 0.2 *sec* reduces the level of PKA, pSubstrate and CaMKII while it increases the level of PP1. Then, I extended the ACh dip to 1 *sec*. This boosted the profiles of the plasticity proteins (red-line) close to their previous healthy case profile shapes (dashed black-line) shown in Figure 2.6. These results indicate that harnessing the acetylcholine signal could restore the corticostriatal dynamics when there is a deficiency in dopamine signaling.

Since extending the ACh dip is able to compensate for a reduction in the dopamine amplitude concentration, next I investigated the acetylcholine dip duration required to restore the total amount of substrate phosphorylation and PKA activation. Figure 2.6A shows the exponential increase in the required duration of the ACh dip to restore the phosphorylated substrate level and PKA activation level as the DA amplitude concentration decreases. After the dopamine amplitude concentration dropped below 250 nM, the ACh dip duration was not able to restore the total substrate phosphorylation and total PKA activation to the healthy level. My additional investigations into attempting to offset signaling losses due to dopamine amplitude concentration under 250 nM showed that increasing the ACh dip duration from 0.4 seconds to 5 seconds increased the profile of PKA and pSusbstrate, as shown in Figures 2.7B and 2.7C, but increasing the ACh dip further produced no significant further increase in the profiles of PKA and pSubstrate. These results show that there is an upper limit on the extending the ACh dip duration to offset dopamine amplitude concentration deficits.

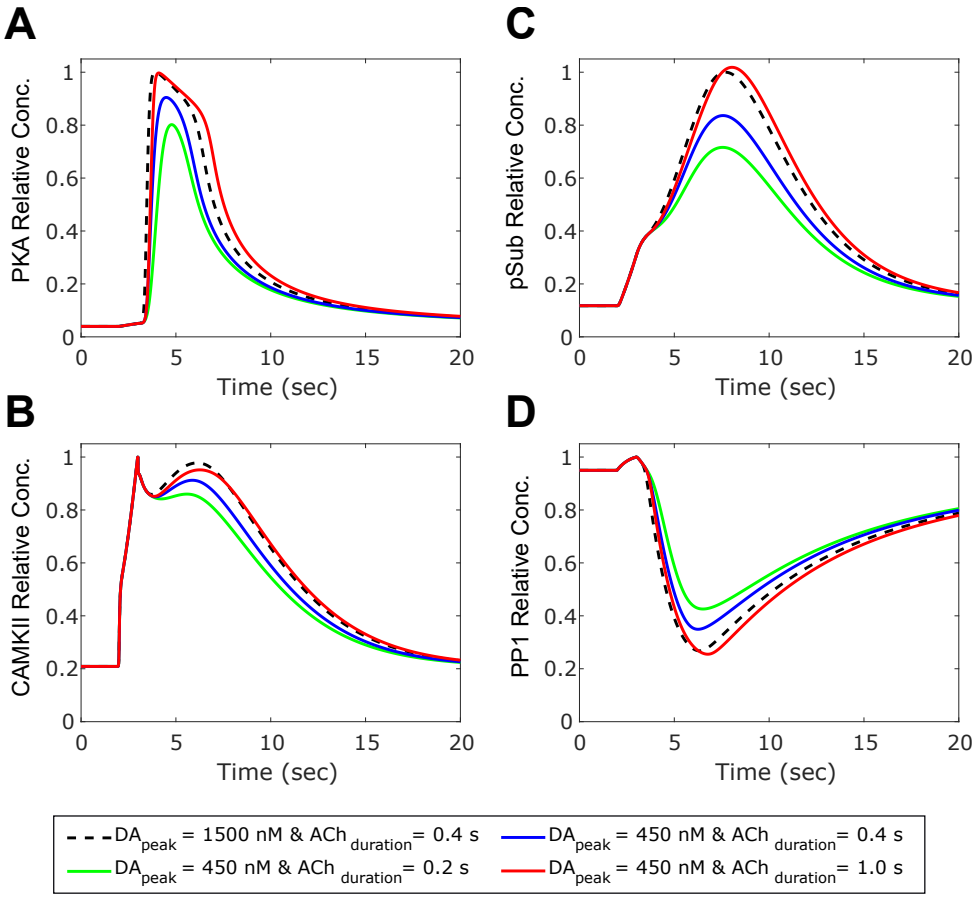

FIGURE 2.6: The effect of the acetylcholine dip duration on key plasticity proteins. The effect of changing the duration of the ACh dip duration from 0.2 *sec* to 1 *sec* on key plasticity signaling proteins such as PKA, CaMKII, pSubstrate, and PP1 when the dopamine amplitude concentration has been reduced by 70 % to 450 nM is shown in **(A)**, **(B)**, **(C)**, and **(D)**, respectively.

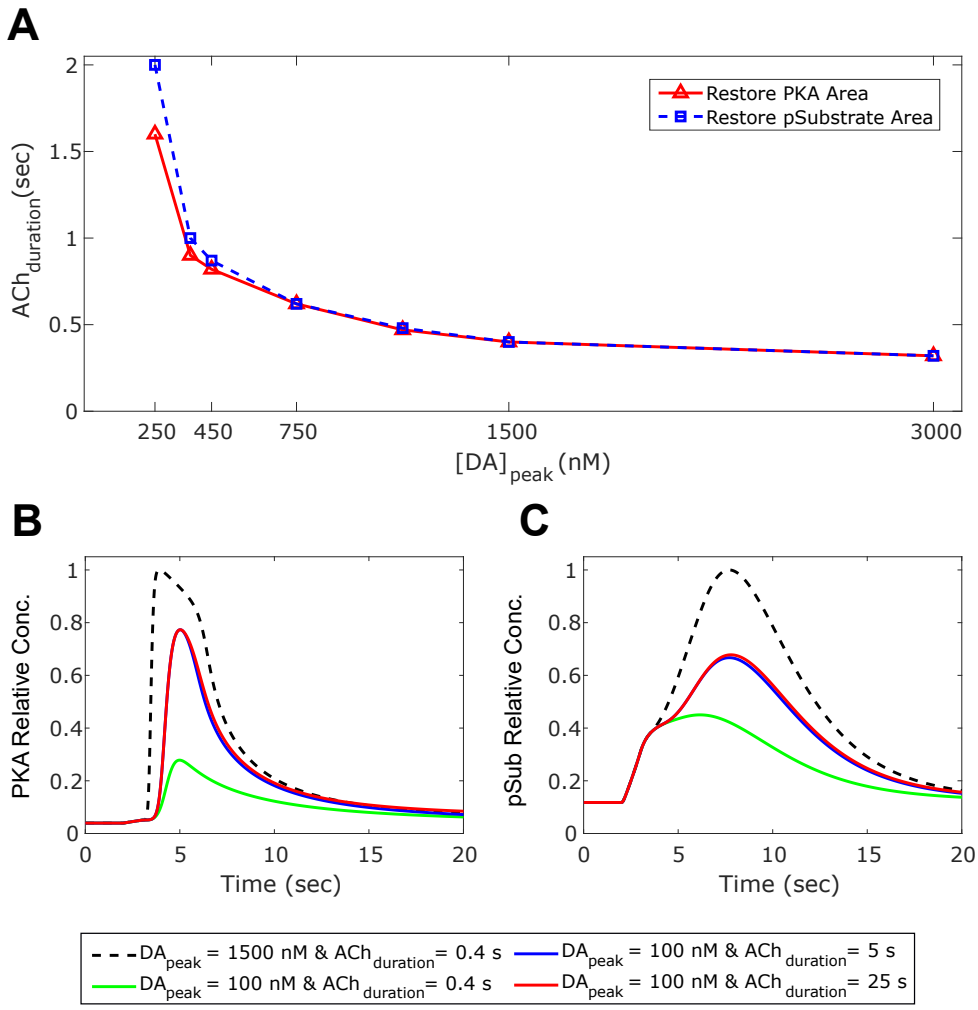

FIGURE 2.7: Harnessing the acetylcholine dip duration to offset dopamine depletion. **(A)** shows the acetylcholine dip duration required to restore the healthy level of total phosphorylated substrate at different dopamine amplitude concentrations. **(B)** and **(C)** show the profiles of PKA and pSubstrate, respectively, for the health (black dashed-line), the dopamine amplitude concentration of 100 nM & acetylcholine dip duration of 0.4 *sec* (green-line), the dopamine amplitude concentration of 100 nM & acetylcholine dip duration of 5 *sec* (blue-line), and the dopamine amplitude concentration of 100 nM & acetylcholine dip duration of 25 *sec* (red-line).

2.3.4 *A second Ca^{2+} signal boosts DA and ACh signaling*

Finally, I explored harnessing a second Ca^{2+} signal to boost the corticostriatal signaling back to the healthy level. A second Ca^{2+} signal means that the presynaptic corticostriatal synapse is stimulated repeatedly prior to the postsynaptic MSN. Practically, this means that the signal is repeated to offset the reduced pathological dynamics from the loss of dopamine neurons. The calcium signal with the second pulse is shown in Figure 2.8A. In Figures 2.8B, 2.8C, 2.8D, and 2.8E, I showed how adding a second calcium pulse for 1 second was able to boost the profiles of the plasticity proteins PKA, pSubstrate, CaMKII, and PP1, respectively. While extending the ACh dip was able to almost restore the exact shape of the healthy profiles of the key plasticity signaling proteins, the second calcium pulse was not able to restore the shape of the profiles for most of the plasticity proteins except for pSubstrate. Since pSubstrate stands in for the cellular proteins that increase the excitability of the MSN, this suggests that harnessing a second calcium signal could restore the healthy plasticity dynamics. When the second calcium pulse was extended from 1 second to 2 seconds, the PKA profile had no significant increase in the level of PKA and the pSubstrate level decreased. The counterintuitive result arose from the balance of CaMKII and PP1, which compete to phosphorylate and dephosphorylate, respectively, the generic substrate. Upon examination of the profiles of the CaMKII and PP1 for the case with a second calcium pulse for 1 second, shown as the red-line compared to the case with out the second calcium pulse shown as the green-line in Figures 2.8D and 2.8E, the increase in the amplitude of CaMKII is much greater than the decrease in the amplitude of PP1. Then, if the profile of the case with a second calcium pulse for a duration of 1 second is compared to the case with a calcium pulse for 2 seconds, the amplitude of the CaMKII profile only increased slightly while the minimum of the PP1 profile is much higher. Therefore, the ratio of the dephosphorylating PP1 to the phosphorylating CaMKII is higher. Figure 2.8F shows the ratio of CaMKII and PP1 over time for the different calcium signal protocols. This figure clearly shows that ratio of CaMKII is highest when the second calcium signal has a duration of 1 second.

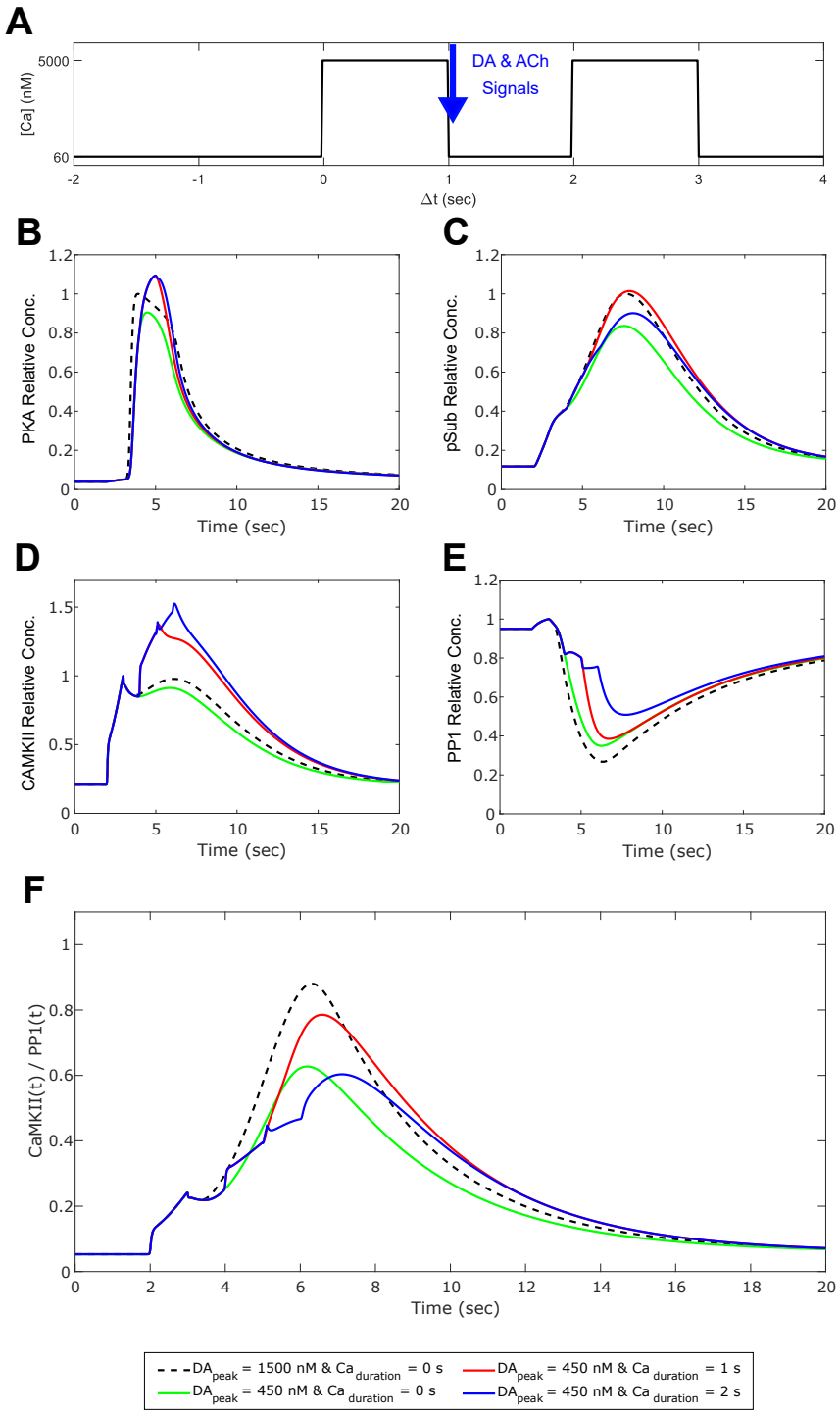

FIGURE 2.8: Effect of a second Ca^{2+} pulse on offsetting dopamine depletion. **(A)** shows the profile of the Ca^{2+} signal with the second pulse relative to the DA and ACh pulses (blue-arrow). **(B-E)** show the boosted profiles of key signaling proteins involved in substrate phosphorylation with the second Ca^{2+} pulse. **(F)** shows the ratio of CAMKII to PP1. **(G)** The biochemical signaling pathways in direct MSNs activated by Ca, DA, and ACh.

2.4 SUMMARY

In this section, I investigated the changes in the corticostriatal plasticity induced by different timings, concentration, and durations of Ca^{2+}, dopamine, and acetylcholine. I first examined how the timing of the calcium signal relative to the dual dopamine and acetylcholine signals altered profile of a generic substrate phosphorylation, which stood in for the phosphorylation of proteins involved in increasing the excitability of the dMSN. Then, I showed how the plasticity time window of the total amount of substrate phosphorylation decreased nonlinearly with the decrease in the amplitude concentration of the dopamine pulse in order to gain insight into how the corticostriatal plasticity dynamics changes with the death of dopamine neurons as PD progresses. Since the dopamine pulse is associated with an acetylcholine dip, I examined the importance of the acetylcholine dip on the plasticity time window of the substrate phosphorylation. I showed that the loss of the acetylcholine dip moved the optimal timing of the dopamine pulse arriving forward, such that the dopamine and the calcium pulses were required to arrive at the same time to induce the maximum level of the substrate phosphorylation. Since the acetylcholine dip influenced the optimal time, I then explored and showed how extending the acetylcholine dip duration could offset losses in the corticostriatal signaling due to the decrease in the amplitude of the dopamine pulse concentration. Finally, I examined how a second calcium pulse could be harnessed to offset the loss of the substrate phosphorylation and the corticostriatal signaling in the reduced dopamine level state.

CHAPTER 3

A COMPUTATIONAL MODEL OF DOPAMINERGIC MODULATION OF HIPPOCAMPAL SCHAFFER COLLATERAL-CA1 LONG-TERM PLASTICITY

3.1 INTRODUCTION

One of the most studied regions of the mammalian brain is the hippocampus, due to its role in learning and memory. In particular, changes in the connections, otherwise know as synapses, between excitatory neurons of different subregions of the hippocampus have been extensively studied. The researchers Lomo and Bliss were the first researchers to describe long-term potentiation (LTP), which is an activity-dependent plasticity phenomena, where the high frequency stimulation of the perforant path of the hippocampus in rabbit increased the strength of the synapse hours after the stimulation protocol (Lomo, 1966; Bliss and Lømo, 1973). The perforant path and the dentate gyrus region of the hippocampus are shown in the schematic of the hippocampus in Figure 3.1. In 1983, Collingridge *et al.* (1983) found that LTP could be blocked by antagonizing the glutamate ionotropic N-Methyl-d-aspartic acid receptor (NMDAR) with the antagonist D-AP5. The dynamics of the AMPAR are much faster than the NMDAR (Andreasen *et al.*, 1989; Blake *et al.*, 1988), but both depolarize the membrane potential when activated. The AMPAR opens upon glutamate binding to the receptor, while it was found that NMDAR requires glutamate to bind to the receptor as well as the ejection of a Mg^{2+} ion due to the depolarization of the membrane potential to open (Herron *et al.*, 1986). Wigström *et al.* (1986) found that LTP exhibited the same properties as Hebbian plasticity, which was the postulate by Hebb (1949). The co-requirement of glutamate binding to the NMDAR and the ejection of the Mg^{2+} provided a biophysical explanation of the Hebbian nature of LTP (Bliss and Collingridge, 1993; Collingridge, 1985). In opposition to LTP, the Schaffer-Collateral CA1 pyramidal neuron (SC-CA1) synpase could also be depotentiated with repeated low frequency stimulation that induced

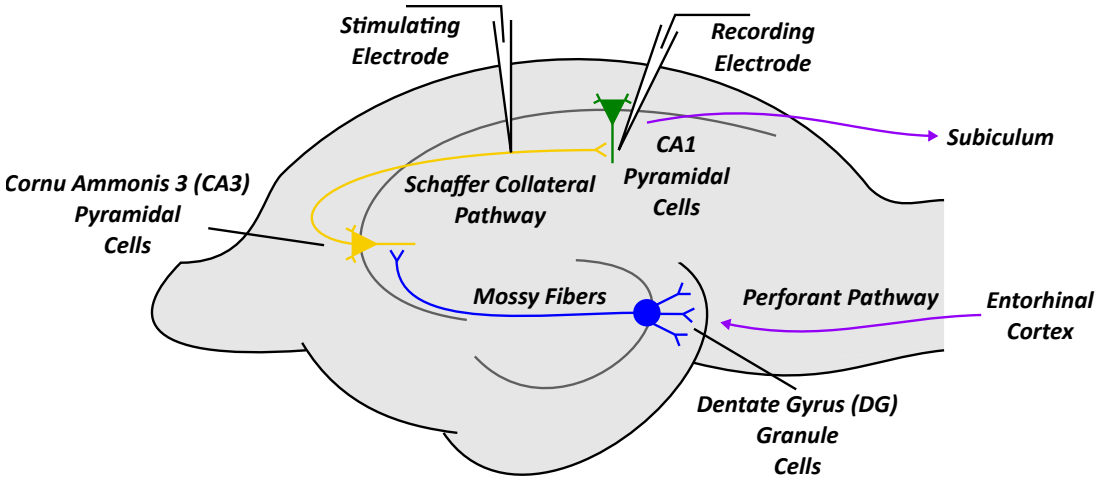

FIGURE 3.1: A schematic of the trisynaptic hippocampal circuit. The entrohinal cortex (EC) projects into the hippocampus through the perforant pathway to the dentate gyrus (DG) granule cells. Then, the DG projects to the CA3 pyramidal neurons through mossy fiber synapses. The CA3 pyramidal neurons project through the Schaffer-collateral (SC) synapse to CA1 pyramidal neurons. Finally, CA1 pyramidal neurons project out of the hippocampus to the subiculum.

long-term depression (LTD) (Dudek and Bear, 1992). Similar to LTP, LTD was found to be dependent on the NMDAR activation (Mulkey and Malenka, 1992).

The ejection of the Mg^{2+} ion from the NMDAR plays an additional role of allowing the influx of Ca^{2+} into the neuron (Alford *et al.*, 1993). Calcium not only depolarizes the membrane potential but also acts as a secondary messenger to activate and influence many signaling pathways, such as cyclic adenosine monophosphate (cAMP)-dependent protein kinase (PKA), Ca^{2+}/calmodulin-dependent kinase II (CAMKII), and protein kinase C (PKC) (Malinow *et al.*, 1989; Matthies and Reymann, 1993; Reymann *et al.*, 1988a,b). These signaling pathways are critical for the consolidation of early-LTP into late-LTP (Kandel *et al.*, 2014). Early-LTP last under an hour while late-LTP lasts hours to days. In addition to these pathways being activated by Ca^{2+}, they are also dependent on various neuromodulators, which bind to their corresponding G-protein coupled receptor, to amplify or inhibit these signaling pathways. It is well-established that the activation of some of these pathways are time-dependent. Particularly, it has been shown in *in vitro* hippocampal slice experiment that the prior HFS-induced LTP occluded further potentiation by directly activating the PKA pathway with the PKA activator Rp-cAMPS (Frey *et al.*, 1993). Furthermore, the

activation of the PKA pathway before High Frequency Stimulation (HFS)-induced LTP prevented additional induction of late-LTP. These experiments showed a clear temporal dependence on the activation of these pathways relative to the activity-dependent plasticity induction protocols. Therefore, researchers began to study how various neuromodulators, such as dopamine, modulate the activity-dependent plasticity induction in the SC-CA1 synpase.

Dopamine released in the hippocampus plays a critical role in regulating spatial learning, novelty detection, and novel object recognition by strengthening memory encoding and pruning existing memories. Due to the role dopamine plays in memory, researchers examined how dopamine modulates SC-CA1 synaptic plasticity in a dose dependent manner in order to understand its role in learning and memory (Mockett *et al.*, 2004; Huang and Kandel, 1995; Lemon and Manahan-Vaughan, 2006; Shivarama Shetty *et al.*, 2016). Researchers found that similar to the activation of the PKA pathways with Rp-CAMPS, after a strong HFS protocol, the activation of dopamine D1/D5 receptors by the dopamine agonist SKF 38393 after a HFS protocol occluded further potentiation of the SC-CA1 synapse by the dopamine agonist (Huang and Kandel, 1995). Additionally, the application of the dopamine agonist SKF 38393 prior to a strong HFS protocol prevented further late-LTP consolidation. Further investigation into the modulation of the SC-CA1 synaptic plasticity by various dopamine agonists showed that dopamine agonist alone induced a slow-onset-potentiation of the synaptic plasticity. The dopaminergic slow-onset-potentiation was found to be dose-dependent where higher concentrations of a dopamine agonists induced more potentiation (Sajikumar and Frey, 2004; Navakkode *et al.*, 2012; Shivarama Shetty *et al.*, 2016). One researcher found that the application of a low concentration of dopamine to the SC-CA1 synapse induced slow-onset-depotentiation (Sajikumar and Frey, 2004). Additionally, an alternative D1/D5 dopamine agonist SKF 83959 has been suggested to selectively activate the PLC pathway to induce depotentiation (Liu *et al.*, 2009; Undieh, 2010). These results taken together suggest that dopamine at high concentrations promote potentiation, while lower levels of dopamine may promote depotentiation of the SC-CA1 synapse. Furthermore, this suggest that the concentration, duration, timing of the application

of the D1/D5 agonist relative to a stimulation protocol, and the specific D1/D5 dopamine agonist plays a significant role in the modulation of activity-dependent plasticity induction in the SC-CA1 synapse.

Exploring the effect of the parameter space of various concentration levels of the applied pharmacological agent as well as the frequency-specific characteristics of the HFS/LFS protocol on the D1/D5 receptors mediated spatiotemporal modulation of high frequency stimulation/ low frequency stimulation (HFS/LFS)-induced long-term potentiation/depotentiation (LTP/LTD) is a combinatorically challenging problem which is both expensive and time-consuming to address in experiments alone. A computational modeling approach integrating experimental findings at various levels (such as molecular and cellular levels) and from diverse experimental protocols in a biophysiological manner could potentially address this challenge. In this regard, computational modeling approaches have been developed to explain molecular level mechanisms underlying LTP/LTD (Triesch *et al.*, 2018; Bhalla and Iyengar, 1999; Kotaleski and Blackwell, 2010; Blackwell and Jedrzejewska-Szmek, 2013; Blackwell and Miningou, 2020; Mäki-Marttunen *et al.*, 2020; Foncelle *et al.*, 2018; Brzosko *et al.*, 2017) and modulation of the neural activity by the activation of G-protein coupled receptors, such as dopamine receptors (Nakano *et al.*, 2010; Nair *et al.*, 2016; Yapo *et al.*, 2017; Blackwell *et al.*, 2019), muscarinic receptors (Nair *et al.*, 2015; Mergenthal *et al.*, 2020), and β-adrenergic receptors (Luczak *et al.*, 2017; Jedrzejewska-Szmek *et al.*, 2017). Furthermore, unified multi-scale models have been developed that combine detailed biochemical molecular level dynamics with electrical dynamics in medium spiny neurons (Mattioni and Le Novère, 2013) and CA1 hippocampal neurons (Bhalla, 2011). Detailed molecular-level modeling of chemical signaling pathways in these works explained the published biochemical data from several diverse experimental protocols on LTP induction in the CA1 pyramidal neurons. Moreover, it provided a comprehensive understanding of critical molecular mechanisms involved in the modulation of this LTP by dopamine. Despite these initial modeling efforts, the literature still lacks a unified modeling approach that integrates biochemical effects on electrophysiology to systematically investigate the

spatiotemporal modulation of HFS/LFS-induced LTP/LTD of the SC-CA1 synapses by the activation of D1/D5 receptors under various parametric conditions.

In this chapter, I have developed a computational modeling approach to integrate the spatiotemporal impact of D1/D5 agonists on the HFS/LFS-induced early and late LTP/LTD at the electrophysiological level. The modeling hypothesis is that the chain of biochemical signaling initiated by HFS/LFS and D1/D5 receptors agonists compete for a limited available biochemical resources to induce and/or modulate late-LTP/LTD in the hippocampal SC-CA1 synapses. I have formulated the hypotheses based on the available experimental results on the modulation of the HFS-induced LTP by various D1/D5 agonists, where authors showed that the application of SKF 38393 more than 150 minutes before the HFS protocol initially enhanced the HFS-induced LTP but after 3 hours the dopaminergic enhancement decayed back to the LTP level induced by only HFS (Huang and Kandel, 1995; Navakkode *et al*., 2012). In contrast, the application of D1/D5 agonists after the HFS protocol does not have a significant effect on HFS-induced LTP (Huang and Kandel, 1995; Otmakhova and Lisman, 1998). Additionally, it has been shown experimentally that D1/D5 receptor modulation of LFS-induced LTD due to the release of SKF 38393 immediately after the LFS protocol disappears when the same amount of SKF 38393 is released 60 minutes after the LFS protocol (Mockett *et al*., 2007). These experiments highlight a reduced efficacy of either the D1/D5 receptors agonist or HFS/LFS protocol when it arrives as the second input. Based on these experimental results, I hypothesize that the first input may use up the shared biochemical resources rendering the second input less effective.

Using the hypotheses mentioned above, I have developed a set of phenomenological models to describe the temporal dose-dependent effect of dopamine D1/D5 receptors agonist on the maximum synaptic conductance using published electrophysiological data from hippocampal CA1 slice experiments on the % change in field excitatory postsynaptic potential (fEPSP) slope in response to D1/D5 agonists SKF 38393, 6-bromo-APB, and dopamine. Since the fEPSP slope is an extracellular EPSP recording from the stratum radiatum of the CA1 area, I have used the recent data on the simultaneous recording of fEPSP slope, and intracellular EPSP slope

(Abrahamsson *et al.*, 2016) to develop a linear correlation and used it to transform the synaptic EPSP from CA1 neuron model into fEPSP. To model the synaptically evoked EPSP, I have used an experimentally validated single compartmental biophysiological model in a Hodgkin-Huxley formalism from (Golomb *et al.*, 2006) to represent the CA1 neuron dynamics. The synaptic dynamics, as well as the dynamics of high/low-frequency stimulation (HFS/LFS), induced LTP/LTD of SC-CA1 synapse are described using published phenomenological models of SC-CA1 synaptic dynamics and LTP/LTD (Graham, 2001; Migliore and Lansky, 1999; Saftenku, 2002). I have used an approximate Bayesian computation method with a sequential Monte Carlo scheme (Toni *et al.*, 2008) to estimate model parameters from the available electrophysiological data in the literature.

3.2 MODEL SYSTEM

3.2.1 *Hippocampal CA1 pyramidal neuron model*

We used an experimentally validated single compartment Hodgkin-Huxley model (Golomb *et al.*, 2006) to represent the CA1 pyramidal neuron dynamics. The details of the model can be found in (Golomb *et al.*, 2006). Here, I briefly described the model. The time evolution of the membrane potential, V, is governed by the sum of various ionic currents, as given by Eq. 3.1.

$$\begin{aligned} C_m \frac{dV}{dt} &= -g_L(V - V_L) - I_{NaT} - I_{NaP} - I_{Kdr} \\ &\quad -I_A - I_M - I_{Ca} - I_C - I_{sAHP} - I_s. \end{aligned} \tag{3.1}$$

In Eq. 3.1, I_{NaT} and I_{NaP} are the transient and persistent sodium (Na^+) currents, respectively. I_{Kdr} is the delayed rectifier potassium (K^+) current, and I_M is the muscarinic-sensitive K^+ current. I_A is the A-type K^+ current. I_{Ca} is the high threshold calcium (Ca^{2+}) current, and I_C is the Ca^{2+}-activated K^+ current for the rapid spike repolarization. I_{sAHP} is the slow Ca^{2+}-activated K^+ current responsible for the slow after hyperolarization and the spike frequency adaptation. I_s is the synaptic current

to the CA1 pyramidal neuron from the Schaffer collateral-CA1 synapse, which I described in the next section. C_m, g_L, and V_L are the membrane capacitance, the leaky current conductance, and the leaky current reversal potential, respectively.

The ionic currents in Eq. 3.1 are voltage-dependent, and I provided their functional forms in Eqs. 3.2a-3.2h.

$$I_{NaT}(V,h) = g_{NaT}m^3h(V-V_{Na}), \tag{3.2a}$$
$$I_{NaP}(V) = g_{NaP}p(V-V_{Na}), \tag{3.2b}$$
$$I_{Kdr}(V,n) = g_{Kdr}n^4(V-V_K), \tag{3.2c}$$
$$I_A(V,b) = g_A a^3 b(V-V_K), \tag{3.2d}$$
$$I_M(V,z) = g_M z(V-V_K), \tag{3.2e}$$
$$I_{Ca}(V,r) = g_{Ca}r^2(V-V_{Ca}), \tag{3.2f}$$
$$I_c(V,c) = g_c dc(V-V_K), \tag{3.2g}$$
$$I_{sAHP}(V,q) = g_{sAHP}q(V-V_K). \tag{3.2h}$$

For a given ionic current I_i where $i \in \{NaT, NaP, Kdr, A, M, Ca, c, sAHP\}$, g_i is the maximum conductance of the i^{th} ionic channel type. V_{Na}, V_K, and V_{Ca} are the reversal potential of the sodium, potassium, and calcium channels, respectively. The dynamics of the gating variables (m,h,p,n,a,b,z,r,d,c,q) are described by Eqs. 3.3a-3.3q. Their activation and deactivation dynamics are described by either a differential equation, a generic activation/inactivation function $x_\infty(V) = \{1+exp[-(V-\theta_x)]/\sigma_x\}^{-1}$, or a combination of both. The dynamics of the Ca^{2+} activated ion channel gating variables d and q depend on the intracellular Ca^{2+} concentrations. I provided the governing equation of the Ca^{2+} dynamics in Eq. 3.3r, where v is the rate of Ca^{2+} into the neuron

and τ_{Ca} is the Ca^{2+} decay constant.

$$
\begin{aligned}
m &= m_\infty(V), && (3.3a)\\
\frac{dh}{dt} &= \frac{\phi[h_\infty(V)-h]}{\tau_h(V)}, && (3.3b)\\
\tau_h(V) &= 0.1 + 0.75 \\
&\quad \times\{1+exp[-(V-\theta_{ht})/\sigma_{ht}]\}^{-1}, && (3.3c)\\
p &= p_\infty(V), && (3.3d)\\
\frac{dn}{dt} &= \phi[n_\infty(V)-n]/\tau_n(V), && (3.3e)\\
\tau_n(V) &= 0.1 + 0.5 \\
&\quad \times\{1+exp[-(V-\theta_{nt})/\sigma_{nt}]\}^{-1}, && (3.3f)\\
a &= a_\infty(V), && (3.3g)\\
\frac{db}{dt} &= [b_\infty(V)-b]/\tau_b, && (3.3h)\\
\frac{dz}{dt} &= [z_\infty(V)-z]/\tau_z, && (3.3i)\\
\frac{dr}{dt} &= [r_\infty(V)-r]/\tau_r, && (3.3j)\\
r_\infty(V) &= \{1+exp[-(V-\theta_r)/\sigma_r]\}^{-1}, && (3.3k)\\
\frac{dc}{dt} &= [c_\infty(V)-c]/\tau_c, && (3.3l)\\
d &= d_\infty([Ca^{2+}]), && (3.3m)\\
c_\infty(V) &= \{1+exp[-(v-\theta_c)/\sigma_c]\}^{-1}, && (3.3n)\\
d_\infty([Ca^{2+}]) &= (1+a_c/[Ca^{2+}])^{-1}, && (3.3o)\\
\frac{dq}{dt} &= [q_\infty([Ca^{2+}])-q]/\tau_q, && (3.3p)\\
q_\infty([Ca^{2+}]) &= (1+a^4/[Ca^{2+}]^4)^{-1}, && (3.3q)\\
\frac{d[Ca^{2+}]}{dt} &= -vI_{Ca} - [Ca^{2+}]/\tau_{Ca}. && (3.3r)
\end{aligned}
$$

We provided the CA1 pyramidal neuron model parameters used in this chapter in Table 3.1.

TABLE 3.1: CA1 Pyramidal Neuron Model Parameters Golomb *et al*. (2006).

Parameter	Value	Parameter	Value
C	1 μF/cm^2	θ_m	-30 mV
g_L	0.05 mS/cm^2	σ_m	9.5 mV
g_{NaT}	35 mS/cm^2	θ_h	-45 mV
g_{NaP}	0.3 mS/cm^2	σ_h	-7 mV
g_{Kdr}	6 mS/cm^2	θ_{ht}	-40.5 mV
g_A	1.4 mS/cm^2	σ_{ht}	-6 mV
g_M	1 mS/cm^2	ϕ	1
g_{Ca}	0.08 mS/cm^2	θ_p	-46 mV
g_c	10 mS/cm^2	σ_p	3 mV
g_{sAHP}	5 mS/cm^2	θ_n	-35 mV
V_L	-70 mV	σ_n	10 mV
V_{Na}	55 mV	θ_{nt}	-27 mV
V_K	-90 mV	σ_{nt}	-15 mV
V_{Ca}	120 mV	θ_a	-50 mV
ν	0.13 cm^2/(ms$\times\mu$A)	σ_a	20 mV
τ_{Ca}	13 ms	θ_b	-80 mV
σ_b	-6 mV	θ_z	-39 mV
σ_z	5 mV	τ_b	15
τ_z	75	τ_r	1
θ_r	-20 mV	σ_r	10 mV
τ_c	2	θ_c	-30 mV
σ_c	7 mV	a_c	6
τ_q	450	a_q	2

3.2.2 *Schaffer collateral - CA1 pyramidal neuron synaptic dynamics*

To represent the dynamics of the synaptic current, I_s, from the Schaffer collateral fiber to the CA1 pyramidal neuron (see Eq. 3.1), I used a phenomenological synaptic model (Graham, 2001), described by Eqs. 3.4a -3.4b. The model captures the synaptic contributions from the AMPA and NMDA neurotransmitters.

$$I_s = g_s n_{syn}(V - E_s) \tag{3.4a}$$

$$g_s = (1-\alpha)g_{AMPA} + \alpha g_{NMDA} \tag{3.4b}$$

In Eq. 3.4a, g_s, V, and E_s are the synaptic conductance, the postsynaptic CA1 pyramidal neuron membrane potential, and the synaptic reversal membrane potential, respectively. n_{syn} is a scaling parameter based on an estimate of the number of excitatory synapses (Megıas *et al.*, 2001). The synaptic conductance g_s (see Eq. 3.4b) is the weighted sum of the AMPA (g_{AMPA}) and NMDA (g_{NMDA}) conductances, where α determines the relative contribution of the AMPA and NMDA conductances. I presented a dynamical model of the AMPA and NMDA conductances in Eqs. 3.4c-3.4h.

$$
\begin{aligned}
g_{AMPA} &= \frac{\bar{g}_s \tau_1 \tau_2}{\tau_2 - \tau_1} h, && \text{(3.4c)} \\
g_{NMDA} &= \frac{\bar{g}_s}{1 + \mu_s [Mg^{2+}] e^{-\gamma_s V}} w, && \text{(3.4d)} \\
\frac{dh}{dt} &= u, && \text{(3.4e)} \\
\frac{du}{dt} &= \frac{-u(\tau_1 + \tau_2) - h}{\tau_1 \tau_2}, && \text{(3.4f)} \\
\frac{dw}{dt} &= r, && \text{(3.4g)} \\
\frac{dr}{dt} &= \frac{-r(\tau_3 + \tau_4) - w}{\tau_3 \tau_4}. && \text{(3.4h)}
\end{aligned}
$$

In Eqs. 3.4c-3.4h, $\bar{g}_s$ is the maximum synaptic conductance of the Schaffer collateral - CA1 pyramidal neuron (SC-CA1) synapse, measured in the presence of AMPA only receptors. The gating variables h and w gate the AMPA and NMDA conductances, respectively. τ_1 and τ_2 are the AMPA ionotropic receptors' rise and decay time constants, respectively. Similarly, τ_3 and τ_4 are the NMDA ionotropic receptors' rise and decay time constants, respectively. The NMDA conductance g_{NMDA} is dependent on both the postsynaptic membrane potential V and the magnesium concentration $[Mg^{2+}]$. μ_s and γ_s are scaling parameters.

The complete synaptic dynamics of the SC-CA1 synapse described by Eqs. 3.4a-3.4h is governed by a set of model parameters $\bar{g}_s, \tau_1, \tau_2, \tau_3, \tau_4, \mu_s, \gamma_s, [Mg^{2+}], \alpha, E_s$. I fixed the model parameters $[Mg^{2+}]$, α, and E_s to 1 μM, 0.1, and 0 mV, respectively (Graham, 2001). Then I inferred the remaining model parameters

using an approximate Bayesian inference approach based on the sequential Monte Carlo (ABC-SMC) (Toni *et al.*, 2008) from experimental data of AMPA and NMDA excitatory postsynaptic current induced by stimulating the SC-CA1 synapse with a brief electrical pulse (Christie and Jahr, 2006). Briefly, I first fitted the parameters $\bar{g}_s$, τ_1, and τ_2 with the ABC-SMC approach using a sum of the squared errors distance function shown in Eq. 3.5c between the AMPA current (Eq. 3.5a) in my model and the experimental data available from (Christie and Jahr, 2006). Then, I fitted the parameters τ_3, τ_4, μ_s, and γ_s using a distance function that measured the distance between the NMDA current (Eq. 3.5b) in my model and the data from (Christie and Jahr, 2006). I provided the inferred model parameters in Table 3.2 and Figure 3.2 shows the histograms representing the approximate posterior distributions for each of the parameters.

$$I_{AMPA} = (1-\alpha) g_{AMPA}(V - E_s), \tag{3.5a}$$

$$I_{NMDA} = \alpha g_{NMDA}(V - E_s), \tag{3.5b}$$

$$d(I_{AMPA}, x_d) = \sum_{i=1}^{n} \left(I_{AMPA}(i) - x_d(i)\right)^2, \tag{3.5c}$$

$$d(I_{NMDA}, x_d) = \sum_{i=1}^{n} \left(I_{NMDA}(i) - x_d(i)\right)^2. \tag{3.5d}$$

TABLE 3.2: SC-CA1 synaptic dynamics parameters.

Parameter	Value	Reference
$[Mg^{2+}]$	1 μM	(Graham, 2001)
α	0.1	(Graham, 2001)
E_s	0 mV	(Graham, 2001)
n_{syn}	1.79×10^4	(Megıas *et al.*, 2001)

TABLE 3.3: Inferred SC-CA1 synaptic dynamics parameters.

Parameter	Value
$\bar{g}_s$	$4.981 \times 10^{-3} \pm 0.7 \times 10^{-3}\ mS$
τ_1	$0.8263 \pm 0.17\ ms$
τ_2	$4.548 \pm 0.74\ ms$
τ_3	$0.8189 \pm 0.49\ ms$
τ_4	$74.788 \pm 12\ ms$
μ_s	$0.2866 \pm 0.096\ \mu M^{-1}$
γ_s	$1.3 \times 10^{-2} \pm 0.52 \times 10^{-2}\ mV^{-1}$

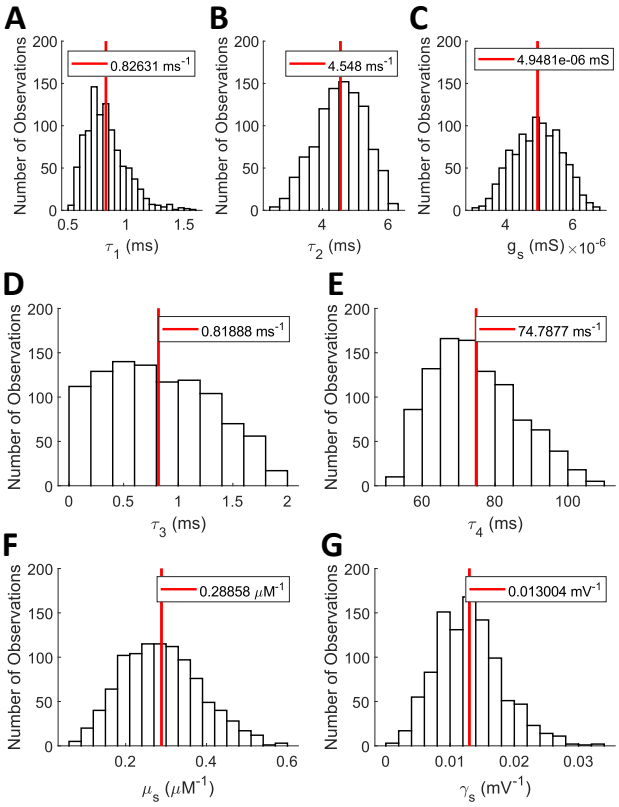

FIGURE 3.2: Inferred posterior distribution of the SC-CA1 synaptic dynamics parameters. Each histogram represents the approximate posterior distributions of the parameters **(A)** τ_1, **(B)** τ_2, **(C)** $\bar{g}_s$, **(D)** τ_3, **(E)** τ_4, **(F)** μ_s, and **(G)** γ_s. The red-line represents the mean value.

3.2.3 *Frequency dependent SC-CA1 LTP/LTD dynamics*

In order to model the dynamics of the high-frequency stimulation (HFS) induced long-term potentiation (LTP) and the low-frequency stimulation (LFS) induced long-term

depression (LTD), I modified a published phenomenological model (Migliore and Lansky, 1999; Saftenku, 2002) and inferred the model parameters using the available hippocampal slice experimental data in the literature on the HFS/LFS induced LTP/LTD. This simplified model assumes that the HFS/LFS induced LTP/LTD is mediated by the change in the maximum synaptic conductance $\bar{g}_s$ of the SC-CA1 synapse due to the changes in the calcium (Ca^{2+}) current that enters through the NMDA receptors. Although the model does not include the intermediate biochemical dynamics, it exhibits multiple fixed points, which allow it to capture the frequency-dependent effects of the HFS/LFS protocol on the induced LTP/LTD. I provided the mathematical representation of the modified model in Eqs. 3.6a-3.6i.

$$I_{Ca,NMDA} = 0.1 I_{NMDA} \frac{V - 20}{V - E_s} \tag{3.6a}$$

$$\frac{dC}{dt} = -\eta C - \gamma_C I_{Ca,NMDA} \tag{3.6b}$$

$$\frac{dN_p}{dt} = \nu C - (\rho_C p_p - I_{Ca} g) N_p + \frac{\rho_C M_p N_p^2}{\rho_C A_p + N_p^2} \tag{3.6c}$$

$$\frac{dN_d}{dt} = \nu C - (\rho_B p_d - I_{Ca} g) N_d + \frac{\rho_B M_d N_d^2}{\rho_B A_d + N_d^2} \tag{3.6d}$$

$$\frac{dP}{dt} = f\left(\frac{dN_p}{dt} - \frac{dN_d}{dt}\right) \tag{3.6e}$$

$$C_{tot} = \int_0^T C dt \tag{3.6f}$$

$$\rho_C = \begin{cases} \rho_1 & C_{tot} < C_{thr,1} \\ \rho_2 & C_{tot} \geq C_{thr,1} \end{cases} \tag{3.6g}$$

$$\rho_B = \begin{cases} \rho_3 & C_{tot} < C_{thr,2} \\ \rho_4 & C_{tot} \geq C_{thr,2} \end{cases} \tag{3.6h}$$

$$Z = 1 + P \tag{3.6i}$$

Eq. 3.6a, together with Eq. 3.1, Eqs. 3.3a-3.3r, and Eqs. 3.4a-3.4h, describe the frequency-dependent HFS/LFS induced modulation by the NMDA Ca^{2+} current, $I_{Ca,NMDA}$. γ_C is the rate constant and $\frac{1}{\eta}$ is the time constant of the dynamics. Eqs. 3.6c-3.6i model the HFS/LFS induced net changes in the maximum synaptic conductance $\bar{g}_s$ (see Eqs. 3.4a-3.4h) of the SC-CA1 synapse. The model parameters ρ_C, ρ_B, p_p, p_d, g, M_p, M_d, A_p, and A_d in Eqs. 3.6c-3.6d control the number of fixed points exhibited by the model. The model parameter f in Eq. 3.6e is a constant scaling factor, which determines the relative contribution of the HFS/LFS induced changes in the maximum synaptic conductance $\bar{g}_s$. ρ_C toggles the equilibrium points in order to shift the weak HFS (ρ_1) to the strong HFS (ρ_2) protocol. Furthermore, ρ_C and ρ_B toggle LFS induced plasticity between the different LTD equilibrium points. The equilibrium points shift when the total amount of calcium, C_{tot}, crosses one of the calcium thresholds $C_{thr,1}$ or $C_{thr,2}$. P is the change in the strength of the SC-CA1 synapse from the control condition. This change has been incorporated in my model by modifying the maximum synaptic conductance $\bar{g}_s$ of the AMPA conductance g_{AMPA} by the factor $1 + P$.

Using Eqs. 3.6a-3.6i, I modified my synaptic current model shown in Eq. 3.4a as

$$g_s = (1-\alpha)(1+P)g_{AMPA} + \alpha g_{NMDA} \tag{3.7}$$

$$I_s = g_s n_{syn}(V - E_s) \tag{3.8}$$

to incorporate the effect of the HFS/LFS induced changes in the synaptic current to the CA1 pyramidal neuron. With this, the complete model of the HFS/LFS induced LTP/LTD is described by Eq 3.1, Eqs 3.2a-3.2h, Eqs 3.3a-3.3r, Eqs 3.4b-3.4h, Eqs 3.6a-3.6i, and Eq 3.8.

To complete my modeling such that my model predicts the experimentally observed HFS/LFS induced LTP/LTD in hippocampal slices, I fixed the model parameters in Eq. 3.1, Eqs. 3.2a-3.2h, Eqs. 3.3a-3.3r, and Eq. 3.4b-3.4h to the estimated model parameters values tabulated in Tables 3.1 and 3.2. I inferred the remaining model parameters in Eqs. 3.6a-3.6i using the available experimental data in the literature from various hippocampal slice experiments on the % change in

field excitatory postsynaptic potential (fEPSP) slope in response to various HFS/LFS protocols (Li *et al.*, 2013; Zhang *et al.*, 2008; Blitzer *et al.*, 1995; Hernandez *et al.*, 2005; Kasahara *et al.*, 2001; Roberto *et al.*, 2003; Papatheodoropoulos and Kostopoulos, 2000; Huang and Kandel, 1995; Stramiello and Wagner, 2008; Fonseca *et al.*, 2006; Karpova *et al.*, 2006; Liu *et al.*, 2009; Mockett *et al.*, 2007; Daoudal *et al.*, 2002; Heynen *et al.*, 1996).

Our model provides the intracellular excitatory post-synaptic potential (iEPSP). Therefore, I required a transformation from iEPSP to fEPSP to compare my model output to the experimental measurements of fEPSPs from the stratum radiatum of the CA1 region. To find a transformation function, I used recent data on the simultaneous recording of fEPSP slope and iEPSP slope from the hippocampal slices (Abrahamsson *et al.*, 2016). Since the experimental data showed an almost linear relation between fEPSP and iEPSP, I performed a least-squares regression to obtain a linear transformation function (see also Figure 3.3A)

$$Q(x) = 0.35912x + 0.12199. \tag{3.9}$$

Here, $Q(x)$ and x are the fEPSP and iEPSP slopes, respectively, at a given time.

Furthermore, to infer the model parameters more efficiently, I derived a linear mapping between the fractional change in the maximum SC-CA1 synaptic conductance $1 + P$ (see Eq. 3.6i) and the % change in the evoked fEPSP measurements in my model by performing a least-squares regression (see Eq. 3.10 as well as Figure 3.3B).

$$G(P) = 62.5414(1 + P) + 37.3962. \tag{3.10}$$

Here, $G(P)$ is the % change in the evoked fEPSP slope at a given time with $G(P) = 100\%$ as the normalized base line value corresponding to $P = 0$.

To find a single set of parameters values for the model parameters η, γ_C, ν, ρ_1, ρ_2, ρ_3, ρ_4, p_p, p_d, g, M_p, M_d, A_p, A_d, and f involved in Eqs. 3.6a-3.6i that captures the experimentally observed HFS and LFS induced LTP and LTD, respectively, in this simplified model is a challenging problem. I first hand-fitted the parameters ρ_1,

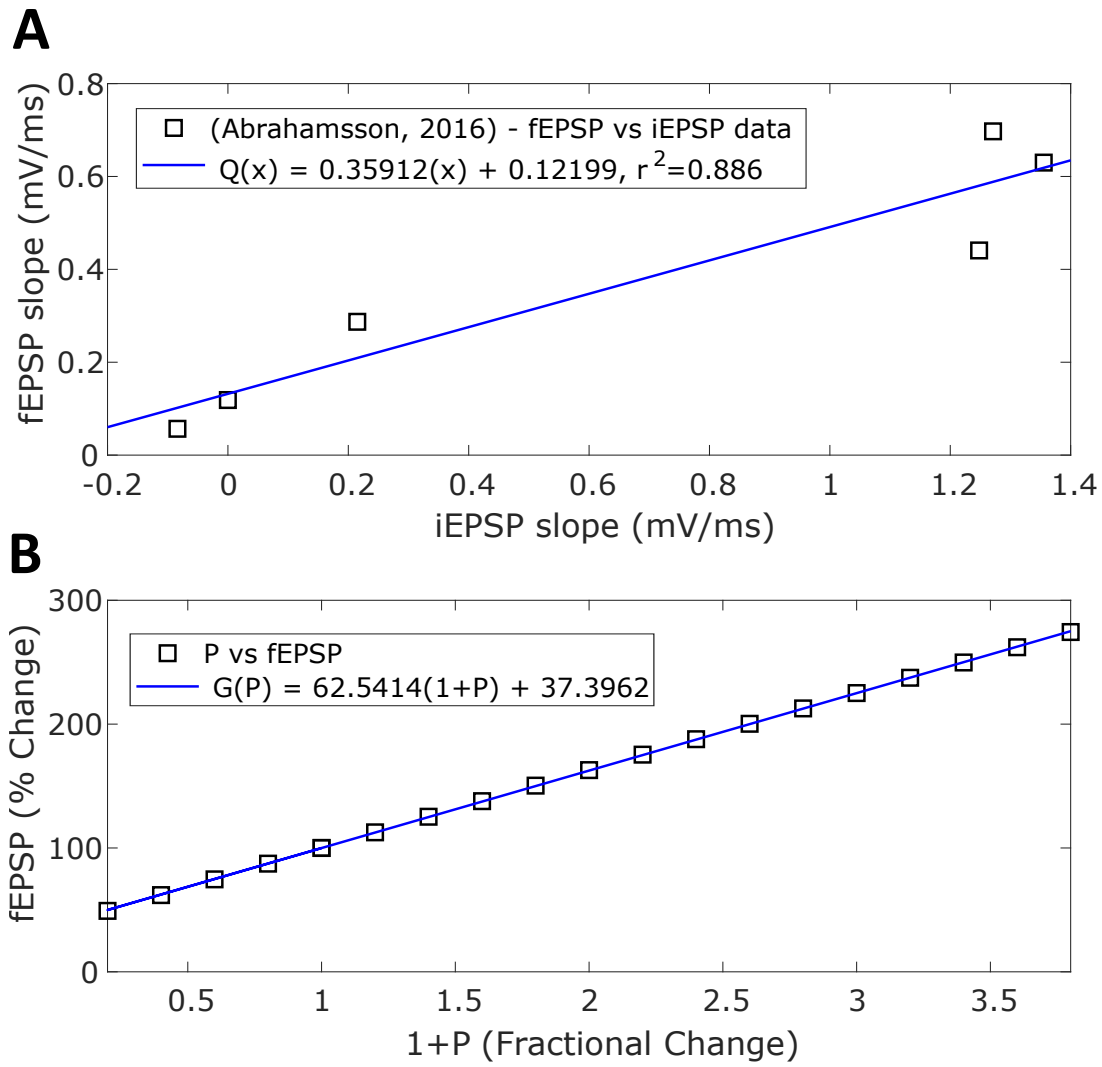

FIGURE 3.3: Mapping Functions. **(A)** shows a linear relationship between fEPSP and iEPSP (black-squares). The fitted linear least-squares regression $Q(x)$ mapping fEPSP to iEPSP is shown as a blue-line. **(B)** shows a linear relationship between the fractional change in the maximum synaptic conductance $(1 + P)$ and % change in the slope of the evoked fEPSPs (black-squares). The linear relationship was fit with a least-squares regression $G(P)$ shown as a blue-line.

ρ_2, ρ_3, and ρ_4 to establish the multiple equilibrium points present in LTP and LTD, as observed in the experimental data. Then, I inferred two sets of parameters values, one for the HFS-induced LTP and another for the LFS-induced LTD, from the available experimental data in the literature on the HFS-induced LTP (Li *et al.*, 2013; Zhang *et al.*, 2008; Blitzer *et al.*, 1995; Hernandez *et al.*, 2005; Kasahara *et al.*, 2001; Roberto *et al.*, 2003; Papatheodoropoulos and Kostopoulos, 2000; Huang and Kandel, 1995; Stramiello and

Wagner, 2008; Fonseca *et al.*, 2006; Karpova *et al.*, 2006) and on the LFS-induced LTD (Huber *et al.*, 2001; Daoudal *et al.*, 2002; Liu *et al.*, 2009; Selig *et al.*, 1995; Mockett *et al.*, 2007; Heynen *et al.*, 1996). The model parameters for the HFS-induced LTP and the LFS-induced LTD were inferred separately using an approximate Bayesian inference approached based on sequential Monte Carlo (Toni *et al.*, 2008). Below I describe the details of the parameter estimation approach from the experimental data for both LTP and LTD.

We first categorized the unknown model parameters into two sets. The first set consisted of model parameters p_p, p_d, M_p, M_d, A_p, and A_d, which are associated with the late-LTP or late-LTD and govern the steady-state changes in the late-LTP or late-LTD. The second set consisted of model parameters f, γ_C, η, and g, which govern the fast early-LTP or early LTD. To infer the model parameters, I noticed that the slow late-LTP or late-LTD parameters are independent of the spiking activity induced by the HFS or LFS protocol in the CA1 pyramidal neuron. This led me to set the NMDA calcium current $I_{Ca,NMDA} = 0$ in Eq. 3.6a which resulted in the decay of C to 0 on the order of few minutes based the fast rate of decay parameter η. I then applied the steady-state conditions on the Eqs. 3.6a-3.6d, which resulted in

$$N_p(N_p^2 p_p - M_p N_p + \rho_C A_p p_p) = 0, \tag{3.11a}$$

$$N_d(N_d^2 p_d - M_d N_d + \rho_B A_d p_d) = 0. \tag{3.11b}$$

Note that Eqs. 3.11a-3.11b are cubic in terms of the model parameters N_p and N_d, and thus the solution of these equations can exhibit at most 6 equilibrium points (3 from Eq 3.11a and 3 from Eq. 3.11b). Upon examination of Eqs. 3.11a and 3.11b, I noticed that two of the equilibrium points are the trivial stable fixed points (i.e., $N_p^{eq,1} = 0$ and $N_d^{eq,1} = 0$). Assuming that 6 equilibrium points exist for Eqs. 3.11a and 3.11b, I further noticed that Eq. 3.11a (or Eq. 3.11b) can exhibit either two stable equilibrium points and one unstable equilibrium point or one stable equilibrium point and two unstable equilibrium points. Based on these observations, I developed a cost (distance) function (see Eq. 3.13) to enforce the existence of 3 equilibrium points with

two stable and one unstable equilibrium points for N_p and N_d in inferring the model parameters. In my notations, $N_p^{eq,1}$ and $N_d^{eq,1}$ represent the stable equilibrium points of the system in the absence of a HFS/LFS protocol. $N_p^{eq,3}$ and $N_d^{eq,3}$ are the stable equilibrium points of the system in the presence of a HFS/LFS protocol. $N_p^{eq,2}$ and $N_d^{eq,2}$ are the unstable equilibrium points.

Then, I used the equilibrium points from Eqs. 3.11a and 3.11b to solve for the scaling parameter f. $N_p^{eq,3}$ and $N_d^{eq,3}$ represent the late-LTP (or late-LTD) equilibrium points induced by HFS (or LFS). I used the mean LTP induced by one train of 100 Hz stimulation for one second in experimental data to compute the scaling parameter f of the LTP model (Roberto *et al.*, 2003; Papatheodoropoulos and Kostopoulos, 2000; Hernandez *et al.*, 2005). Additionally, the scaling parameter f of the LTD model was computed using the experimental data on the mean LTD induced by either a stimulation protocol of 900 pulses at 1 Hz or 1200 pulses at 3 Hz (Mockett *et al.*, 2007; Liu *et al.*, 2009; Huber *et al.*, 2001). Since the LTD protocols consisting of 900 pulses at 1 Hz or 1200 pulses at 3 Hz induced the same level of LTD in experiments, I averaged the scaling parameter f computed from each protocol to determine f in the LTD case.

Using Eq. 3.10 and the solution of the differential equation 3.6e ($f(N_p - N_d)$), I computed f as

$$f = \frac{(\bar{x}_d^{eq} - 37.3962)/(62.5414) - 100\%}{(N_p^{eq,3} - N_d^{eq,3}) \times 100\%}. \tag{3.12}$$

Here $\bar{x}_d^{eq}$ represents the average HFS/LFS induced LTP/LTD from the corresponding experimental data.

It is computationally expensive to infer the frequency dependent HFS/LFS induced LTP/LTD model parameters using the the biophysical CA1 pyramidal Hodgkin-Huxley model (Eq. 3.1) and the HFS/LFS model (Eqs. 3.6a-3.6e) together. Therefore, I used a reduced model to fit the remaining parameters γ_C, η, g, p_p, p_d, M_p, M_d, A_p, and A_d. In the reduced model, I only considered the frequency dependent plasticity model (Eqs. 3.6a-3.6e) and the characteristic NMDA calcium current for each HFS and LFS protocol when fitting the frequency dependent plasticity parameters. In

order to determine the % change in the fEPSP slope, I used Eq. 3.10 to map the change in the conductance P to % change in fEPSP slope. Then, the reduced model was used to infer the frequency dependent model parameters using an approximate Bayesian inference approach based on the sequential Monte Carlo (ABC-SMC) (Toni *et al.*, 2008) with a modified mean sum of squared errors distance function, shown in Eq. 3.13 averaged over the m experimental data sets.

$$
\begin{aligned}
d(N_p, N_d, x_d) = \frac{1}{m} \sum_{j=1}^{m} \sum_{i=1}^{n_j} \Bigg[& \\
& \frac{\big[G\big(f(N_p[t_i] - N_d[t_i]) + 1\big) - x_j[i]\big]^2}{n_j} \Bigg] \\
& + \mathrm{Y}\big(f < 0\big) \\
& + \mathrm{Y}\big(Imag\big(Np, Nd\big) == 0\big) \\
& + \mathrm{Y}\big(N_d^{eq,2} < 0.05 N_d^{eq,3}\big) \\
& + \mathrm{Y}\big(N_p^{eq,2} < 0.05 N_p^{eq,3}\big). \qquad (3.13)
\end{aligned}
$$

The first term on the right hand side of the distance function $d(N_p, N_d, x_d)$ (see Eq. 3.13) captures the error between the % change in the slope of evoked fEPSPs from my model and the corresponding % change in the fEPSP slope data from m different LTP/LTD experimental datasets available from the literature. The % change in the slope of evoked fEPSPs was normalized (i.e. 100%) to the slope measured prior to any HFS/LFS protocol. Each of the experimental data sets had n_j number of data points measuring the % change in the slope of evoked fEPSPs, $x_{i,j}$, after the HFS/LFS protocol. I used a mapping function $G(P)$ (see Eq. 3.10) to compute the % change in the evoked fEPSP slope in my model, where $1 + P$ represents the corresponding fractional change in the maximum synaptic conductance of the SC-CA1 synapse from the baseline (i.e., $P = 0$). The fractional synaptic conductance change from the baseline in my model was determine by $P(t_i) = f(N_p(t_i) - N_d(t_i))$. The baseline for the % change in fEPSP is 100%, which corresponds to $P = 0$ (see Eq. 3.6i) at the time t_i of the experimental data point $x_{i,j}$.

The second term on the right hand side of the distance function $d(N_p, N_d, x_d)$ (see Eq. 3.13) ensures that only the parameters (p_p, p_d, M_p, M_d, A_p, and A_d) that produce a positive scaling parameter f are accepted. The need for this term arises out of the differential equations describing N_p and N_d in Eqs. 3.6c and 3.6d, which are identical except for the parameters. Therefore, it is possible that the ABC-SMC algorithm could select parameters for p_p, M_p, and A_p that are typically selected for p_d, M_d, and A_d and *vice versa*. This would result in $N_p^{eq,3} < N_d^{eq,3}$ for the LTP model and $N_d^{eq,3} < N_p^{eq,3}$ for the LTD model, which would require f to be negative to match the experimental data. Thus, f must be constrained to a strictly positive number.

The last three terms on the right hand side of the distance function $d(N_p, N_d, x_d)$ (see Eq. 3.13) penalize the equilibrium points that are complex or have unstable equilibrium points $N_p^{eq,2}$ and $N_d^{eq,2}$ that are less than 5% of $N_p^{eq,3}$ and $N_d^{eq,3}$, which are the stable equilibrium points of the system in the presence of a HFS/LFS protocol. The first term $\Upsilon(Imag(Np, Nd) == 0)$ ensures that the fractional change in the maximum synaptic conductance is always a real number. The last term $\Upsilon(N_d^{eq,2} < 0.05N_d^{eq,3}) + \Upsilon(N_p^{eq,2} < 0.05N_p^{eq,3})$ ensures that that the small evoked fEPSPs used to measure the plasticity of the SC-CA1 synapse prior to any HFS/LFS administration does not induce any unwanted LTP/LTD, such that N_p and N_d decay to $N_p^{eq,1}$ and $N_d^{eq,1}$ after each fEPSP measurement prior to HFS/LFS administrations. Υ is the weighting factor.

We first used the inferred model parameters of the LTP model to validate whether my model captured the frequency-dependent effects of HFS protocol on the induced LTP, as observed in the experiments. The inferred parameters are provided in Table 3.4. Figures 3.4 and 3.5 show the histograms representing the approximate posterior distributions for the HFS and LFS parameters, respectively. Figures 3.6A, 3.6B, 3.6C, and 3.6D show the comparison between the prediction from my model and the experimental data for four different HFS protocols, i.e., 3 trains of pulses as 100 Hz for 1 second with intertrain intervals of 0.5 seconds, 10 minutes, 20 seconds, and 10 seconds, respectively. Additionally, the LTP induced by a HFS protocol of four trains of 100 pulses at 100 Hz is shown in Figure 3.7D. Here, the HFS-induced % fEPSP slope change from the control, shown as a black square-line, follows the same trend as the

TABLE 3.4: HFS Frequency Induced LTP Plasticity Parameters.

Parameters	LTP Parameter Value
M_p	$4.83 \times 10^{-8} \pm 4.92 \times 10^{-9}\ \mu A\ ms^{-1}$
p_p	$1.01 \times 10^{-5} \pm 1.03 \times 10^{-6}\ ms^{-1}$
A_p	$2.30 \times 10^{-6} \pm 2.54 \times 10^{-7}\ \mu A^2$
M_d	$4.91 \times 10^{-7} \pm 5.16 \times 10^{-8}\ \mu A\ ms^{-1}$
p_d	$2.23 \times 10^{-4} \pm 2.51 \times 10^{-5}\ ms^{-1}$
A_d	$6.81 \times 10^{-7} \pm 7.88 \times 10^{-8}\ \mu A^2$
γ_C	$0.0364 \pm 0.0036\ ms^{-1}$
η	$0.0035 \pm 0.000382\ ms^{-1}$
ν	$0.107 \pm 0.0122\ ms^{-1}$
g	$214.1 \pm 24.6\ \mu A^{-1}\ ms^{-1}$
f	$460\ \mu A^{-1}$
ρ_1	2.2
ρ_2	1
ρ_3	1
ρ_4	1
$C_{thr,1}$	0.45
$C_{thr,2}$	0

experimental data and achieves the same LTP magnitude change for all five protocols (Karpova *et al.*, 2006; Blitzer *et al.*, 1995; Hernandez *et al.*, 2005; Stramiello and Wagner, 2008; Zhang *et al.*, 2008; Li *et al.*, 2013). In order to capture the LTP induced by a weaker HFS protocol, the equilibrium points were shifted by ρ_C to capture the lower LTP level induced by a weaker HFS protocol. ρ_1 was hand-fitted to match the LTP induced by one and two trains of pulses at 100 Hz (Hernandez *et al.*, 2005). Additionally, C_{thr} was chosen such that three or more trains of HFS at 100 Hz switched the parameter ρ_C to ρ_2. Figure 3.7A shows my model is able to capture the LTP dynamics induced by 1 train of 100 Hz pulses reasonably well (Roberto *et al.*, 2003; Papatheodoropoulos and Kostopoulos, 2000; Hernandez *et al.*, 2005). However, my model underpredicts the experimental HFS-induced magnitude change evoked from 2 trains of 100 Hz pulses (Kasahara *et al.*, 2001; Hernandez *et al.*, 2005) (see Figure 3.7B). Even though my model underpredicts the magnitude change from 2 trains, experimental data shows that the magnitude change induced by 2 trains (see Figure 3.7C) is not significantly different from the magnitude change induced by 1 train (Hernandez *et al.*, 2005).

TABLE 3.5: LFS Frequency Induced LTD Plasticity Parameters.

Parameters	Parameter Value
M_p	$4.95 \times 10^{-7} \pm 5.06 \times 10^{-8}\ \mu A\ ms^{-1}$
p_p	$2.16 \times 10^{-4} \pm 2.41 \times 10^{-5}\ ms^{-1}$
A_p	$9.76 \times 10^{-7} \pm 1.11 \times 10^{-7}\ \mu A^2$
M_d	$5.81 \times 10^{-8} \pm 5.41 \times 10^{-9}\ \mu A\ ms^{-1}$
p_d	$1.63 \times 10^{-5} \pm 1.81 \times 10^{-6}\ ms^{-1}$
A_d	$2.07 \times 10^{-6} \pm 2.40 \times 10^{-7}\ \mu A^2$
γ_C	$0.0238 \pm 0.0027\ ms^{-1}$
η	$0.0024 \pm 0.000276\ ms^{-1}$
ν	$0.0348 \pm 0.0038\ ms^{-1}$
g	$52.0 \pm 6.13\ \mu A^{-1} ms^{-1}$
f	$281.3\ \mu A^{-1}$
ρ_1	1
ρ_2	1.31
ρ_3	1
ρ_4	0.35
$C_{thr,1}$	3
$C_{thr,2}$	4.5

We then used the inferred model parameters of the LTD model to validate whether my model captured the frequency-dependent effects of LFS protocol on the induced LTD, as observed in the experiments. To validate my model, I considered seven different LFS protocols. The first LFS protocol consisted of 900 pulses delivered to the SC-CA1 synapse at the frequency of 1 Hz. Figure 3.8A shows the comparison between the prediction from my model and the experimental data from different experiments. As shown in this figure, my model predicted an approximately 19% decrease in the evoked fEPSP slope compared to an average of 18% decrease in experimental data (experimental data varied between 10% and 25%) (Huber *et al.*, 2001; Daoudal *et al.*, 2002; Liu *et al.*, 2009; Selig *et al.*, 1995). The second LFS protocol I used was 1200 pulses at 3 *Hz*, which produced a decrease in the normalized slope of the evoked fEPSPs of approximately 19% in my model compared to 21% in the experimental data (Mockett *et al.*, 2007) (see Figure 3.8B). Then, I considered the administration of 900 pulses at 3 *Hz*. Experimental data showed a decrement of 15% in the evoked fEPSP

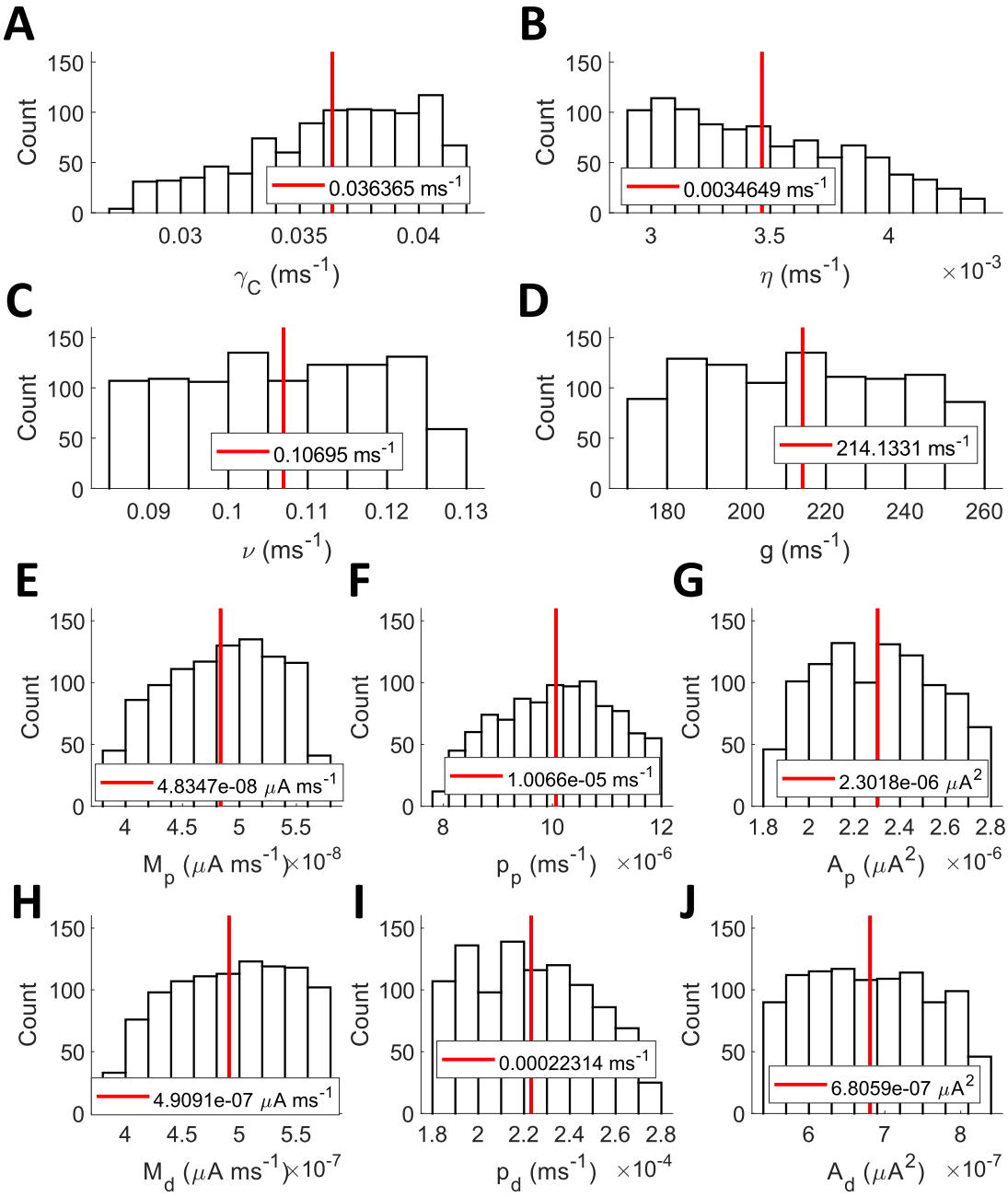

FIGURE 3.4: Inferred posterior distribution of the HFS-induced LTP parameters. Each histogram represents the approximate posterior distributions of the parameters **(A)** γ, **(B)** η, **(C)** M_p, **(D)** P_p, **(E)** A_p, **(F)** ν, **(G)** g, **(H)** M_d, **(I)** P_d, and **(J)** A_d. The red-line represents the mean value.

slope (Heynen *et al.*, 1996) while my model predicted 19% of decrement (see Figure 3.8C).

Next, I considered multiple LFS trains. Again, I captured the multiple equilibrium points of LTD induced by different LFS protocols with the parameters ρ_2 and ρ_4,

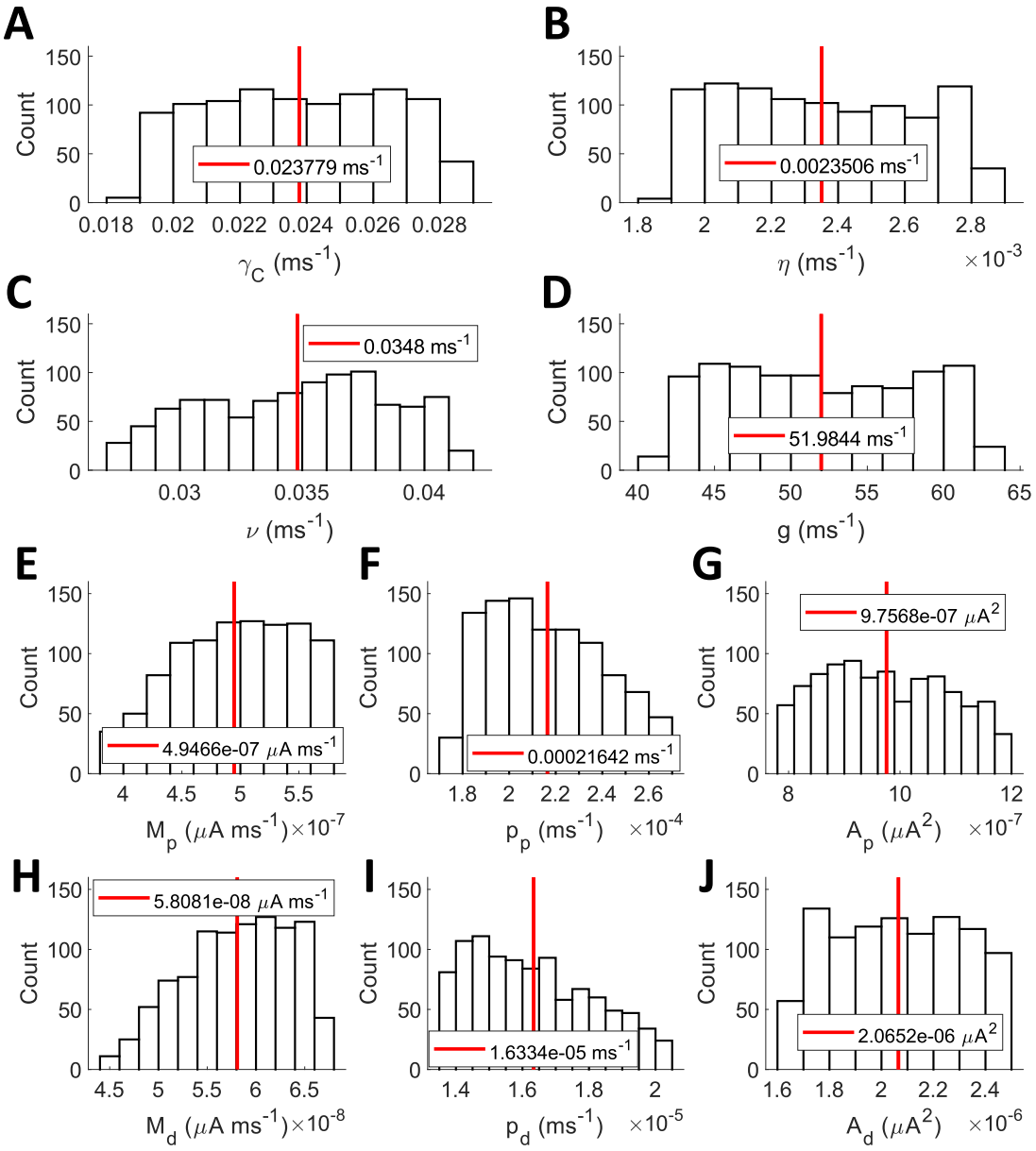

FIGURE 3.5: Inferred posterior distribution of the LFS-induced LTD parameters. Each histogram represents the approximate posterior distributions of the parameters **(A)** γ, **(B)** η, **(C)** M_p, **(D)** P_p, **(E)** A_p, **(F)** ν, **(G)** g, **(H)** M_d, **(I)** P_d, and **(J)** A_d. The red-line represents the mean value.

which I fitted by hand to match the experimental data (Liu *et al.*, 2009; Huber *et al.*, 2001). Here, I used the same LTD parameters in Table 3.5 that were used to model one train of LFS. Then I hand-fitted the toggle parameters ρ_2 and ρ_4, in order to capture the multiple equilibrium points of the LFS-induced LTD. The LTD toggle parameters are found in Table 3.5, as well. Figure 3.9A shows a comparison between my model's

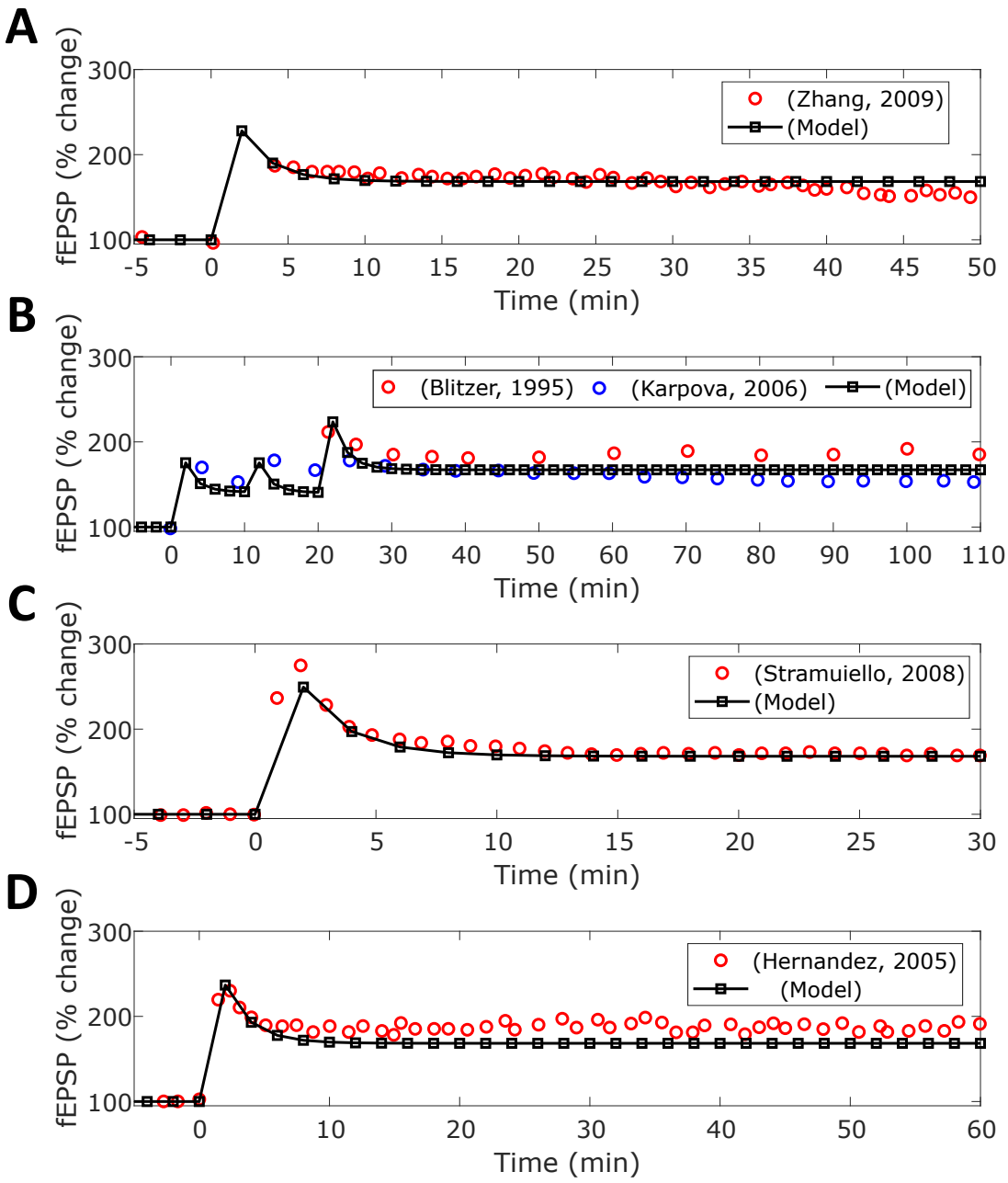

FIGURE 3.6: HFS-induced LTP. I provided three trains of 100 pulses delivered at 100 *Hz* to my SC-CA1 model with different inter-train intervals. The inter-train intervals were **(A)** 0.5 seconds, **(B)** 10 minutes, **(C)** 20 seconds, and **(D)** 10 seconds. The HFS-induced LTP in experiment is represented by the colored-circles and the LTP predicted by my model is shown as the black-squares. The root mean squared error between the experimental data and the model prediction for Zhang (Zhang *et al.*, 2008), Blitzer (Blitzer *et al.*, 1995), Karpova, (Karpova *et al.*, 2006), Stramuiello (Stramiello and Wagner, 2008), and Hernandez (Hernandez *et al.*, 2005) is 8.4 %, 18.2 %, 12.8 %, 6.5 %, and 18.8 %, respectively.

prediction and the experimental data from (Liu *et al.*, 2009; Huber *et al.*, 2001) on the LFS-induced LTD for a LFS protocol consisting of 3 trains of 900 pulses at 1 *Hz*. As shown here, the model accurately predicts the experimentally observed decrease in the synaptic strength of the SC-CA1 synapse after each train of LFS. Figure 3.9B shows a comparison between the model predicted LTD in the SC-CA1 synapse with the experimental data from (Sajikumar and Frey, 2004) for a LFS protocol consisting of 900 bursts at 1 *Hz* of 3 pulses at 20 *Hz*. Figure 3.9C compares the model predicted LTD in the SC-CA1 synapse with the experimental data from (Mockett *et al.*, 2007) for a LFS protocol consisting of 2400 pulses at 3 *Hz*. Finally, Figure 3.9D compares the model predicted LTD in the SC-CA1 synapse with the experimental data from (Mockett *et al.*, 2007) for a LFS protocol consisting of 2 trains of 1200 pulses at 3 *Hz*.

3.2.4 *Dopaminergic modulation of HFS/LFS induced LTP/LTD in hippocampal SC-CA1 synapses*

In this section, I describe a phenomenological model that I developed to integrate the dose-dependent effects of D1/D5 agonists relative to the HFS/LFS on the maximum synaptic conductance (see Eq. 3.8) of the SC-CA1 synapse. my model together with the models described in the previous sections (see Eqs 3.1-3.8) is capable of predicting the experimentally observed dose-dependent modulation of HFS/LFS-induced LTP/LTD by D1/D5 agonists. Eqs. 3.14a-3.14d show my model in the form of a set of kinetic reactions.

$$E + [T_{E,OFF}] \underset{k_2}{\overset{k_1}{\rightleftharpoons}} [T_{E,ON}], \tag{3.14a}$$

$$[T_{E,ON}] + [T_{OFF}] \overset{k_3}{\rightarrow} [T_{E,OFF}] + [T_{l-LTP,ON}], \tag{3.14b}$$

$$I + [T_{I,OFF}] \underset{k_4}{\overset{k_5}{\rightleftharpoons}} [T_{I,ON}], \tag{3.14c}$$

$$[T_{I,ON}] + [T_{OFF}] \overset{k_6}{\rightarrow} [T_{I,OFF}] + [T_{l-LTD,ON}], \tag{3.14d}$$

These reactions describe the modulation of the maximum synaptic conductance $\bar{g}_s$ of the SC-CA1 synapse by a D1/D5 agonist, such as SKF 38393, 6-Br-APB, or

dopamine, in the absence of a LTP/LTD protocol (i.e., HFS/LFS). Investigations on the biochemical mechanisms underlying the modulation of SC-CA1 long-term synaptic plasticity by D1/D5 agonists have revealed two competing pathways, the excitatory adenyl cyclase (AC) pathway and the inhibitory phosopholipase C (PLC) pathway (Undieh, 2010; Panchalingam and Undie, 2000, 2005). In my model, I captured the dynamics exhibited by the excitatory AC pathway, that induces slow-onset-potentiation, using Eqs. 3.14a and 3.14b. The response of the inhibitory PLC pathway, that induces a slow depotentiation in the SC-CA1 synapses, is captured by Eqs. 3.14c and 3.14d. The change in the maximum synaptic conductance is dependent on the activation of either the AC or PLC pathway through the tags $T_{E,ON}$ and $T_{I,ON}$, respectively. These pathways compete for T_{OFF} to produce late-LTP (l-LTP) ($T_{l-LTP,ON}$) or late-LTD (l-LTD) ($T_{l-LTP,ON}$) changes to the SC-CA1 synaptic strength through the maximum synaptic conductance.

Mathematically, I modeled these reactions in a deterministic kinetic rate modeling framework using Eqs. 3.15c-3.15h and Eq 3.15m with $\theta_{late} = 0$ and $T_{stim} = 0$ in Eq. 3.15m. Eqs. 3.15a-3.15b are the Hill equations that model the dose response of a D1/D5 agonist at a given concentration $[Drug]$. The activation of the AC and PLC pathways is bound by a maximal response (E_{max} and I_{max}). The fraction of maximal response is determined by the Hill parameters $EC50$, E_{max}, $IC50$, I_{max}, and nH for each D1/D5 agonist. I estimated the Hill coefficients using the available experimental data on the % change in the CA1 fEPSP slope in response to the applied concentration of the D1/D5 agonist (Shivarama Shetty *et al.*, 2016; Sajikumar and Frey, 2004; Navakkode *et al.*, 2012).

The specific D1/D5 agonist and its temporal dosing profile determine the relative activation of the AC and PLC pathways. The activation dynamics of the AC ($T_{E,ON}$) and PLC ($T_{I,ON}$) pathway are described by Eqs. 3.15c - 3.15f. Eqs. 3.15g - 3.15h show the consumption dynamics of T_{OFF} to produce $T_{l_{LTP}}$ and $T_{l_{LTD}}$.

Eqs. 3.15m - 3.15r model the integrative effect of HFS/LFS mediated LTP/LTD and D1/D5 agonist on the SC-CA1 LTP/LTD. The combined effect of HFS/LFS and D1/D5 agonist on the maximum synaptic conductance of the SC-CA1 synapse is described in Eq. 3.15o. Here, the term $f\left(\frac{dN_p}{dt} - \frac{dN_d}{dt}\right)$ captures the contribution from

the HFS/LFS protocol and the term $\left(\frac{dT_{l-LTP}}{dt} - \frac{dT_{l-LTD}}{dt}\right)$ captures the contribution from a D1/D5 agonist. Experimental data from hippocampal slices show that the LTP-induced by a combination of strong HFS protocol and a D1/D5 agonist in SC-CA1 synapses slowly decays back to the HFS only induced late LTP in a period of 2-4 hours (Huang and Kandel, 1995; Navakkode *et al*., 2012). I hypothesized that this may be due to the maximum available biochemical resources for inducing late LTP and captured this effect in my model by introducing a decay term $k_{sat}(P - P_{sat}^{LTP})$. Particularly, whenever the induced LTP exceeds the saturation level, defined by P_{sat}^{LTP} in the presence of a D1/D5 receptors agonist at time t_{DA}, k_{sat} takes a nonzero value. The term $k_{basal}P$ models the effect of D1/D5 antagonist, such as SCH 23390. The parameter k_{basal} takes a nonzero value k_{sat} whenever SCH 23390 is applied to block the D1/D5 receptors. Finally, the term $sign\left(E + k_I I\right)k_E T_{stim} T_{DR}$ models the nonlinear interaction of the D1/D5 receptors activation and HFS/LFS on the induced LTP/LTD.

$$E = \frac{E_{max}}{1 + (EC50/[Drug])^{nH}} \tag{3.15a}$$

$$I = \frac{I_{max}}{1 + (IC50/[Drug])^{nH}} \tag{3.15b}$$

$$\begin{aligned} \frac{dT_E^{ON}}{dt} &= k_1[E][T_E^{OFF}] - k_2[T_E^{ON}] \\ &\quad -k_7[T_E^{ON}][T_I^{ON}] \end{aligned} \tag{3.15c}$$

$$\frac{dT_E^{OFF}}{dt} = -\frac{dT_E^{ON}}{dt} \tag{3.15d}$$

$$\begin{aligned} \frac{dT_I^{ON}}{dt} &= k_3[I][T_I^{OFF}] - k_4[T_I^{ON}] \\ &\quad - k_8[T_I^{ON}][E]^2 \end{aligned} \tag{3.15e}$$

$$\frac{dT_I^{OFF}}{dt} = -\frac{dT_I^{ON}}{dt} \tag{3.15f}$$

$$\frac{dT_{l-LTP}}{dt} = k_5[T_I^{ON}]^2[T^{OFF}] \tag{3.15g}$$

$$\frac{dT_{l-LTD}}{dt} = k_6[T_E^{ON}]^2[T^{OFF}] \tag{3.15h}$$

$$\frac{dT_{stim}}{dt} = k_{stim} T_{stim}^{OFF} \left| \frac{dN_p}{dt} - \frac{dN_d}{dt} \right| - \frac{T_{stim}}{\tau_{stim}} \tag{3.15i}$$

$$\frac{dT_{stim}^{OFF}}{dt} = -k_{stim} T_{stim}^{OFF} \left| \frac{dN_p}{dt} - \frac{dN_d}{dt} \right| + \frac{T_{stim}}{\tau_{stim}} \tag{3.15j}$$

$$\frac{dT_{DR}}{dt} = k_{DA} \left| E + k_I I \right| T_{DR}^{OFF} - \frac{T_{DR}}{\tau_{DR}} \tag{3.15k}$$

$$\frac{dT_{DR}^{OFF}}{dt} = -k_{DA} \left| E + k_I I \right| T_{DR}^{OFF} + \frac{T_{DR}}{\tau_{DR}} \tag{3.15l}$$

$$\begin{aligned} \frac{dT^{OFF}}{dt} &= -\frac{dT_{l-LTP}}{dt} - \frac{dT_{l-LTD}}{dt} \\ &\quad -k_{late} T_{OFF} \theta_{late} \\ &\quad - sign\big(E + k_I I\big) k_E |T_{stim} T_{DR}| \end{aligned} \tag{3.15m}$$

$$\theta_{late} = \begin{cases} 1 & |Np - Nd| > 0 \\ \\ 0 & |Np - Nd| = 0 \end{cases} \tag{3.15n}$$

$$\begin{aligned} \frac{dP}{dt} &= f\left(\frac{dN_p}{dt} - \frac{dN_d}{dt}\right) - k_{basal}P \\ &\quad -k_{sat}\left(P - P_{sat}^{LTP}\right) \\ &+ \left(\frac{dT_{l-LTP}}{dt} - \frac{dT_{l-LTD}}{dt}\right) \\ &+ sign\big(E + k_I I\big)k_E T_{stim} T_{DR} \end{aligned} \tag{3.15o}$$

$$k_{basal} = \begin{cases} k_{sat} & [DA]_{basal} = 0 \\ \\ 0 & [DA]_{basal} > 0 \end{cases} \tag{3.15p}$$

$$k_{sat} = \begin{cases} 0 & P \leq P_{sat}^{LTP} \ \ \& \ \ t < t_{DA} \\ \\ k_{sat} & P > P_{sat}^{LTP} \ \ \& \ \ t \geq t_{DA} \end{cases} \tag{3.15q}$$

(3.15r)

To infer the unknown model parameters k_1, k_2, k_3, k_4, k_5, k_6, k_7, k_8, k_{sat}, k_{late}, k_E, k_I, k_{stim}, k_{DA}, τ_{stim}, and τ_{DA} from the available experimental data, I observed that the set of Eqs. 3.15a-3.15h are independent of the set of Eqs. 3.15i-3.15r. This allowed me to infer the unknown model parameters efficiently using the ABC-SMC approach. Specifically, I first inferred the model parameters of the first set of equations (Eqs. 3.15a-3.15h), and which was then followed by the inference of model parameters of the second set of equations (Eqs 3.15i-3.15r).

We first inferred the 8 unknown model parameters k_1, k_2, k_3, k_4, k_5, k_6, k_7, and k_8 in Eqs. 3.15a-3.15h using the ABC-SMC method (Toni *et al.*, 2008). For the parameter inference, I used the input-output data (% change in fEPSP slope from control in response to various concentrations of the D1/D5 agonists SKF 38393, 6-bromo-APB, and dopamine) available from recent rat hippocampal slice experiments (Shivarama Shetty *et al.*, 2016; Navakkode *et al.*, 2012; Sajikumar and Frey, 2004). It has been shown in (Shivarama Shetty *et al.*, 2016) that the application of a

TABLE 3.6: Hill Function Parameters.

Parameters	Value	Reference
EC_{50}^{DA}	40 μM	(Sajikumar and Frey, 2004)
E_{max}^{DA}	60%	(Sajikumar and Frey, 2004)
IC_{50}^{DA}	0.1 μM	(Sajikumar and Frey, 2004)
I_{max}^{DA}	-25%	(Sajikumar and Frey, 2004)
nH^{DA}	2	(Sajikumar and Frey, 2004)
EC_{50}^{SKF}	20 μM	(Shivarama Shetty *et al.*, 2016)
E_{max}^{SKF}	60%	(Shivarama Shetty *et al.*, 2016)
IC_{50}^{SKF}	0.1 μM	(Shivarama Shetty *et al.*, 2016)
I_{max}^{SKF}	-5.0%	(Shivarama Shetty *et al.*, 2016)
nH^{SKF}	1	(Shivarama Shetty *et al.*, 2016)
$EC_{50}^{6-Br-APB}$	15 μM	(Shivarama Shetty *et al.*, 2016)
$E_{max}^{6-Br-APB}$	40%	(Shivarama Shetty *et al.*, 2016)
$IC_{50}^{6-Br-APB}$	0.01 μM	(Shivarama Shetty *et al.*, 2016)
$I_{max}^{6-Br-APB}$	-3.0%	(Shivarama Shetty *et al.*, 2016)
$nH^{6-Br-APB}$	1	(Shivarama Shetty *et al.*, 2016)

D1/D5 agonist alone, in the absence of a HFS-based LTP protocol, can potentiate the SC-CA1 synapses in a dose-dependent manner. Moreover, these dopaminergic mediated potentiations occur on a slow timescale (typically, several minutes to hours). Since HFS or LFS was not applied when measuring the slow-onset dopaminergic potentiation, I only considered the dopaminergic model (Eqs. 3.15a-3.15h) when inferring the parameters k_1, k_2, k_3, k_4, k_5, k_6, k_7, and k_8. I considered a modified mean sum of squared errors distance function (Eq. 3.16b) averaged over the m experimental data sets that compares the distance between the i^{th} experimental % change in fEPSP slope ($x_j[i]$) of the j^{th} data set to the corresponding % change in fEPSP slope in the model $x_m[t_i]$ at time t_i. In addition to the mean sum of squared error, the distance function contains an additional non-steady state penalty in the second term on the right hand side of Eq. 3.13 . Table 3.7 shows my inferred parameters value represented in terms of the mean $\pm$ standard deviation and Figure 3.10 shows the histograms representing the approximate posterior distribution for each parameter.

TABLE 3.7: Dopaminergic Potentiation Parameters.

Parameters	Value
k_1	$8.26 \times 10^{-6} \pm 2.17 \times 10^{-6}\ ms^{-1}$
k_2	$7.10 \times 10^{-8} \pm 2.99 \times 10^{-8}\ ms^{-1}$
k_3	$3.24 \times 10^{-6} \pm 4.25 \times 10^{-6}\ ms^{-1}$
k_4	$1.44 \times 10^{-7} \pm 5.27 \times 10^{-7}\ ms^{-1}$
k_5	$2.89 \times 10^{-7} \pm 7.45 \times 10^{-8}\ ms^{-1}$
k_6	$2.35 \times 10^{-6} \pm 4.31 \times 10^{-6}\ ms^{-1}$
k_7	$1.63 \times 10^{-7} \pm 8.69 \times 10^{-7}\ ms^{-1}$
k_8	$5.32 \times 10^{-4} \pm 6.90 \times 10^{-4}\ ms^{-1}$
k_{sat}	$1.34 \times 10^{-7} \pm 1.07 \times 10^{-8}\ ms^{-1}$
k_{stim}	$557 \pm 128\ ms^{-1}$
k_E	$1.51 \times 10^{-6} \pm 2.20 \times 10^{-7}\ ms^{-1}$
k_I	2.49 ± 0.306
k_{late}	$4.36 \times 10^{-7} \pm 4.49 \times 10^{-8}\ ms^{-1}$
k_{DA}	$1.0 \times 10^{-3} \pm 2.36 \times 10^{-4}\ ms^{-1}$
τ_{stim}	$7.73 \times 10^{4} \pm 1.69 \times 10^{4}\ ms$
τ_{DR}	$2.46 \times 10^{5} \pm 4.26 \times 10^{4}\ ms$
P_{sat}^{LTP}	1.12

Figure 3.12 shows the slow-onset-potentiation of the SC-CA1 pyramidal synapse by various dopamine agonist observed in the experimental data (Shivarama Shetty *et al.*, 2016; Navakkode *et al.*, 2012; Sajikumar and Frey, 2004) and in my model.

$$x_m[t_i] = G\big(T_{l-LTP}[t_i] - T_{l-LTD}[t_i]\big), \tag{3.16a}$$

$$d(x_m, x_d) = \frac{1}{m}\sum_{j=1}^{m}\sum_{i=1}^{n_j}\frac{\big(x_m[t_i] - x_j[i]\big)^2}{n_j} + \big(x_m[400\ min] - x_m[370\ min]\big)^2. \tag{3.16b}$$

We then inferred the 8 unknown model parameters k_{sat}, k_{late}, k_E, k_I, k_{stim}, k_{DA}, τ_{stim}, and τ_{DR} in Eqs. 3.15i-3.15r using the ABC-SMC method (Toni *et al.*, 2008). For parameter inference, I used the input-output data (% change in fEPSP slope from control by various D1/D5 agonists and HFS/LFS simultaneously) available from rat hippocampal slice experiments (Huang and Kandel, 1995; Mockett *et al.*, 2007;

Sajikumar and Frey, 2004; Navakkode *et al.*, 2012; Otmakhova and Lisman, 1996; Chen *et al.*, 1995). Using my full model to infer the parameters k_{sat}, k_{late}, k_E, k_I, k_{stim}, k_{DA}, τ_{stim}, and τ_{DA} is computationally expensive. Therefore, I considered a reduced model that consisted of the frequency dependent plasticity model (Eqs. 3.6a-3.6e), the dopaminergic model (Eqs. 3.15a-3.15h), the temporal dopaminergic-frequency dependent stimulation interaction model (Eqs. 3.15i-3.15r), and the characteristic NMDA calcium current for each HFS and LFS protocol. I considered a mean sum of squared errors distance function (Eq. 3.17) averaged over the m experimental data sets. The distance function measures the squared distance between i^{th} % change in fEPSP slope ($x_j[i]$) of the j^{th} data set to the corresponding % change in fEPSP slope in the model ($G(P[t_i])$) at time t_i. The model % change in fEPSP slope was determined by mapping the change in the fractional conductance (P) to % change in fEPSP slope with Eq. 3.10. Table 3.7 shows my inferred parameters value represented in terms of the mean $\pm$ standard deviation and Figure 3.11 shows the histograms representing the approximate posterior distribution for each parameter.

$$d(x_m, x_d) = \frac{1}{m}\sum_{j=1}^{m}\sum_{i=1}^{n_j}\frac{\left[G(P[t_i]) - x_j[i]\right]^2}{n_j}. \tag{3.17}$$

3.2.5 *The Complete Model*

Using Eq. 3.15o, the effect of both the HFS/LFS induced changes and dopaminergic induced changes in the synaptic current to the CA1 pyramidal neuron is incorporated through P in Eq. 3.8 rewritten as

$$g_s = (1-\alpha)(1+P)g_{AMPA} + \alpha g_{NMDA} \tag{3.18}$$

$$I_s = g_s n_{syn}(V - E_s). \tag{3.19}$$

With this, my complete model describing the modulation of the HFS/LFS induced LTP/LTD by a dopamine agonist in a dose-dependent manner is given by Eq. 3.1, Eqs. 3.2a-3.2h, Eqs. 3.3a-3.3r, Eqs. 3.4b-3.4h, Eqs. 3.6a-3.6i, Eqs. 3.15a-3.15r, and

Eq. 3.19. Furthermore, the experimental data used to fit and validate my model are shown in Tables 3.8 and 3.9, respectively.

TABLE 3.8: List of experimental protocols and data used to fit my model.

Experimental Protocol	Reference
3 train of HFS + DA ($\Delta t = -165$)	(Navakkode *et al.*, 2012)
1 train of HFS + 6-bromo-APB ($\Delta t = -5$)	(Otmakhova and Lisman, 1996)
1 train of HFS + SCH	(Huang and Kandel, 1995)
1 train of HFS + SCH	(Sajikumar *et al.*, 2008)
LFS (1200 pulses, 3 Hz) + SKF ($\Delta t = 0$)	(Mockett *et al.*, 2007)
LFS (1200 pulses, 3 Hz) + SKF ($\Delta t = 60$)	(Mockett *et al.*, 2007)
LFS (450 pulses, 1 Hz) + SKF ($\Delta t = -5$)	(Chen *et al.*, 1995)
1 train of HFS	(Roberto *et al.*, 2003)
	(Papatheodoropoulos and Kostopoulos, 2000)
2 train of HFS	(Hernandez *et al.*, 2005)
3 train of HFS	(Zhang *et al.*, 2008)
	(Stramiello and Wagner, 2008)
	(Hernandez *et al.*, 2005)
LFS (900 pulse, 1 Hz)	(Huber *et al.*, 2001)
	(Selig *et al.*, 1995)
	(Daoudal *et al.*, 2002)
	(Liu *et al.*, 2009)
LFS (1200 pulse, 3 Hz)	(Mockett *et al.*, 2007)
LFS (900 pulse, 3 Hz)	(Heynen *et al.*, 1996)

3.2.6 *Bayesian Parameter Estimation*

We inferred my model parameters using an approximate Bayesian computation sequential Monte Carlo framework (Toni *et al.*, 2008). This approach approximates the posterior distribution $\pi(\theta|x)$ of desired parameters θ based on available experimental data x_d. The approximate Bayesian computation sequential Monte Carlo algorithm is as follows:

0. Set population indicator to $t = 0$.

1. Set particle indicator to $i = 1$.

2. Draw θ^{**} from $\pi(\theta)$

TABLE 3.9: List of experimental protocols and data used to validate my model.

Experimental Protocol	Reference
3 train of HFS + SKF ($\Delta t = -212$)	(Navakkode *et al.*, 2012)
1 train of HFS + 6-bromo-APB ($\Delta t = 35$)	(Otmakhova and Lisman, 1996)
HFS + SCH	(Huang and Kandel, 1995)
LFS (2400 pulses, 3 Hz) + SKF ($\Delta t = 0$)	(Mockett *et al.*, 2007)
LFS (2×1200 pulses, 3 Hz) + SKF ($\Delta t = 0$)	(Mockett *et al.*, 2007)
LFS (900 pulse-bursts, 1 Hz) + SCH	(Sajikumar and Frey, 2004)
4 train of HFS	(Li *et al.*, 2013)
3 train of HFS	(Blitzer *et al.*, 1995; Karpova *et al.*, 2006)
2 train of HFS	(Kasahara *et al.*, 2001)
LFS (3×900 pulse, 1 Hz)	(Liu *et al.*, 2009; Huber *et al.*, 2001)
LFS (3×900 pulse-bursts, 1 Hz)	(Sajikumar and Frey, 2004)
LFS (2400 pulses, 3 Hz)	(Mockett *et al.*, 2007)
LFS (2×1200 pulses, 3 Hz)	(Mockett *et al.*, 2007)

3. Simulate $x^* \sim f(x|\theta^{**})$ and if $d(x^*, x_d) \geq \epsilon_t$ return to Step 1.

4. Set $w_t^{(i)} = 1$.

5. If $i < N$ return to Step 2 and set $i = i + 1$.

6. Normalize weights.

7. Set population indicator to $t = 1$.

8. Set particle indicator to $i = 1$.

9. Sample θ^* from previous population $\{\theta_{t-1}^{(i)}\}$ with weights w_{t-1} and perturb the particle to obtain $\theta^{**} \sim K_t(\theta|\theta^*)$. If the $\pi(\theta^{**}) = 0$ repeat step.

10. Simulate $x^* \sim f(x|\theta^{**})$ and if $d(x^*, x_d) \geq \epsilon_t$ return to Step 9.

11. Set $\theta_t^{(i)} = \theta^{**}$ and calculate the weight

$$w_t^{(i)} = \sum_{j=1}^{N} w_{t-1}^{(j)} K_t(\theta_{t-1}^{(j)}, \theta_t^{(i)})$$

12. If $i < N$ set $i = i + 1$ and return to Step 9.

13. Normalize weights if $t < T$ and set $t = t + 1$, then return to Step 8.

3.3 RESULTS

3.3.1 *The relative time between D1/D5 receptors activation and HFS significantly impact the temporal modulation of HFS-induced LTP in hippocampal SC-CA1 synapses*

We begin this section by summarizing the results from the limited *in vitro* hippocampal slice experiments on the importance of the time window of the activation of the D1/D5 receptors relative to the high-frequency stimulation (HFS) protocol used to induce the long-term potentiation (LTP) in the Schaffer collateral-CA1 pyramidal (SC-CA1) synapses. In a classical experiment (Huang and Kandel, 1995), Huang and Kandel showed that the 15 minutes administration of D1/D5 agonist SKF 38393 212 minutes before the HFS protocol enhanced the LTP of the synapse immediately after the HFS protocol but decayed to approximately the fEPSP level induced by only HFS after 2 hours. In the same experiment, the authors found no noticeable changes in the LTP of a SC-CA1 synapse when they administered SKF 38393 50 minutes after the HFS protocol. In (Navakkode *et al.*, 2012), Navakkode et al. investigated the HFS-mediated LTP modulation in SC-CA1 synapses by dopamine. In *in vitro* slice experiments, the authors showed that the application of $50\mu M$ of dopamine in three five minute pulses spaced ten minutes apart three hours prior to an HFS protocol of three trains of 100 pulses at 100 Hz induced a transient enhancement of HFS induced LTP that decayed to the level LTP induced by only HFS in 2 hours. These results highlight the activation of the D1/D5 receptors a long time before HFS significantly enhances the HFS-induced LTP of the SC-CA1 synapse. By contrast, the activation of D1/D5 receptors more than an hour after HFS does not significantly modulate the HFS-induced LTP. However, it is not clear from these results whether the activation of D1/D5 receptors can still modulate the HFS-induced LTP of a SC-CA1 synapse if one administers SKF 38393 sufficiently close to the timing of the HFS protocol (a few minutes before or after HFS). A few experiments (Stramiello and Wagner, 2008, 2010) have investigated this question in hippocampal slices under the bath application of SKF 38393. The results from these experiments suggest that the

activation of D1/D5 receptors at an earlier time than 200 minutes can also modulate the HFS-induced LTP of a SC-CA1 synapse. In summary, the available experimental results suggest that the relative timing between the HFS protocol and the activation of the D1/D5 receptors plays an essential role in the dopaminergic modulation of HFS-induced LTP of a SC-CA1 synapse. However, it is still not clear from these experiments how various concentrations and relative timings of D1/D5 agonists modulate the temporal dynamics of the HFS-induced LTP of a SC-CA1 synapse.

We used my developed model (see Eq. 3.1, Eqs. 3.2a-3.2h, Eqs. 3.3a-3.3r, Eqs. 3.4b-3.4h, Eqs. 3.6a-3.6i, Eqs. 3.15a-3.15r, and Eq. 3.19) to quantify how different relative timings of DA and the D1/D5 agonist SKF 38393 modulate the HFS-induced LTP of a SC-CA1 synapse. I first used my model under a similar experimental protocol condition as described in (Huang and Kandel, 1995) to demonstrate the capability of my model in predicting the experimental results shown in (Huang and Kandel, 1995). To do so, I delivered 50 μM SKF 38393 for 15 minutes to my SC-CA1 model more than 200 minutes before or 50 minutes after the HFS protocol. For the HFS protocol, I used 3 trains of 100 Hz pulses for 1 second with a 10 minute inter-train interval and stimulated my SC-CA1 synapse model (see Eqs 3.4a-3.4h and Eqs 3.6a-3.8 in the Model System section) to induce LTP. I measured the change in the SC-CA1 synaptic strength through the percentage change in the slope of evoked fEPSPs normalized to the slope of evoked fEPSPs prior to any induction of potentiation. Figures 3.13A and 3.13B show the comparison between the experimental (Huang and Kandel, 1995) and model predicted D1/D5 enhancement in the HFS-induced LTP by SKF 38393. As shown in Figure 3.13A, my model makes a quantitative prediction of the time-dependent enhancement in the late LTP reported by Huang and Kandel (Huang and Kandel, 1995) when SKF 38393 is delivered 200 minutes before the HFS administration. Moreover, my model predicts the experimental observation from Huang and Kandel (Huang and Kandel, 1995) that 50 μM administration of SKF 38393 leads to no significant changes in the HFS-induced LTP when it is delivered 50 minutes after the HFS protocol (see Figure 3.13B).

Next, I compared my model's prediction to the experimental results from (Navakkode *et al.*, 2012) on the transient enhancement in the late LTP by 50 μM

application of dopamine (DA). Since I fitted the dopaminergic portion of my model to specific D1/D5 agonists (see Eqs. 3.15a-3.15h in the Model System section), I used the DA specific parameters specified in Table 3.6 to model the spatiotemporal effect of DA on the HFS-induced late LTP of the SC-CA1 synapse. By following the exact stimulation protocol used in the experiment (Navakkode *et al.*, 2012), I injected 50 μM of DA in three pulses 165 minutes before the HFS protocol consisting of three trains of 100 pulses at 100 Hz in my model and measured the change in the fEPSP slope. As shown in Figure 3.14, my model is able to quantitatively predict an enhancement of approximately 27% in the HFS-induced LTP by DA, measured 60 minutes after the HFS protocol, as reported in the experiment. My quantitative prediction 100 minutes after the HFS protocol began to diverge from the experimental data. At this point, the experimental data decayed much faster compared to my model predictions as well as the decay observed in (Huang and Kandel, 1995). The divergence of my model from the experimental data is potentially due to the simple linear decay dynamics of my model, which consists of one decay constant parameter (k_{sat}). Since the decay of the potentiation induced by HFS quickens 60 minutes after the HFS protocol, my model is not able to capture the change in the decay.

Finally, I used my model to make specific predictions by conducting two simulation experiments where I administered 50 μM SKF 38393 30 minutes before the HFS protocol (see Figure 3.15A) and 10 minutes after the HFS protocol (see Figure 3.15B). Based on the experimental results on the two extreme cases (i.e., SKF 38393 application 200 minutes before or 50 minutes after the HFS protocol) and the slow-onset potentiation of the SC-CA1 synapses by SKF 38393, one would expect a reduction in the SKF 38393 mediated LTP enhancement as the time difference between the SKF 38393 administration and the HFS protocol decreases. As shown in Figure 3.15A, the injection of 50 μM SKF 38393 30 minutes before HFS in my model led to approximately 20% enhancement in the HFS-induced late LTP 60 minutes after HFS compared to 30% enhancement when SKF 38393 was delivered 200 minutes before the HFS protocol. Additionally, the injection of SKF 38393 10 minutes after the end of the HFS protocol resulted in no significant enhancement (approximately 4% enhancement

after 60 minutes of the HFS protocol) in HFS-induced late LTP (see Figure 3.15B) due to the occlusion by HFS.

In sum, my model shows reasonable quantitative predictions of existing experimental results on the HFS-induced late LTP modulation of SC-CA1 synapses by SKF 38393 and DA. It generates new predictions based on the relative timing between HFS and SKF 38393 administrations by capturing the dynamical mechanism of the HFS-induced late LTP modulation by SKF 38393 and DA. Moreover, my simulation results suggest that the enhancement in the HFS-induced LTP of the hippocampal SC-CA1 synapse by D1/D5 agonists may depend on the timing and order of the applied agonists relative to the HFS protocol in a nonlinear fashion.

3.3.2 *6-bromo-APB enhances weak HFS-induced early LTP in hippocampal SC-CA1 synapses*

In hippocampal slices from rats (Otmakhova and Lisman, 1996), Otmakhova and Lisman showed that the 5 minutes application of a D1/D5 receptor agonist 6-bromo-APB 5 minutes before a weak HFS protocol of 10 bursts of 4 pulses at 100 Hz with a 30 ms interval enhanced the HFS-induced LTP in the hippocampal SC-CA1 synapses by approximately 11% immediately after the weak HFS protocol and approximately 8% after 40 minutes. Furthermore, the application of 6-bromo-APB 35 minutes after the weak HFS protocol produced no significant changes in the weak HFS-induced LTP. These results highlight the time dependent modulation of a weak HFS-induced LTP in SC-CA1 synapses by the D1/D5 agonist 6-bromo-APB. Moreover, 6-bromo-APB interacts with HFS in a nonlinear fashion to modulate the HFS-induced LTP.

Before I used my model to predict the above experimental results, I first validated my model's capability in predicting slow-onset potentiation induced by 6-bromo-APB in the absence of a HFS protocol for inducing LTP in the SC-CA1 synapse. *In vitro* experimental data from (Shivarama Shetty *et al.*, 2016) showed that the application of $5\mu M$ 6-bromo-APB for 5 minutes three times (5 minutes inter-spacing) led to the slow-onset potentiation of the SC-CA1 synapse. Under the same protocol as described in (Shivarama Shetty *et al.*, 2016), I used my model (see Eqs. 3.15a-3.15h in the Model System section) to predict this slow-onset potentiation by 6-bromo-APB.

Figure 3.16A compares the prediction from my model with the experimental data in (Shivarama Shetty *et al.*, 2016). As shown in this figure, my model captures the essential dynamics to predict the slow-onset potentiation induced by 6-bromo-APB.

We then used my model to predict the experimental results from (Otmakhova and Lisman, 1996) on the modulation of a weak HFS-induced LTP by 6-bromo-APB. Figure 3.16B compares the prediction from my model with the experimental data from (Otmakhova and Lisman, 1996) when 6-bromo-APB was applied 5 minutes before the HFS protocol for 5 minutes. As shown in this figure, my model is able to capture the key dynamical features presented in the data qualitatively, such as a sharp enhancement in the HFS-induced LTP just after the HFS protocol (see Figure 3.16C) and the temporal changes in the LTP over time. Figure 3.16C highlights the faster dynamics of dopaminergic potentiation when the dopaminergic agonist 6-bromo-APB is applied close to a weak HFS protocol compared to the much slower potentiation dynamics observed by the application of only 6-bromo-APB in Figure 3.16A.

While my model accurately captures the dopaminergic potentiation dynamics, the model predictions of the overall change in SC-CA1 potentiation differs significantly from the experimental data quantitatively. I wondered whether this is because of the differences in the HFS-induced LTP predicted from my model and the experimental data. Would my model predict the data quantitatively better if I had the exact HFS-induced LTP changes predicted by my model as in the experimental data? To investigate this question, I tuned the HFS model parameters in Eq. 3.6c (p_p and M_p) through hand-fitting to match the HFS-induced LTP data from the experiment in the absence of 6-bromo-APB. I then again used my model to predict the result on the modulation of the weak HFS-induced LTP by 6-bromo-APB. Figures 3.17A and 3.17B compare the prediction from my model and the experimental data. As shown in Figure 3.17A, my model's performance improved significantly in predicting the experimental data quantitatively. This illustrates that my combined model (HFS+6-bromo-APB) captured the essential biophysiological mechanisms underlying the modulation of HFS-induced LTP by 6-bromo-APB in the hippocampal SC-CA1 synapses.

Finally, I used my model to predict the experimental result on the modulation of the weak HFS-induced LTP by 6-bromo-APB when 6-bromo-APB was applied 35 minutes after the HFS protocol. Figure 3.18 compares my model's prediction with the hand-fit parameters to the experimental data (Otmakhova and Lisman, 1996). As shown in Figure 3.18, my model accurately predicts the experimental data, i.e., no significant enhancement in the LTP by 6-bromo-APB. This highlights my model's capability at capturing the time dependency of dopaminergic modulation of SC-CA1 synaptic plasticity.

3.3.3 *Antagonizing D1/D5 receptors blocks HFS induced late-LTP in hippocampal SC-CA1 synapses*

One of the critical questions in understanding dopamine's role in the hippocampal SC-CA1 long-term synaptic plasticity is whether the basal level of dopamine is essential for the induction of LTP, or it only plays a role in modulating the late LTP. Several research groups have examined this question pharmacologically by blocking the D1/D5 receptors using a D1/D5 selective antagonist SCH 23390 in hippocampal slices from rats (Huang and Kandel, 1995; Sajikumar and Frey, 2004). Huang and Kandel (Huang and Kandel, 1995) showed that pharmacologically blocking the D1/D5 receptors using SCH 23390 blocks the HFS-induced late LTP in hippocampal SC-CA1 synapses with a minimal effect on early LTP. Similarly, Sajikumar et al. (Sajikumar *et al*., 2008) showed that the application of SCH 23390 blocked the late-LTP induced by a weak HFS protocol of 100 pulses at 100 *Hz* in the SC-CA1 synapses.

We again used my model described in the previous sections (see Eqs. 3.1,3.6a - 3.6d, 3.6f - 3.6i, 3.15a -3.15r, and 3.19 in the Model System section) to predict these experimental findings quantitatively. I incorporated the effect of SCH 233390 on the late LTP by introducing a model parameter k_{basal}, which takes a nonzero value whenever SCH 23390 is applied to block the D1/D5 receptors (see Eq. 3.150 in the Model System section). The parameter k_{basal} decreases the HFS-induced LTP predicted by my model to the baseline in approximately 400 minutes when D1/D5 receptors are blocked with the simultaneous application of SCH 23390 and HFS, as observed in the experimental studies.

Figure 3.19A compares my model predictions with the experimental results from Huang and Kandel (Huang and Kandel, 1995) and Sajikumar et al. (Sajikumar *et al.*, 2008) on the blockade of weak HFS (100 pulses at 100 *Hz*) induced late LTP by SCH 23390. As shown in this figure, my model reasonably predicts the decay of the weak HFS-induced LTP to the baseline (i.e., 100%) in approximately 400 minutes, as observed in the experimental data. Figure 3.19B compares my model predictions with the experimental results from Huang and Kandal (Huang and Kandel, 1995) on the blockade of a strong HFS protocol (3 trains of 100 pulses at 100 *Hz*) induced LTP in the hippocampal SC-CA1 synapses by SCH 23390. As shown in this figure, my model struggles to make quantitative prediction of the changes in the early LTP but provides a reasonable prediction of changes in the late LTP.

3.3.4 *Concentration dependent effect of SKF 38393 on the modulation of HFS-induced LTP*

It has been shown in hippocampal slice experiments that SKF 38393 induces a slow-onset potentiation in SC-CA1 synapses in the absence of a LTP induction protocol (Shivarama Shetty *et al.*, 2016; Huang and Kandel, 1995) and this potentiation strongly depends on the SKF 38393 concentration in a nonlinear fashion. However, no experimental results exist on how various concentrations of SKF 38393 impact the modulation of HFS-induced late LTP. After validating my model with the available experimental data on the modulation of HFS-induced late LTP by D1/D5 agonists and antagonists in the previous sections, I used my model (see Eqs. 3.1,3.6a -3.6d, 3.6f - 3.6i, 3.15a -3.15r, and 3.19) with SKF 38393 parameters given in Table 3.6 in the Model System section to investigate this question.

We systematically investigated the effect of seven different concentrations of SKF 38393, ranging between $1 - 50$ μM, on the modulation of strong HFS-induced LTP in the hippocampal SC-CA1 synapses while varying the relative time difference between the SKF 38393 injection and the applied HFS protocol. Figures 3.20A, 3.20B and 3.20C show the predictions of my model when seven different concentrations of SKF 38393 (i.e., 1 μM, 2 μM, 5 μM, 10 μM 15 μM, 25 μM, and 50 μM) were administered 212 minutes, 30 minutes, and 15 minutes, respectively, before a strong HFS protocol (3 trains of 100 pulses at 100 Hz). I applied each concentration of SKF 38393 for 15

minutes, which induced the slow-onset potentiation in the SC-CA1 synapse before the HFS protocol. As shown in these figures, my model predicted a slow decay of the SKF 38393 induced slow-onset potentiation in the hippocampal SC-CA1 synapse after the application of a strong HFS protocol. Particularly, my model predicted a bifurcation regime where the higher concentration of SKF 38393 (5 μM or higher) led to significant modulation of HFS-induced LTP while lower concentration of SKF 38393 (below 5 μM) led to insignificant changes in the HFS-induced LTP. Moreover, the observed concentration dependent enhancement of HFS-induced LTP decreased as the time difference between the application the HFS protocol and the injection of SKF 38393 increased. This highlights not only the importance of timing but also the dopamine agonist concentration on the dopaminergic modulation of a strong HFS-induced potentiation of the SC-CA1 synapse.

We noted in Figure 3.20C that when I applied SKF 38393 immediately before the HFS protocol, my model predicted a bifurcation regime in the modulation of the HFS-induced LTP depending on the concentration of SKF 38393. At a high concentration ($5 - 50 \quad \mu M$), SKF 38393 further potentiated the HFS-induced LTP whereas at a low concertation ($1 - 2 \quad \mu M$), SKF 38393 depressed the HFS-induced LTP. A potential mechanism underlying this observation may be the domination of the PLC pathway at a low concentration of SKF 38393, which has been shown to be critical for the induction of LTD (Reyes-Harde and Stanton, 1998; Horne and Dell'Acqua, 2007). It has been hypothesized that there exists a D1-like dopamine receptor that is coupled to a Gq-protein and selectively activates the phospholipase C (PLC) pathway (Liu *et al.*, 2009; Undieh, 2010). This receptor may explain the observation that while 1 μM of SKF 38393 induced no significant potentiation after 4 hours but a small transient depotentiation was observed up to one hour after the application of the dopamine agonist in (Shivarama Shetty *et al.*, 2016) Furthermore, HFS primarily activates the CAMKII/PKA pathway (Frey *et al.*, 1993) but also slightly activates the PLC pathway (Neyman and Manahan-Vaughan, 2008; Undieh, 2010). Therefore, the CAMKII/PKA pathway dominates to produce LTP. If a low concentration of SKF 38393 arrives immediately before the HFS protocol, the PLC pathway may still be active and could be boosted by the HFS protocol. The higher activity of the PLC pathway may slightly

counteract the CAMKII/PKA pathway and reduce the level of LTP induced by the HFS protocol.

Additionally, my model also correctly predicted the dynamical features of the nonlinear interaction between SKF 38393 and HFS when I applied SKF 38393 just before the HFS protocol. As shown in Figure 3.17B, the application of the weak HFS protocol immediately after the administration of a dopamine agonist 6-bromo-APB quickened the dynamics and amplified the effect of the agonist on the SC-CA1 synapse. Therefore, high concentrations of SKF 38393, which induced slow-onset potentiation (Shivarama Shetty *et al*., 2016), quickly enhanced LTP induced potentiation, while low concentrations of SKF 38393 depressed LTP induced potentiation.

We then used my model to investigate the concentration-dependent modulation of HFS-induced LTP by SKF 38393 delivered after the HFS protocol (3 trains of 100 pulses at 100 Hz). Figures 3.21A, 3.21B, and 3.21C show the model predicted enhancement in the HFS-induced LTP by SKF 38393 at seven different concentrations (1 μM, 2 μM, 5 μM, 10 μM 15 μM, 25 μM, and 50 μM) when SKF 38393 was delivered 10, 30, and 60 minutes, respectively, after the HFS protocol. As noted in these figures, the overall enhanced potentiation in the HFS-induced LTP by SKF 38393 decreased with the distance between the applied SKF 38393 and the HFS protocol. This supports my limited resources hypothesis, since more resource may be consumed by the HFS-induced LTP consolidation with the increased distance between the HFS and SKF 38393. Moreover, the potentiation by SKF 38393 decreased with the decrease in the SKF 38393 concentration.

Next, I investigated the effect of the same seven concentrations of SKF 38393 on the modulation of a weak HFS-induced LTP as the time difference was varied between the injection of SKF 38393 and the application of the weak HFS (100 pulses at 100 *Hz*). Based on my limited resource hypothesis, I expect that the weak HFS-induced LTP in SC-CA1 synapses will further be potentiated by the higher concentrations of SKF 38393. Particularly, SKF 38393 can convert the weaker levels of LTP to stronger levels of LTP in SC-CA1 synapse if a high concentration of SKF 38393 is administered significantly before the HFS protocol.

Figures 3.22A, 3.22B, 3.22C compare predictions from my model when SKF 38393 was applied 212, 30, and 15 minutes, respectively, before the weak HFS protocol. In each case, the injection of SKF 38393 alone induced the slow-onset potentiation of the SC-CA1 synapse that plateaued after the weak HFS protocol in all cases except when a concentration greater than 10 μM was applied 212 minutes before a weak HFS protocol. Since the weak HFS protocol alone doesn't saturate the induced LTP, concentrations of SKF 38393 greater than 10 μM delivered 212 minutes before the weak HFS protocol enhanced the LTP to the saturated LTP level typically achieved by a strong HFS protocol. Thus, these high concentrations and timing of SKF 38393 injection slowly decayed back to the saturated LTP level. When I applied the weak HFS protocol immediately after the injection of SKF 38393 (see Figure 3.22C), the weak HFS protocol quickened the modulation by SKF 38393. Importantly, the high concentrations of SKF 38393 enhanced the weak HFS-induced LTP, while the low concentrations of SKF 38393 suppressed the weak HFS-induced potentiation.

Then, I applied the dopamine agonist SKF 38393 10, 30, and 60 minutes after the weak HFS protocol as shown in Figures 3.23A, 3.23B, and 3.23C, respectively. In contrast to the concentration dependent dopaminergic modulation of strong HFS induced LTP model predictions in Figures 3.20 and 3.21, the dopaminergic enhancement of the weak HFS-induced LTP did not decay for most of the concentrations and timings of SKF 38393. This supports my limited resource hypothesis. The weak HFS protocol consumed less resources and never saturated, which allowed the dopamine agonist to further enhance the weak HFS-induced LTP without decaying back to the pure HFS-induced LTP baseline. Additionally, the efficacy of the concentration dependent enhancement of the weak HFS-induced LTP decreased as the time interval between the administration of the weak HFS protocol and the injection of SKF 38393 increased.

3.3.5 *The relative time between D1/D5 receptors activation and LFS protocol significantly impacts the temporal modulation of LFS-induced LTD in hippocampal SC-CA1 synapses*

We begin this section by summarizing the results from the limited *in vitro* hippocampal slice experiments on the importance of the time window of the activation of the dopamine D1/D5 receptors relative to a low-frequency stimulation (LFS) protocol used to induce the long-term depression (LTD) in the Schaffer collateral-CA1 pyramidal (SC-CA1) synapses. In *in vitro* hippocampal slice experiments (Mockett *et al.*, 2007), the authors applied 100 μM SKF 38393 for 20 minutes immediately after a LFS protocol of 1200 pulses at a frequency of 3 Hz. They observed a complete reversal of the LFS-induced LTD an hour after the SKF application. Next, the authors applied SKF 38393 an hour after the same LFS protocol in order to understand the temporal interaction of the two inputs. The application of 100 μM SKF 38393 one hour after the same LFS protocol produced no significant change in the SC-CA1 plasticity. Chen showed that the application of 3 μM of SKF 38393 during a LFS protocol produced further depotentiation of the SC-CA1 synapse in addition to the depotentiation induced by LFS alone (Chen *et al.*, 1995). Additionally, the application of the D1/D5 antagonist SCH 23390 blocked the consolidation of LTD (Sajikumar and Frey, 2004) similar to the antagonist's effect on HFS consolidation of LTP. In summary, the available experimental results suggest that the D1/D5 receptor mediated modulation of the LFS-induced LTD of the SC-CA1 synapse depends on the relative timing between the two inputs. It is not clear from these limited results whether the activation of D1/D5 receptors before an LFS protocol can reverse a LFS-induced LTD into LTP.

In order to investigate the temporal interaction of D1/D5 receptor activation by a dopamine agonist and a LFS protocol, I developed a SC-CA1 plasticity model able to predict the temporal dynamics of the dopaminergic modulation of LFS-induced LTD by various dopamine agonists (see Eqs. 3.1,3.6a -3.6d, 3.6f - 3.6i, 3.15a -3.15r, and 3.19 in the Model System section). my model for LFS-induced LTD modulation by D1/D5 agonists is similar to the HFS-induced LTP modulation model described in the

previous sections except that I fitted the frequency-dependent plasticity parameters in Eqs. 3.6a -3.6d and 3.6f - 3.6i using the LFS specific data. These parameters are described in Table 3.5.

We validated my SC-CA1 model with the experimental data from Mockett et. al. (Mockett *et al.*, 2007) where 100 μM SKF 38393 was delivered immediately and 60 minutes after a LFS protocol of 1200 pulses at 3 Hz. Figures 3.24A and 3.24B compare the synaptic plasticity change in the SC-CA1 synapse predicted by my model with the experimental data when SKF 38393 was applied immediately and 60 minutes, respectively, after the LFS protocol used in the experiment. As shown in Figure 3.24A, when I delivered SKF 38393 immediately after the LFS protocol in my model, the LFS-induced LTD reversed completely. This matched the reversal of LFS-induced LTD observed in experimental data (Mockett *et al.*, 2007). Next, I applied SKF 38393 60 minutes after a LFS protocol of 1200 pulses at 3 Hz. The application of SKF 38393 60 minutes after the LFS protocol induced only a slight potentiation of approximately 4% (see Figure 3.24B). A similar inflection was also observed in the experimental data (Mockett *et al.*, 2007), although it was not large enough to be statistically significant.

After validating my model with the experimental data from Mockett et. al. (Mockett *et al.*, 2007), I used my model to predict the dopaminergic modulation of LFS-induced LTD when SKF 38393 was delivered 100 and 30 minutes before a LFS protocol of 1200 pulses at 3 Hz. Figure 3.25A shows the prediction from my model when SKF 38393 was delivered 100 minutes before the LFS protocol. As shown in this figure, 100 μM of SKF 38393 delivered 100 minutes before the LFS protocol potentiated the SC-CA1 synapse by 48% and converted the LFS-induced LTD into LTP. Then, I applied 100 μM of SKF 38393 30 minutes before the same LFS protocol. Figure 3.25B shows a 30 minute timing between the application of the dopamine agonist and the following LFS protocol flipped the LFS-induced LTD to LTP too, although the overall potentiation was less than if it were applied 100 minutes before the LFS protocol. my model predictions, if correct, suggest that the application of SKF 38393 before a LFS protocol could potentially convert the LFS-induced LTD into LTP.

3.3.6 *Dopaminergic modulation of LFS induce LTD predictions with other LFS protocols*

In (Mockett *et al.*, 2007), Mockett et al. also investigated whether SKF 38393 could also reverse a strong LFS-induced LTD in SC-CA1 synapses. Specifically, they showed in their experiments that a 20 minutes application of 100 μM SKF 38393 immediately after a LFS protocol of 2400 pulses delivered at a frequency of 3 Hz potentiated the SC-CA1 synapse by approximately 12% (although no complete reversal of the LFS-induced LTD was observed). Furthermore, the delivery of 100 μM SKF 38393 immediately after a LFS protocol of 2 trains of 1200 pulses at 3 Hz with a 5 minute intertrain interval potentiated the SC-CA1 synapse by approximately 8%. The authors stated that the 5 minutes time difference may allow for more intracellular LTD consolidation to become more resistant to any modulation by D1/D5 receptor activation. Therefore, the LFS protocol with the 5 minute gap between two applications of 1200 pulses at 3 Hz was modulated less by SKF 38393. From these results, the author's *in vitro* experimental data suggests that the SKF 38393 mediated changes in the LFS-induced LTD strongly depend on the LFS protocol.

To test the predictive capability of my model, I used my LTD model to see whether my model can predict the experimental results shown by Mockett et al. (Mockett *et al.*, 2007) on the SKF 38393 mediated changes in the LFS-induced LTD under different LFS protocols. I used the same model described in the previous section. First, I applied 100 μM SKF 38393 for a 20 minute duration immediately after a LFS protocol of 2400 pulses delivered at 3 Hz to my model, identical to the one used in (Mockett *et al.*, 2007). My model predicted 14% potentiation of the SC-CA1 synapse as compared to approximately 12% in the experiment (see Figure 3.26A) and captured the temporal changes mediated by SKF 38393 in the LFS-induced LTD, reasonably well. It should be noted here that I did not use these data to infer my model parameters. Next, I applied 20 minutes of 100 μM SKF 38393 immediately after the LFS protocol of 2 trains of 1200 pulses at 3 Hz, identical to the one used in (Mockett *et al.*, 2007). Figure 3.26B shows the comparison between the prediction from my model and the experimental data from (Mockett *et al.*, 2007). My model predicted the observed fEPSP slope changes observed in the experimental data well. In summary, my model quantitively predicted

the experimentally observed LFS-induced LTD changes altered by SKF 38393 in SC-CA1 synapses for different LFS protocols.

Since my model predicted the experimentally observed modulation of LFS-induced LTD in SC-CA1 synapses by SKF 38393 quantitively under various LFS protocols, I used my model to further investigate the SKF 38393 mediated modulation of SC-CA1 synapses for two different LFS protocols. The first LFS protocol consisted of three trains of 900 pulses at 1 Hz with 15 minute intertrain intervals and the second protocol consisted of 900 bursts of three pulses delivered at 1 Hz. The rationale for considering these two LFS protocols is that they both induce a similar level of LTD but have a large difference in the duration of the applied LFS protocol. In both cases, I administered 20 minutes of 100 μM SKF 38393 to my model immediately after the LFS protocol similar to the protocol used in Mockett et. al. (Mockett *et al.*, 2007) in order to further examine how consolidation of LTD influences the extent SKF 38393 is able to modulate the SC-CA1 LTD. Figures 3.27A and 3.27B show the SKF 38393 mediated modulation of the LFS-induced LTD by these two different LFS protocols. The application of 100 μM SKF 38393 immediately after three trains of 900 pulses at 1 Hz potentiated the SC-CA1 synapse by approximately 8% while SKF 38393 applied immediately after the LFS protocol of 900 bursts at 1 Hz potentiated the SC-CA1 synapse by approximately 18%. It should be noted that none of the protocols led to the complete reversal of the LFS-induced LTD. This follows the same trend observed in the experimental data (see Figures 3.26A and 3.26B) where the longer the LFS protocol, the less potentiation induced by SKF 38393. Mockett et. al. (Mockett *et al.*, 2007) hypothesized that longer LFS protocols may allow the LFS-induced LTD more time to consolidate, which would reduce the ability of the dopamine agonist to modulate the LTD. If this hypothesis is true, then the release of SKF 38393 immediately after two different LFS protocols with dramatically different stimulation times would have more obviously different effects on the dopaminergic modulation of LFS-induced LTD for each protocol, as predicted by my model (see Figure 3.27).

3.3.7 *Antagonizing the D1/D5 receptor blocks LFS induced late-LTD*

In this section, I investigated the capability of my model in predicting experimental data on the modulation of SC-CA1 long-term synaptic plasticity by the simultaneous application of the D1/D5 receptor antagonist SCH 23390 and a LFS protocol. In *in vitro* experiment, Frey et. al. (Sajikumar and Frey, 2004) observed that the application of the D1/D5 receptor antagonist SCH 23390 blocked consolidation of LFS-induced LTD in SC-CA1 synapses. They applied 0.1 μM SCH 23390 for 60 minutes starting 30 minutes before the LFS protocol of 900 bursts of 3 pulses at 1 Hz and observed the reversal of LFS-induced LTD back to the baseline over a period of 450 minutes. Since the blockage of basal levels of dopamine binding to D1/D5 receptors with SCH 23390 blocked the consolidation of LTD, Frey (Sajikumar and Frey, 2004) hypothesized that dopamine is required for the induction of late-LTD.

We used my model (see Eqs. 3.1,3.6a -3.6d, 3.6f - 3.6i, 3.15a -3.15r, and 3.19) to predict the experimental data from (Sajikumar and Frey, 2004) under the same protocol, quantitatively. I incorporated the effect of SCH 23390 in my model through a model parameter k_{basal}. This parameter takes a non-zero value in the presence of SCH 23390 (see Eq.3.150). Figure 3.28 compares the prediction from my model with the experimental data from Frey et. al. (Sajikumar and Frey, 2004). As shown in this figure, my model predicts the reversal of the LFS-induced LTD in the presence of SCH 23390, as observed in the experiment.

3.3.8 *Concentration dependent spatiotemporal modulation of LFS-induced LTD by SKF 38393*

In this section, I used my model to investigate the effect of the concentration of SKF 38393 and its application time relative to the LFS protocol on the modulation of LFS-induced LTD in SC-CA1 synapses. Experimental data from *in vitro* hippocampal slice experiments have shown that the modulation of a LFS-induced LTD in SC-CA1 synapses strongly depends on the applied concentration and timing of SKF 38393 relative to the LFS protocol. Particularly, Chen et. al. (Chen *et al.*, 1995) showed that the application of 3 μM of SKF 38393 during a LFS protocol of 450 pulses at 1

Hz enhanced the induced LTD by approximately 18% (see Figure 3.29). This result highlights a different role that a dopamine agonists can play if applied at a low concentration. Furthermore, the experimental observation was consistent with the observed slow-onset depotentiation of the SC-CA1 synapse by the application of low concentrations of dopamine alone (Sajikumar and Frey, 2004).

To investigate the capability of my model in predicting the observed depotentiation of SC-CA1 synapse at a low concentration of SKF 38393 by Chen et.al. (Chen *et al.*, 1995), I applied the same low concentration of SKF 38393 to my model (see Eqs. 3.1,3.6a -3.6d, 3.6f - 3.6i, 3.15a -3.15r, and 3.19 in Model System section) under the same LFS protocol. Figure 3.29 compares the prediction from my model with the experimental data from (Chen *et al.*, 1995). As shown in this figure, my model predicts the experimental data on the SKF 38393 modulated LFS-induced LTD at a low concentration quantitatively (enhancement in the LFS-induced LTD by approximately 20% an hour after the LFS protocol). Additionally, my model captures the temporal dynamics of these modulations.

After validating my model with the limited experimental data, I further used my model to investigate how various concentrations and timing of the application of SKF 38393 relative to a LFS protocol modulates the LFS-induced LTD in SC-CA1 synapses. I applied seven different concentrations ($1 - 100\ \mu M$, 20 minutes duration) of SKF 38393 at various times before and after a LFS protocol of 1200 pulses at 3 *Hz*. Figures 3.30A, 3.30B, and 3.30C show the predictions from my model on the SKF 38393 mediated modulation of the LFS-induced LTD for timings of SKF 38393 applied 212, 30, and 20 minutes, respectively, before the LFS protocol. Here, SKF 38393 alone induced a slow onset potentiation of the SC-CA1 synapse that plateaued after the LFS protocol in Figure 3.30A. In Figure 3.30B, the LFS protocol applied 30 minutes after the administration of SKF 38393 reduced the concentration dependent slow-onset potentiation by SKF 38393, since there was less time for the consolidation of the SKF 38393 induced potentiation. After the LFS protocol, the SKF 38393 induced potentiation remained at the saturation level. The application of SKF 38393 20 minutes before the LFS protocol highlighted the concentration dependent bifurcation of the SKF 38393 mediated modulation of the LFS-induced LTD, similar

to the LTP case (see Figure 3.20C). Particularly, low concentrations of SKF 38393 enhanced the depotentiation of the SC-CA1 synapse, while high concentrations of SKF 38393 reversed LFS induced-LTD to varying degrees.

Next, I used my model to investigate how various concentrations of SKF 38393 modulate the LFS-induced LTD in SC-CA1 synapses when SKF 38393 is applied at different times relative to LFS but after the LFS protocol. Figures 3.31A, 3.31B, and 3.31C show the prediction from my model when I applied SKF 38393 10, 30, and 60 minutes after the same LFS protocol (1200 pulses at 3 *Hz*). As shown in these figures, the concentration dependent potentiation by SKF 38393 decreased for the same given concentration as the relative timing between the application of SKF 38393 and the LFS increased. Moreover, the potentiation by SKF 38393 was much smaller compared to when the SKF 38393 was applied before the LFS protocol to induce LTD, which is consistent with results in the previous sections.

3.4 SUMMARY

In this chapter, I modeled the dose-dependent modulation of high/low-frequency stimulation (HFS/LFS) induced long-term potentiation/depression (LTP/LTD) of a Schaffer collateral – CA1 pyramidal neuron (SC-CA1) synapse by three dopamine D1/D5 receptor agonists, SKF 38393, dopamine and 6-bromo-APB. My model predicted the experimentally observed temporal effects of these D1/D5 agonists' concentrations, and the relative time between the applied agonist and the HFS/LFS induction on both the early and the late LTP/LTD, quantitatively. Specifically, I derived the following conclusions from my modeling results:

1. For a given concentration and duration of a dopamine D1/D5 receptors agonist, the maximum change in the late LTP/LTD occurred when the agonist was delivered a long-time (approximately 200 minutes) before the HFS/LFS induction, which is consistent with the experimental results from Huang et.al. (Huang and Kandel, 1995).

2. For a given concentration and duration of a dopamine D1/D5 receptors agonist, the maximum change in the late LTP/LTD decreased slowly with the decrease in the time difference between the application of the agonist and the HFS/LFS protocol when the agonist was applied before the HFS/LFS protocol but not immediately before or during the HFS/LFS protocol. The conclusion is consistent the experimental data available in the literature (Huang and Kandel, 1995; Navakkode *et al*., 2012).

3. For a given concentration and duration of a dopamine D1/D5 receptors agonist, the maximum change in the late LTP/LTD quickly decreased with the increase in the time gap between the application of the dopamine agonist and the HFS/LFS protocol when the agonist was applied after the HFS/LFS protocol. The conclusion is consistent with the experimental data available from (Mockett *et al*., 2007).

4. For a given concentration and duration of a dopamine D1/D5 receptors agonist, application of the agonist immediately before or during an HFS/LFS protocol enhanced the dopaminergic modulation of the SC-CA1 synapse in a highly nonlinear fashion (sharp changes), which is consistent with the experimental data from (Otmakhova and Lisman, 1996; Chen *et al*., 1995).

5. For a given concentration and duration of a dopamine D1/D5 receptors agonist, high concentrations of the agonist injected immediately before or during a HFS/LFS protocol modulated SC-CA1 synaptic plasticity by further potentiating the HFS/LFS induced potentiation/depotentiation. This result is consistent with the experimentally observed data from (Otmakhova and Lisman, 1996).

6. For a given concentration and duration of a dopamine D1/D5 receptors agonist, low concentrations of the agonist injected immediately before or during a HFS/LFS protocol modulated SC-CA1 synaptic plasticity by further depotentiating the HFS/LFS induced potentiation/depotentiation. This is consistent with the limited experimental data from (Chen *et al*., 1995).

7. For a fixed duration of the applied dopamine D1/D5 receptors agonist and a large time gap between the dopamine agonist and the HFS/LFS protocol, the dopaminergic mediated modulation of LTP/LTD increased with an increase in the concentration level of the applied agonist.

Our modeling approach to integrate the LTP/LTD effects mediated by HFS/LFS and D1/D5 agonists is based on the hypothesis that there exists limited resources for the consolidation of the HFS/LFS-induced LTP/LTD into the late-LTP/LTD. I formulated this hypothesis based on the limited experimental data from (Mockett *et al.*, 2007; Huang and Kandel, 1995; Navakkode *et al.*, 2012; Chen *et al.*, 1995; Sajikumar and Frey, 2004; Sajikumar *et al.*, 2008). Particularly, it was shown in an *in vitro* hippocampal slice experiment that the application of 100 μM of SKF 38393 immediately after the LFS protocol reversed the consolidation of the late-LTD, whereas the application of 100 μM of SKF 38393 an hour after the LFS protocol produced no significant reversal of the late-LTD consolidation (Mockett *et al.*, 2007). Similarly, the application of 50 μM SKF 38393 200 minutes before HFS induction resulted in a substantial magnitude change of HFS induced LTP, while the delivery of 50 μM SKF 38393 50 minutes after resulted in no enhancement of HFS induced LTP (Huang and Kandel, 1995). Additionally, it was shown that the direct activation of PKA by sp-cAMPS 10 minutes after a strong HFS protocol induced only a small additional potentiation of the SC-CA1 synapse, while the activation of the PKA by sp-cAMPS 180 minutes before a strong HFS protocol resulted in only a transient potentiation of the SC-CA1 synapse by the HFS protocol (Frey *et al.*, 1993). This result mirrored the observation by (Huang and Kandel, 1995) with the application the dopamine agonist SKF 38393 before and after a strong HFS protocol. It suggests that the biochemical pathways activated by HFS and PKA both converge onto the same pathway (Frey *et al.*, 1993) and consume a limited resource to produce late-LTP, since the leading protocol occludes the following protocol. Furthermore, the application of a protein synthesis inhibitor in combination with a HFS (Sajikumar *et al.*, 2008) or LFS (Sajikumar and Frey, 2004) protocol blocked the consolidation of early-LTP or early-LTD into late-LTP or late-LTD, respectively. Various authors observed a similar result when the dopamine receptors were blocked by the D1/D5 antagonist SCH 23390

(Sajikumar *et al.*, 2008; Huang and Kandel, 1995). These results taken together suggest that the limited resource could possibly be a protein substrate critical for the protein synthesis of plasticity proteins responsible for consolidation of LTP and LTD, or it could possibly be the limited availability of protein synthesis machinery. I believe that it would be worth performing additional experiments that would support the limited resource hypothesis by applying a dopamine agonist immediately before two different LFS protocols that induce similar levels of LTD but have drastically different stimulation durations, such as the application of 100 μM SKF 38393 immediately after three trains of 900 pulses at 1 Hz (see Figure 3.27A) and immediately after the a LFS protocol of 900 bursts of 3 pulses at 1 Hz (see Figure 3.27B). This will not only validate my modeling hypothesis of the limited resources but support many predictions from my model.

We have developed my modeling framework in a way so that any part of the model can be swapped out if an improved model becomes available. For example, if a better HFS/LFS model becomes available, the new HFS/LFS model could replace the frequency dependent plasticity dynamics in Eqs. 3.6a- 3.6i without making substantive changes in the entire model. In order to fully incorporate the new model's dynamics into the rest of the model, the output of the frequency dependent model to the other segments of my SC-CA1 model must be updated, as well. Therefore, the derivative of the output of the new HFS/LFS model, which determines the SC-CA1 synaptic plasticity change, must be updated in Eqs. 3.15i, 3.15j, 3.15n, and 3.15o. Additionally, my model could possibly be used to make prediction about the dopaminergic modulation of spike-timing dependent plasticity (STDP) by swapping out the frequency dependent plasticity model for a STDP model. The rest of the parameters would then need to be re-fit to the STDP specific experimental data. Finally, the dopaminergic model could be expanded to other dopamine agonists if the concentration dependent slow-onset potentiation experimental data becomes available. The inherent segmented nature of my model makes it more flexible and may allow incorporation of different types of plasticity and neuromodulators to be considered in the future.

Our model assumes that SKF 38393 can induce a slow-onset-potentiation in the SC-CA1 synapses in the absence of an LTP/LTD stimulation protocol (HFS/LFS). Although I found some controversy on this in the literature (Mockett *et al*., 2007, 2004; Huang and Kandel, 1995; Lemon and Manahan-Vaughan, 2006; Shivarama Shetty *et al*., 2016), recent experiments on applying various concentration levels of SKF 38393 in the absence of any HFS/LFS protocol (Shivarama Shetty *et al*., 2016; Shetty and Sajikumar, 2017) support my modeling assumption. While the lack of sufficient data may limit the quality of my model, it still provides important insights into the gaps in my current understanding. Moreover, it suggests specific experiments that I believe will help to fill in the gaps in my understanding of the spatiotemporal modulation of SC-CA1 synapses by dopamine.

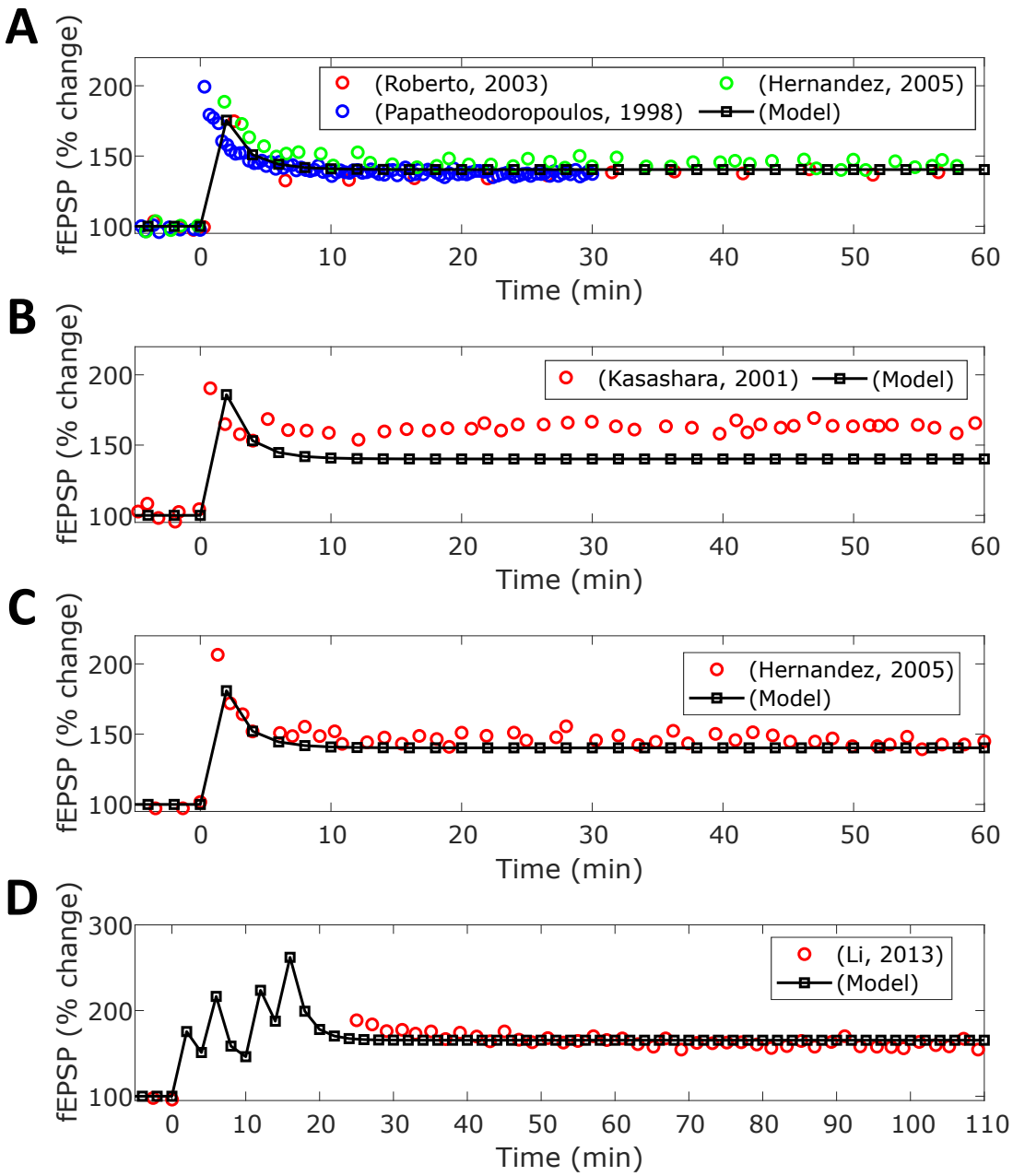

FIGURE 3.7: HFS-induced LTP with different HFS protocols. I provided one, two, and four trains of 100 pulses delivered at 100 *Hz* to my SC-CA1 model with different inter-train intervals. In **(A)**, I applied one trains of HFS. **(B)** and **(C)** shows the induced LTP from two trains of HFS with an inter-train interval of 10 seconds and 20 seconds, respectively. **(D)** shows the HFS-induced LTP from four trains of HFS with an inter-train of 5 minutes. In each case, the HFS-induced LTP observed in experiment is represented by the colored-circles and the LTP induced in my model is shown as the black-squares. The root mean squared error between the experimental data and the model prediction for Roberto (Roberto *et al.*, 2003), Hernandez (Hernandez *et al.*, 2005), Papatheodoropoulos, (Papatheodoropoulos and Kostopoulos, 2000), Kasashara (Kasahara *et al.*, 2001), Hernandez (Hernandez *et al.*, 2005), and Li (Li *et al.*, 2013) is 5 %, 4.9 %, 6.8 %, 22.1 %, 7.3 %, and 7.6 %, respectively.

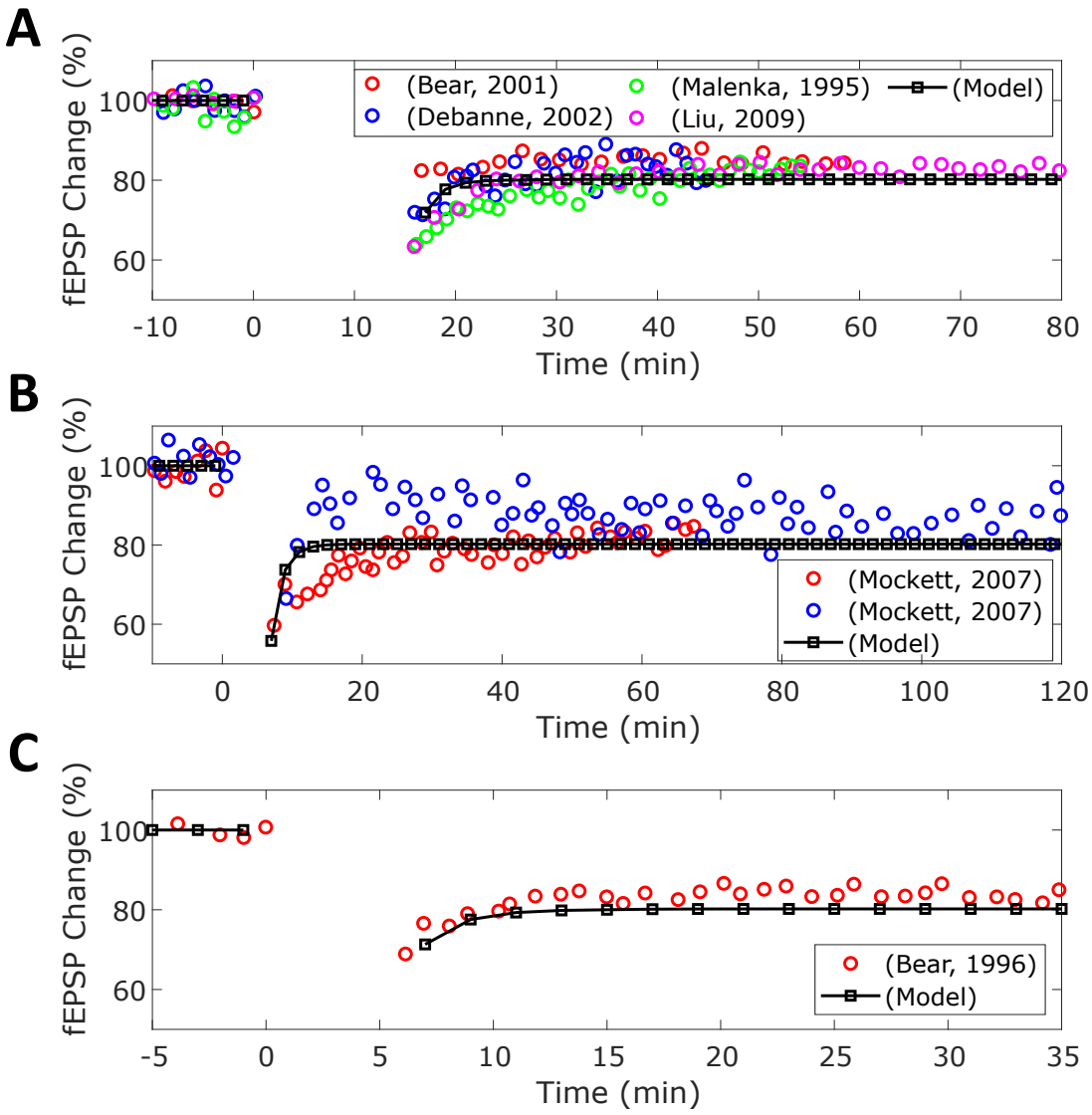

FIGURE 3.8: LFS-induced LTD. I provided three different LFS trains to my SC-CA1 model and compared the induced LTP in my model (black-squares) to the induced LTP in experiment (colored-circles). I considered LFS protocols consisting of **(A)** 900 pulses at 1 *Hz*, **(B)** 1200 pulses at 3 *Hz* and **(C)** 900 pulses at 3 *Hz*. The root mean squared error between the experimental data and the model prediction for Bear (Huber *et al.*, 2001), Malenka (Selig *et al.*, 1995), Debanne (Daoudal *et al.*, 2002), Liu (Liu *et al.*, 2009), Mockett (Mockett *et al.*, 2007), Mockett (Mockett *et al.*, 2007), and Bear (Heynen *et al.*, 1996) is 5.5 %, 4 %, 4.7 %, 3 %, 5.5 %, 8.9 %, and 3.8 %, respectively.

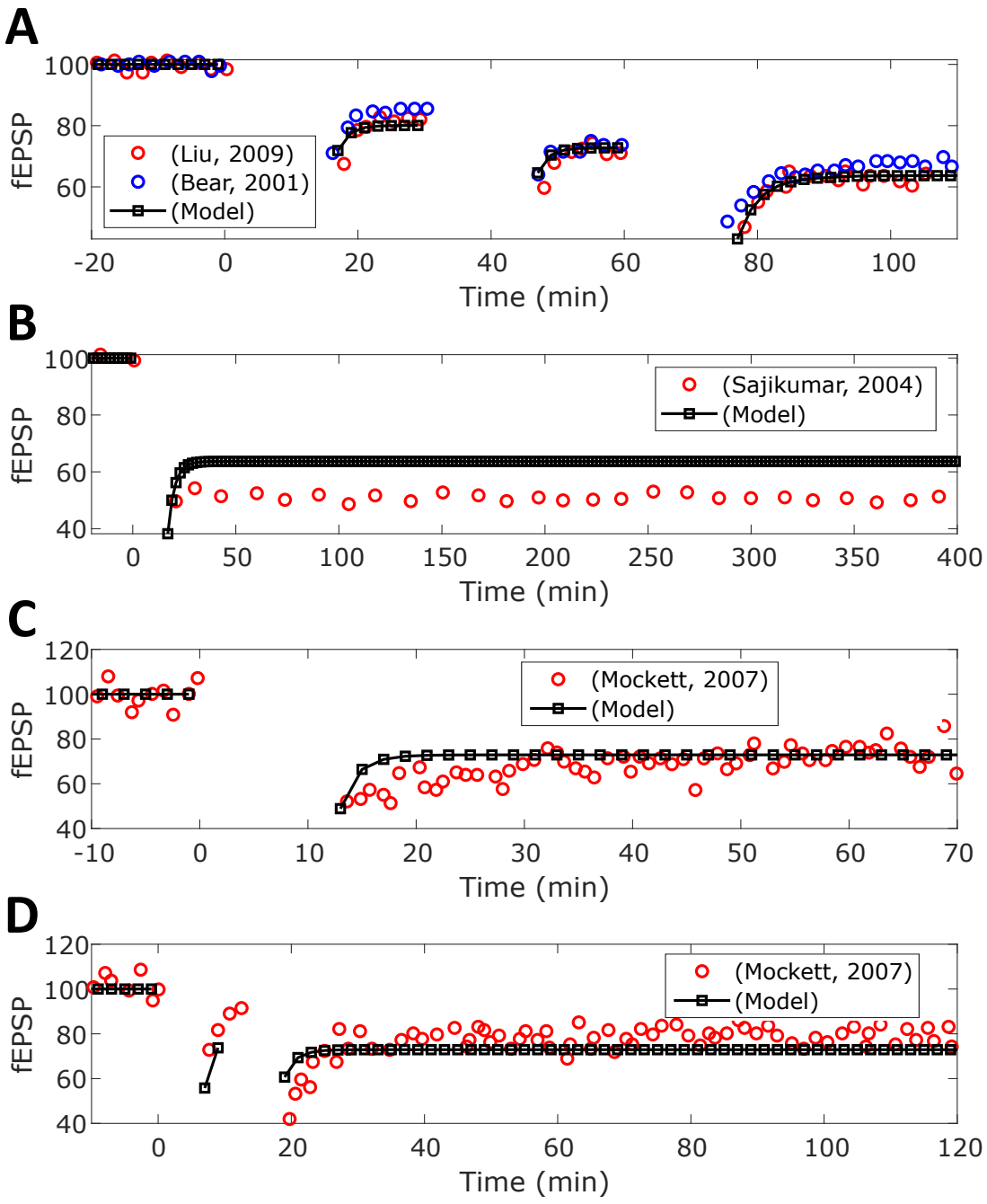

FIGURE 3.9: LFS-induced LTD with other LFS protocols. I provided four other LFS protocols to my SC-CA1 model and compared the induced LTP in my model (black-squares) to the induced LTP in experiment (colored-circles). I considered LFS protocols consisting of **(A)** three trains of 900 pulses at 1 *Hz* with a inter-train interval of 15 minutes, **(B)** 900 burst of 3 pulses at 1 *Hz* where the pulses in the burst were delivered at 20 *Hz*, **(C)** 2400 pulses at 3 *Hz*, and **(D)** two trains of 1200 pulses at 3 *Hz*. The root mean squared error between the experimental data and the model prediction for Liu (Liu *et al.*, 2009), Bear (Huber *et al.*, 2001), Sajikumar (Sajikumar and Frey, 2004), Mockett (Mockett *et al.*, 2007), and Mockett (Mockett *et al.*, 2007) is 2.3 %, 3.3 %, 12.5 %, 7.9 %, and 6.8 %, respectively.

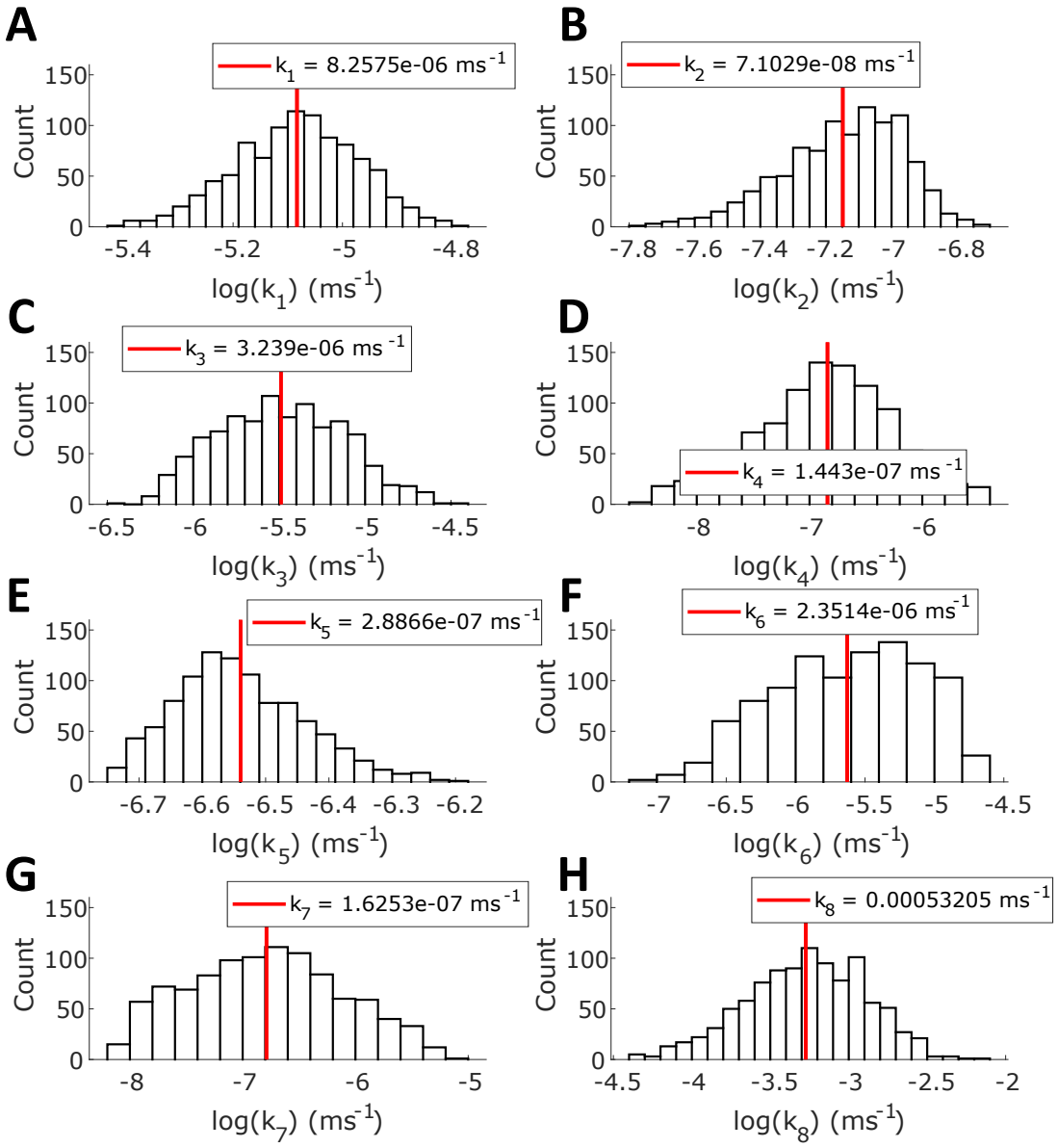

FIGURE 3.10: Inference of dopaminergic model parameters. Each histogram represents the approximate posterior distributions of the parameters **(A)** k_1, **(B)** k_2, **(C)** k_3, **(D)** k_4, **(E)** k_5, **(F)** k_6, **(G)** k_7, and **(H)** k_8. The red-line represents the mean log value.

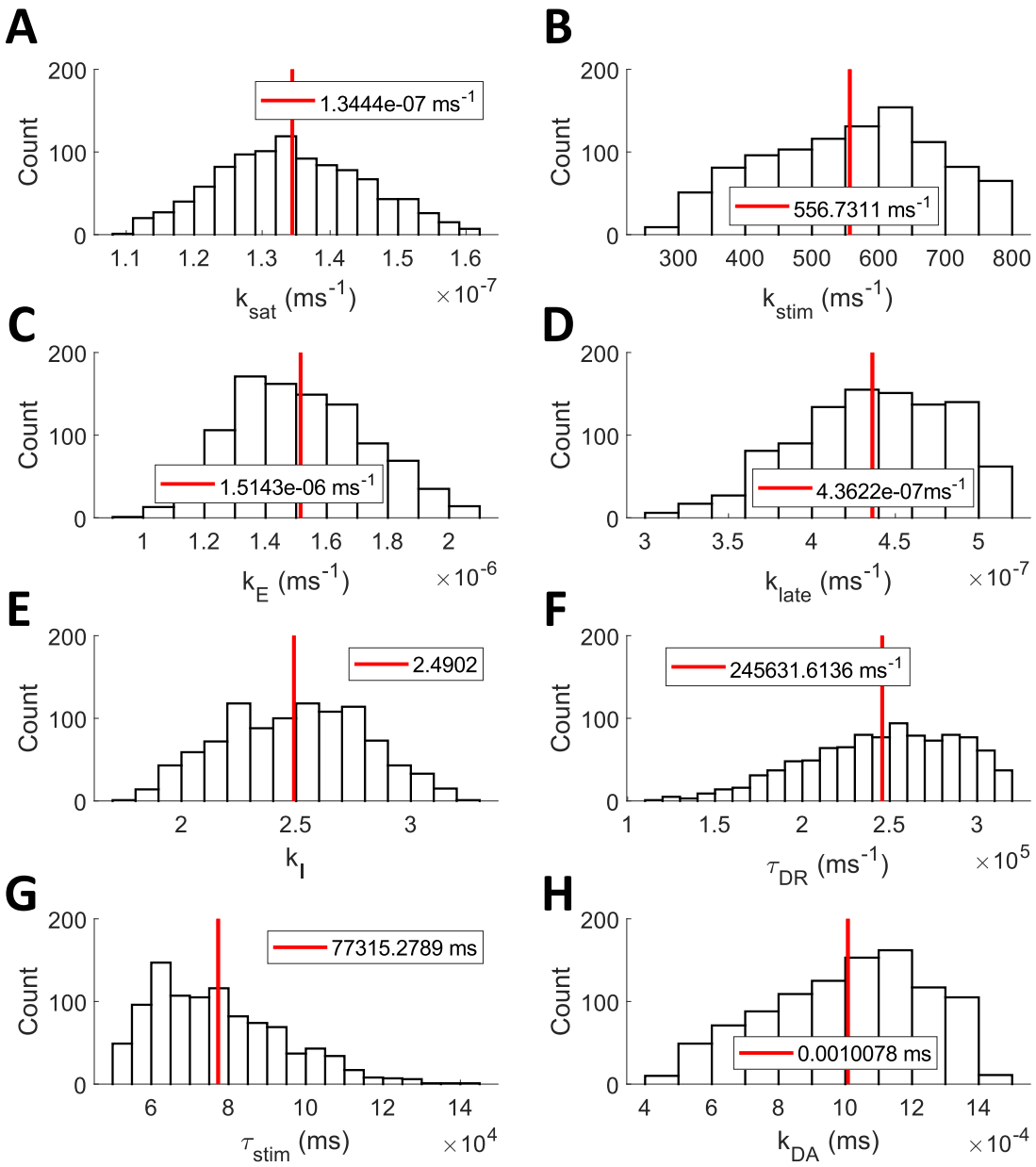

FIGURE 3.11: Inference of dopaminergic modulation of HFS and LFS model parameters. Each histogram represents the approximate posterior distributions of the parameters **(A)** k_{sat}, **(B)** k_{stim}, **(C)** k_E, **(D)** k_I, **(E)** k_{late}, **(F)** k_{DA}, **(G)** τ_{stim}, and **(H)** τ_{DA}. The red-line represents the mean value.

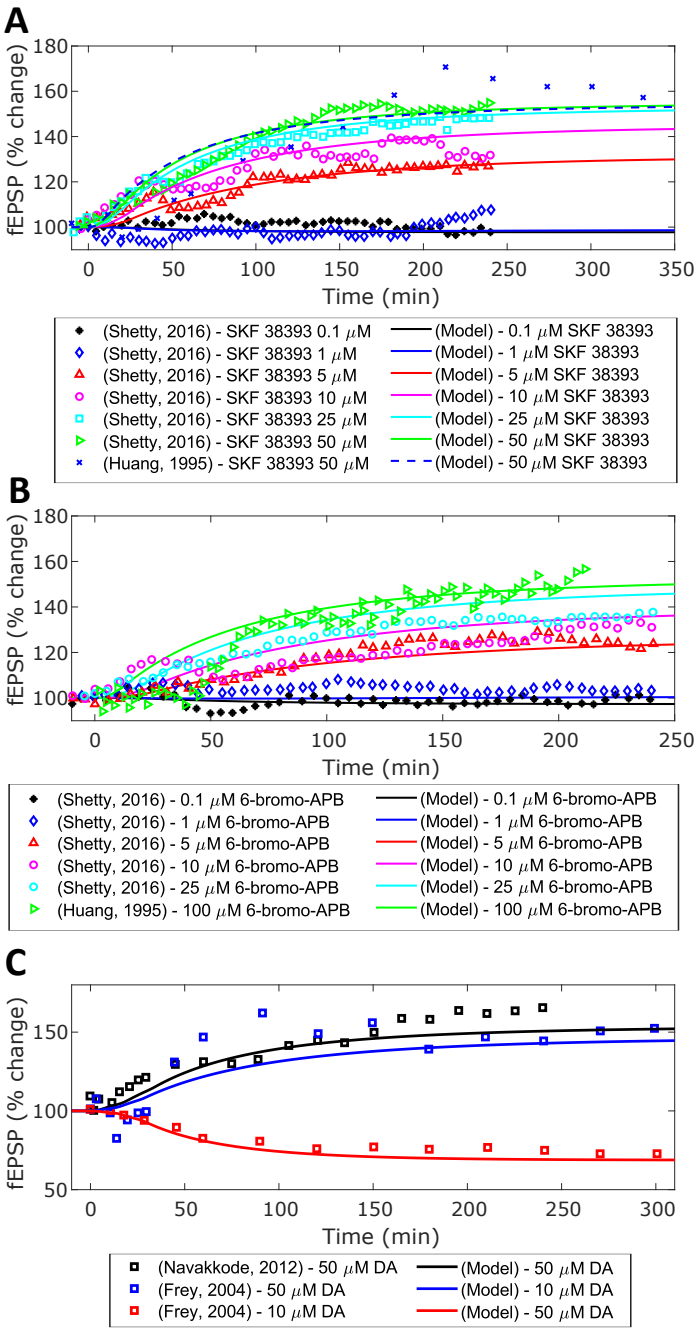

FIGURE 3.12: Dopaminergic slow-onset-potentiation by SKF 38393, 6-bromo-APB, and dopamine. I provided the dose dependent slow-onset-potentiation induced by the application of the dopamine agonists **(A)** SKF 38393, **(B)** 6-bromo-APB, **(C)** and dopamine. In the Shetty experimental data (Shivarama Shetty *et al.*, 2016), the dopaminergic agonist was applied three times for 5 minutes with 5 minute intervals at 0 minutes. The dopaminergic agonists applied by Huang (Huang and Kandel, 1995) was applied for 15 minutes at 0 minutes. Frey (Sajikumar and Frey, 2004) applied dopamine three times for 3 minutes with 10 minute intervals at 0 minutes, and Navakkode (Navakkode *et al.*, 2012) applied dopamine three times for 5 minutes with 10 minute intervals at 0 minutes.

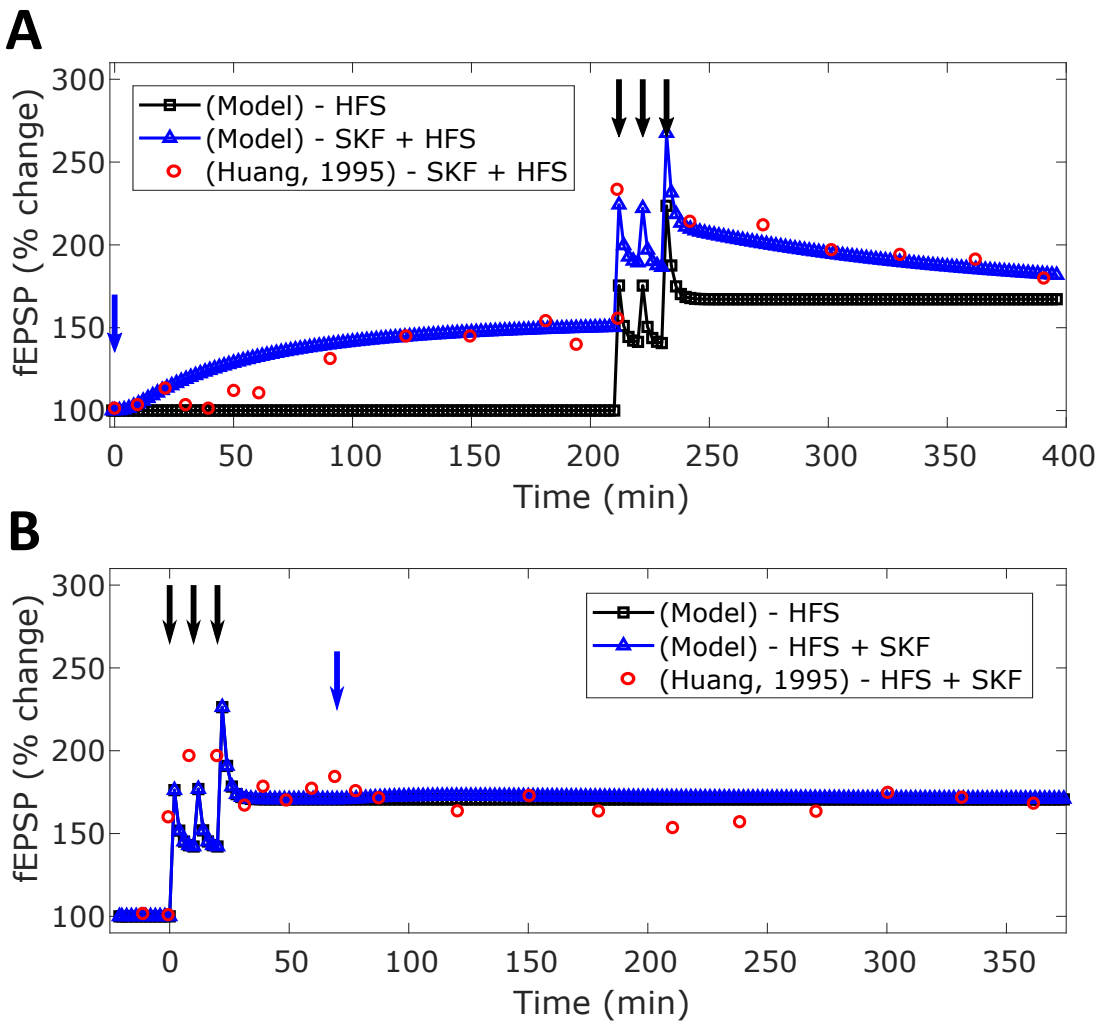

FIGURE 3.13: Quantitative comparison between the model predicted and experimentally observed (Huang and Kandel, 1995) modulation of HFS-induced LTP in hippocampal SC-CA1 synapse by D1/D5 agonist SKF 38393. The induced LTP of the SC-CA1 synapse is measured in terms of the percentage (%) change in evoked fEPSP slope from the control. The black-squares represents the application of the HFS protocol of three trains of pulse at 100 Hz for 1 second with a 10 minute intertrain interval, while the blue-triangles represent the same HFS protocol in combination with 50 μM SKF 38393 for 15 minutes applied at various time distances from the HFS protocol ($\Delta t = t_{SKF} - t_{HFS}$). **(A)** shows the HFS-induced LTP without (black-squares) and with (blue-triangles) 50 μM SKF 38939 delivered 212 minutes before the HFS protocol. The experimentally reported SKF 38393 enhancement of LTP (Huang and Kandel, 1995) is shown as the red-circles ($\Delta t = -212$ min). The root mean squared error between the experimental data and the model prediction is 10.3 % change in $fEPSP$. **(B)** shows the SKF 38393 enhancement of the HFS-induced LTP when 15 minutes of 50 μM SKF 38393 is delivered 50 minutes after the HFS administration ($\Delta t = 50$ min). The root mean squared error between the experimental data and the model prediction is 19.8 % change in $fEPSP$.

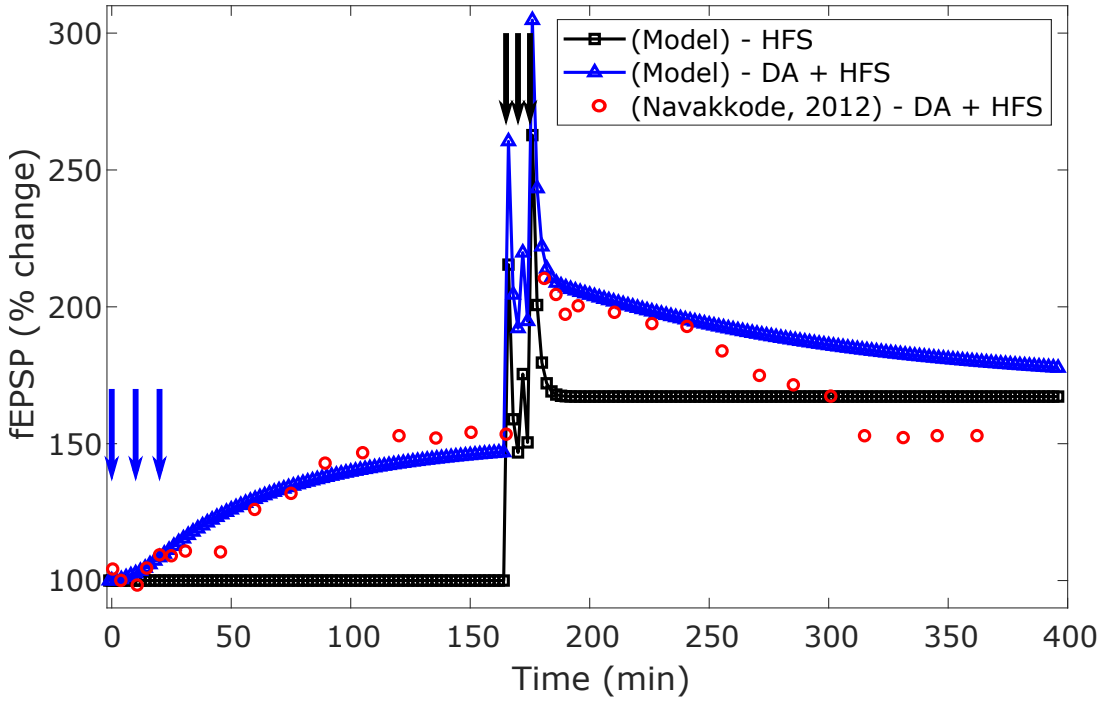

FIGURE 3.14: Quantitative comparison between the model predicted and experimentally observed (Navakkode *et al.*, 2012) modulation of HFS-induced LTP in hippocampal SC-CA1 synapse by dopamine (DA). The induced LTP of the SC-CA1 synapse is measured in terms of the percentage (%) change in evoked fEPSP slope from the control. DA is applied 165 minutes before the HFS stimulation protocol of three trains of 100 pulses at 100 Hz with a 5-minute inter-train interval. The HFS induced LTP when (blue-triangles) 50 μM DA is delivered before the HFS protocol is compared to the HFS only induced LTP (black-squares). The experimentally reported dopaminergic enhancement of LTP (Navakkode *et al.*, 2012) is shown as the red-circles ($\Delta t = -165$ min). The root mean squared error between the experimental data and the model prediction is 28.8 % change in $fEPSP$.

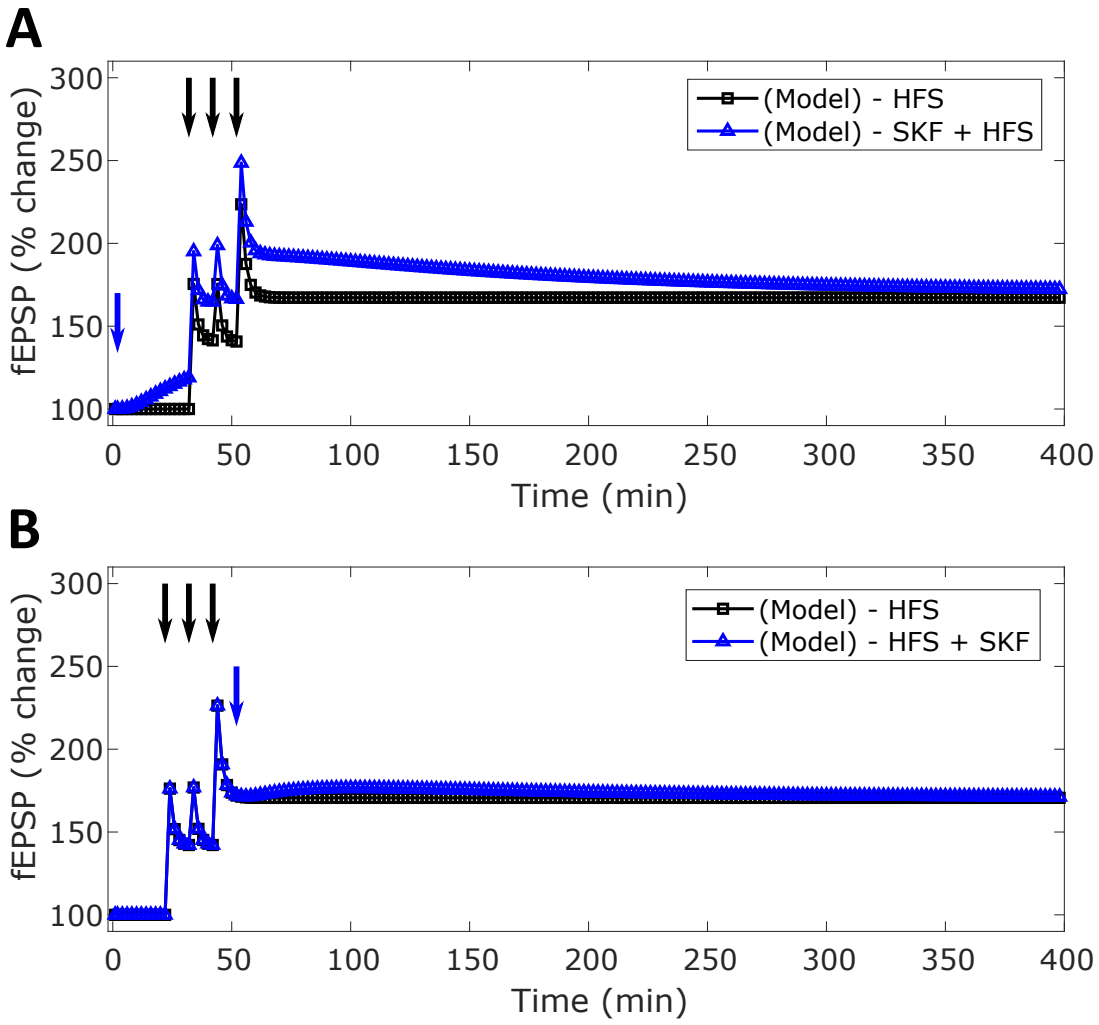

FIGURE 3.15: Predictions from the model on the modulation of HFS-induced LTP in the hippocampal SC-CA1 synapse by D1/D5 agonist SKF 38393 when the D1/D5 agonist SKF 38393 is delivered closer in time relative to the applied HFS protocol. In these simulation results, SKF 38393 is applied 30 minutes before **(A)** and 10 minutes after **(B)** the HFS protocol of 3 trains of 100 pulses at 100 Hz with a 10 minute inter-train intervals. The induced LTP of the SC-CA1 synapse is measured in terms of the percentage (%) change in evoked fEPSP slope from the control. **(A)** shows approximately 20% enhancement immediately after the HFS protocol in the HFS-induced LTP by SKF 38393 when delivered 30 minutes before the HFS protocol (blue-triangles) of ($\Delta t = -30$ min). The LTP induced by only HFS is shown as the black-squares. **(B)** shows a small (negligible) enhancement in the HFS-induced LTP when SKF 38393 is delivered 10 minutes (blue-triangles) after the HFS protocol ($\Delta t = 10$ min).

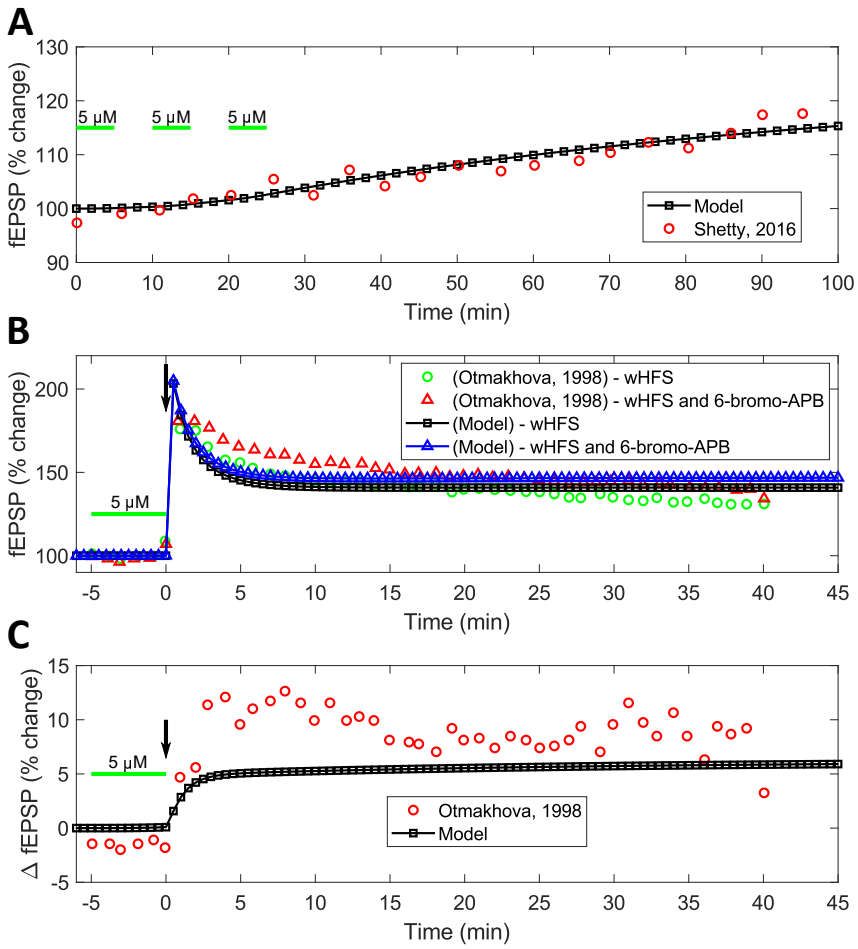

FIGURE 3.16: Comparison between the model predicted and experimentally observed modulation of weak HFS-induced LTP in hippocampal SC-CA1 synapse by D1/D5 agonist 6-bromo APB. The induced LTP of the SC-CA1 synapse is measured in terms of the percentage (%) change in evoked fEPSP slope from the control. **(A)** shows the slow-onset potentiation due to the application of 5 μM of 6-bromo-APB for 5 minutes with 5 minute intervals (green-bars) observed in the experiment (Shivarama Shetty *et al.*, 2016) (red-circles) and predicted by my model (black-squares). **(B)** shows the dopaminergic enhancement by 5 μM of 6-bromo-APB for 5 minutes (green-bar) of LTP induced by a weak HFS protocol of 10 bursts of 4 pulses at 100 Hz with a 30 ms interval (black-arrow). The green-circles show the LTP induced by the weak HFS protocol alone and the red-triangles show the LTP induced by the weak HFS with 6-bromo-APB in the experiment (Otmakhova and Lisman, 1996). In the result predicted by my model, the induced LTP from a weak HFS protocol is shown as black-squares and the LTP induced by a weak HFS protocol with the 5 μM of 6-bromo-APB is shown as the blue-triangles. The root mean squared error between the experimental data and the model prediction is 5.9 % and 7.5 % for the weak HFS protocol and the weak HFS protocol plus 6-bromo-APB. **(C)** shows the absolute dopaminergic enhancement of LTP (Δ fEPSP) by 6-bromo-APB in the experiment (Otmakhova and Lisman, 1996) (red-diamonds) and my model (black-squares) computed by subtracting the measured potentiation of the weak HFS plus 6-bromo-APB from potentiation by weak HFS alone.

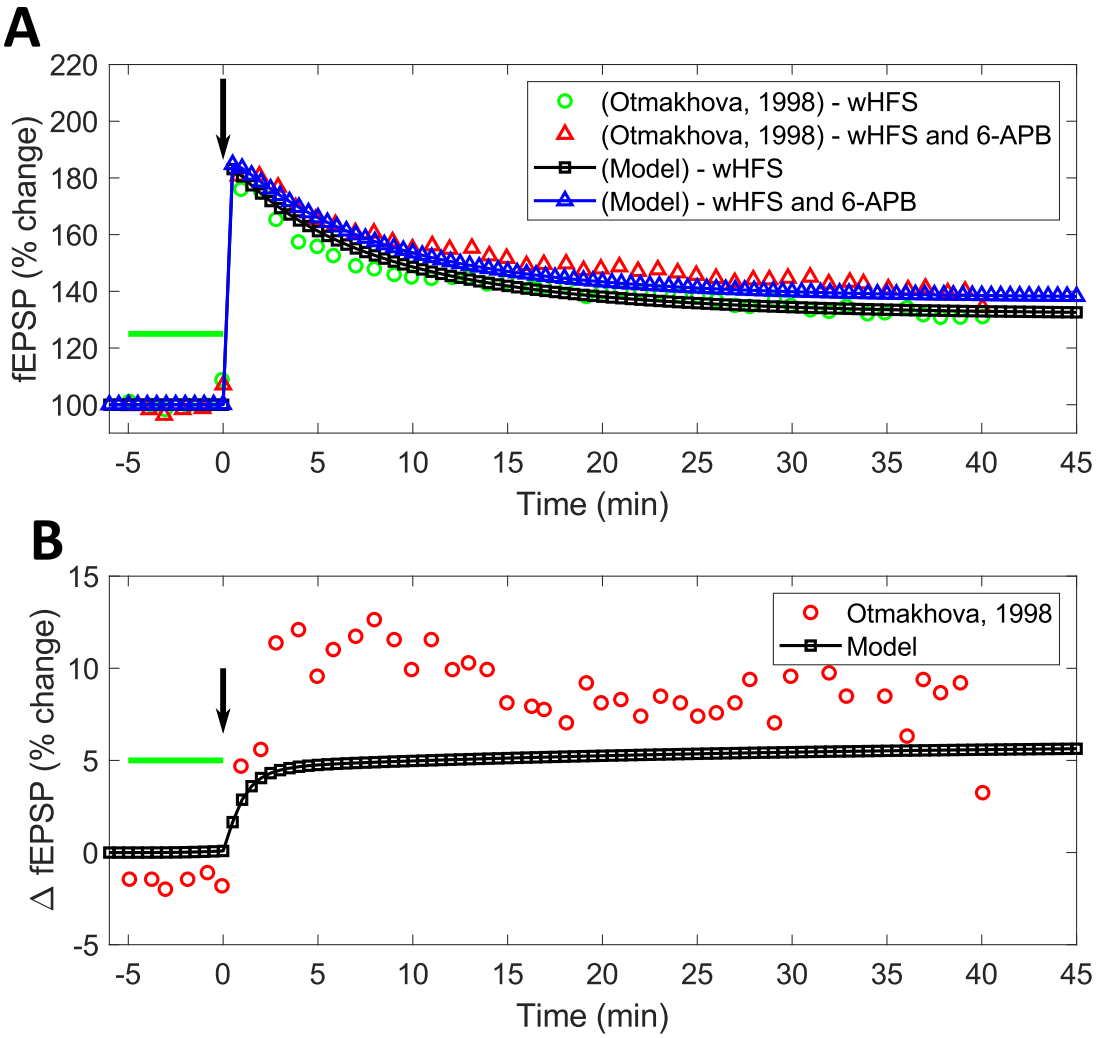

FIGURE 3.17: Enhancement in the model predictions shown in Figure 3.16 with improved HFS-induced LTP prediction. I tuned the model parameters of the HFS model to match the experimental data on weak HFS-induced LTP from (Otmakhova and Lisman, 1996). Then I used my model to again predict the changes in the weak HFS-induced LTP after the application 5 μM of 6-bromo-APB for 5 minutes (green-bar). **(A)** shows the enhancement in the weak HFS-induced LTP by 6-bromo-APB with the new parameters. The experimental and model predicted data on the simultaneous application of weak HFS protocol and 6-bromo-APB are shown by the red-triangles and blue-triangles, respectively. The experimental and model predicted data on the weak HFS application alone are shown by the green-circles and black-squares, respectively. The root mean squared error between the experimental data and the model prediction is 3.5 % and 3.6 % for the weak HFS protocol and the weak HFS protocol plus 6-bromo-APB, respectively. **(B)** shows the comparison between the absolute dopaminergic enhancement of LTP (Δ fEPSP) by 6-bromo-APB observed in the experiment (Otmakhova and Lisman, 1996) (black-squares) and predicted my model (red-squares) with the modified HFS model parameters. Δ fEPSP is computed by subtracting the measured potentiation of the weak HFS plus 6-bromo-APB from potentiation by the weak HFS alone. The modified HFS model parameters in Eq. 3.6c are $p_p = 1.5099 \times 10^{-6}\ \ ms^{-1}$, $M_p = 7.4938 \times 10^{-9}\ \ ms^{-1}$, and $f = 298$.

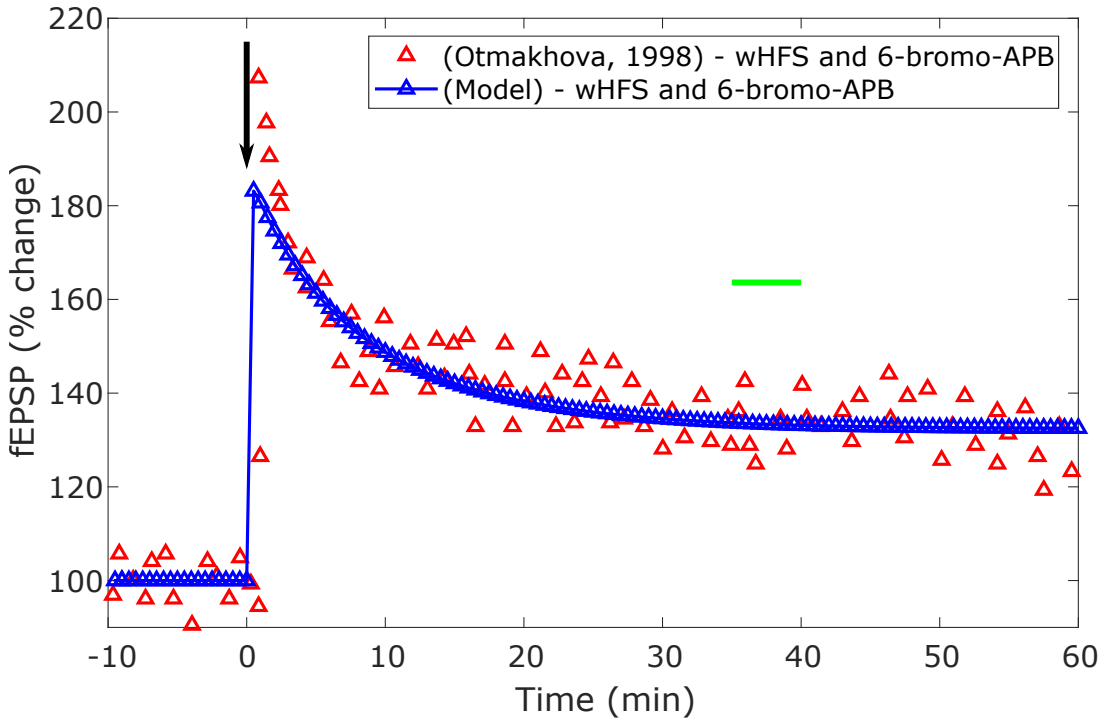

FIGURE 3.18: Comparison between the model predicted and the experimentally observed (Otmakhova and Lisman, 1996) modulation of a weak HFS-induced LTP when 6-bromo-APB was delivered after the weak HFS protocol. The dopaminergic agonist 6-bromo-APB is applied 35 minutes after a weak HFS protocol of 10 bursts of 4 pulses at 100 Hz with a 30 ms interval (black-arrow). The model parameters of the HFS model is the same as the one used in Figure 3.17. The induced LTP of the SC-CA1 synapse is measured in terms of the percentage (%) change in evoked fEPSP slope from the control. The 6-bromo-APB enhanced weak HFS-induced LTP predicted by the model is shown as the blue-triangles and observed in the experiment as the red-triangles (Otmakhova and Lisman, 1996). The root mean squared error between the experimental data and the model prediction is 8.1 %. The modified HFS model parameters in Eq. 3.6c are $p_p = 1.5099 \times 10^{-6}\ \ ms^{-1}$, $M_p = 7.4938 \times 10^{-9}\ \ ms^{-1}$, and $f = 298$.

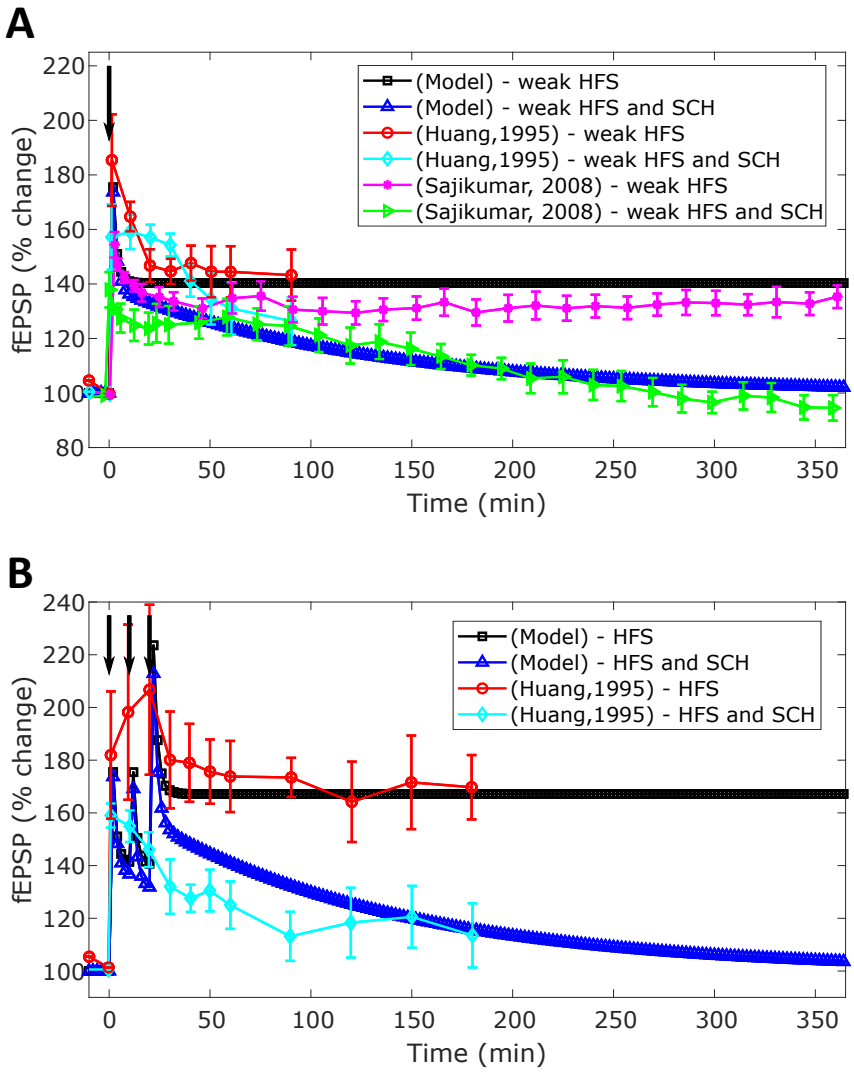

FIGURE 3.19: The effect of basal dopamine level on HFS-induced LTP. **(A)** compares the LTP induced by a weak HFS protocol of 100 *Hz* stimulation in the presence of a D1/D5 antagonist SCH 23390 from experiments (shown in cyan-diamonds and green-triangles) (Huang and Kandel, 1995; Sajikumar *et al.*, 2008) with the predictions from my model (blue-triangles). The only HFS-induced LTP from the experiments are shown in red-circles and magenta-stars and from the model is shown in black-squares. The root mean squared error between the weak HFS experimental data and the weak HFS model prediction for Huang (Huang and Kandel, 1995) and Sajikumar (Sajikumar *et al.*, 2008) is 10.1 % and 8.5 %, respectively. The root mean squared error between the weak HFS plus SCH 23390 experimental data and the weak HFS plus SCH 23390 model prediction for Huang (Huang and Kandel, 1995) and Sajikumar (Sajikumar *et al.*, 2008) is 17 % and 9.9 %, respectively. **(B)** compares the LTP induced by a strong HFS protocol (3 trains of 100 *Hz*) in the presence of a D1/D5 antagonist SCH 23390 from the experiment (cyan-diamond) (Huang and Kandel, 1995) with the prediction from my model (blue-triangles). The only HFS-induced LTP from the experiment is shown in red-circles and from the model is shown in black-squares. The root mean squared error between the experimental data and the model prediction for strong HFS data and strong HFS plus SCH 23390 is 28.3 % and 15.1 %, respectively.

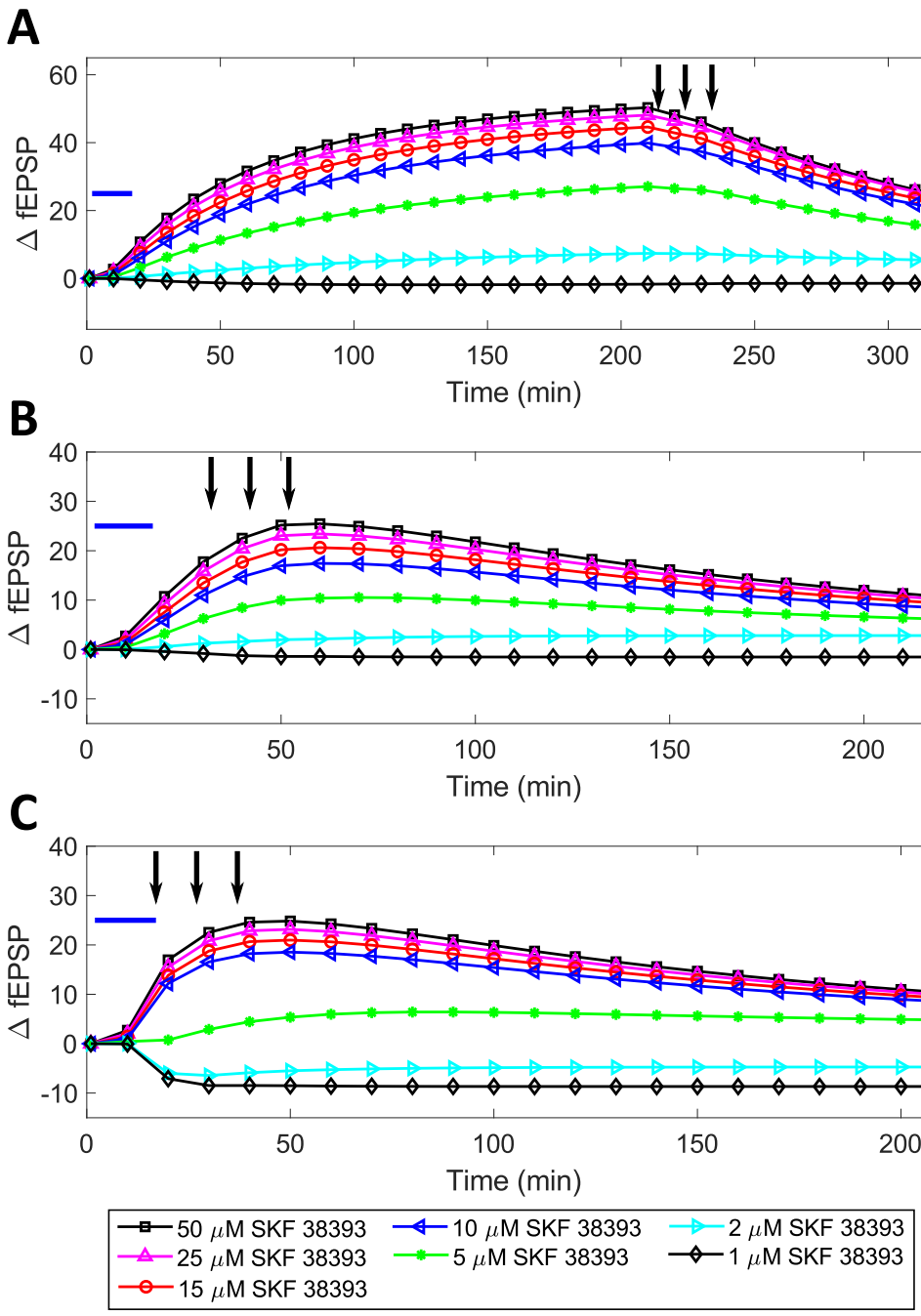

FIGURE 3.20: Model predictions on the effect of the concentration and timing of SKF 38393 relative to a strong HFS protocol (3 trains of 100 pulses at 100 Hz) in modulating HFS-induced LTP when SKF 38393 was delivered before the HFS protocol. SKF 38393 (blue-bar) was delivered **(A)** 212 minutes ($\Delta t = -212$ min), **(B)** 30 minutes ($\Delta t = -30$ min), and **(C)** 15 minutes ($\Delta t = -15$ min) before the strong HFS protocol (black-arrow). ΔfEPSP is computed by subtracting the measured potentiation of the strong HFS plus SKF 38393 from the potentiation by the strong HFS alone. The strong HFS protocol on its own results in a 67% increase of the synaptic strength.

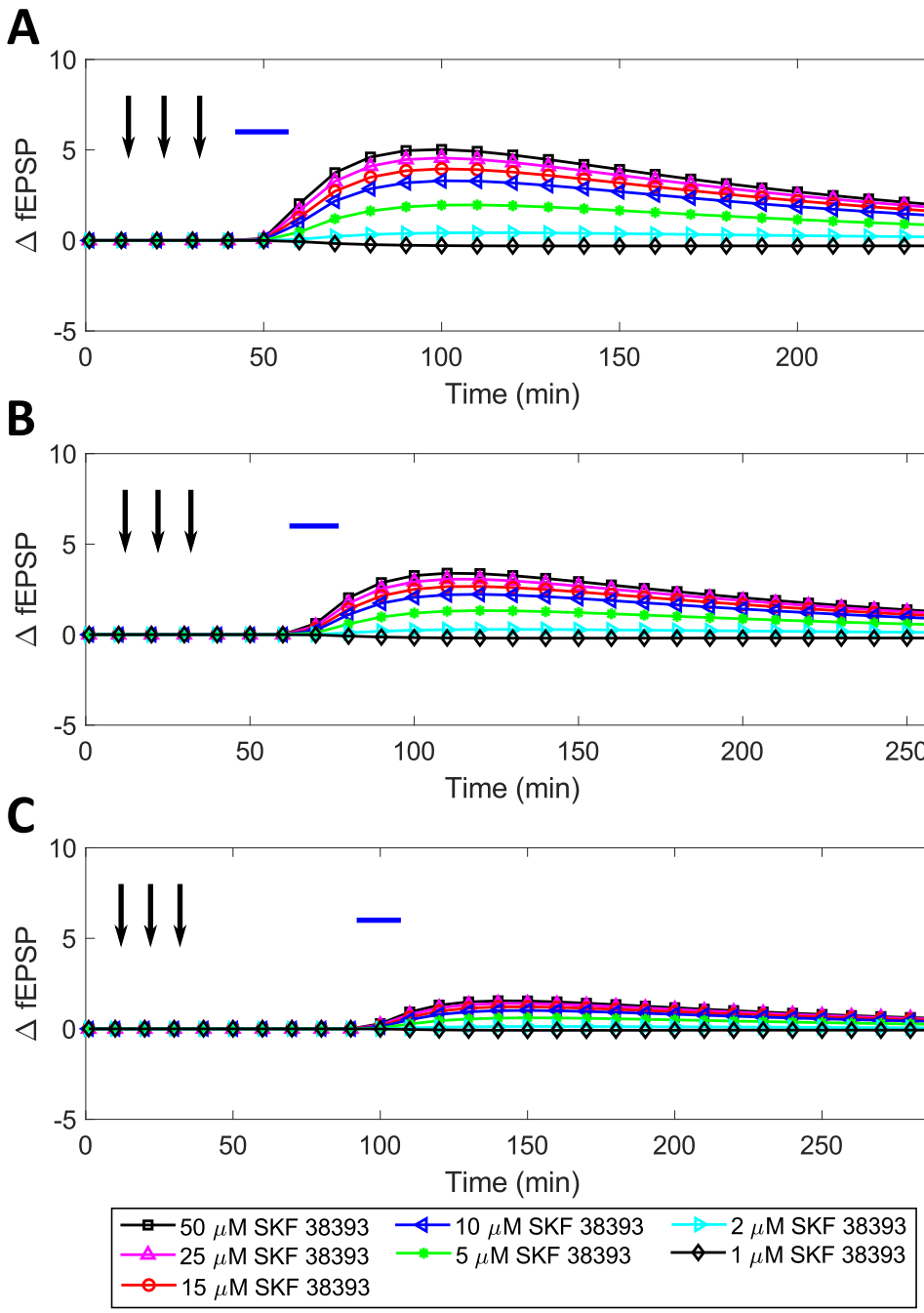

FIGURE 3.21: Model predictions on the effect of the concentration and timing of SKF 38393 relative to a strong HFS protocol (3 trains of 100 pulses at 100 Hz) in modulating HFS-induced LTP when SKF 38393 was delivered after the HFS protocol. SKF 38393 (blue-bar) was delivered **(A)** 10 minutes ($\Delta t = 10$ min), **(B)** 30 minutes ($\Delta t = 30$ min), and **(C)** 60 minutes ($\Delta t = 60$ min) after the end of the strong HFS protocol (black-arrow). ΔfEPSP is computed by subtracting the measured potentiation of the strong HFS plus SKF 38393 from the potentiation by the strong HFS alone. The strong HFS protocol on its own results in a 67% increase of the synaptic strength.

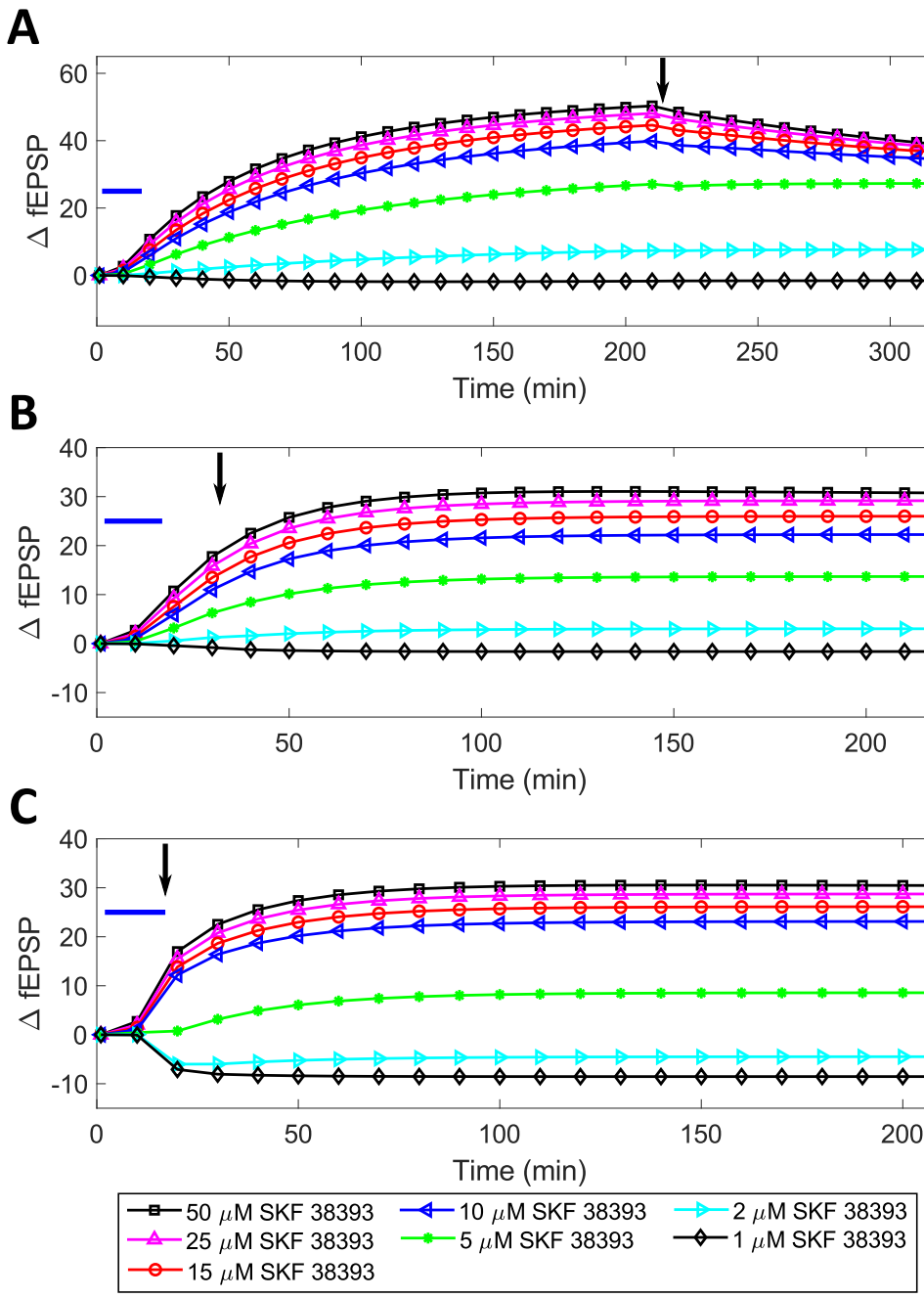

FIGURE 3.22: Model predictions on the effect of the concentration and timing of SKF 38393 relative to a weak HFS protocol (1 train of 100 pulses at 100 Hz) in modulating HFS-induced LTP when SKF 38393 was delivered before the HFS protocol. SKF 38393 (blue-bar) was delivered **(A)** 212 minutes ($\Delta t = -212$ min), **(B)** 30 minutes ($\Delta t = -30$ min), and **(C)** 15 minutes ($\Delta t = -15$ min) before the weak HFS protocol (black-arrows). ΔfEPSP is computed by subtracting the measured potentiation of the weak HFS plus SKF 38393 from the potentiation by the weak HFS alone. The weak HFS protocol on its own results in a 41% increase of the synaptic strength.

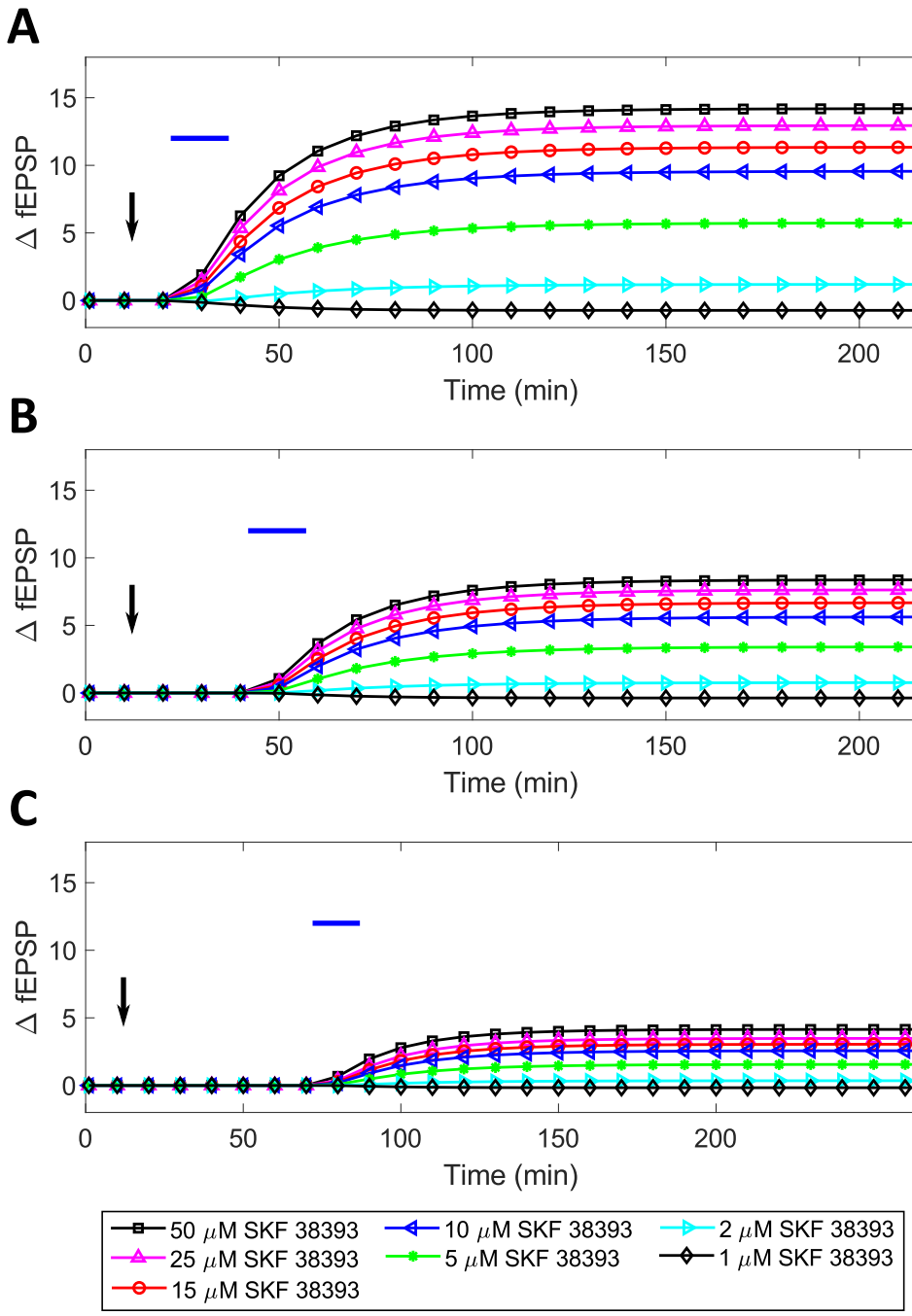

FIGURE 3.23: Model predictions on the effect of the concentration and timing of SKF 38393 relative to a weak HFS protocol (1 train of 100 pulses at 100 Hz) in modulating HFS-induced LTP when SKF 38393 was delivered after the HFS protocol. SKF 38393 (blue-bar) was delivered **(A)** 10 minutes ($\Delta t = 10$ min), **(B)** 30 minutes ($\Delta t = 30$ min), and **(C)** 60 minutes ($\Delta t = 60$ min) after the weak HFS protocol (black-arrows). ΔfEPSP is computed by subtracting the measured potentiation of the weak HFS plus SKF 38393 from the potentiation by the weak HFS alone. The weak HFS protocol on its own results in a 41% increase of the synaptic strength.

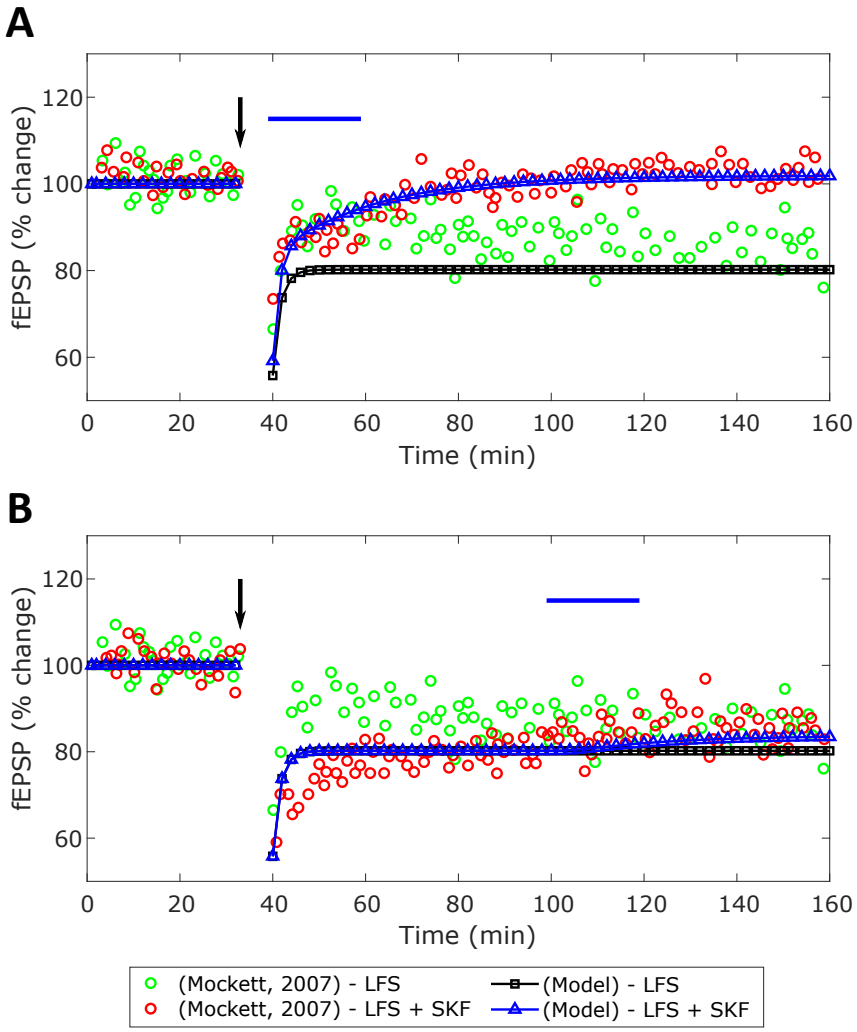

FIGURE 3.24: Quantitative comparison between the model predicted and experimentally observed (Mockett *et al.*, 2007) modulation of LFS-induced LTD in the hippocampal SC-CA1 synapse by a D1/D5 agonist SKF 38393. The induced LTD of the SC-CA1 synapse is measured in terms of the percentage (%) change in evoked fEPSP slope from the control. The black-squares represents the application of the LFS protocol of 1200 pulses at 3 Hz, while the blue-triangles represent the same LFS protocol in combination with 100 μM SKF 38393 for 20 minutes applied at time relative to the LFS protocol ($\Delta t = t_{SKF} - t_{LFS}$). **(A)** shows the LFS-induced LTD without (black-squares) and with (blue-triangles) 100 μM SKF 38939 delivered immediately after the LFS protocol. The experimentally reported SKF 38393 enhancement of LTD (Mockett *et al.*, 2007) is shown as the red-circles ($\Delta t = 0$ min). The root mean squared error between the experimental data and the model prediction for LFS data and LFS plus SKF 38393 is 8.9 % and 3.2 %, respectively. **(B)** shows the comparison between the prediction from my model and the experimental data (Mockett *et al.*, 2007) where 100 μM SKF 38393 was administered 60 minutes after the same LFS protocol ($\Delta t = 60$ min). The root mean squared error between the experimental data and the model prediction for LFS data and LFS plus SKF 38393 is 8.9 % and 4.8 %, respectively.

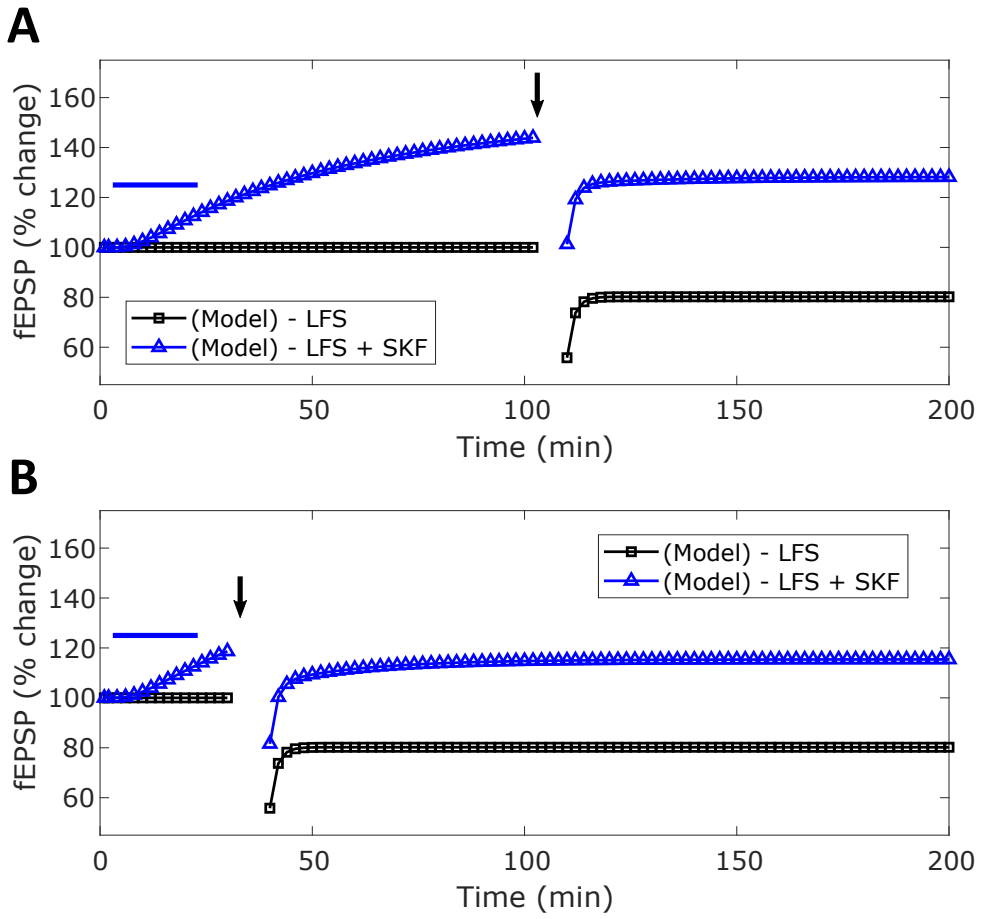

FIGURE 3.25: Predictions from my model on the modulation of LFS-induced LTD in the hippocampal SC-CA1 synapse by D1/D5 receptor agonist SKF 38393 when SKF 38393 is delivered prior to the LFS protocol. In these simulation results, 100 μM of SKF 38393 is applied 100 **(A)** and 30 minutes **(B)** before a LFS protocol of 1200 pulses at 3 Hz. **(A)** shows the modulation of the LFS-induced LTD by SKF 38393 when SKF 38393 was delivered 100 minutes before the LFS protocol marked as the blue-triangles ($\Delta t = 100$). The LTD induced by LFS alone is shown as the black-squares. **(B)** shows the modulation of the LFS-induced LTD by SKF 38393 when SKF 38393 was delivered 30 minutes before the LFS protocol ($\Delta t = 30$).

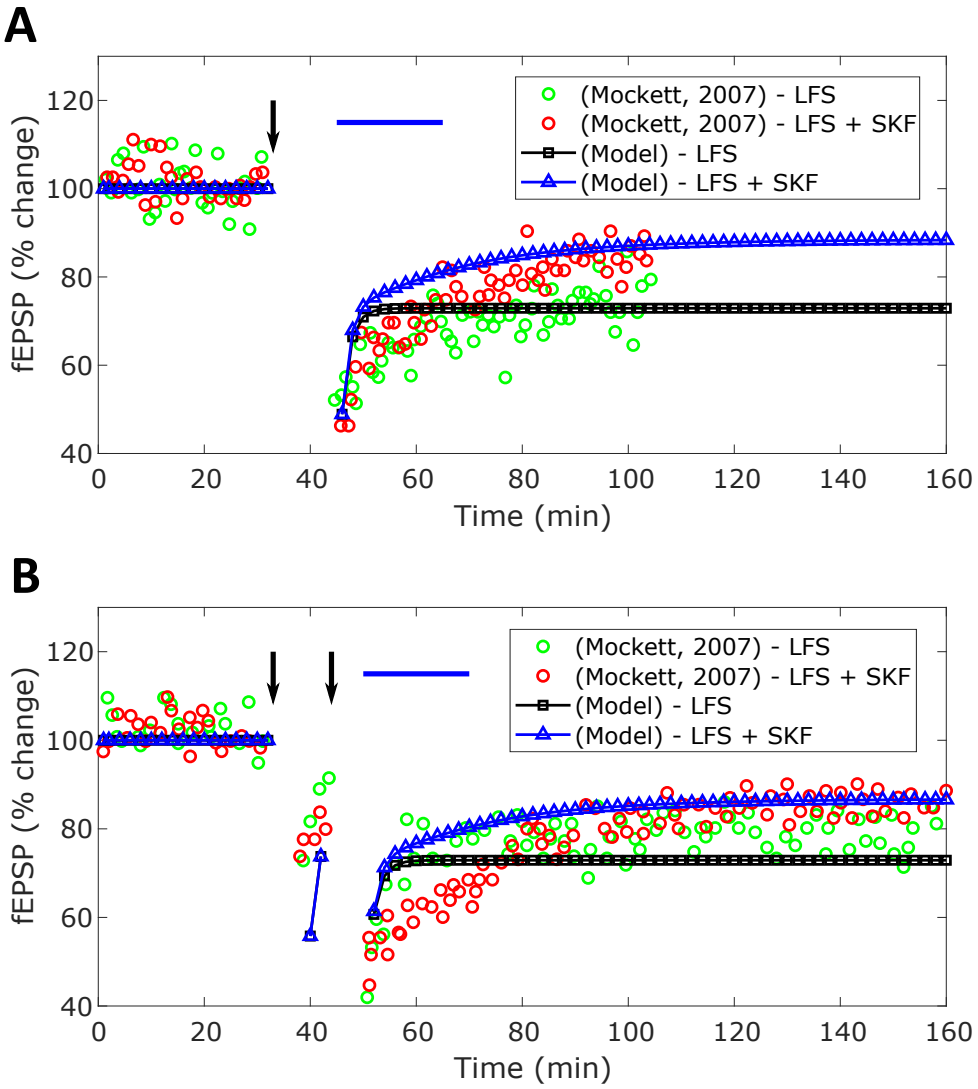

FIGURE 3.26: Quantitative comparison between the model predicted and experimentally observed (Mockett *et al.*, 2007) modulation of the LFS-induced LTD under various LFS protocol by SKF 38393. The induced LTD of the SC-CA1 synapse is measured in terms of the percentage (%) change in evoked fEPSP slope from the control. **(A)** shows the comparison between the potentiation of the LFS-induced LTD in the SC-CA1 synapse with the 20 minutes application of 100 μM SKF 38393 immediately after the LFS protocol of 2400 pulses at 3 Hz reported in the experiment (red-circles) and predicted by my model (blue-triangles). The model predicted LFS-induced LTD by the LFS protocol alone is shown as the black-squares. The root mean squared error between the experimental data and the model prediction for LFS data and LFS plus SKF 38393 is 7.1 % and 8 %, respectively. **(B)** shows the comparison between the potentiation of the LFS-induced LTD in the SC-CA1 synapse when 20 minutes of 100 μM SKF 38393 was administered immediately after a LFS protocol of two trains of 1200 pulses at 3 Hz with a 5 minute intertrain interval reported in the experiment (red-circles) and predicted by my model (blue-triangles). The root mean squared error between the experimental data and the model prediction for LFS data and LFS plus SKF 38393 is 7 % and 11 %, respectively.

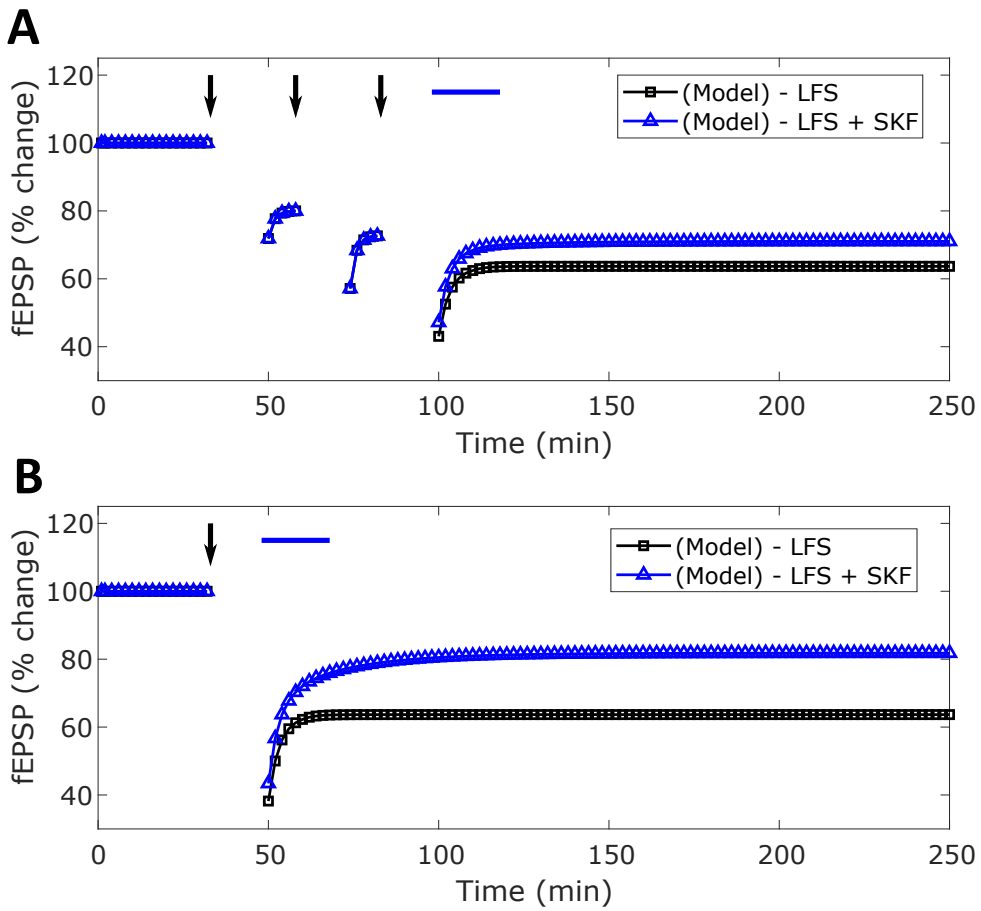

FIGURE 3.27: Predictions from my model on the modulation of the LFS-induced LTD under various LFS protocol by SKF 38393. 100 μM SKF 38393 was applied for 20 minutes immediately after two different LFS protocols. **(A)** shows the model predicted enhancement in the LFS-induced LTD by SKF 38393 for a LFS protocol of 3 trains of 900 pulses at 1 Hz with 10 minute intertrain intervals. **(B)** shows the model predicted enhancement in the LFS-induced LTD by SKF 38393 for a LFS protocol of 900 bursts at 1 Hz where each burst consists of 3 pulses delivered at 20 Hz. The SKF 38393 modulated LFS-induced LTD is shown as blue-triangles and the LFS-induced LTD in the absence of SKF 38393 is denoted as the black-squares.

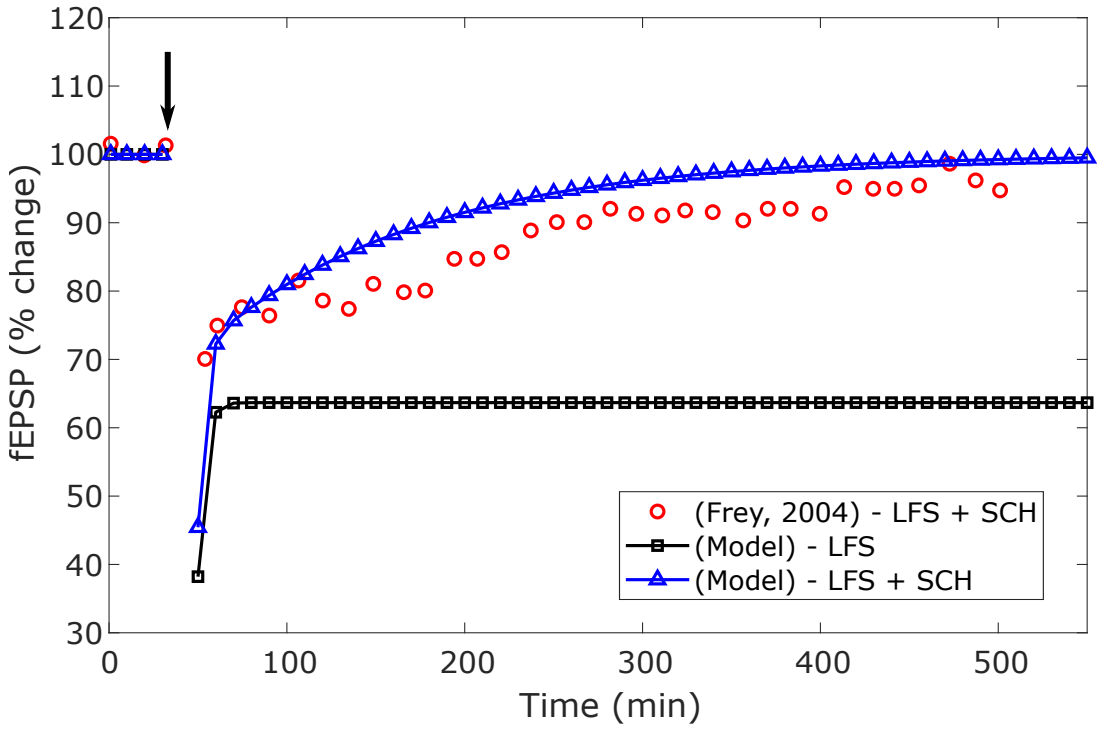

FIGURE 3.28: Quantitative comparison between the model predicted and experimentally observed (Sajikumar and Frey, 2004) modulation of LFS-induced LTD in the SC-CA1 synapse in the presence of a D1/D5 receptors antagonist SCH 23390. The D1/D5 receptors were blocked with the application of 0.1 μM SCH 23390 during a LFS protocol of 900 bursts of 3 pulses at 1 Hz where the 3 pulses of each burst were delivered at 20 Hz (black-arrow). The slow reversal of the LFS-induced LTD observed in the experiment and predicted by my model are shown as the red-circles and the blue-triangles, respectively. The LTD induced by LFS alone is denoted by the black-squares. The root mean squared error between the experimental data and the model prediction is 5.6 %.

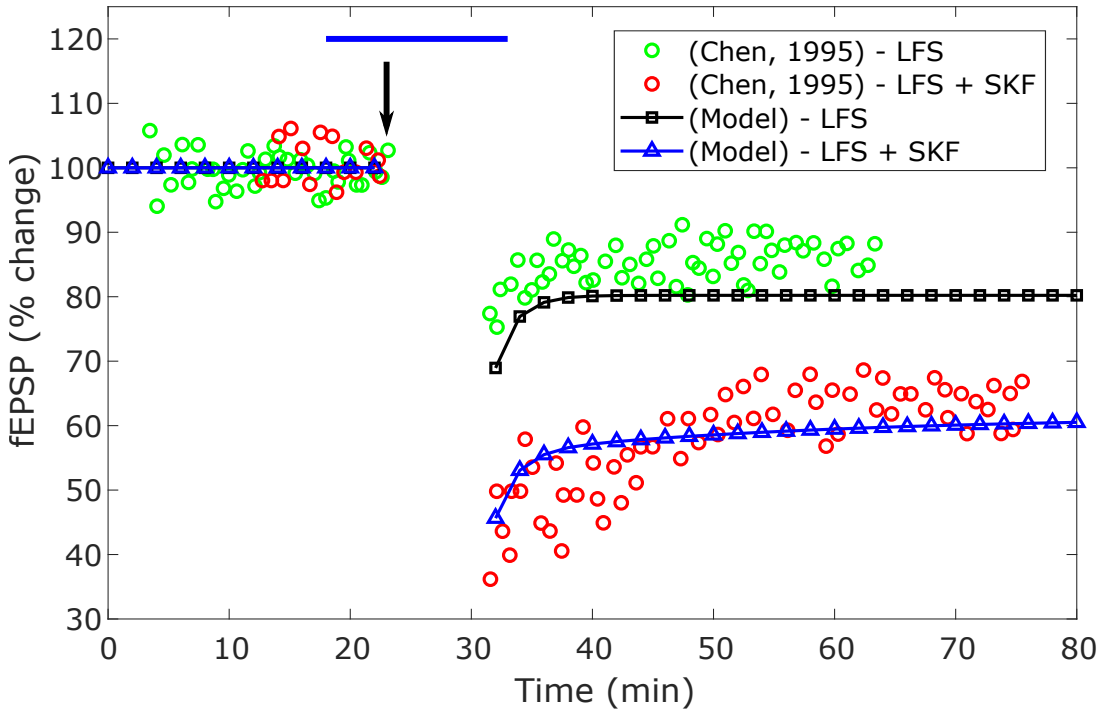

FIGURE 3.29: Quantitative comparison between the model predicted and experimentally observed (Chen *et al.*, 1995) modulation of LFS-induced LTD in the SC-CA1 synapse by SKF 38393 applied at a low concentration. A low concentration of 3 μM SKF 38393 was applied for a 15 minute duration (blue-bar) and 5 minutes before a LFS protocol of 450 pulses at 1 Hz (black-arrow). The experimentally observed and model predicted changes in the LFS-induced LTD by SKF 38393 are shown as the red-circles and blue-triangles, respectively. The LTD induced by LFS alone in the experiment and predicted by my model are denoted as the green-circles and black-squares, respectively. The root mean squared error between the experimental data and the model prediction for LFS data and LFS plus SKF 38393 is 6.1 % and 6.4 %, respectively.

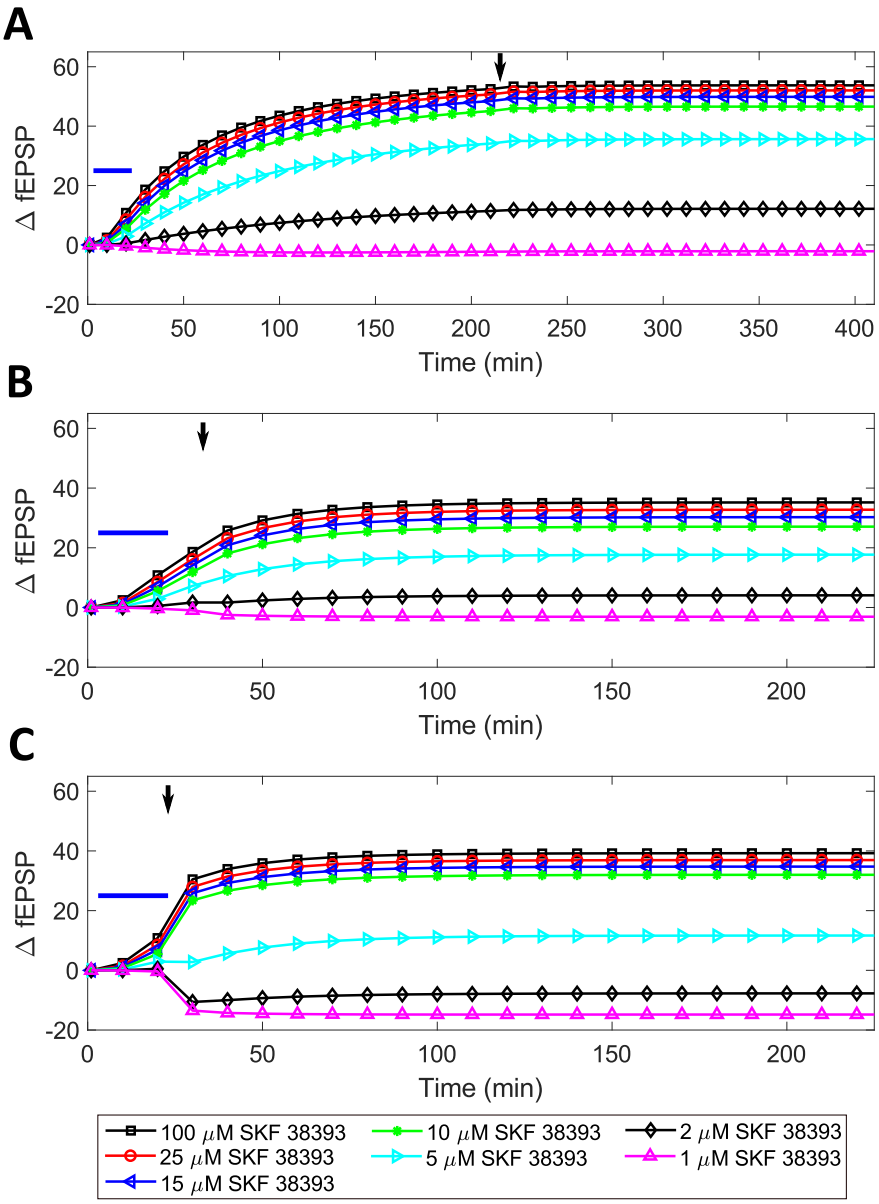

FIGURE 3.30: Model predictions on the effect of the concentration and timing of SKF 38393 relative to the LFS protocol (1200 pulses delivered at 3 Hz) in modulating the LFS-induced LTD when SKF 38393 was applied before the LFS protocol for 20 minutes. SKF 38393 (blue-bar) was delivered **(A)** 212 minutes ($\Delta t = -212$ min), **(B)** 30 minutes ($\Delta t = -30$ min), and **(C)** 20 minutes ($\Delta t = -20$ min) before the LFS protocol (black-arrow). ΔfEPSP is computed by subtracting the measured depotentiation of LFS plus SKF 38393 from the depotentiation by LFS alone. The LFS protocol on its own results in a 20% decrease of the synaptic strength.

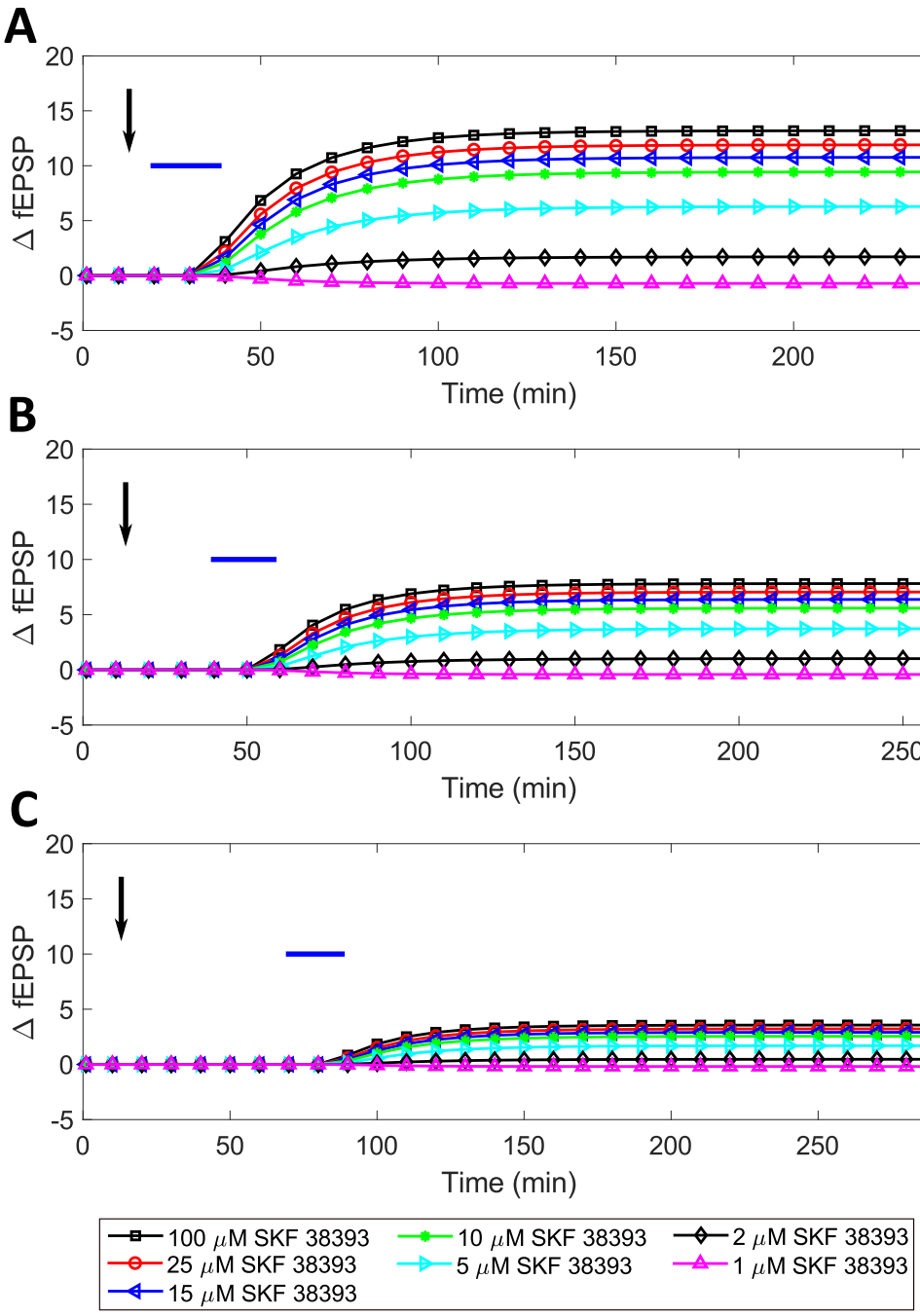

FIGURE 3.31: Model predictions on the effect of the concentration and timing of SKF 38393 relative to the LFS protocol (1200 pulses delivered at 3 *Hz*) in modulating the LFS-induced LTD when SKF 38393 was applied after the LFS protocol for 20 minutes. SKF 38393 (blue-bar) was delivered **(A)** 10 minutes, **(B)** 30 minutes, and **(C)** 60 minutes after the LFS protocol (black-arrow). ΔfEPSP is computed by subtracting the measured depotentiation of LFS plus SKF 38393 from the depotentiation by LFS alone. The LFS protocol on its own results in a 20% decrease of the synaptic strength.

CHAPTER 4

Controlling Synchronization of Spiking Neuronal Networks by Harnessing Synaptic Plasticity

4.1 INTRODUCTION

I now move from pharmaceutical neuromodulation strategies into the development of electrical neuromodulation. The first use of electrical brain stimulation was in 1948 by a neurosurgeon Lawerance Pool at Columbia Unversity to treat depression and anorexia (Coffey, 2009). In (Heath, 1963, 1977), Robert Heath at Tulane University developed a high frequency chronic stimulation of the septal area of the brain technique to treat schizophrenia and pain. Norweigen neurophysiologist Carl Wilhem Sem-Jacobsen extended neural electrical stimulation to treat symptoms of patients with Parkinson's disease (PD) (Sem-Jacobsen, 1966). The modern use of electrical high frequency stimulation called deep brain stimulation (DBS) is to treat symptoms of movement disorders, such as essential tremor and PD tremor (Benabid *et al.*, 1987). As evidence began to emerge about the unwanted side effects of PD drugs, such as L-DOPA induced dyskinesia, and PD patients who were resistant to PD drugs, DBS emerged as another tool to treat severe symptoms of PD. Initially, the subthalamic nucleus (STN) was identified as the optimal taget to disrupt the pathologically synchronous neural firing pattern observed in patients with PD and suppress the PD tremor (Mitchell *et al.*, 1989; Aziz *et al.*, 1991; Pollak *et al.*, 1993). Then, another stimulation target in the basal ganglia was determined to be the globus pallidus interna (GPi) to suppress the PD tremor (Siegfried and Lippitz, 1994). The first implantable pulse generating device where the battery was implanted below the clavical to supply power to the stimulating electrodes was developed by Medtronic and targeted the STN (Krauss *et al.*, 2020). Over the last two decades, additional DBS hardware was developed by Activa, Abbott, Boston Scientific, SceneRay, PINS, Neuropace, and Aleva Neurotherapeutics that expanded the parameter space of the

DBS protocol and treat other disease characterized by highly synchronous activity, such as epilepsy.

The expansion of the DBS parameters allowed for further optimization of the protocol in order to improve the efficacy and the efficiency of DBS. Since constant stimulation was required to suppress PD symptoms, more efficient and effective DBS wave forms became critical to preserve the life of the battery and the device (Temperli *et al.*, 2003; Deuschl *et al.*, 2006; Popovych and Tass, 2014). Recently, closed-loop approach have been used to design an effective energy efficient desynchronizing pulse (Popovych and Tass, 2014), such as a single pulse minimum energy desynchronizing control input (Deuschl *et al.*, 2006; Wilson and Moehlis, 2014; Monga *et al.*, 2018; Mauroy *et al.*, 2014; Nabi *et al.*, 2013b,a) and closed-loop delayed feedback (Vlachos *et al.*, 2016; Popovych *et al.*, 2005; Hauptmann *et al.*, 2005; Kiss *et al.*, 2007; Popovych *et al.*, 2017). For the minimum energy control strategy, the control input designs a pulse to push the state to a phaseless-set point where the inherent noise of the systems kicks each neuron into a slightly different spiking cycle with its own phase (Nabi *et al.*, 2013b,a). Recently, a closed-loop delayed feedback control strategy was developed by Vlachos *et al.* (2016) that used the time-delayed average population membrane potential as feedback to desynchronize the network. Since this approach only feeds the past population activity, the applied desynchronizing input is only active whenever the network becomes synchronous. While these approaches provide an optimal desynchronization strategy, most of them assume that the network connections are static and ignore the inherent plastic nature of neuronal synapses (Abbott and Nelson, 2000).

Hebbian plasticity is a well-known form of activity-dependent synaptic plasticity (Abbott and Nelson, 2000). This form of plasticity enforces productive connections between neurons that produce action potentials and depresses unproductive connections that do not elicit action potentials (Hebb, 1949). One form of activity-dependent synaptic plasticity is spike-time dependent plasticity (STDP) (Song *et al.*, 2000). This rule increases the weight of a synaptic connection when the pre-synaptic neuron fires before the post-synaptic neuron within a given time window and decreases the weight when the order is reversed (Song *et al.*, 2000). An increase

or decrease in the synaptic weight is coined long-term-potentiation (LTP) or long-term-depression (LTD), respectively. The introduction of plasticity into a neuronal network creates multiple stability points with different levels of synchronous activity (Popovych and Tass, 2014; Pfister and Tass, 2010; Tass and Hauptmann, 2007). Since the connections are plastic, an external stimulus can move the network from one stability point to another in order to drive the network from a synchronous to an asynchronous state.

Recently, another approach has been developed by Tass (Tass, 2003a,b; Pfister and Tass, 2010; Tass and Hauptmann, 2007; Tass, 2003b,a; Tass and Majtanik, 2006; Ebert *et al.*, 2014; Zeitler and Tass, 2015) that takes advantage of the inherent plastic nature of synpases (Abbott and Nelson, 2000) to produce a long lasting desynchronize of spiking neural networks once the stimulation protocol is removed. It is called coordinate reset (CR) stimulation. This protocol works by forcing different sections of the synchronous spiking neural network to fire out of phase with each other, which produces an asynchronous firing pattern. Due to the inherent domination of LTD over LTP in asynchronous bistable networks, the network naturally depresses the average synaptic weight to a level that produces an asynchronous firing patter (Pfister and Tass, 2010). CR stimulation is no longer required once the average synaptic weight of the network enters the asynchronous regime.

While the CR protocol is effective, it has its own limitations. CR stimulation solely relies on a bistable network due to LTD dominating LTP during asynchronous firing patterns, which may not be present in pathological networks. Furthermore, this strategy is only able to depress the average synaptic weight and is not able to increase the synaptic weight. Recent investigations into new treatments for Alzheimer's disease (AD) have shown that an increase in γ-oscillations in the hippocampus promotes the clearing of amyloid β-plaque from the brain (Martorell *et al.*, 2019; Singer *et al.*, 2018). In this case, the pathological case is an asynchronous firing pattern and the healthy case is a synchronous firing pattern. As a result, CR stimulation will fail. Therefore, I require a novel stimulation protocol that is able to have full control over the synaptic plasticity and full control over the synchrony level of the neural network. This new stimulation protocol would be able to treat more neurological

diseases besides ones characterized by excessive synchronization. Furthermore, if the synchronization is not due to a high average synaptic weight but a low average synaptic weight, CR stimulation would fail again. A novel protocol that could increase or decrease the average synaptic weight would succeed, since it could rewire the pathological network to restore healthy network dynamics.

In this work, I have developed a novel stimulation strategy " Forced Temporal Spike-Time Stimulation (FTSTS)" which addresses above shortcomings of the CR-based stimulation approach. While all other stimulation strategies focus on desynchronizing neural activity within a network, my strategy focuses on harnessing the underlying synaptic plasticity of the network to control the average network synaptic strength by forcing the spiking neurons to fire in specific temporal patterns. Thus, my strategy provides complete control over the synchrony level of networks for a long period of time, not just desynchronization. I demonstrate the efficacy of FTSTS strategy in controlling the desired synchrony level in large excitatory-inhibitory (E-I) networks. I show in simulation that the FTSTS strategy can effectively desynchronize the neural activity in networks where LTP dominates LTD on average. Further, I combine the FTSTS strategy with the CR stimulation strategy to demonstrate how this can enhance the overall performance of the CR stimulation strategy in desynchronizing large networks.

This chapter begins with a description of models used to describe the spiking E-I networks dynamics, STDP rules, and a measure of synchrony as well as the stability analysis of E-I networks in Section 4.2. In Section 4.3, I first provide a mechanistic understanding of the FTSTS strategy by considering control of synchrony in a two neuron E-I network. I then demonstrate the efficacy of the FTSTS strategy in desynchronizing large E-I networks subject to different plasticity rules, and uncertainties in the network parameters and the designed stimulation parameters. Finally, I show how the FTSTS strategy can be incorporated within the CR stimulation strategy to improve the overall performance of the CR stimulation strategy. This section ends with a detailed discussion on the comparison of my approach with the existing stimulation strategies for desynchronization of spiking neural networks as well as the limitations of my strategy in Section 4.4.

4.2 SYSTEM MODEL

4.2.1 *Excitatory-Inhibitory (EI) Network Model*

I consider networks of 2,000 and 10,000 spiking neurons consisting of 80 % excitatory (E) and 20 % inhibitory (I) neurons (Vlachos *et al.*, 2016; Brunel and Hansel, 2006). The following Leaky-Integrate-and-Fire (LIF) model describes a single excitatory or inhibitory neuron's dynamics in the E-I network.

$$\tau_m \frac{dv_E(t)}{dt} = -v_E(t) + Z_E(t) + \mu_E + \sigma_E \sqrt{\tau_m}\chi(t) + V^E_{stim}(t), \tag{4.1}$$

$$\tau_m \frac{dv_I(t)}{dt} = -v_I(t) + Z_I(t) + \mu_I + \sigma_I \sqrt{\tau_m}\chi(t) + V^I_{stim}(t). \tag{4.2}$$

Here, $v_E(t)$ and $v_I(t)$, in millivolts (mV), represent the membrane potential of the excitatory and inhibitory neurons respectively. τ_m (in ms) is the membrane time constant. $Z_i(t)$ denotes the synaptic input to the i^{th} population of neurons where $i \in \{E, I\}$. The synapses between the excitatory and inhibitory populations are randomly connected with a probability of ϵ. The synaptic input function

$$Z_i(t) = \frac{J_{ij}}{C_{ij}} S_{ij}(t) \tag{4.3}$$

defines the input to the i^{th} neuron population. In Equation (3), J_{ij} represents the synaptic strength between a presynaptic neuron in population j and postsynaptic neuron in population i, in mV, where $i \in \{E, I\}$ and $j \in \{E, I\}$. For example, the synaptic strength of an I-to-E synapse is J_{EI}. $C_{ij} = 0.3N_{tot}$ denotes a scaling factor where N_{tot} is the total number of neurons in the network. $S_{ij}(t)$ is the synaptic function. The Gaussian distributed baseline current to the i^{th} type neuron is denoted as

$$\mu_i + \sigma_i \sqrt{\tau_m}\chi(t) \tag{4.4}$$

with a mean baseline current of μ_i and a variance of $\sigma_i^2\tau_m$. $\chi(t)$ is white noise with a mean of 0 and a variance of 1. Finally, $V_{stim}^i(t)$ denotes the external stimulation input to the i^{th} neuron population.

The synaptic function $S_{ij}(t)$ is modeled as ((Brunel and Hansel, 2006)):

$$\tau_d \frac{dS_{ij}(t)}{dt} = -S_{ij}(t) + X_{ij}(t), \tag{4.5}$$

$$\tau_r \frac{dX_{ij}(t)}{dt} = -X_{ij}(t) + W_{ij}(t)\delta(t - t_{pre} + t_{delay}). \tag{4.6}$$

Here, X_{ij} describes the input to the i^{th} population of neurons from the j^{th} population of neurons. The time constants governing the decay and rise time are τ_d (in ms) and τ_r (in ms), respectively. Synaptic connections between the i^{th} and j^{th} neuron populations are randomly connected with a probability of ϵ. The weight of each synaptic connection is defined as W_{ij}. Throughout the work, I assume that E-to-I connections ($W_{IE}(t)$) are plastic and the I-to-E connections (W_{EI}) are static except in Section 4.3.9 and Figure 4.11 where I consider both connections to be plastic. Unless otherwise specified, I further assume no synaptic connectivity among neurons in excitatory or inhibitory populations. The Dirac-Delta function $\delta(t - t_{pre} + t_{delay})$ models the synaptic input to a postsynaptic neuron from a presynaptic neuron when the presynaptic neuron fires at time t_{pre} (in ms) with a synaptic delay of t_{delay} (in ms).

4.2.2 *Spike-Timing Dependent Plasticity (STDP) Model*

The coupling value of the plastic E-to-I synapse ($W_{IE}(t)$) is governed by STDP (Song *et al.*, 2000), which is defined as follows:

$$W_{IE}(t + \Delta t) = W_{IE}(t) + \Delta W_{IE}(t), \tag{4.7}$$

where $\Delta W_{IE}(t)$ is given as

$$\Delta W_{IE}(t) = \eta_e a_{LTP} A_{post}(t) \quad if \ t_{pre} - t_{post} < 0, \tag{4.8a}$$

$$\Delta W_{IE}(t) = \eta_e a_{LTD} A_{pre}(t) \quad if \ t_{pre} - t_{post} > 0. \tag{4.8b}$$

Here, $\Delta W_{IE}(t)$ defines the change in the synaptic weight determined by the spike-time of a presynaptic (t_{pre}) and postsynaptic (t_{post}) neuron. The rate at which the E-to-I synaptic coupling changes is governed by the learning rate η_e. Additionally, the relative contribution of LTD and LTP to $\Delta W_{IE}(t)$ is denoted by a_{LTP} and a_{LTD}. (Song *et al.*, 2000; Ebert *et al.*, 2014). Since LTD generally dominates LTP, a_{LTD} is 10% larger than a_{LTP}. $A_{post}(t)$ and $A_{pre}(t)$ are described by the following two exponential functions:

$$\tau_{LTP} \frac{dA_{post}}{dt} = -A_{post} + A_0 \delta(t - t_{post}), \tag{4.8c}$$

$$\tau_{LTD} \frac{dA_{pre}}{dt} = -A_{pre} + A_0 \delta(t - t_{pre}). \tag{4.8d}$$

Here, the size of the LTP and LTD time window is defined by the STDP time constants τ_{LTP} and τ_{LTD}. In a similar fashion to a_{LTP} and a_{LTD}, τ_{LTD} is set to be 10% greater than τ_{LTP}. Upon the firing of a presynaptic or postsynaptic neuron, a small value A_0 is added to the appropriate exponential STDP decay function. The E-to-I synaptic weight is defined as the coupling value $W_{IE}(t)$ multiplied by the synaptic strength J_{IE} (i.e., $J_{IE} W_{IE}(t)$).

4.2.3 *Synchrony Measurement*

I measure the synchrony level of the network by computing the Kuramoto order parameter ($R(t)$) based on the spike times of neurons in the excitatory population (Kuramoto, 1984; Daido, 1992; Tass, 2007; Ebert *et al.*, 2014). The phase ($\phi_k(t)$) of the k^{th} neuron in the excitatory population is calculated using the following equation

$$\phi_k(t) = \frac{2\pi(t_{k,i+1} - t)}{t_{k,i+1} - t_{k,i}}, \tag{4.9}$$

where $t_{k,i}$ is the i^{th} spike time for the k^{th} neuron. The Kuramoto order parameter ($R(t)$) and the average phase of the neurons ($\psi(t)$) are calculated using

$$R(t)e^{i\psi(t)} = \frac{1}{N_E}\sum_{k=1}^{N_E} e^{i\phi_k(t)}. \tag{4.10}$$

Here, N_E represents the number of excitatory neurons. A highly synchronous network has a Kuramoto order paramter of $R(t) = 1$ and a completely asynchronous network has a value of $R(t) = 0$.

4.2.4 *Determination of Synchronous and Asynchronous Regimes*

It is well-known that plastic neural networks exhibit multiple stability points (Popovych and Tass, 2014; Song *et al.*, 2000; Pfister and Tass, 2010; Tass and Hauptmann, 2007). Similar to other networks, my E-I network exhibits two stability points at a high and low average E-to-I synaptic weight value. Figure 4.1A shows the average E-to-I synaptic weight converging to either $J_{IE}W_{IE} = 10$ mV or $J_{IE}W_{IE} = 290$ mV. The average synaptic weight converges to $J_{IE}W_{IE} = 290$ mV if the initial average synaptic weight is greater than 100 mV and converges to $J_{IE}W_{IE} = 10$ mV when it less than 100 mV. Additionally, I find that the network becomes more synchronous as the average E-to-I synaptic weight increases, which is shown in Figure 4.1B in terms of the Kuramoto order parameter $R(t)$. Therefore, the network exhibits a high level of synchrony at high synaptic weights and a low level of synchrony at low synaptic weights.

4.2.5 *Model Parameters*

I use the model parameters defined in Table 4.1 unless stated otherwise. All the simulation are performed in Matlab R2016b. The differential equations are solved using Euler's method with a step size of 0.1 ms.

4.3 RESULTS

I begin by providing an insight into the underlying mechanism of my stimulation strategy "Forced Temporal Spike-Time Stimulation" (FTSTS) using an illustrative example of a two neuron E-I network in Section 4.3.1. Next, I demonstrate the

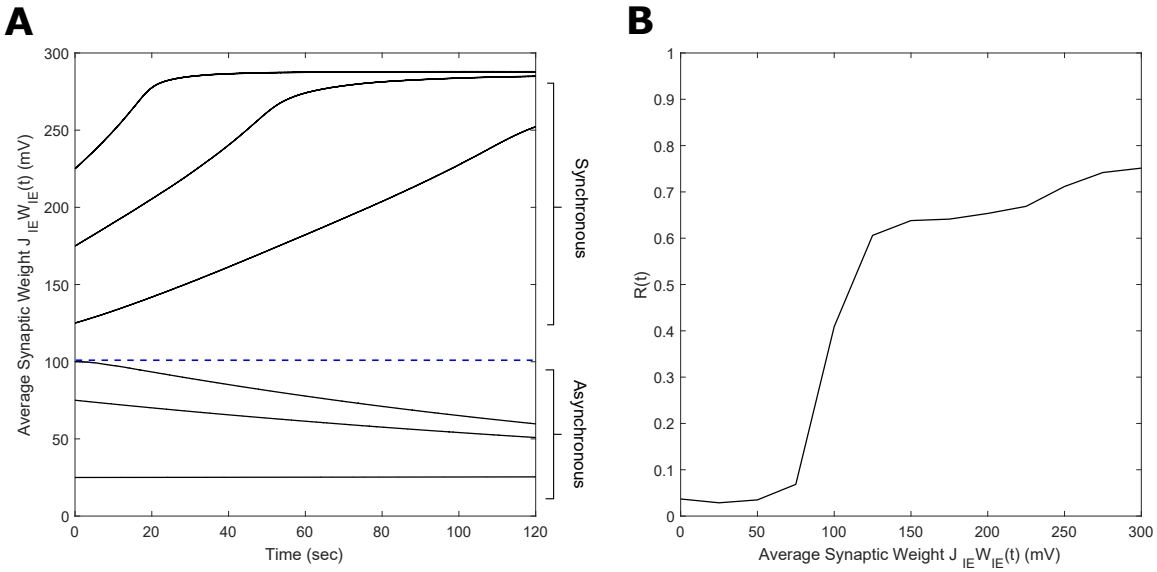

FIGURE 4.1: The synchrony level and stability points of a plastic 2,000 spiking neuron E-I network. **(A)** The average synaptic weight either converges to the maximum or minimum value. Each line represents the trajectory of the synaptic weight with a different initial condition. The stability threshold is depicted as a blue dashed line. **(B)** The synchrony level of the network, represented by the Kuramoto order parameter R(t), increases with increasing average synaptic weight ($J_{IE}W_{IE}(t)$).

TABLE 4.1: The model parameters of my E-I network.

Neuron Parameters (Vlachos *et al.*, 2016; Brunel and Hansel, 2006) (Song *et al.*, 2000; Hauptmann and Tass, 2009)	**Value**
v_{reset}	0 mV
$v_{threshold}$	20 mV
μ_E	20.8 mV
μ_I	18 mV
σ_E	1 mV
σ_I	3 mV
τ_m	10 ms
τ_d	1 ms
τ_r	1 ms
τ_{delay}	5 ms
J_{EI}	100 mV
$J_{IE}W_{IE}(t)$	$\in [10, 290]$ mV
$W_{EI,0}$	1
ϵ	0.25
a_{LTD}	-1.1
a_{LTP}	1
τ_{LTD}	22 ms
τ_{LTP}	20 ms
A_0	0.005
η_e	0.25
c_P	0.038
c_D	0.02
τ_P	10 ms
τ_D	25 ms

efficacy of the FTSTS strategy in controlling synchronized activity of a 2,000 and 10,000 neuron E-I networks (see Sections 4.3.2, 4.3.3). I then show the robustness of the FTSTS strategy in the presence of uncertainties in the designed stimulation pulses, model parameters and network connectivity (see Sections 4.3.4, 4.3.5, 4.3.6, 4.3.7). Next, in Section 4.3.8, I combine the FTSTS strategy with the existing coordinate reset (CR) stimulation strategy to show the efficacy of the FTSTS-CR strategy over the CR stimulation strategy. Finally, in Sections 4.3.9 and 4.3.10, I demonstrate that FTSTS strategy can desynchronize E-I networks with additional plastic synapses and symmetric spike-time plasticity rules.

4.3.1 *Control of E-to-I Synaptic Weight in a Two Neuron Network*

I considered an excitatory-inhibitory (E-I) network of two neurons to develop my "Forced Temporal Spike-Time Stimulation" (FTSTS) strategy. I set a scaling factor of $C_{ij} = 10N_i$ and probability of connectivity of $\epsilon = 1$ (see Section 4.2.1 for the meaning of these variables). Based on the STDP rule of activity-dependent plasticity, I designed stimulation inputs for both the inhibitory ($V^I_{stim}(t)$) and excitatory ($V^E_{stim}(t)$) neuron that forced the postsynaptic inhibitory neuron to spike before the presynaptic excitatory neuron, as shown in Figures 4.2B and 4.2C, respectively. The protocol stimulated the postsynaptic inhibitory neuron and the presynaptic excitatory neuron using charge-balanced rectangular pulses with an equal and opposite amplitude (U_{stim}). Figure 4.2E shows the induced firing patterns in neurons, which decreased the average E-to-I synaptic weight of the network as shown in Figure 4.2D. On the other hand, the average E-to-I synaptic weight increased when $V^E_{stim}(t)$ and $V^I_{stim}(t)$ were switched such that the presynaptic excitatory neuron fired before the postsynaptic inhibitory neuron. The increased synaptic weight observed from the induced spiking pattern in Figure 4.2G is shown in Figure 4.2F.

4.3.2 *FTSTS Effectively Controls the Neuronal Synchronization in a 2000 Neuron Network*

I applied the FTSTS strategy to an E-I network of 1600 excitatory and 400 inhibitory neurons to demonstrate how my strategy can be used to control the synchrony of

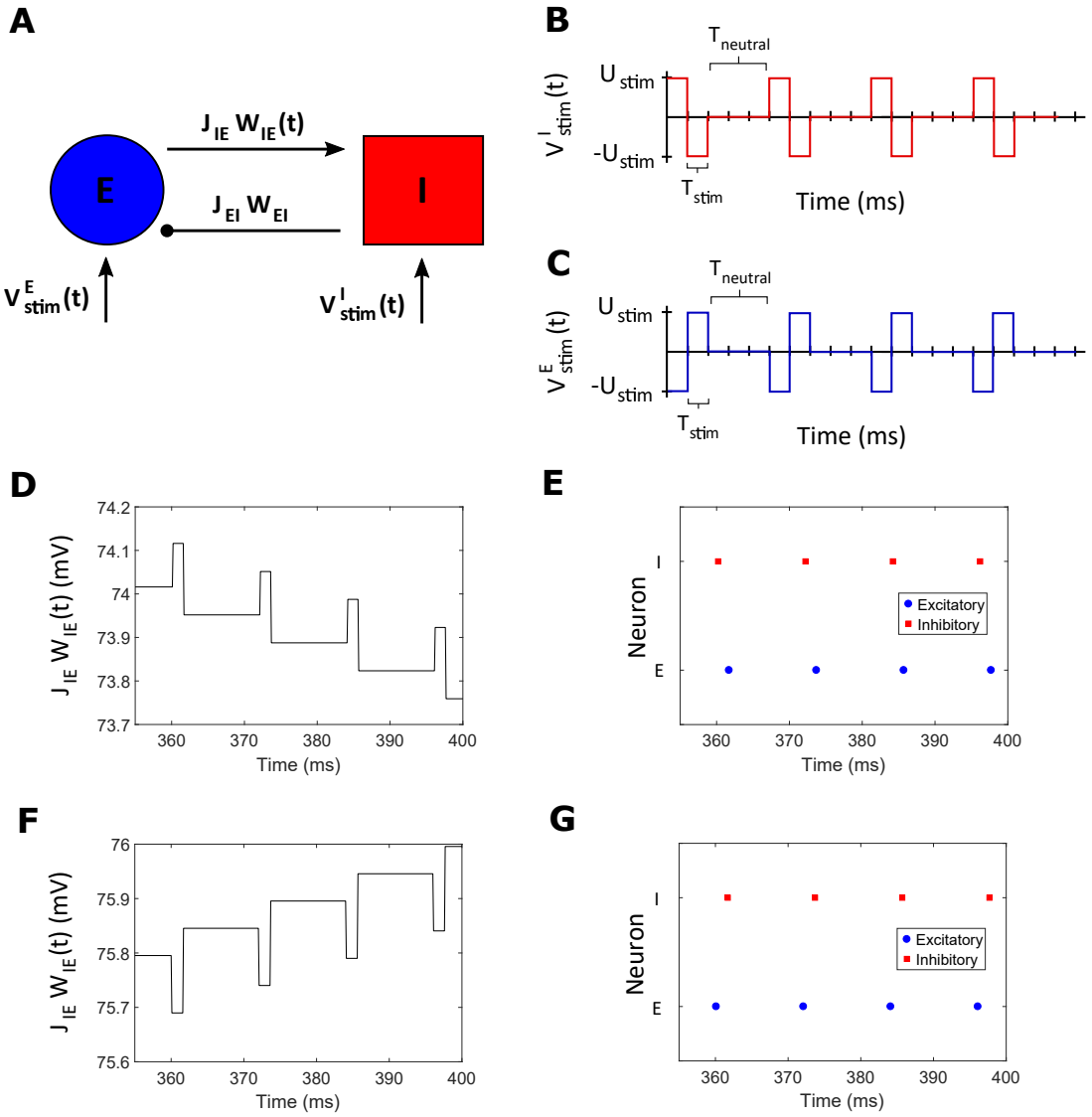

FIGURE 4.2: The FTSTS protocol for a two neuron E-I network. **(A)** shows an excitatory-inhibitory network. **(B)** and **(C)** show the FTSTS input pattern for the inhibitory and excitatory neuron, respectively. The FTSTS pulse parameters are U_{stim} = 300 mV, T_{stim} = 1 ms, and $T_{neutral}$ = 10 ms. This FTSTS protocol depresses the E-to-I synaptic weight as shown in **(D)**. The drop in synaptic weight is due to FTSTS inducing a post-before-pre spiking pattern in the E-I network, which is shown in **(E)**. On the other hand, **(F)** shows how swapping the FTSTS inputs to the excitatory and inhibitory neuron increases the E-to-I synaptic weight. This induces the pre-before-post spiking pattern shown in **(G)**.

neuronal activity in large networks. In a larger network of neurons, my strategy forces the postsynaptic inhibitory population of neurons to spike before the presynaptic excitatory neuron population. I assumed that all the neurons in each specific population receives the same input. The applied FTSTS inputs to each neuron population are shown in Figures 4.3A and 4.3B. These inputs induced a specific spiking pattern, as shown in Figure 4.3F, which depressed the average E-to-I synaptic weight (shown in Figure 4.3C). The period of stimulation is highlighted with a solid black line in Figure 4.3C. Since the network has an asynchronous regime that converges to a low average E-to-I synaptic weight, I only required enough input to drive the network into the asynchronous regime. Therefore, I provided enough input to depress the synaptic weight of the network to 75 mV, which is slightly over the synchronous-asynchronous regime boundary (see Figure 4.1). As a result, the system naturally converged to the low synaptic weight stability point when the FTSTS protocol was turned off. The synchronous and asynchronous firing patterns before and after the stimulation protocol are displayed in Figures 4.3E and 4.3G, respectively. The synchrony level of the network as it transitioned from the synchronous to asynchronous regime is shown in Figure 4.3D. The activity of the E-I network prior to the applied stimulation (the first 2 seconds) was measured around $R(t) = 0.75$. When the stimulation protocol was turned on, the measured synchrony level became low (see Figure 4.3D). This is due to the asynchronous firing between each FTSTS pulse. When the FTSTS protocol was turned off, the network remained in the asynchronous regime at the measured network synchrony level of $R(t) = 0.05$ (see Figure 4.3D).

Next, I demonstrate how my FTSTS strategy can also be used to synchronize the asynchronous network activity. To do so, I swapped the inputs to the inhibitory and excitatory neurons used in the desynchronization case, which are shown in Figures 4.4A and 4.4B. This stimulation protocol forced the presynaptic excitatory neuron population to fire prior to the postsynaptic inhibitory neuron populations, which is shown in Figure 4.4F. Similar to the two neuron case, swapping the inputs to the excitatory and inhibitory neurons induced LTP in the network and increased the average E-to-I synaptic weight of the network, as shown in Figure 4.4C. Again I are only required to drive the network into the synchronous regime (i.e., the average

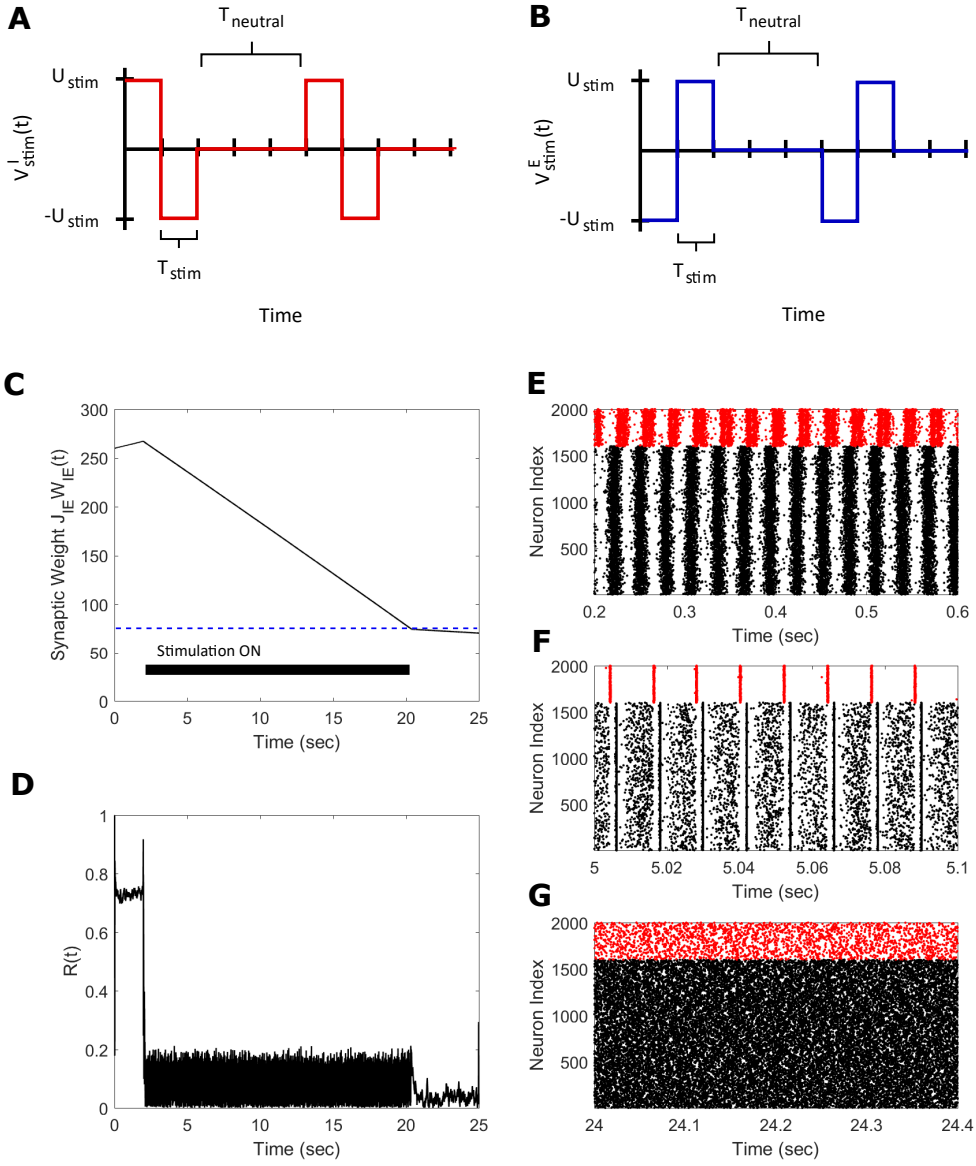

FIGURE 4.3: Desynchronization of neural activity in 2,000 neuron E-I network. **(A)** shows the FTSTS waveform for inhibitory neurons. **(B)** shows the FTSTS waveform for excitatory neurons. **(C)** shows the time evolution of the average E-to-I synaptic weight. As shown here, the average E-to-I synaptic weight of network is decreased to 75 mV (blue-line), where the stimulation is turned off. **(D)** shows the synchrony level of excitatory neurons as a function of time. **(E)**, **(F)**, and **(G)** show the spiking patterns before, during, and after the FTSTS protocol, respectively. The FTSTS pulse parameters are U_{stim} = 100 mV, T_{stim} = 1 ms, and $T_{neutral}$ = 10 ms.

E-I synaptic weight above 100 mV) to synchronize the network. Therefore, the stimulation protocol was turned off when the average E-to-I synaptic weight reached 125 mV, which was slightly over the threshold. Here, the network will remain in the synchronous regime and the average E-to-I synaptic weight will converge to the high synaptic weight stability point. The spiking patterns of the E-I network before, during, and after the FTSTS protocol are shown in Figures 4.4E, 4.4F, and 4.4G, respectively. Figure 4.4D shows the changes in the network synchrony level before, during, and after the FTSTS protocol. As shown in Figure 4.4D, the network synchrony increased from $R(t) = 0.05$ to $R(t) = 0.6$ after the removal of the stimulation. It should be noted that the synchrony level increases significantly during the stimulation in this case compared to the case of desynchronization (see Figure 4.3D for comparison). This is due to the large input of $U_{stim} = 200$ mV compared to the input used in Figure 4.3, which forces the neurons to fire in a highly synchronous firing pattern. If a smaller input is used to resynchronize the network, it would be more noisy during the FTSTS protocol and the FTSTS would be required for a longer period of time to resynchronize the network.

4.3.3 *Desynchronization of Neural Activity in a Large E-I Network*

I applied my FTSTS protocol to demonstrate its applicability in larger networks. For demonstration purposes, I considered a E-I network with 8,000 excitatory and 2,000 inhibitory neurons. I set the probability of connectivity of the E-to-I and I-to-E synapses ϵ to 0.01. The FTSTS protocol induced the same post-before-pre firing patterns in the larger network which decreased the average E-to-I synaptic weight, as shown in Figure 4.5A. The stimulation protocol desynchronized the network in approximately 22 seconds, which is comparable to the desynchronization time of the 2,000 neuron network. The changes in the network synchrony level before, during, and after the FTSTS protocol are shown in Figure 4.5B. As noted in Figure 4.5B, the initial synchrony level of $R(t) = 0.8$ is reduced to approximately $R(t) = 0.05$ after the FTSTS protocol. Once the stimulation protocol reduced the average E-to-I synaptic weight below 75 mV (i.e., the asynchronous regime), I no longer required the external inputs to keep the network in the asynchronous regime.

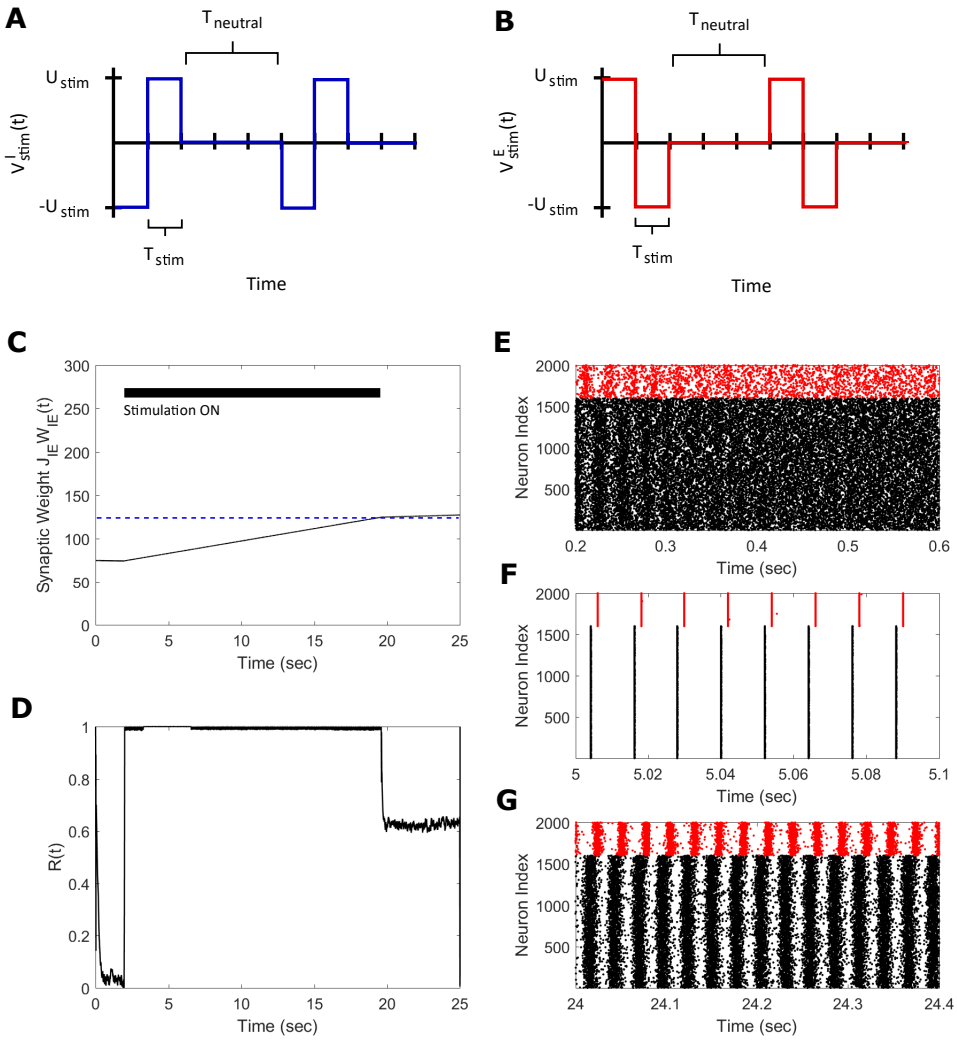

FIGURE 4.4: Resynchronization of neural activity in 2,000 neuron E-I network. **(A)** shows the FTSTS waveform for inhibitory neurons. **(B)** shows the FTSTS waveform for excitatory neurons. Note that the FTSTS waveforms for inhibitory and excitatory populations are swapped from the desynchronization case (see Figures 4.3A and 4.3B). **(C)** shows the time evolution of the average E-to-I synaptic weight. As shown here, the average E-to-I synaptic weight of network is increased to 125 mV (blue-line), where the stimulation is turned off. **(D)** shows the synchrony level of the network as a function of time. **(E)**, **(F)**, and **(G)** show the spiking patterns before, during, and after the FTSTS protocol respectively. The FTSTS pulse parameters are U_{stim} = 200 mV, T_{stim} = 1 ms, and $T_{neutral}$ = 10 ms.

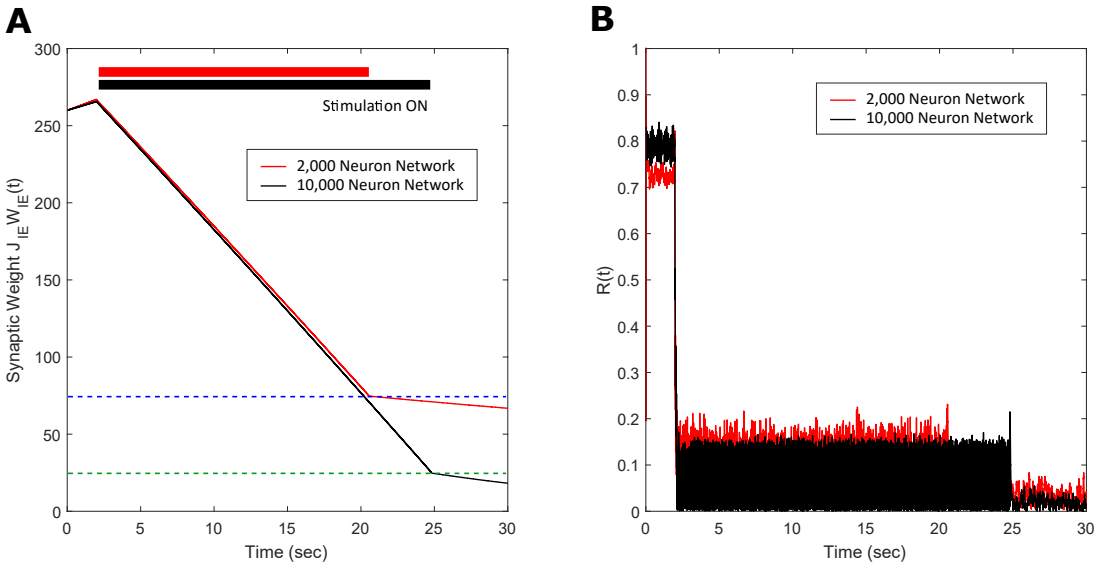

FIGURE 4.5: Desynchronization of neural activity in 10,000 neuron E-I network. **(A)** shows the decrease in the average E-to-I synaptic weight of the network during and after the FTSTS stimulation (black line), which is compared to the decrease of the average synaptic of the 2,000 neuron E-I network (red line) by FTSTS. Due to the change in network dynamics for the 10,000 neuron network, the synaptic weight was decreased to 25 mV in order to push it into the asynchronous regime (green-dashed line).**(B)** shows the network synchrony level during and after the FTSTS stimulation. The FTSTS pulse parameters used in this simulation are U_{stim} = 100 mV, T_{stim} = 1 ms, and $T_{neutral}$ = 10 ms.

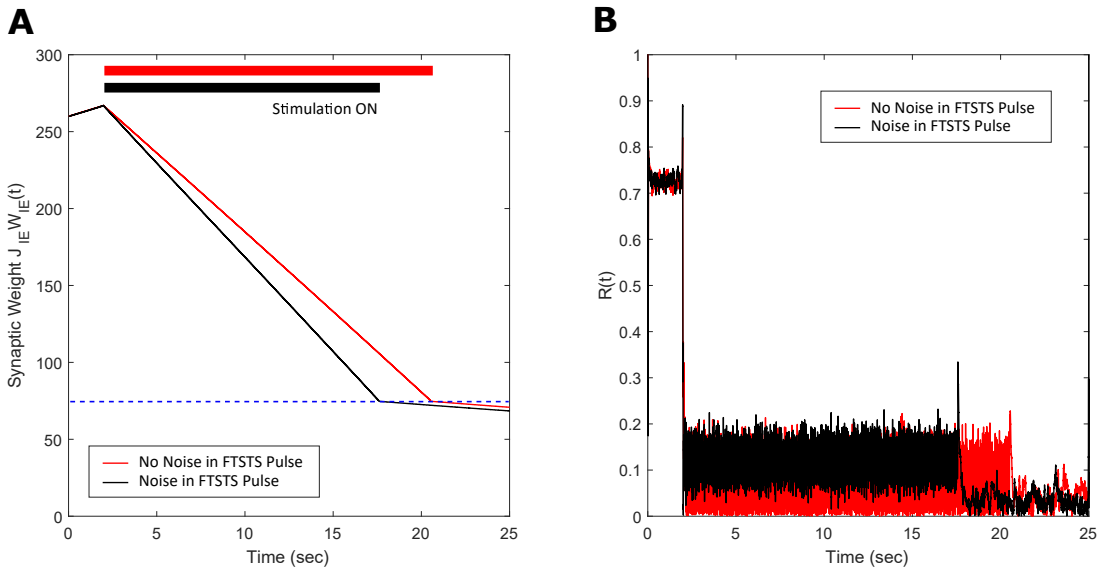

FIGURE 4.6: Robustness of the FTSTS strategy against random variations in the FTSTS pulse amplitude. The FTSTS pulse amplitude for each pulse has been chosen from a Gaussian distribution with mean U_{stim} and a variance of $\frac{U_{stim}}{10}$. **(A)** shows the decrease in the average E-to-I synaptic weight of the network during and after the FTSTS stimulation (black line). The red line shows the decrease in average synaptic weight of a network without random variation in the applied FTSTS pulse amplitude. **(B)** shows the network synchrony level during and after the FTSTS stimulation. The FTSTS pulse parameters used in this simulation are U_{stim} = 100 mV, T_{stim} = 1 ms, and $T_{neutral}$ = 10 ms.

4.3.4 *Robustness to Uncertainties in the FTSTS Pulse Parameters*

Here, I demonstrate the robustness of my protocol in desynchronizing a 2,000 neuron E-I network against uncertainties in the FTSTS pulse parameters. In particular, I considered uncertainty in the FTSTS pulse amplitude U_{stim}, which I modeled in the form of a Gaussian distribution with mean U_{stim} and variance $\frac{U_{stim}}{10}$. Each of the applied pulse amplitude during stimulation was randomly chosen from this distribution. As shown in Figure 4.6B, the FTSTS strategy efficiently desynchronized the network by driving the network into the asynchronous regime. Figure 4.6A shows the changes in the average synaptic weight of the network before, during, and after the FTSTS protocol.

4.3.5 *Robustness to Uncertainties in the Network Model Parameters*

In this section, I show the robustness of my FTSTS strategy against uncertainties in the network model parameters. For demonstration, I considered variations in the membrane time constant τ_m of neurons in the network. I randomly assigned the membrane time constant τ_m of individual neurons in the 2,000 neuron E-I network from a uniform distribution $\mathcal{U}(8, 12)$ to show the efficacy of my FTSTS strategy in desynchronizing the network activity. Figures 4.7A shows my simulation results for $\tau_m \in \mathcal{U}(8, 12)$. Here, the FTSTS protocol forced the average E-to-I synaptic weight of the network into the asynchronous regime within approximately 15 seconds of stimulation which led to desynchronization of the network activity after the removal of the stimulation, as shown in Figure 4.7B. As noticed here, the stimulation protocol desynchronized the network faster in this case compared to the case in Figure 4.3C where there is no variation in the membrane time constant. This is not surprising as an increase variability in the membrane time constant would induce more noise and desynchronize the firing pattern of the neurons initially, which is seen in Figure 4.7B with a lower initial Kuramoto order parameter value.

4.3.6 *Addition of E-to-E and I-to-I Synaptic Connections*

In this section, I show the efficacy of the FTSTS strategy in desynchronizing 2000 neuron E-I network in the presence of E-to-E and I-to-I synaptic connectivity. I assumed that the synaptic strength of all synapses within the network are static except E-to-I synapses. I set the synaptic strength of the static I-to-E, E-to-E and I-to-I synapses as $J_{EI} = 90$ mV, $J_{EE} = 50$ mV, and $J_{II} = 50$ mV respectively with scaling factors of $C_{EE} = N_{tot}$ and $C_{II} = N_{tot}$, where $N_{tot} = N_E + N_I$. The probability of connectivity of the E-to-E and I-to-I was 0.1. The addition of E-to-E and I-to-I synapses within the E-I network didn't change the bifurcation of the regime into synchronous and asynchronous with respect to the network average E-I synaptic weight qualitatively. My simulation results show that the FTSTS strategy effectively desynchronized the network activity, shown in Figure 4.8B, in the presence of E-to-E

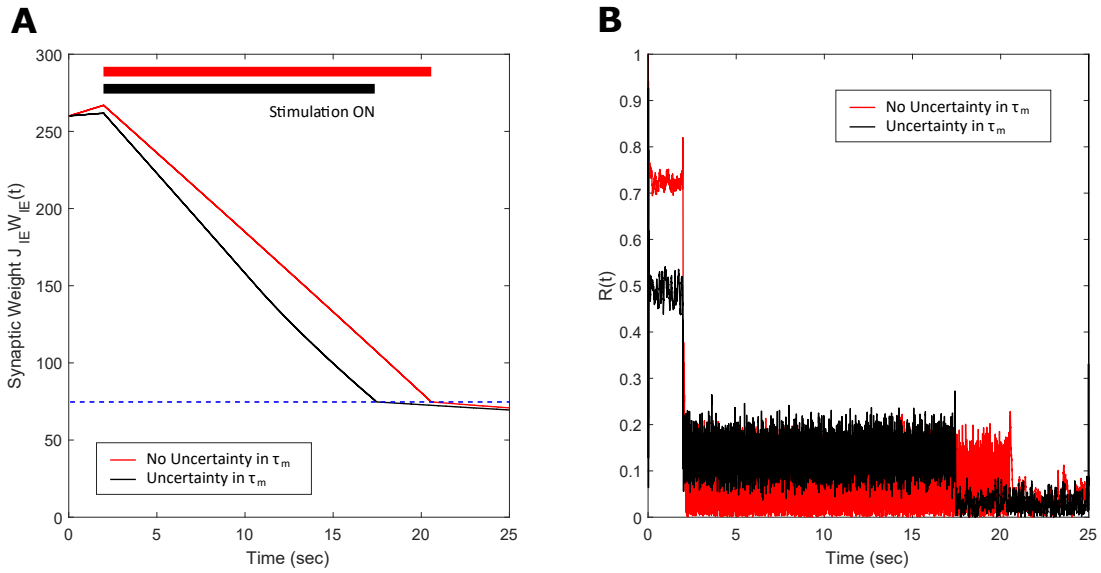

FIGURE 4.7: Robustness of the FTSTS strategy against uncertainty in the membrane time constant of neurons in the 2,000 neuron E-I network. **(A)** shows the changes in the average E-to-I synaptic weight of the network, which is compared to a network without uncertainty in the membrane time constant (red line). **(B)** shows the network synchrony level of the network throughout the simulation where the membrane time constant τ_m of individual neurons in the network is drawn from a uniform distribution $\mathcal{U}(8, 12)$. The applied FTSTS pulse parameters are U_{stim} = 100 mV, T_{stim} = 1 ms, and $T_{neutral}$ = 10 ms.

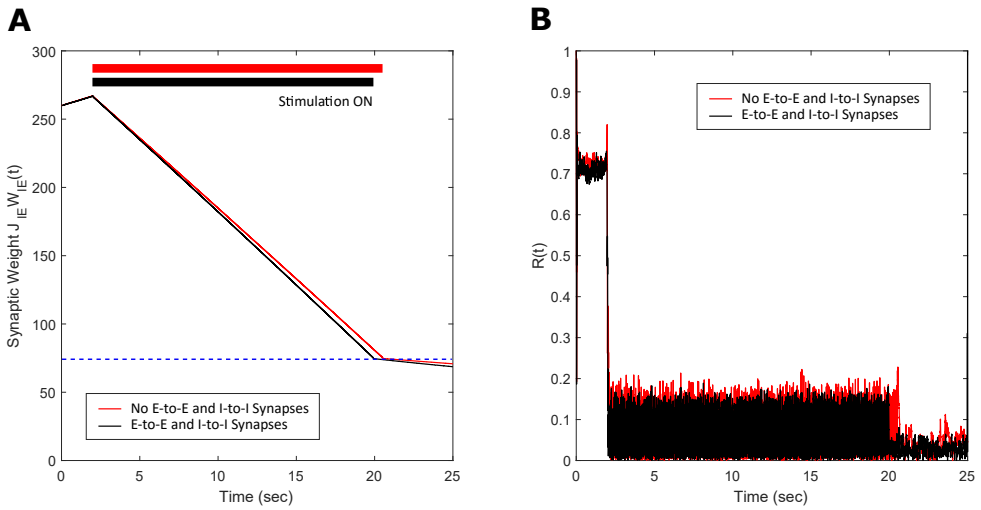

FIGURE 4.8: Efficacy of the FTSTS strategy in desynchronizing 2,000 neuron E-I network in the presence of E-to-E and I-to-I synaptic connectivity (black line). **(A)** and **(B)** show the changes in the average E-to-I synaptic weight of the network and the network synchrony level respectively. The red line in **(A)** shows the decrease in average synaptic weight of a network with only E-to-I and I-to-E synapses. The FTSTS pulse parameters are U_{stim} = 100 mV, T_{stim} = 1 ms, and $T_{neutral}$ = 10 ms.

and I-to-I synapses by driving the average E-to-I synaptic weight of the network into the asynchronous stability regime, as shown in Figure 4.8A.

4.3.7 *Robustness to Partial Spatially Inseparable Excitatory and Inhibitory Neuron Population*

In this section, I show the robustness of the FTSTS strategy for a case where E-I populations are not well separated. I assume that 25% of the excitatory and 25% of the inhibitory population are not spatially separable. Therefore, this inseparable population of E-I neurons receives inputs designed for the excitatory and the inhibitory population. Figure 4.9A shows that the FTSTS strategy is still able to push the average synaptic weight of the network into the asynchronous regime. The change in slope during the FTSTS protocol in Figure 4.9A is most likely due to the synaptic weight of the separable populations reaching the minimum weight value. At this point, the disruption from the stimulation protocol and the low average synaptic weight of the network helped to further depress the synaptic weight of the neurons.

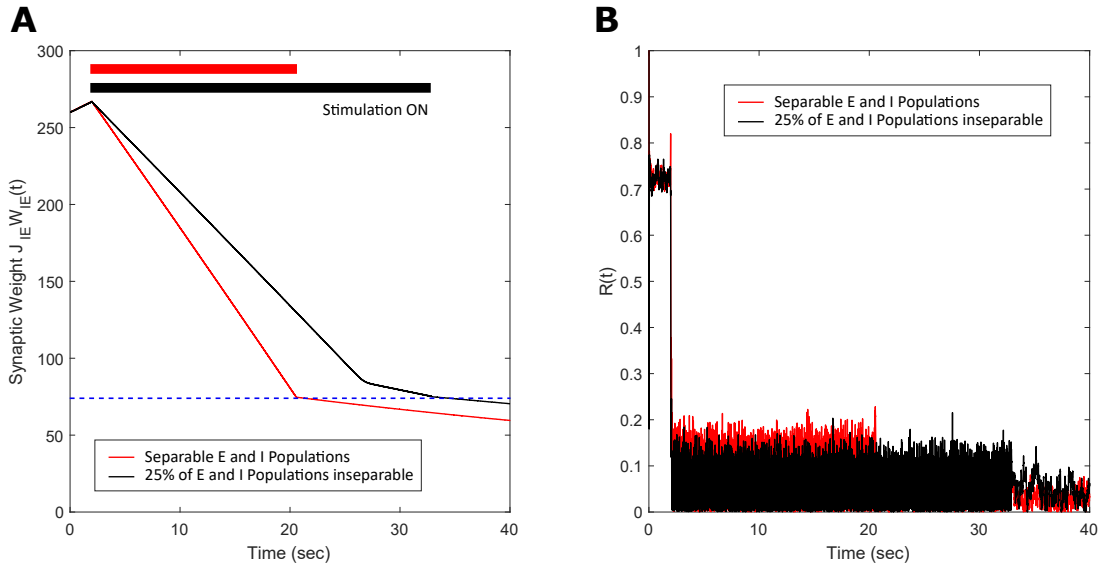

FIGURE 4.9: Efficacy of the FTSTS strategy in desynchronizing 2,000 neuron E-I network where 25% of the population is inseparable and receives both the excitatory and inhibitory population input. **(A)** shows the change in the average E-to-I and I-to-E synaptic weight of the network (black line), which is compared to the completely separable case considered in Figure 4.3 (red line). **(C)** shows the network synchrony level during the simulation. The FTSTS pulse parameters are U_{stim} = 100 mV, T_{stim} = 1 ms, and $T_{neutral}$ = 10 ms.

Figure 4.9B shows the reduction of the network synchrony with the Kuramoto order parameter dropping from $R(t) = 0.72$ to $R(t) = 0.05$.

4.3.8 *Integration of FTSTS with the Coordinate Reset Strategy*

In this section, I demonstrate how my FTSTS strategy could be incorporated within the standard coordinate reset (CR) stimulation protocol to effectively stimulate a large population of neurons. One way to implement the CR stimulation protocol is to divide the synchronous population of neurons into four subpopulations, which receive separate but identical inputs at different times over the course of period T (Tass, 2003b,a). T is the overall period of the synchronous neuron population without input. If the neuron population is divided into four subpopulations, then each subpopulation approximately will receive input every $T/4$. The order that each subpopulation receives input is randomly assigned at every period. In order to compare the CR to the FTSTS strategy, I individually divide the excitatory and

inhibitory population into four subpopulations (8 subpopulations for the E-I network). Figures 4.10E and 4.10G show the CR stimulation pattern applied for one period to the excitatory and inhibitory population, respectively. These figures show the stimuli provided to the first quarter of neurons in the E-I network with one pulse to excitatory subpopulation 1 (Figure 4.10E, blue) and one pulse to the inhibitory subpopulation 2 (Figure 4.10G, orange). The stimuli to the second quarter of the E-I network is a pulse delivered to the excitatory subpopulation 3 (Figure 4.10E, yellow) and a pulse to the inhibitory subpopulation 1 (Figure 4.10G, blue). This is repeated for the remaining subpopulations in the excitatory and inhibitory populations. After every subpopulation has been stimulated over period T, a new random stimulation order is assigned for each subpopulation. The efficiency of the CR approach is shown in Figure 4.10A. Here, the CR stimulation depresses the average synaptic weight of the network over the course of approximately 100 seconds. This causes a drop in synchrony from $R(t) = 0.7$ to $R(t) = 0.05$, which is shown in Figure 4.10C.

I integrated this strategy with my FTSTS strategy and applied it to an E-I network, consisting of 2,000 neurons, in the presence of E-to-E and I-to-I synaptic connectivity. I randomly divided each excitatory and inhibitory population into four subpopulations. Then, I adjusted the CR stimulation pattern to incorporate my FTSTS protocol (FTSTS-CR), such that each randomly selected pair of excitatory and inhibitory subpopulations are forced to spike post-before-pre. The FTSTS-CR stimulation pattern for one period is shown in Figures 4.10F and 4.10H. For a single FTSTS-CR pulse, I set U_{stim} = 100 mV, T_{stim} = 1 ms and $T_{neutral}$ = 7 ms. Similar to CR, I repeated this stimulation protocol for the other subpopulations in a random sequence for one period. Then, a new stimulation order is assigned for the next period T. My protocol forces a randomly selected inhibitory subpopulation to fire prior to a randomly selected excitatory subpopulation, which over the course of 60 seconds depresses the average E-to-I synaptic weight of the entire population into the asynchronous regime as shown in Figure 4.10B. When the average E-to-I synaptic weight reached a preset value of 75 mV (asynchronous regime), I turned off the stimulation protocol. Figure 4.10D shows that the network remained in the

desynchronized state at a synchrony level of $R(t) = 0.05$ for the rest of the simulation after removal of the FTSTS-CR protocol.

4.3.9 *Robustness to Additional Plastic Synapses*

In previous sections, I presented my results for networks where I considered only E-to-I plastic synapses. In this section, I demonstrate the efficacy of my FTSTS strategy in desynchronizing networks where both E-to-I and I-to-E synaptic connections are plastic. I modeled the plasticity dynamics of I-to-E synapses using an anti-Hebbian STDP plasticity rule (Bell *et al.*, 1997; Luz and Shamir, 2012). For anti-Hebbian STDP, I used Equations (8) and (9) with the changed parameters $a_{LTD} = 1$ and $a_{LTP} = -1.1$ so that pre-before-post spike times decrease and post-before-pre spike times increases the synaptic weight. My simulation results (see Figures 4.11A and 4.11B) show that the FTSTS strategy can potentially desynchronize the network by depressing both the E-to-I and I-to-E synaptic weights. Additionally, Figure 4.11C shows a decrease in the network synchrony from $R(t) = 0.82$ to $R(t) = 0.05$.

4.3.10 *Robustness to a Symmetric Plasticity Rule*

I demonstrate how a modified FTSTS protocol is able to control the synaptic weight of an E-I network with a symmetric plasticity rule. I use the same network described in Section 4.2 with the following changes to the plasticity rule. The E-to-I synaptic weight is govern by the following equation (Tass and Hauptmann, 2009; Hauptmann and Tass, 2009)

$$\Delta W_{IE}(t) = c_P e^{-|ISI_{IE}|/\tau_p} - c_D e^{-|ISI_{IE}|/\tau_D}, \tag{4.11}$$

where ISI_{IE} is the inter-spike-interval between spike-times of inhibitory and excitatory neurons in an E-to-I synapse. c_P and c_D are the potentiation and depotentiation learning rates respectively. τ_P is the potentiation time constant and τ_D is the depotentiation time constant. The symmetric plasticity parameters can be found in Table 4.1.

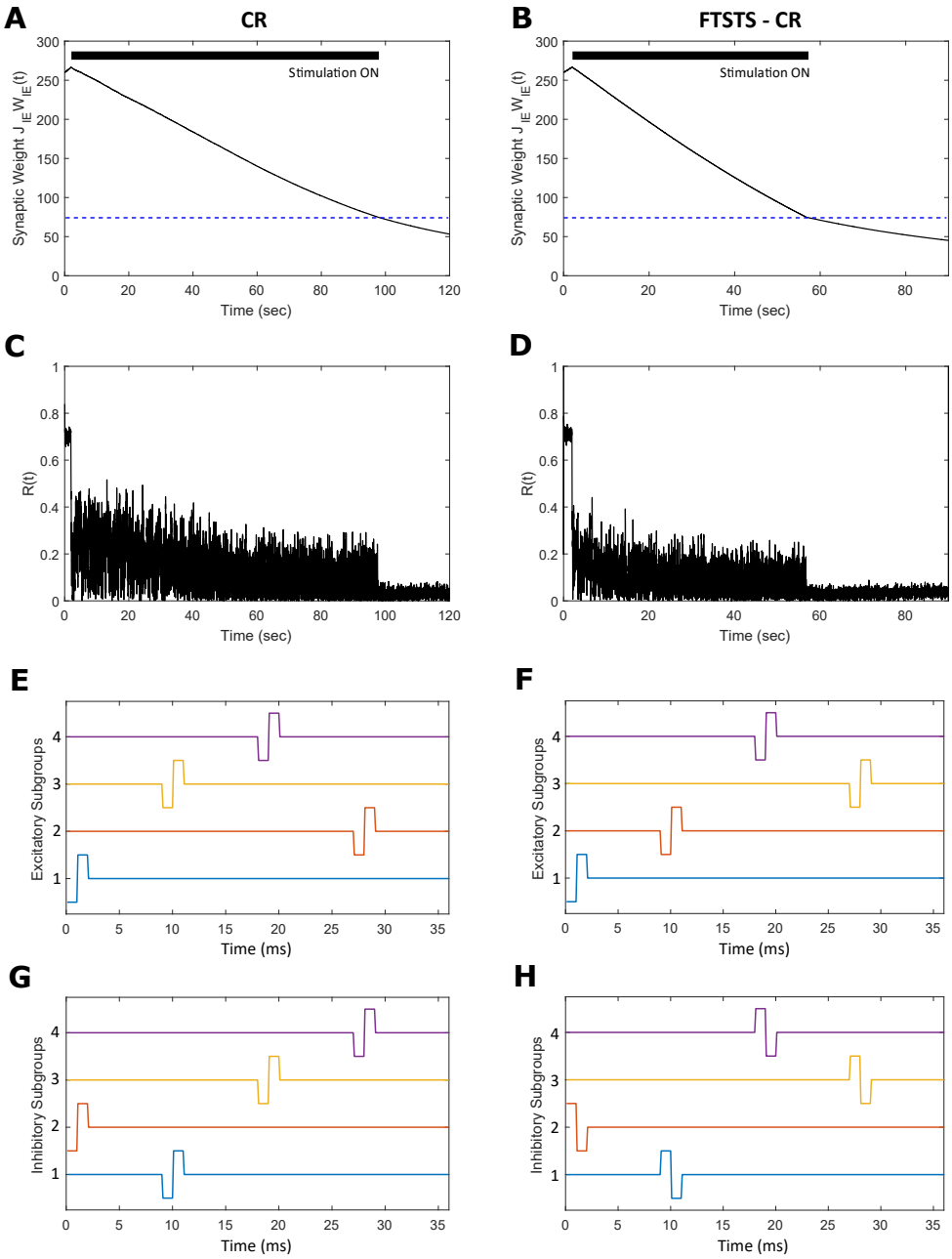

FIGURE 4.10: Efficacy of the FTSTS-CR strategy in desynchronizing 2,000 neuron E-I network in the presence of E-to-E and I-to-I synaptic connectivity. Each excitatory and inhibitory population of neurons is individually divided into 4 subpopulations (8 subpopulations for the E-I network). **(A)** and **(C)** show the changes in the average E-to-I synaptic weight of the network and the network synchrony level respectively for the CR desynchronization strategy. The FTSTS-CR is compared to the CR approach in **(B)** and **(D)**, which show the changes in the average E-to-I synaptic weight of the network and the network synchrony level respectively. **(E)** and **(G)** show one cycle of coordinate reset (CR) stimulation applied to the subpopulations in each excitatory and inhibitory neuron population. **(F)** and **(H)** show one cycle of the FTSTS-CR stimulation protocol applied to the excitatory and inhibitory populations. The designed FTSTS-CR and CR pulse parameters are U_{stim} = 100 mV, T_{stim} = 1 ms, and $T_{neutral}$ = 7 ms.

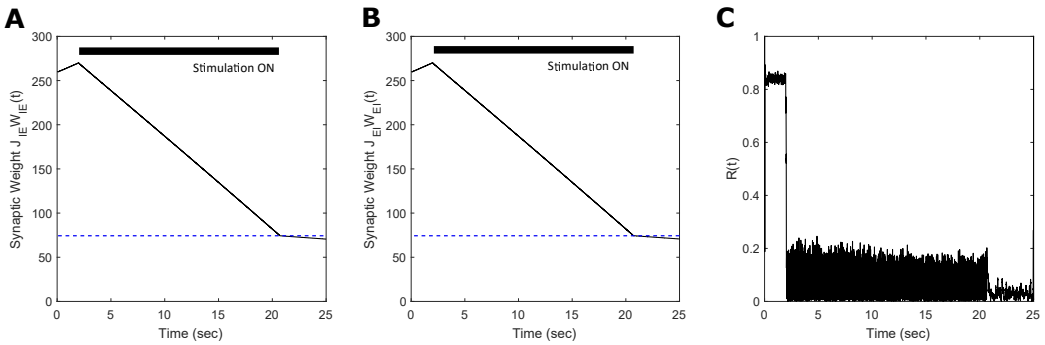

FIGURE 4.11: Efficacy of the FTSTS strategy in desynchronizing 2,000 neuron E-I network in the presence of Hebbian E-to-I and anti-Hebbian I-to-E plasticity. **(A)** and **(B)** show the change in the average E-to-I and I-to-E synaptic weight of the network, respectively. **(C)** shows the network synchrony level during the simulation. The FTSTS pulse parameters are U_{stim} = 100 mV, T_{stim} = 1 ms, and $T_{neutral}$ = 10 ms.

In order to apply my FTSTS protocol for desynchronizing E-to-I network with a symmetric plasticity rule, I modified the FTSTS protocol by offsetting the pulse to the inhibitory population by T_{offset}. This forced ISIs that promote either an increase or decrease in the synaptic weight. Using my modified FTSTS protocol, I show in Figure 12A that my FTSTS strategy can efficiently depress the synaptic weight of the synchronous network and desynchronize the network by forcing larger ISI_{IE} values. Additionally, my protocol can also increase the average synaptic weight of the network to resynchronize the network by forcing short ISI_{IE} values. Figure 4.12B shows the increase in the average E-to-I synaptic weight. The subsequent increase in the synchrony level is shown in Figure 4.12D, where the order parameter increases from $R(t) = 0.05$ to $R(t) = 0.6$.

4.3.11 *Comparison to Previous Desynchronization Strategies*

My FTSTS strategy differs from existing stimulation strategies for desynchronizing spiking neural networks in many ways. My strategy is based on harnessing the underlying synaptic plasticity compared to most of the desynchronization strategies reported in literature (Deuschl *et al.*, 2006; Wilson and Moehlis, 2014; Monga *et al.*, 2018; Mauroy *et al.*, 2014; Nabi *et al.*, 2013b; Vlachos *et al.*, 2016; Popovych *et al.*, 2005; Hauptmann *et al.*, 2005; Kiss *et al.*, 2007; Popovych *et al.*, 2017). Most of these strategies ignore the inherent synaptic plasticity among neurons in the network in designing the stimulation protocol for desynchronizing the network activity (One exception is "Coordinate Reset" (CR) (Pfister and Tass, 2010; Tass and Hauptmann, 2007; Tass, 2003b,a; Tass and Majtanik, 2006; Ebert *et al.*, 2014; Zeitler and Tass, 2015)). As a result, these strategies effectively desynchronize the network activity if the stimulation protocol is active. Once the stimulation protocol is turned off, the network resynchronizes rapidly because of the disappearance of the asynchronous regime in the absence of stimulation. My strategy alleviates this problem, like CR, by explicitly incorporating and harnessing Hebbian-based STDP, which allows the network to stay in the asynchronous regime for a longer-time period after the stimulation is turned off (see Figure 4.3).

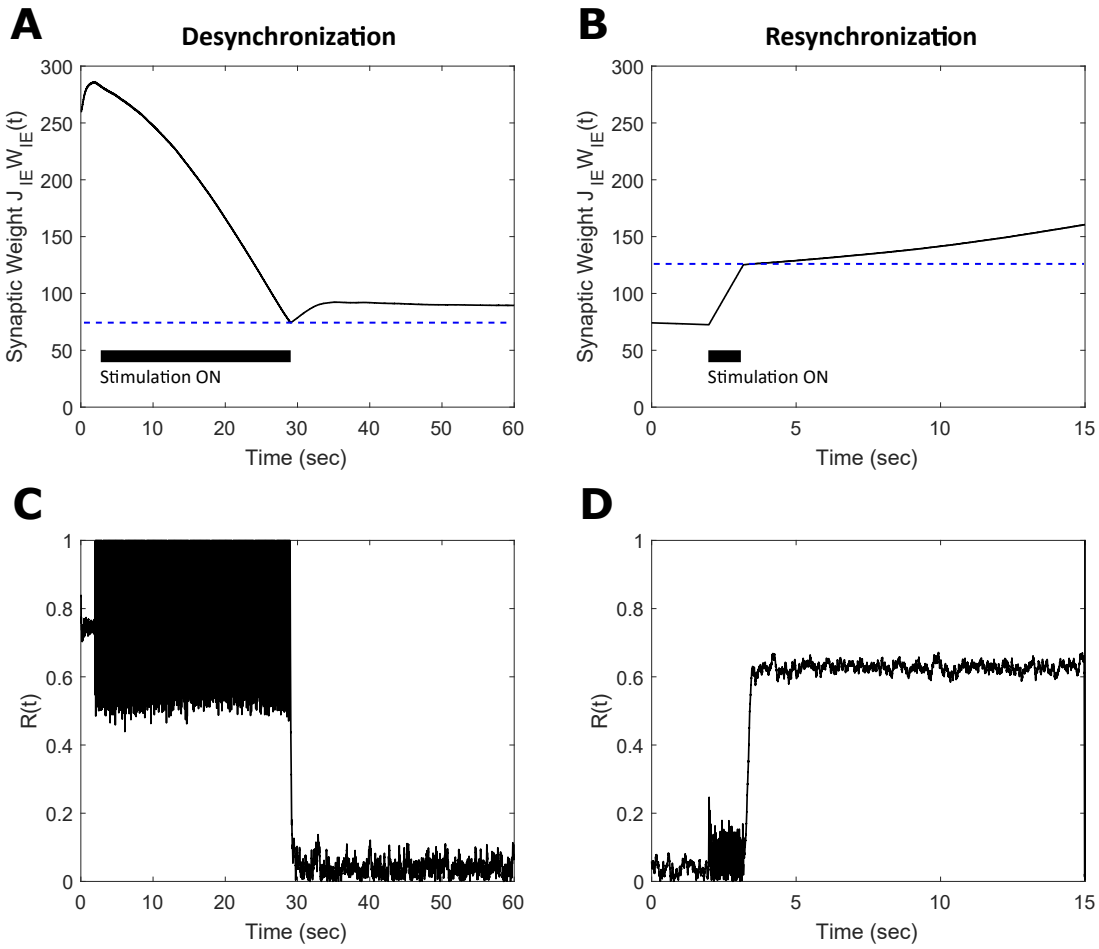

FIGURE 4.12: Efficacy of the FTSTS strategy in desynchronizing (**(A)** and **(C)**) and resynchronizing (**(B)** and **(D)**) a 2,000 neuron E-I network with symmetric plasticity. **(A)** shows the decrease in average synaptic weight of the network with the modified FTSTS protocol for symmetric plasticity. **(C)** shows the change in the synchrony of the network before, during, and after stimulation. **(B)** shows the increase in average synaptic weight of the network with the modified FTSTS protocol for symmetric plasticity. **(D)** shows the change in the synchrony of the network before, during, and after stimulation. The FTSTS parameters used to decrease the average E-to-I synaptic weight are U_{stim} = 200 mV, T_{stim} = 1 ms, $T_{neutral}$ = 22 ms, and T_{offset} = 11 ms. The FTSTS parameters used to increase the average E-to-I synaptic weight are U_{stim} = 100 mV, T_{stim} = 1 ms, $T_{neutral}$ = 10 ms, and T_{offset} = 5 ms.

Almost all the stimulation strategies focus on desynchronizing the network activity by randomizing the firing patterns of neurons through direct stimulation. In comparison, my FTSTS strategy focuses on decreasing the average synaptic weight of the network by taking advantage of the Hebbian-based STDP protocol, which leads to the desynchronization of network activity. For example, the CR-based stimulation strategy desynchronizes the network activity by forcing different subpopulations of neurons to fire out of phase with each other, which resets the phase and desynchronizes the network (Pfister and Tass, 2010; Tass and Hauptmann, 2007; Tass, 2003b,a; Tass and Majtanik, 2006; Ebert *et al.*, 2014; Zeitler and Tass, 2015). This generates an artificial asynchronous firing pattern that increases the basin of attraction of the asynchronous regime (i.e., lower synaptic weight stability point) (Popovych and Tass, 2014; Pfister and Tass, 2010). The underlying synaptic plasticity within the network then drives the average synaptic weight of the network towards the lower synaptic weight stability point (see Figures 4.10 and 4.13 for comparison of my approach to the CR-based stimulation strategy).

My developed framework can be incorporated into other desynchronization strategies, such as CR, to improve their efficacy. Figure 4.10 shows a comparison between the FTSTS-CR and CR performances in desynchronizing an E-I network consisting of 2,000 neurons with E-I synaptic plasticity (see Section 4.3.8 for details of model parameters and specifics about the design of FTSTS-CR stimulation strategy). Since the FTSTS-CR stimulation strategy focused on decreasing the average synaptic weight of network, which as a result desynchronized the neural activity (see Figures 4.10B and 4.10D), this strategy outperformed the CR stimulation strategy shown in Figures 4.10A and 4.10C.

One of the limitations of the CR stimulation strategy is that the long-lasting effects occur only in networks where the long-term depression (LTD) dominates the long-term potentiation (LTP) of the synapses on average so that the network exhibits bistability (Pfister and Tass, 2010). It has been found that LTP dominates in specific aberrant neuronal pathways and brain regions such as the striatum indirect pathway underlying Parkinson's disease and hippocampus underlying epilepsy (Shen *et al.*, 2008; Johnston, 2004; Mathern *et al.*, 1998). In such brain networks, the CR and FTSTS-

CR stimulation strategy would both fail to produce long-lasting desynchronization of the network activity but the FTSTS-CR will have a longer acute desynchronization effect compared to the CR protocol. To demonstrate this, I applied the CR stimulation strategy to an E-I network consisting of 2,000 neurons where LTP dominates LTD. As shown in Figure 4.13D, the network synchrony level is disrupted during the stimulation period of 140 s but increased to a synchrony level of $R(t) = 0.7$ after removal of the stimulus. Since CR stimulation, in this scenario, only induces acute desynchronization of the network and does not reduce the average synaptic weight, the average synaptic weight of the network remains in the synchronous regime the entire time, as shown in Figure 4.13B. As a result, the network resynchronized rapidly after the removal of the CR stimulus. I compare the desynchronization efficacy of the FTSTS-CR and CR approach in Figures 4.13A and 4.13B, respectively. During the period of FTSTS-CR stimulation, there is a decrease in the average synaptic weight (see Figure 4.13A). This results in a reduction in the synchrony level to $R(t) = 0.05$ when the FTSTS-CR stimulus is removed. While this desynchronization is transient due to the domination of LTP, the network remains desynchronized for a longer period of time compared to CR as shown in Figure 4.13C.

4.4 SUMMARY

In this chapter, I developed and presented a novel stimulation strategy "Forced Temporal Spike-Time Stimulation (FTSTS)" for controlling synchronous activity of neurons in large spiking neural networks. Compared to other desynchronization strategies for large-scale spiking neural networks reported in the literature, my strategy focuses on controlling the average network synaptic weight by harnessing synaptic plasticity using a Hebbian-based spike-timing dependent plasticity (STDP) protocol that as a result controls the synchronization of neurons within the network. I presented a two neuron excitatory-inhibitory (E-I) network as an example to provide a mechanistic understanding of my approach. I later demonstrated the efficacy and robustness of the FTSTS strategy on large networks by varying the model parameters, synaptic connectivity and noisy inputs to the network. These results

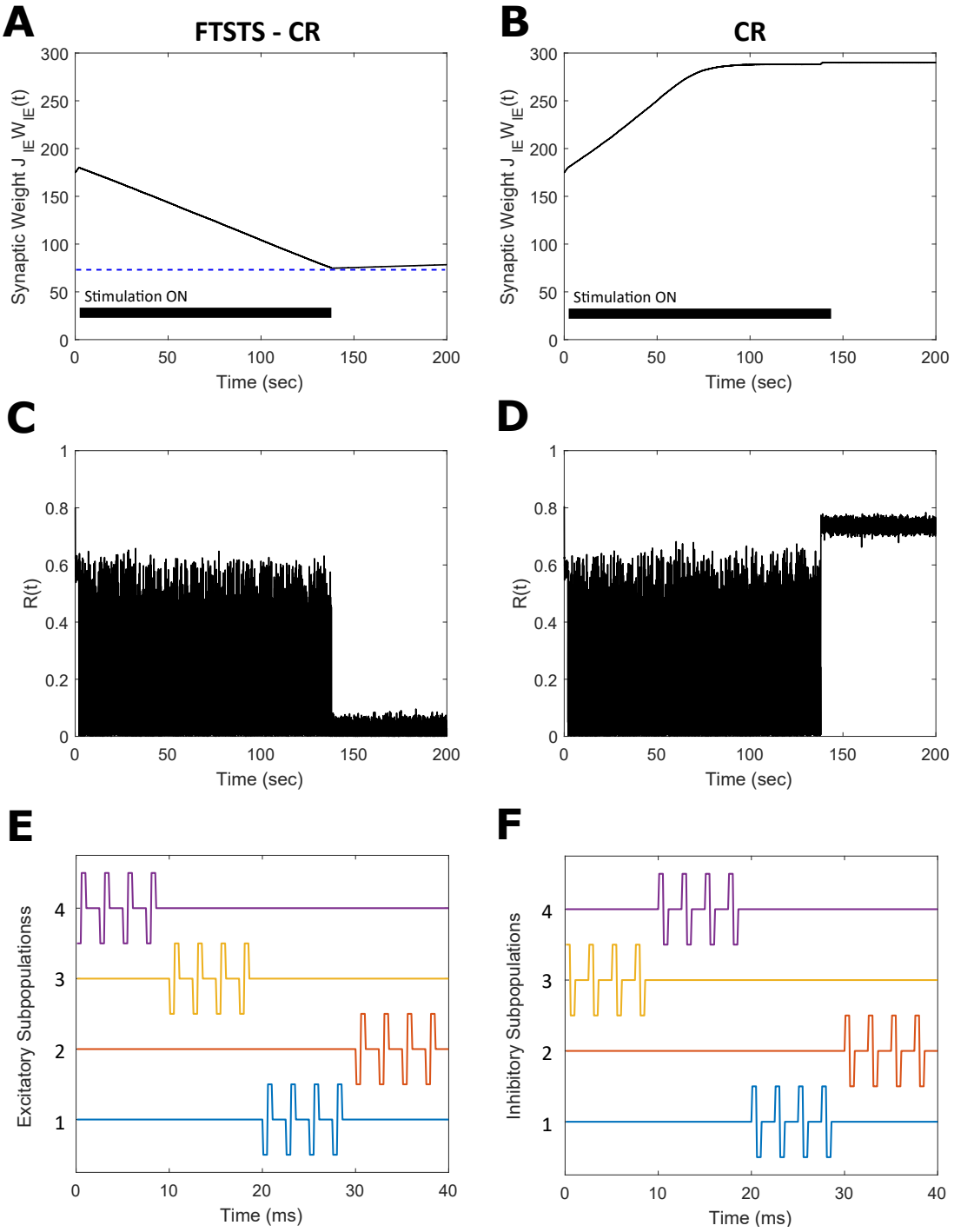

FIGURE 4.13: Comparison of the FTSTS-CR stimulation strategy with the coordinate-reset (CR) stimulation strategy on a network where LTP dominates LTD. **(A)** and **(C)** show the changes in the average E-to-I synaptic weight of the network and the network synchrony level respectively for the FTSTS-CR stimulation strategy. **(B)** and **(D)** show the changes in the average E-to-I synaptic weight of the network and the network synchrony level respectively for the CR stimulation strategy. **(E)** and **(F)** show the FTSTS-CR stimulation pattern. The FTSTS-CR pulse parameters are U_{stim} = 200 mV, T_{stim} = 0.5 ms, and $T_{neutral}$ = 3 ms. The STDP plasticity parameters are $a_{LTD} = -1$, $a_{LTP} = 1.01$,$\tau_{LTD} = 20$ ms, and $\tau_{LTP} = 20$ ms.

are also summarized in Figure 4.14 for clarity. While I only considered a LIF network, my method will lead to similar outcomes qualitatively for other neuronal models, since my approach is based on Hebbian activity-dependent plasticity. One of the prominent features of my FTSTS strategy is that it allows both synchronization and desynchronization of network activity by reversing the stimulation protocol (see Figures 4.3 and 4.4), thus provides a complete control over the synchronization level of neural activity within a given network.

In this work, I have considered excitatory-inhibitory (E-I) networks with plastic E-to-I synapses. In general, My approach is applicable to other types of spiking neural networks such as purely excitatory or inhibitory networks as well as to networks with other plastic synapses such as E-to-E or I-to-I synapses. One of the limitations of my approach is that it assumes the same stimulus waveform is delivered to individual neurons within a subpopulation. Although I have demonstrated in simulation that my FTSTS strategy effectively desynchronizes the neuronal firings in a network even when the stimulation waveform parameters for individual neurons are drawn randomly from a given distribution (see Figure 4.6) and are contaminated with input designed for the opposite population (Figure 4.9), it is still able to utilize the relationship between pre and post firings to effectively harness the synaptic plasticity. Multi-laser optogenetics and recent development in optogenetics to excite or inhibit the same neuron using two different light wavelengths could potentially alleviate this limitation for experimental implementation of my strategy (Forli *et al.*, 2018). Additionally, I assumed the majority of the excitatory and inhibitory neuron populations were spatially separate, which allows for the neuron populations to be separately stimulated. Two examples of spatially separate excitatory and inhibitory neuron populations are the striatum and cortex or the globus pallidus external segment (GPe) and subthalamic nucleus (STN) (Lanciego *et al.*, 2012; Hegeman *et al.*, 2016). The GPe-STN network has traditionally been targeted for DBS-HFS to treat PD and could be potential area to test this hypothesis. Although I have not optimized the FTSTR pulses to achieve a better performance or to make it more energy efficient, it is not difficult to formulate optimization problems that minimizes the average synaptic

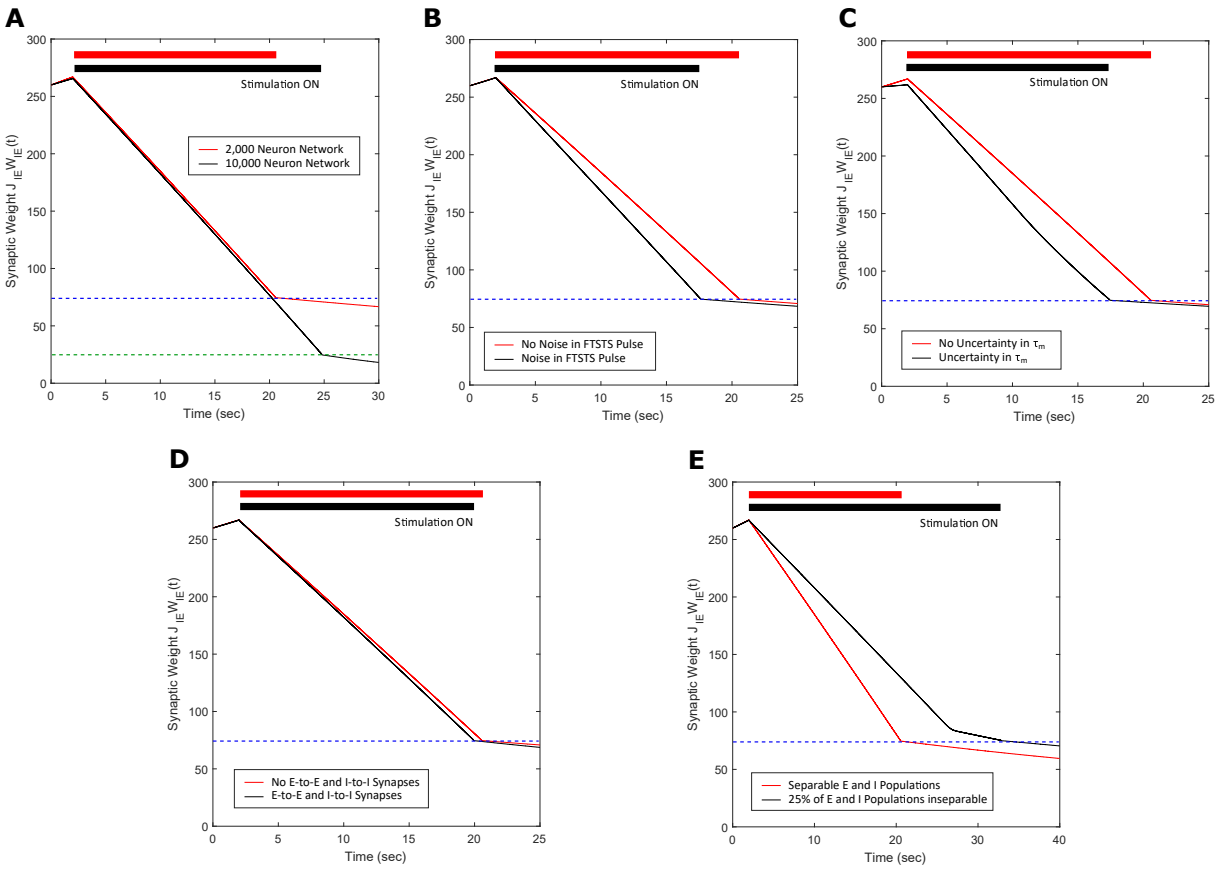

FIGURE 4.14: Summary of the robustness studies (red line) of the FTSTS approach with varying network and input parameters compared to the base E-I network in Figure 4.3 (black line). **(A)** Desynchronization of neural activity in 10,000 neuron E-I network. **(B)** Robustness of the FTSTS strategy against random variations in the FTSTS pulse amplitude. **(C)** Robustness of the FTSTS strategy against uncertainty in the membrane time constant of neurons in the 2,000 neuron E-I network. **(D)** Efficacy of the FTSTS strategy in desynchronizing 2,000 neuron E-I network in the presence of E-to-E and I-to-I synaptic connectivity. **(E)** Efficacy of the FTSTS strategy in desynchronizing 2,000 neuron E-I network where 25% of the population is inseparable and receives both the excitatory and inhibitory population input. The FTSTS pulse parameters for all the studies are U_{stim} = 100 mV, T_{stim} = 1 ms, and $T_{neutral}$ = 10 ms.

weight, network synchrony level, and applied stimulation energy simultaneously to achieve a better overall performance.

CHAPTER 5

Controlling Epileptic Seizures using Forced Temporal Spike-Time Stimulation

5.1 INTRODUCTION

In the previous chapter, I developed a novel neurostimulation protocol called “Forced Temporal Spike-Time Stimulation" (FTSTS) that I showed in simulation was able to efficiently desynchronize large excitatory-inhibitory (E-I) spiking neuron networks and keep the network desynchronized without further input by harnessing the synaptic weight of the network (Schmalz and Kumar, 2019). My neurostimulation protocol consisted of two biphasic out-of-phase pulses. One of the pulses was delivered to the excitatory neuron population and the other to the inhibitory neuron population. The pulse pair controlled the relative spike times of each neuron population in order to control the average synaptic weight of the network and move the synchronous E-I network from the synchronous to the asynchronous state. Furthermore, if the pulse-pairs were exactly reversed, the FTSTS protocol was capable of synchronizing an asynchronous neuron population. In my previous work, I showed the capability of this selective FTSTS protocol in desynchronizing and resynchronizing neuron activity in a generic excitatory-inhibitory (E-I) network model of various sizes and dynamics. Based on these promising results, I wondered if my novel neurostimulation strategy could potentially be used to terminate epileptic seizures, which is another neurological disease characterized by highly synchronous neural activity.

Epilepsy affects 65 million people world wide and is typically characterized by highly synchronized episodes of neural activity that can lead to loss of autonomy (Thurman *et al.*, 2011; Moshé *et al.*, 2015). In most cases, epileptic symptoms are treatable with anti-epileptic drugs, although not all patients respond to the drugs (Perucca, 1998; Kwan and Brodie, 2000; Brodie *et al.*, 2012). This type of epilepsy is coined drug resistant epilepsy (DRE). Patients with DRE become prime

candidate for direct neurostimulation therapies, such as vagus nerve stimulation (Handforth *et al.*, 1998; Stefan *et al.*, 2012) or deep brain stimulation (DBS) (Fisher *et al.*, 2010), which have proven to be effective in reducing epileptic episodes. DBS is a neurostimulation therapy where electrodes are implanted into a specific part of the brain and electrical high frequency stimulation (HFS) is applied to suppress the epileptic activity (Zangiabadi *et al.*, 2019). While this approach works well at suppressing the epileptic activity when it arises, it doesn't address the underlying synaptic connections that generate the epileptic episodes. Therefore, seizures will reemerge in the future and require continued re-application of DBS.

Building upon my prior work, I investigated the capability of the FTSTS protocol in desynchronizing the pathologically synchronous firing patterns present during epileptic seizures. I considered a biophysically constrained neocortical-onset seizure model that captured the key features of neocortical seizures, such as the fast inward moving ictal discharges and the slow outward wavefront of ictal recruitment (Liou *et al.*, 2020). Additionally, the model captured the predisposition of subsequent seizures after an initial seizure. The propagation of the neocortical seizure throughout the network and the emergence of a second spontaneous seizure is shown in Figure 5.1A. I applied my FTSTS protocol to this biophysically constrained seizure model. My preliminary results showed that my FTSTS protocol, which was previously applied to a generic E-I network, disrupted the initial seizure and suppressed the emergence of future spontaneous seizures (see Figure 3.13B). Furthermore, if I applied the exact reverse of the FTSTS protocol, additional spontaneous neocortical seizure episodes began to emerge after the first seizure (see Figure 3.13C). While my preliminary results highlighted the capability of the FTSTS protocol at desynchronizing a biophysically constrained epileptic neocortical network model, the optimal parameters of the FTSTS protocol have not yet been determined.

In this chapter, I investigate the parameter space of the "Forced Temporal Spike-Time Stimulation" (FTSTS) protocol in order to determine the optimal parameters to efficiently control the average E-to-I synaptic weight. I consider a biophysically constrained neocortical-onset seizure model consisting of 1000 spiking neurons and measured the rate of change in the average E-to-I synaptic weight induced by the

FTSTS protocol over the five second interval of the applied FTSTS protocol. I demonstrate that my FTSTS protocol is able to control the average excitatory-to-inhibitory synaptic weight, and it can increase or decrease the future prevalence of spontaneous or induced seizures. Then I determined the optimal FTSTS pulse parameters to increase and decrease the average excitatory-to-inhibitory synaptic weight. Finally, I integrate two optogenetic channelrhodopsin dynamics Chronos and Chrimson into my FTSTS protocol in order to overcome spatial constraints of electrically stimulating the excitatory and inhibitory neurons.

5.2 SYSTEM MODEL

5.2.1 *Neocortical Seizure Model*

Throughout this paper, I have used a recently published computational model of neocortical-onset seizures (Liou *et al.*, 2020), validated with the clinical data from epileptic patients, to simulate the seizure dynamics. Briefly, the model consists of a spatially homogeneous one-dimensional neural network consisting of 500 excitatory and 500 inhibitory neurons. The membrane potential, V, of each neuron is described by the following conductance-based integrate-and-fire model:

$$\begin{aligned} C\frac{dV}{dt} &= g_L(E_L - V) + \frac{g_E}{f_{max}}(E_E - V) + \frac{g_I}{f_{max}}(E_{Cl} - V) \\ &\quad + \frac{g_K}{f_{max}}(E_K - V) + I_{app}. \end{aligned} \tag{5.1a}$$

Here, C is the membrane capacitance, and I_{app} is the external electrical current. The model considers four conductances: leaky (g_L), glutamatergic syanptic (g_E), GABAergic synaptic (g_I), and slow after hyperpolarization sAHP (g_K). f_{max} is a scaling term equal to the maximum firing rate or the inverse of the refractory period. Each conductance has a corresponding reversal potential E_L, E_E, E_I, and E_K. The spike-times are stochastically determined based on the instantaneous firing rate $f = f_0 \exp\left(\frac{V-\phi}{\beta}\right)$, where f_0 is a scaling parameter, ϕ is firing threshold, and β is the uncertainty of an action potential threshold. If a spike occurs, the membrane potential is set to the average of 40 mV and the current membrane potential $V(t_i)$ at

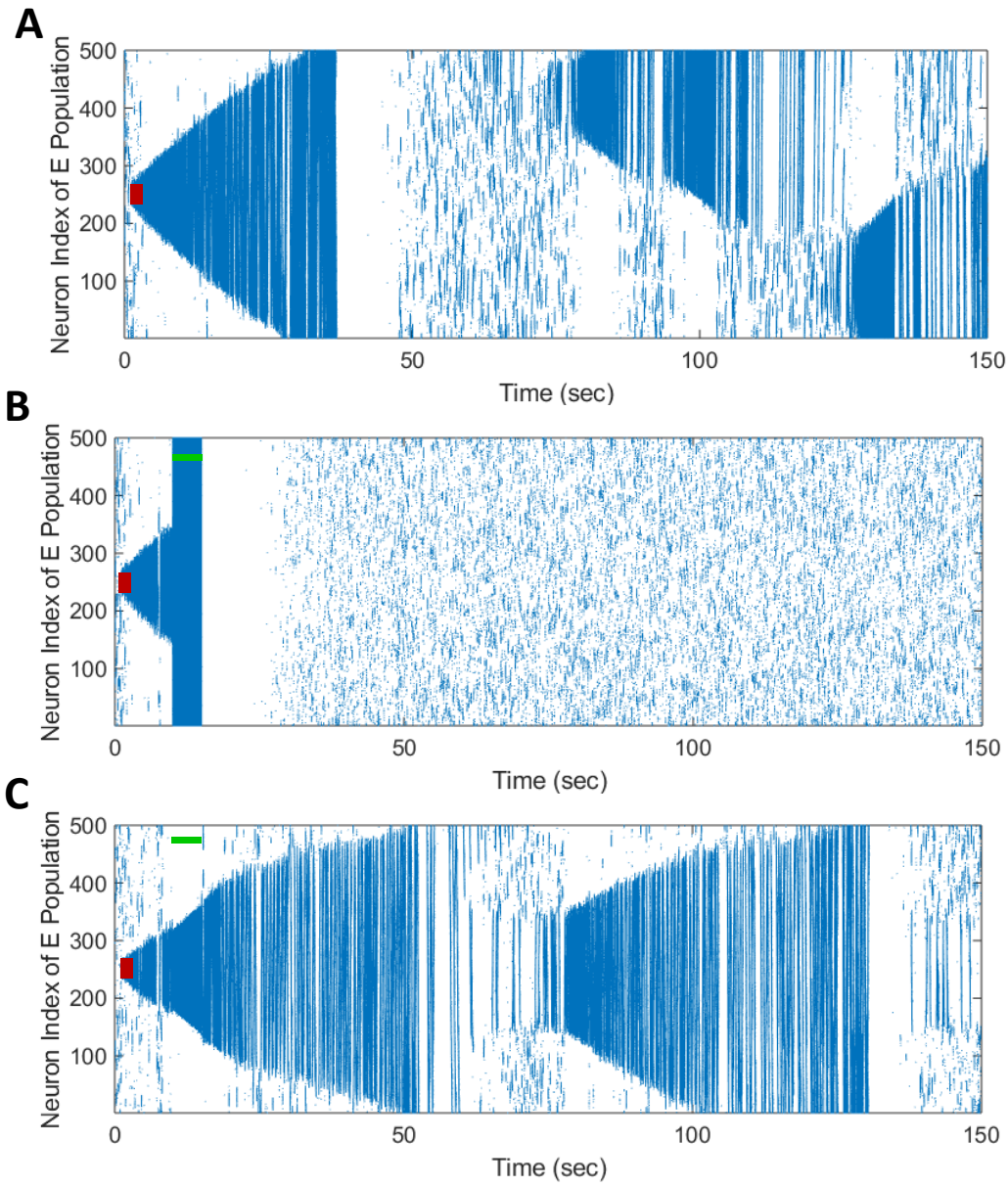

FIGURE 5.1: Preliminary investigation into the use of "Forced Temporal Spike-Time Stimulation" (FTSTS) to suppress neocortical epileptic episodes. A seizure was initiated in the biophysically-constrained neocortical model by applying a seizure input of 200 pA for 3 s (red-bar). **(A)** shows the propagation of the seizure throughout the network and its termination after approximately 40 s. Then, a second seizure emerged approximately 50 s after the termination of the first seizure. I applied the FTSTS protocol six seconds after the seizure initiating input (green-bar). **(B)** shows the termination of the initial seizure and the suppression of further seizure for the rest of the simulation. I then applied the exact opposite FTSTS protocol. **(C)** shows the increased prevalence of spontaneous seizures after the FTSTS protocol.

t_i where t_i is the time of a spike. After the spike, the membrane potential is reset to $V(t_{i+1}) = V(t_{i-1}) - 20$ mV at t_{i+1}. The dynamics of the firing threshold that dictates the probability of a spike occurring is governed by Eq. 5.1b.

$$\tau_\phi \frac{d\phi}{dt} = \phi_0 - \phi. \tag{5.1b}$$

Here, τ_ϕ is a time constant, ϕ_0 is the baseline threshold, and Δ_ϕ is added to ϕ at the time of a spike. The excitatory and inhibitory synaptic dynamics are captured by g_E and g_I, respectively (see Eq. 5.1a). The conductance dynamics of the excitatory and inhibitory synapses are governed by the exponential decay functions of Eqs. 5.1c and 5.1d.

$$\tau_{syn} \frac{dg_E}{dt} = -g_E, \tag{5.1c}$$

$$\tau_{syn} \frac{dg_I}{dt} = -g_I. \tag{5.1d}$$

Here, τ_{syn} is the time constant. If an excitatory or inhibitory neuron spikes, then the weight of the synapse between the i^{th} pre-synaptic and j^{th} post-neuron is added to the j^{th} post-neuron's conductance $\big(g_j(t_i) = g_j(t_{i-1}) + W(i,j)\big)$. Furthermore, the inhibitory GABAergic synaptic input reversal potential is dependent on the chloride concentration gradient. The gradient determines the reversal potential (E_{Cl}) of the GABAergic synapse using the following Nernst equation:

$$E_{Cl} = -26.7 \log \frac{[Cl_{out}]}{[Cl_{in}]}, \tag{5.1e}$$

where $[Cl_{out}]$ and $[Cl_{in}]$ are the external and internal chloride concentration, respectively. The external chloride concentration is assumed to be constant and the internal chloride dynamics is modeled by the first-order kinetics

$$\frac{d[Cl_{in}]}{dt} = -\frac{I_{Cl}}{V_d F} - \frac{[Cl_{in,eq}] - [Cl_{in}]}{\tau_{Cl}}, \tag{5.1f}$$

TABLE 5.1: Model parameters of spiking neurons.

Neuron Parameters	Value	Neuron Parameters	Value
C	100 pF	Δ_ϕ	-55 mV
g_L	4 nS	τ_{Cl}	5000 mS
E_L	-57 mV	V_d	0.2357 pL
E_E	0 mV	$[Cl]_{in,eq}$	6 mM
E_K	-90 mV	$[Cl]_{out}$	110 mM
f_0	0.002 Hz	τ_K	5000 ms
β	1.5 mV	Δ_K	40 nS
τ_{ref}	5 ms	σ_E	0.02
τ_{syn}	15 ms	σ_I	0.03
τ_ϕ	100 ms	f_{max}	0.2 Hz
ϕ_0	-55 mV	F	96500 $C\ mol^{-1}$
η	10^{-3}	τ_{STDP}	15 ms

where the chloride current is $I_{Cl} = g_I(V - E_{Cl})$, V_d is the volume of distribution of $[Cl_{in}]$, F is Faraday's constant, and τ_{Cl} is the time constant of the $[Cl_{in}]$ dynamics. The equilibrium intracellular concentration of chloride is $[Cl_{in,eq}]$. Finally, the slow after-hyperpolarization (sAHP) conductance dynamics is modeled as

$$\tau_K \frac{dg_K}{dt} = -g_K, \tag{5.1g}$$

where τ_K is a time constant. If a spike occurs, then $\frac{\Delta_K}{\tau_K}$ is added to g_K. I provide the parameters for Eqs. 5.1a - 5.1g in Table 5.1.

5.2.2 *Network Synaptic Connectivity*

The synaptic connection between an excitatory and an inhibitory neuron is modeled in a distance-dependent form. Briefly, the strength of the excitatory synapses is normally distributed about each excitatory neuron with mean zero and spatial variance of σ_E^2, as described by the spatial distribution kernel K_E in Eq. 5.2a. The strength of inhibitory synaptic connections is modeled by the spatial distribution kernel K_I (see Eq. 5.2b). In addition to the normally distributed synaptic strength with mean zero and spatial variance of σ_I^2 in Eq. 5.2b), there also exists weak uniformly distributed synapses in the inhibitory network, which are represented by the term U. The contribution of the

normally distributed inhibitory synapse is $1-\gamma$ and the contribution of the uniformly distributed inhibitory synapses is γ.

$$K_E \sim N(0,\sigma_E^2), \tag{5.2a}$$

$$K_I \sim (1-\gamma)N(0,\sigma_I^2)+\gamma U, \tag{5.2b}$$

5.2.3 *Spike-Time Dependent Plasticity Model*

Throughout this work I have assumed that E-to-E and E-to-I synapses in the neocortical model are plastic. Furthermore, I have assumed that the change in the synaptic strength is activity-dependent, and I modeled the changes in the synaptic strength of both type of synapses using a Hebbian-based spike-timing dependent plasticity (STDP) rule (Song *et al.*, 2000; Bi and Poo, 1998). Eqs. 5.3a-5.3e describe the STDP dynamics.

$$W_{i,j}(t+\Delta t) = W_{i,j}(t)+\Delta W_{i,j}(t), \tag{5.3a}$$

$$\Delta W_{i,j}(t) = \eta A_{post}(t) \quad if\ \ t_{pre}-t_{post}<0, \tag{5.3b}$$

$$\Delta W_{i,j}(t) = -\eta A_{pre}(t) \quad if\ \ t_{pre}-t_{post}>0, \tag{5.3c}$$

$$\tau_{STDP}\frac{dA_{post}}{dt} = -A_{post}+\delta(t-t_{post}), \tag{5.3d}$$

$$\tau_{STDP}\frac{dA_{pre}}{dt} = -A_{pre}+\delta(t-t_{pre}). \tag{5.3e}$$

Here, $W_{i,j}(t)$ represents the weight (or strength) of a synapse connecting the j^{th} presynaptic neuron to the i^{th} postsynaptic neuron. The synaptic weight at time $t+\Delta t$ (i.e., $W_{i,j}(t+\Delta t)$) is updated by the change in the synaptic weight ($\Delta W(t)$) determined by the time difference between j^{th} presynaptic (t_{pre}) and i^{th} postsynaptic (t_{post}) neuron spike times (see Eq. 5.3a). The parameter η represents the learning rate, i.e., the rate at which the synaptic weight is updated each time. The contributions of the long-term potentiation (LTP) and long-term depression (LTD) to the overall change in the synaptic weight depending on the time difference between postsynaptic and

presynaptic neuron spike-times are modeled using the exponential functions $A_{post}(t)$ and $A_{pre}(t)$ (see Eqs. 5.3d and 5.3e). The STDP time constant τ_{STDP} defines the STDP spike time window (Song *et al.*, 2000). At the time of the postsynapitc neuron spiking (t_{post}) or the presynaptic neuron spiking at (t_{pre}), Eqs. 5.3d and 5.3e are updated by the dirac-delta functions $\delta(t - t_{post}) = 1$ and $\delta(t - t_{pre}) = 1$, respectively. I provide the STDP parameters used in this paper in Table 4.1.

5.2.4 *Forced Temporal Spike-Timing Stimulation*

Throughout this work, I have used my previously developed Forced Temporal Spike-Timing Stimulation (FTSTS) strategy (Schmalz and Kumar, 2019) which has shown to be effective in controlling the synchronization of neurons in E-I networks by harnessing the synaptic plasticity of the network. Briefly, my FTSTS protocol consists of excitatory and inhibitory charge-balanced biphasic stimulation pulses delivered to individual neurons in each of the subpopulation.

In order to optimize the FTSTS protocol, I must first define the parameters of the FTSTS pulse pair. The protocol consists of a pulse pair where each pulse is delivered to a separate neuron population with synaptic connections between the two neuron populations. In my biophysically constrained neocortical seizure model the two neuron populations are the excitatory and inhibitory neocortical neurons. Each pulse has the same amplitude (A), pulse width (W), and pulse interval (T), which is inversely related to frequency (F). These parameters are shown in Figure 5.2A. Additionally, each pulse has a polarity of 1 or -1 where a polarity of -1 inverts the pulse. A polarity of 1 is defined as the negative portion of the biphasic pulse leading the postive portion, while a polarity of -1 is the exact reverse. The polarity of the pulse delivered to the excitatory population is a_E and the polarity of the pulse delivered to the inhibitory population is a_I. Since the polarity can only be 1 or -1, there exists four possible pulse-pair polarity combinations. Figure 5.2 shows pulse-pair polarity combinations, which are standard FTSTS ($a_E = 1$ and $a_I = -1$), inverted standard FTSTS ($a_E = -1$ and $a_I = 1$), mirrored FTSTS ($a_E = 1$ and $a_I = 1$), and inverted mirrored FTSTS ($a_E = -1$ and $a_I = -1$). The final parameter of the FTSTS pulse-pair is the train-offset time ($\Delta\phi$), which is the time difference between

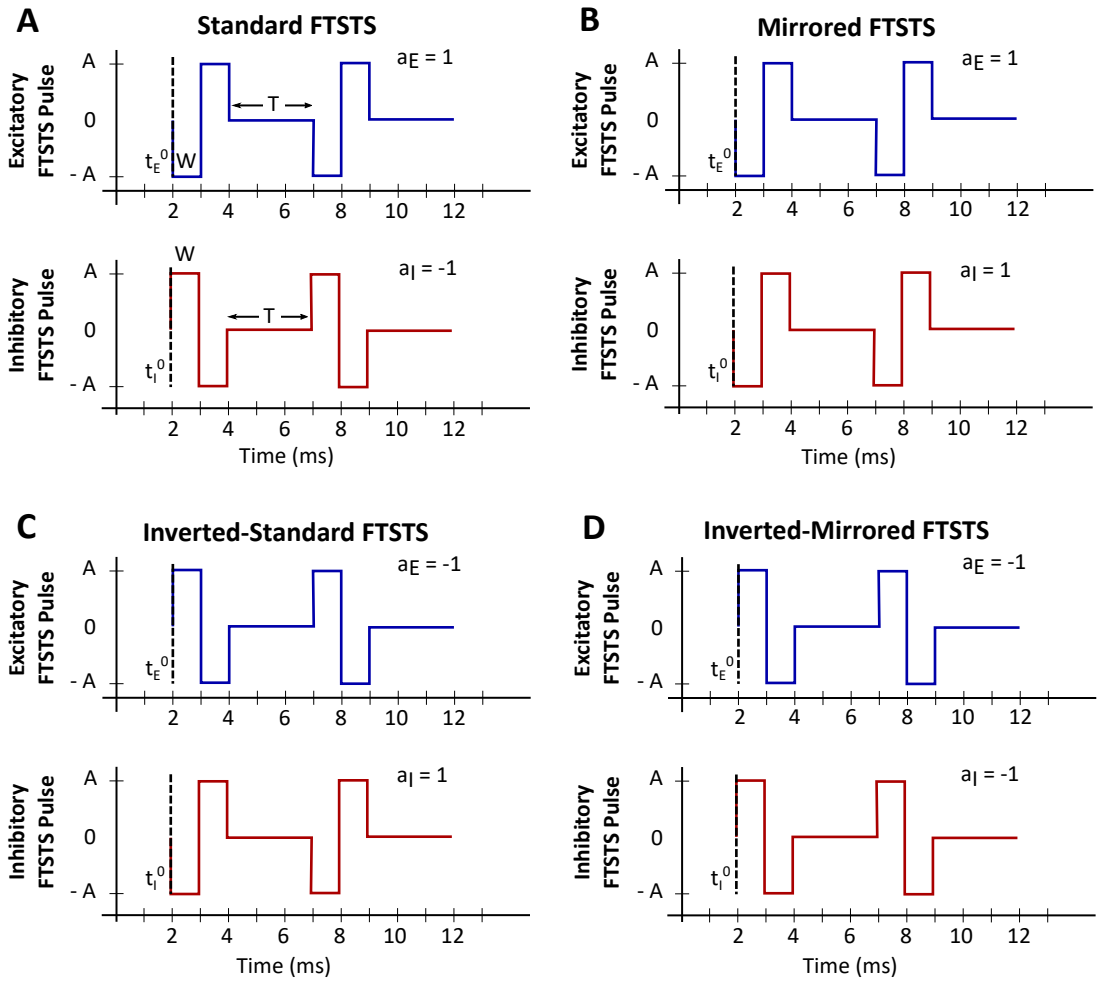

FIGURE 5.2: Forced Temporal Spike-Time Stimulation (FTSTS) parameters. The FTSTS pulse-pair parameters consist of amplitude (A), pulse width (W), pulse interval (T), and polarity (a_E and a_I). The four different polarities are shown in **(A)** standard FTSTS, **(B)** mirrored FTSTS, **(C)** inverted-standard FTSTS, and **(D)** inverted-mirrored FTSTS.

the start time of the inhibitory population pulse (t_I^0) and the start time of the excitatory population pulse (t_E^0) shown in Eq. 5.4. Figure 5.3 shows three examples of different train-offset times ($\Delta\phi = -1$, $\Delta\phi = 0$, and $\Delta\phi = 1$) for each of the four polarities.

$$\Delta\phi = t_I^0 - t_E^0 \tag{5.4}$$

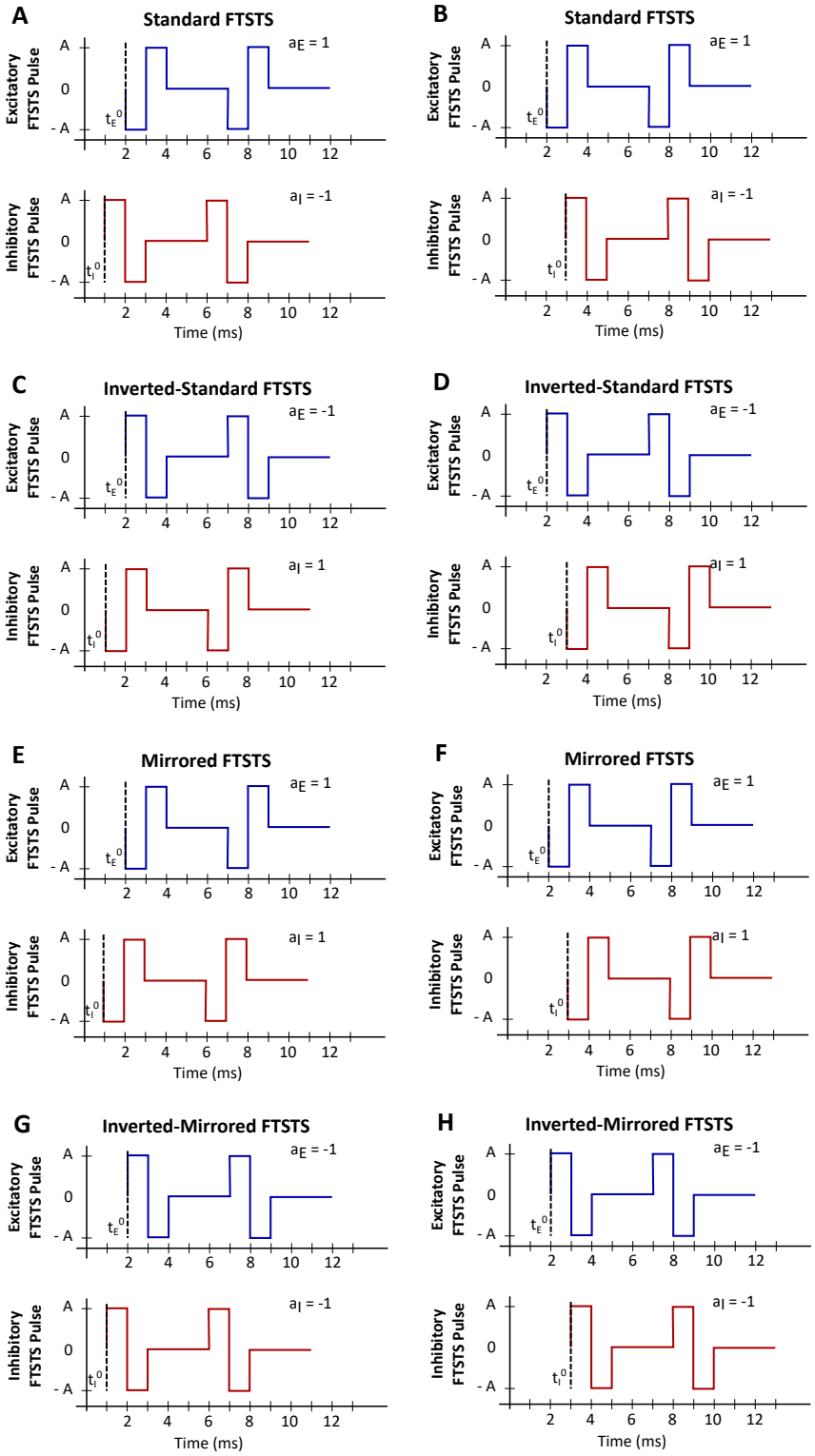

FIGURE 5.3: The train-time offset of the FTSTS pulse-pair. **(A)**, **(C)**, **(E)** and **(G)** show examples of a train-offset time of -1 *ms* for standard FTSTS, inverted-standard FTSTS, mirrored FTSTS, and inverted-mirrored FTSTS, respectively. **(B)**, **(D)**, **(F)** and **(H)** show examples of a train-offset time of 1 *ms* for standard FTSTS, inverted-standard FTSTS, mirrored FTSTS, and inverted-mirrored FTSTS, respectively.

5.2.5 *Optogentic FTSTS Protocol*

We modeled the channelrhodopsin light activated current with a reduced model developed by (Shewcraft *et al.*, 2020) and (Witt *et al.*, 2013). The current through the channelrhodopsin (see Eq 5.5a) is defined as the product of the conductance prefactor (g_{ChR2}), the conductance waveform (F_{ChR2}), and the membrane potential driving force ($V - V_{ChR2}$), where V_{ChR2} is the reversal potential. The conductance waveform is dependent on the intensity of the applied light (W_{light}) and the duration the light is applied ($t - t_{on} - d$). Here, t_{on} is the time the optical stimulation is applied and d is a light dependent activation delay. The parameters of the light dependent delay variable d are d_A, d_B, and d_C. τ_{act} and τ_{inact} represent the activation and deactivation time constants. The light intensity dependent variables A_{act}, $A_{inact}^{(1)}$, $A_{inact}^{(2)}$, and $A_{persist}$ modulate the open state of the channelrhodopsin. A_{act} represents the light dependent activation of the channelrhodopsin. $A_{inact}^{(1)}$ and $A_{inact}^{(2)}$ determine closing the rate of the channelrhodopsin. Finally, $A_{persist}$ is the persistent activation of the channelrhodopsin during prolonged optical stimulation. The activation and deactivation parameters are a_0, a_{min}, b_0, b_1, b_2, c_{inact}, and k_{inact}. The channelrhodopsin dynamics while the optical stimulation is being applied are shown in Eqs. 5.5a - 5.5h. The channelrhodopsin follows a simple exponential decay once the optical input is turned off. I considered two different channelrhodopsins, which were Chronos and Crimson channelrhodopsin. The exponential decay parameter were set as the experimentally measured value for each channelrhodopsin (Klapoetke *et al.*, 2014). Additionally, the intensity of the light for each channelrhodopsin ($W_{light}^{Chronos}$ and $W_{light}^{Chrimson}$) was determined from the literature, such that there was no light interference (Klapoetke *et al.*, 2014). The channelrhodopsin parameters are listed in Table 5.2.

TABLE 5.2: Channelrhodopsin photocurrent parameters.

Neuron Parameters	Value	Neuron Parameters	Value
W_{inact}	0.11	W_{light}^{Chonos}	0.0308
$\tau_{inact}^{(1)}$	9.06 ms	$W_{light}^{Chrimson}$	0.0023
d_A	0.27	b_0	0.16
d_B	-0.05	b_1	0.013
d_C	-0.0126	b_2	0.027
$\tau_{act}^{(0)}$	0.74 ms	$\tau_{inact}^{(2)}$	59.6 ms
c_{act}	12	c_{inact}	0.29
k_{act}	25	k_{inact}	2.4
a_0	1	V_{ChR2}	0 mV
a_{min}	0.4	g_{ChR2}	294 nS
$W_{0.5}$	0.38	$\tau_{off}^{Chronos}$	3.6 ms
		$\tau_{off}^{Chrimson}$	15.8 ms

$$I_{ChR2} = -g_{ChR2} F_{ChR2} (V - V_{ChR2}), \tag{5.5a}$$

$$F_{ChR2} = A_{act}\left(1 - e^{-\frac{t-t_{on}-d}{\tau_{act}}}\right) \left(A_{persist} + A_{inact}^{(1)} e^{-\frac{t-t_{on}-d}{\tau_{inact}^{(1)}}} + A_{inact}^{(2)} e^{-\frac{t-t_{on}-d}{\tau_{inact}^{(2)}}}\right), \tag{5.5b}$$

$$d = d_A + d_B W_{light} + \frac{d_C}{W_{light}}, \tag{5.5c}$$

$$\tau_{act} = \tau_{act}^{(0)} + c_{act} e^{-k_{act} W_{light}}, \tag{5.5d}$$

$$A_{act} = a_0 + \frac{a_{min} - 1}{1 + \left(\frac{W_{0.5}}{W_{light}}\right)^2}, \tag{5.5e}$$

$$A_{inact}^{(1)} = b_0 + \frac{b_1}{b_2 + (W_{light} - W_{inact})^2}, \tag{5.5f}$$

$$A_{inact}^{(2)} = c_{inact} e^{-k_{inact} W_{light}}, \tag{5.5g}$$

$$A_{persist} = 1 - A_{inact}^{(1)} - A_{inact}^{(2)}. \tag{5.5h}$$

5.3 RESULTS

5.3.1 *Novel FTSTS Reduces Seizure Prevalence*

First, I observed the emergence of seizures in the biophysically constrained neocortical-onset seizure model. I initiated a seizure in the model with a seizure initiating input of 200 pA applied for 3 s to 50 neocortical neurons. The seizure propagated through the entire network and terminated after 40 s. After the initial seizure, spontaneous spiking activity was observed for approximately 50 s. Then, a second seizure spontaneously emerged, which was followed by a third seizure. Figure 5.4A shows the raster plot of the neocortical model and the three seizures. During each neocortical seizure, the average E-to-I synaptic weight of the network increased (see Figure 5.4B). As the seizure propagated throughout the network, the plastic synaptic connections between the excitatory and inhibitory neurons were rewired by the seizure. The percent change in each individual excitatory-to-inhibitory synaptic weights is shown as a heat map in Figure 5.4C. The more dark-red the color is in the heat map, the greater the percent increase in the synaptic weight, and the more dark blue the color is in the heat map, the greater the percent decrease in the synaptic weight. The synaptic weights were rewired by the seizure such that the synaptic projections from the excitatory neurons to the inhibitory neurons in front of the seizure wave were decreased and the synaptic projections from the excitatory neurons to the inhibitory neurons behind the seizure wave front were decreased. This rewiring prevented the inhibitory neurons in front of the seizure from inhibiting the seizure progression through the network.

Then, I applied my “Forced Temporal Spike-Time Stimulation" (FTSTS) protocol to the biophysically constrained neocortical-onset seizure model to determine if my novel stimulation protocol was able to suppress synchronous network spiking activity in a biophysically constrained model. I initiated a seizure by applying the same seizure initiating input for 3 s. After removing the input, the seizure began to propagate thoughout the neocortical network. I applied the inverted FTSTS protocol (see Figure 5.2G) with an amplitude of 2 nA and pulse interval of 10 ms at the 10 sec mark for 5 sec. The FTSTS protocol disrupted the synchronous spiking activity of the

neocortical seizure and terminated the neocortical seizure (see Figure 5.5A). During the rest of the simulation, I observed no additional spontaneous seizures. Figure 5.5B shows the average excitatory-to-inhibitory synaptic weight during the simulation and the induced increase in the average synaptic weight from the inverted FTSTS protocol. The FTSTS protocol increased the strength of all the connections between the excitatory neurons and the inhibitory neurons, which is shown in Figure 5.5E. This increase in the synaptic connections erased the re-wiring of the synaptic connections by the seizure. Therefore, this reduced the predisposition of the neocortical network to rewiring synaptic connection network connections to produce spontaneous seizures. This highlights the ability of my FTSTS protocol to harness the synaptic weight of the neocortical network to suppress the prevalence of spontaneous seizures.

Next, I applied the exact reverse of the inverted FTSTS protocol (i.e standard FTSTS see Figure 5.2A) during the initial seizure. The standard FTSTS protocol was applied for 5 seconds, which was denoted as the green-bar in Figure 5 C. The FTSTS protocol depressed the average E-to-I synaptic weight of the neocortical network by approximately 8 *nS* over the 5 second FTSTS window (see Figure 5.5D). Figure 5.5C shows an increased level of seizure activity in the neocortical network after the FTSTS protocol. After the FTSTS protocol, the duration of the initial seizure was much longer and the second seizure was much larger than the two small seizures observed in Figure 5.4A. The FTSTS protocol decreased the synaptic weight of the excitatory to inhibitory neurons (see Figure 5.5D), which lowered the activation of the inhibitory neurons during the seizure. The lower inhibitory neuron activity prevented the inhibitory neurons from slowing or stopping the neocortical seizure. The final change in the exciatory to inhibitory synaptic weight at the end of the simulation is shown in Figure 5.5F as a heat map. Again, the synapses projecting from the excitatory neurons to the inhibitory neurons in front of the seizure were weakened, while synapses projecting behind the seizure were strengthened. This neural synaptic weight structure made the neocortical network prone to spontaneous in the future. After showing my FTSTS protocol was able to control the average synaptic weight of the neocortical network, I wondered what the best FTSTS parameter would be to control the average E-to-I synaptic weight.

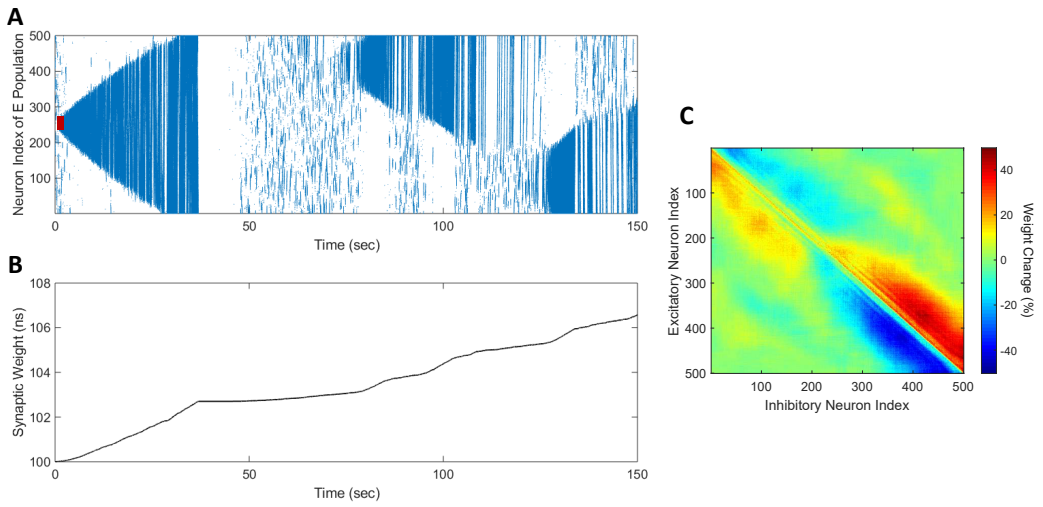

FIGURE 5.4: Propagation of the neocortical seizure though network. A seizure initiating input applied for 3 s (red-bar) to a biophysically constrained neocortical network model initiated a seizure. **(A)** shows the propagation of the initial seizure and the emergence of a second seizure after the first seizure terminated. **(B)** shows the increase in the average synaptic weight during each seizure event. **(C)** shows the percent change in the strength of the excitatory to inhibitory synaptic weight of each synapse at the end of the simulation ($t = 150$ *sec*).

5.3.2 *Effect of Amplitude on FTSTS Efficacy*

Next, I examined the effect of the amplitude of the FTSTS protocol on the efficacy for all four polarities. In the biophysically constrained neocortical-seizure model, I induced a seizure with an input of 200 pA applied for 3 seconds. My FTSTS was applied 6 seconds after the seizure input for a duration 5 seconds, which is shown in Figure 5.4 as the green-bar. I varied the amplitude of the FTSTS protocol from 1 nA to 2.5 nA and measured the change in the average synaptic E-to-I weight before and after the FTSTS protocol. I applied the FTSTS protocol at a frequency of 83 Hz with a pulse width of 1 s and train-offset time of 0 ms. Figure 5.6 shows the measured change in the average E-to-I synaptic weight of the neocortical network for each corresponding FTSTS amplitude. The standard FTSTS protocol increased the magnitude of the negative average synaptic weight rate change over the 5 second FTSTS duration for all amplitudes greater than 1.75 nA. As the amplitude of the FTSTS protocol increased, I observed a larger magnitude of the negative average synaptic weight rate of change, which decreased the average synaptic weight of network more efficiently.

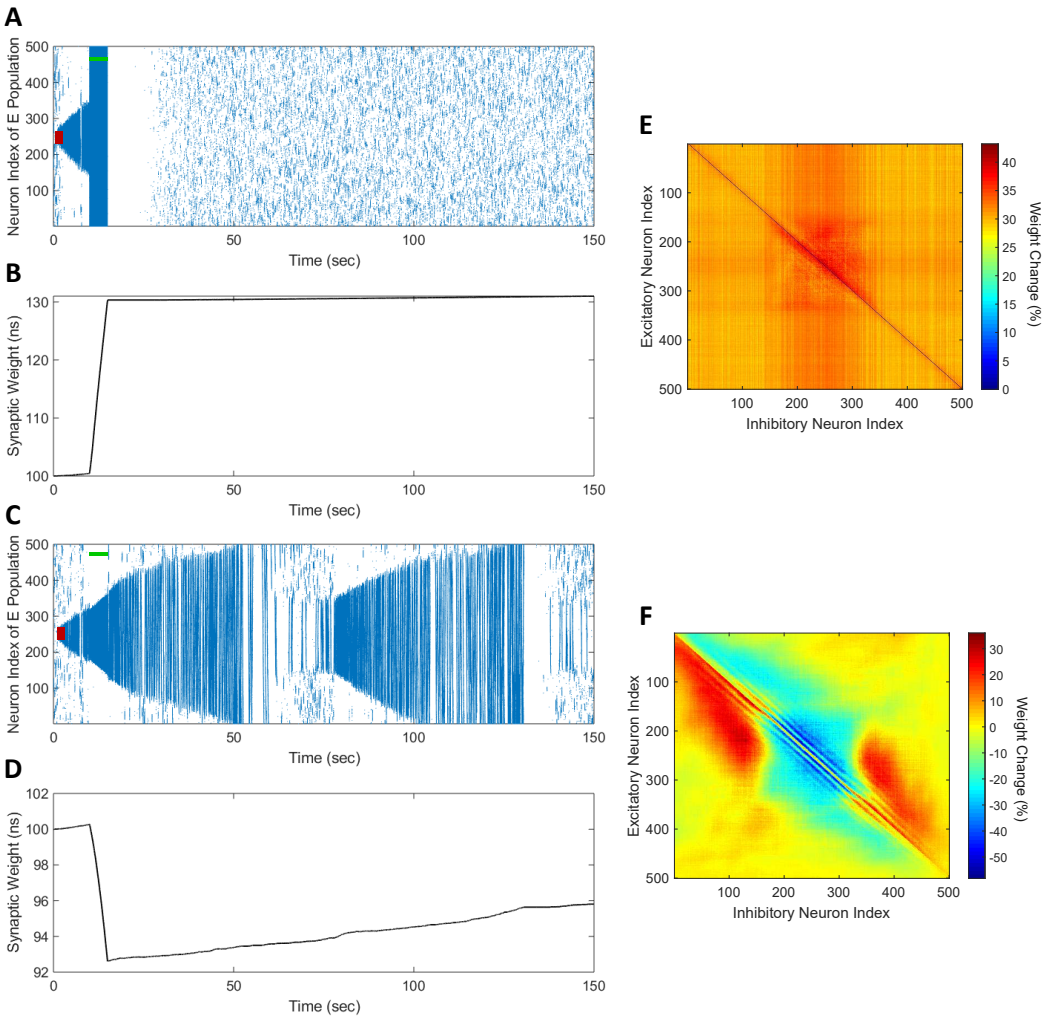

FIGURE 5.5: Control of the spontaneous seizure state with FTSTS. A seizure initiating input applied for 3 s (red-bar) to a biophysically constrained neocortical network model initiated a seizure that begins to propagate through the network. **(A)** shows the suppression of neocortical seizure activity by my FTSTS protocol (green-bar). My FTSTS protocol increased the average synaptic **(B)** while it was applied. **(C)** shows the promotion of spontaneous neocortical seizures by exactly flipping the FTSTS protocol (green-bar). The inverted FTSTS decreased the average excitatory-to-inhibitory synaptic weight in **(D)** over the 5 second duration the protocol was applied. **(E)** and **(F)** show the percent change in the excitatory-to-inhibitory synaptic weights at the end of the simulation ($t = 150$ *sec*) from applying inverted FTSTS and standard FTSTS, respectively.

The increased amplitude forced more neurons to fire in a temporal pattern of post-synaptic neurons before pre-synaptic neurons, which decreased the synaptic strength. Then, I applied the exact opposite polarity of each FTSTS pulse ($a_E = -1$ and $a_I = 1$) in order to determine the efficacy of the FTSTS protocol at increasing the

average synaptic weight of the biophysically constrained model. Figure 5.6 shows the measured increase in the positive average synaptic weight rate change for each inverted standard FTSTS pulse amplitude. The reversed polarities of the pulses forced the presynaptic neurons to fire before the postsynaptic neurons, which resulted in an overall increase in the average synaptic weight of the network.

In addition to the standard FTSTS protocol, I also considered the effect of the amplitude of the FTSTS protocol on the efficacy of two mirrored FTSTS polarities. A mirrored FTSTS protocol delivered pulses to the excitatory and inhibitory populations with the same polarities. I considered two mirrored polarity pairs. The first was the standard mirrored FTSTS polarity pair ($a_E = 1$ and $a_I = 1$). The second was the inverted mirrored FTSTS polarity pair ($a_E = 1$ and $a_I = 1$). The train-offset time was held constant at 0 ms. Therefore, the same pulse train was applied to both neuron populations. Since the mirrored FTSTS protocols provided the same pulse shape to both neuron populations, there was no temporal difference in the spike times induced by FTSTS. As expected, the mirrored and inverted mirrored FTSTS protocols failed to change the average synaptic weight of the network without a train-offset time between the two trains of pulses delivered to the excitatory and inhibitory populations, as shown in Figure 5.4. While mirrored FTSTS without a train-offset failed to induce a change in the average synaptic weight, mirrored FTSTS protocols with a nonzero train-offset time should induce a weight change.

5.3.3 *Effect of Phase Difference and Amplitude on FTSTS Efficacy*

In order to understand how the phase difference in the FTSTS pulse pair effects the efficacy of FTSTS, I varied the train-offset time of the FTSTS protocol at various pulse amplitude for each of the four polarities. The FTSTS protocol was applied six seconds after the end of the seizure initiating input for a duration of five seconds. The rate change in the average synaptic weight was determined by measuring the change in the average E-to-I synaptic weight over the five second window of the FTSTS application. The efficacy was defined as a large change in the rate of the average synaptic weight change over the five second FTSTS application. Again, I varied the amplitude from 1 nA to 2.5 nA and the train-offset time from 0 to 12 ms, while I held the pulse width

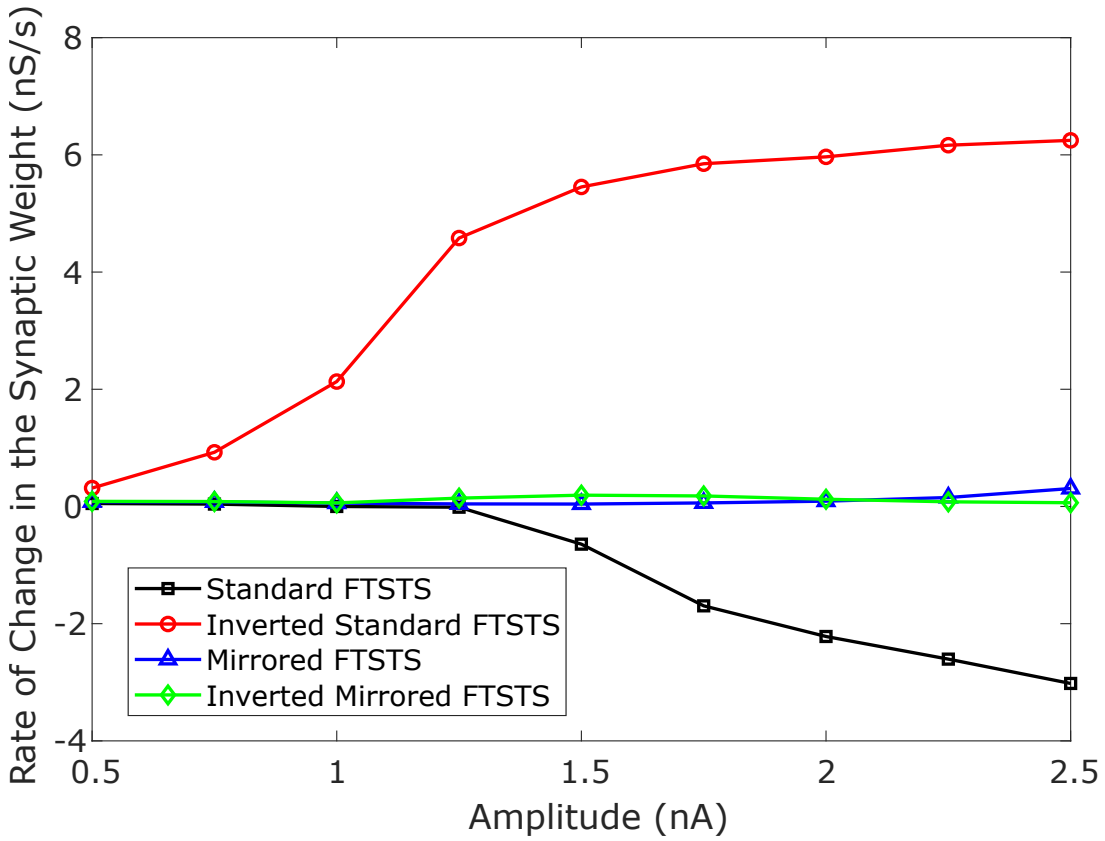

FIGURE 5.6: Effect of amplitude on the FTSTS protocols. The amplitude of the FTSTS protocol was varied from 1 nA to 2.5 nA. I measured the induced change in the average synaptic weight at each pulse amplitude with a standard FTSTS polarity where $a_E = 1$ & $a_I = -1$ (black-square), inverted FTSTS polarity where $a_E = -1$ & $a_I = 1$ (red-circle), mirrored FTSTS polarity where $a_E = 1$ & $a_I = 1$ (blue-triangle), and inverted mirrored FTSTS polarity where $a_E = -1$ & $a_I = -1$ (greed-diamond). The phase difference was held constant ($\Delta\phi = 0$).

and pulse interval constant at 1 ms and 10 ms, respectively. I noted for this constant pulse width and pulse interval that the train-offset time completes a cycle every 12 ms. Thus, a train-offset time of 0 ms was equal to a train-offset time of 12 ms and a train-offset time of -1 ms was equal to a train-offset time of 11 ms. This allowed me to construct a surface plot of the full train-offset cycle vs pulse amplitude for each pulse-pair polarity.

First, I considered the standard FTSTS polarity. The general trend observed in the previous section that the efficacy increased with the amplitude was observed at each train-offset time. Figure 5.7A shows the surface plot of the effect of the amplitude versus the train-offset time on the magnitude of the average synaptic weight change

(efficacy). I observed an optimal train-offset time of -11.5 *ms* (0.5 *ms*) to decrease the average synaptic weight and an optimal train-offset time of -10 *ms* (2 *ms*) to increase the average synaptic weight of the network. A train-offset time of 0.5 *ms* (-11.5 *ms*) for the standard FTSTS polarity occurred when the positive portion of the inhibitory population pulse began 0.5 *ms* before the positive portion of the excitatory population pulse. This forced small positive spike-time difference between the presynaptic inhibitory neurons and postsynaptic excitatory neurons. Small positive spike-time differences resulted in a decrease in the average synaptic weight. Based on this result, one would expect the best train-offset time to increase the synaptic weight to be 1.5 *ms* (10.5 *ms*), which would correspond to the positive portion of the excitatory population pulse starting 0.5 *ms* before the positive portion of the inhibitory population pulse. This predicted best train-offset time was not observed. I observed the best train-offset time to increase the average synaptic weight was 2 *ms* (-10 *ms*). A possible reason for this deviation was that I defined the positive polarity as beginning with the negative portion of the biphasic pulse followed by the positive portion. Therefore, the positive portion of the excitatory population pulse must overcome the inhibition of the excitatory neuron population by the negative portion of the pulse, which resulted in a slower response of the excitatory neurons. This required the inhibitory neurons to be stimulated a little later to achieve a more favorable temporal spike-time pattern between the excitatory and inhibitory populations. Since the inhibitory population pulse had a negative polarity, the positive portion of the pulse led the negative portion. Therefore, the positive portion of the biphasic pulse did not have to overcome any inhibition of the neuron population by its negative counterpart. While my exploration of the amplitude and train-offset time parameter space highlighted the best amplitude and train-offset parameters to decrease or increase the average synaptic weight of the network, it also highlighted the importance of the FTSTS pulse polarity.

Then, I considered the exact opposite pulse polarity of the standard FTSTS protocol. This polarity was called inverted standard FTSTS and is shown in Figure 5.2C. I examined the full train-offset time cycle for this polarity at various pulse amplitudes. Over the five second window that the FTSTS protocol was applied, I measured the rate of change in the synaptic weight. Figure 5.7C shows the surface

plot of how the train-offset time and the pulse amplitude affect the rate of change in the synaptic weight. For all the train-offset time, the efficacy of the FTSTS protocol increased with the increase in amplitude. The most effective train-offset time to increase the synaptic weight was -0.5 ms (11.5 ms) and to decrease the synaptic weight was -2 ms (10 ms). Again, the lack of symmetry in the best train-offset time was observed for the inverted standard FTSTS polarity. The pulses delivered to the inhibitory population led with the negative portion of the biphasic pulse. Therefore, the positive portion of the biphasic pulse must overcome this initial inhibition, which created a delay in the evoked spike-times. If the inhibitory population was required to fire before the excitatory population, the train-offset time must increase to accommodate for the delay in spike-times. The asymmetry in the optimal spike-times underscores the importance of the polarities of the FTSTS pulse.

In order to further examine the role that polarity plays in the efficiency of the FTSTS protocol, I examined the remaining two polarity pair combination where the polarities were the same for each neuron population pulse. The two polarity pairs considered were the mirrored FTSTS ($a_E = 1$ and $a_I = 1$) and the inverted mirrored FTSTS ($a_E = -1$ and $a_I = -1$). I examined the effect of the train-offset time and pulse amplitude on the efficacy of both protocols, which was measured as the rate of change in the average synaptic weight. Figures 5.7B and 5.7D show the surface plot of the efficacy at various train-offset times and pulse amplitudes for the mirrored and inverted mirrored FTSTS polarities, respectively. In both figures, the efficacy of the FTSTS protocol increased with the increase in the pulse amplitude. The most effective train-offset times was -0.5 ms (11.5 ms) to increase the synaptic weight and -11.5 ms (0.5 ms) to decrease the synaptic weight for both polarities. Unlike the previous two cases, the optimal train-offset time was symmetric, since the positive polarity spike-time delay occurred in both pulses for the mirrored polarity. The most effective out of these two polarities was the inverted mirrored. While the mirrored FTSTS protocol had symmetric optimal train-offset time, the leading negative portion of the biphasic pulse still inhibited the response of both neuron populations to the positive portion of the biphasic pulse that followed it. The inverted mirrored FTSTS pulse began with the

positive portion of the biphasic pulse so the protocol could more efficiently force the neurons to fire in a temporally specific pattern to control the average synaptic weight.

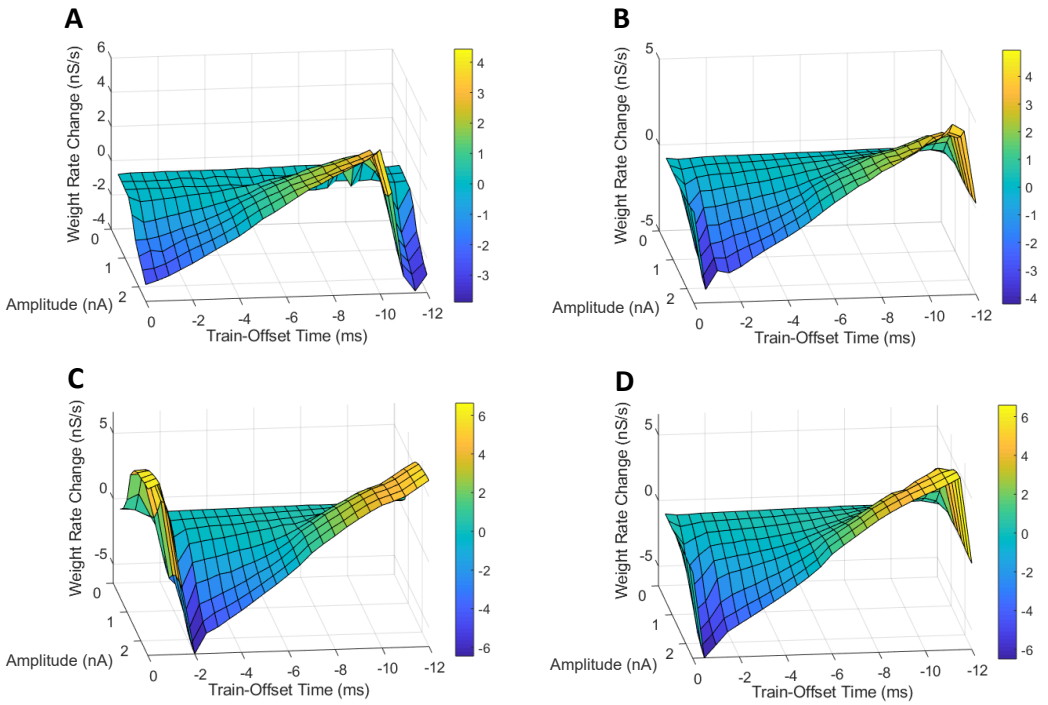

FIGURE 5.7: Efficacy of train-offset time and amplitude on FTSTS. The efficacy of the FTSTS was measured for various amplitudes and phase differences. The change in the average synaptic weight from the 5 seconds application of the FTSTS protocol during a seizure (see Figure 5.4). The effect of the amplitude and phase difference of the FTSTS protocol for the four possible polarities **(A)** the standard FTSTS polarity ($a_E = 1$ and $a_I = -1$), **(B)** mirrored FTSTS polarity ($a_E = 1$ and $a_I = 1$), **(C)** inverted standard FTSTS polarity ($a_E = -1$ and $a_I = 1$), and **(D)** inverted mirrored FTSTS polarity ($a_E = -1$ and $a_I = -1$) on FTSTS efficacy were considered.

5.3.4 *Effect of Frequency on FTSTS Efficacy*

Next, I examined the effect of stimulation frequency on the efficacy of the FTSTS protocol at different train-offset times and polarity pairs. The FTSTS protocol was applied for a 5 second duration, which was applied 6 seconds after the seizure initiating input. The rate of change in the average synaptic weight was measured over the 5 second window to obtain the efficacy. I considered six different inter pulse intervals (5 ms, 10 ms, 20 ms, 30 ms, 40 ms, 50 ms, and 100 ms) that were inversely related to the stimulation frequency (143 Hz, 83 Hz, 45 Hz, 31 Hz, 24 Hz, 19 Hz,

and 9.8 Hz). Furthermore, I examined how the different frequencies interacted with different train-offset times between -3.5 ms to 3.5 ms to influence the efficacy of the FTSTS protocol, while the pulse width and pulse amplitude were held constant at 1 ms and 2 nA.

We began by examining the effect of the stimulation frequency on the standard FTSTS protocol. The effect of train-offset time and frequency on the synaptic weight rate change for the standard FTSTS polarity is shown in Figures 5.8A. In general, an increase in the frequency increased the efficacy of the FTSTS protocol. The exception to this trend occured at the two highest frequencies for all train-offset times expect 1.5 ms and 0.5 ms. When the frequency was increased from 83 Hz to 143 Hz, the efficacy decreased at these higher magnitude train-offset times. The highest frequency that I considered was 143 Hz, which corresponds to a pulse interval of 5 ms. The short pulse interval forced a presynaptic-before-postsynaptic neuron spike-time difference and also a postsynaptic-before-presynaptic neuron spike-time differences. These two spike-time difference were within a few ms of each other at the shorter pulse interval. For example, consider a train-off-set time of 0 ms for the standard FTSTS polarity with a pulse interval of 5 ms shown in Figure 5.8A. This protocol attempts to force a presynaptic before postsynaptic neuron spike time difference of 1 ms but it also induces a postsynaptic before presynaptic neuron spike time difference of 5 ms at this pulse interval. The close values of the spike-time difference counteract each other and reduce the rate of the synaptic E-to-I weight is increases or decreases. At lower frequencies, there was a larger difference between the presynaptic before postsynaptic neuron spike times and the postsynaptic before presynaptic neuron spike times. Out of the pulse intervals that I considered, the optimal pulse interval was 10 ms, which balanced the increased efficacy from the more desired forced spike time difference and decreased efficacy from the undesired forced spike time difference at higher frequencies. At the best train-offset time observed in the previous section, the best train-offset time to increase the average synaptic weight was 2 ms at the highest pulse interval 10 ms but at the higher pulse intervals the best train offset-time was 1.5 ms. This difference in best train-offset times was most likely due to the undesired induced spike time difference counteracting the protocol more with the shorter train-offset

time (5 *ms*). I observed the same best train-offset time of 0.5 *ms* to decrease the average synaptic weight at the higher stimulation frequency. Therefore, the best pulse interval and train-offset time for the standard FTSTS polarity to increase the average synaptic weight was 10 *ms* (83 *Hz*) and 2 *ms*, respectively. Additionally, the optimal pulse interval and train-offset time to decrease the average synaptic weight was 5 *ms* (142 *Hz*) and 0.5 *ms*, respectively.

Next, I examined the effect of the frequency and the train-offset time on the efficacy of the inverted standard FTSTS protocol. Figure 5.8C shows the average E-to-I synaptic weight change at different frequency and train-offset times for the inverted standard FTSTS polarity. The efficacy of the FTSTS protocol increased with the frequency of stimulation except at the highest two frequencies. At the highest two frequencies, the efficacy decreased for all train-offset times when the frequency was increase from 83 *Hz* (pulse interval of 10 *ms*) to 143 *Hz* (pulse interval of 5 *ms*). Again, this is due to the undesired forced spike-times counteracting the desired forced spike-time difference at the shorter pulse interval. The optimal pulse interval and train-offset time for the inverted standard FTSTS polarity to increase the average synaptic weight was 10 *ms* (83 *Hz*) and -0.5 *ms*, respectively. Furthermore, the optimal pulse interval and train-offset time to decrease the average synaptic weight was 10 *ms* (83 *Hz*) and -2 *ms*, respectively.

Then, I analyzed the effect of frequency and train-offset time on the efficacy of the mirrored FTSTS protocol. Figure 5.8B shows that the efficacy of the FTSTS protocol increases with the frequency except for the two highest frequencies. I observed a decrease in the average synaptic weight rate change when the frequency was increased from 83 *Hz* (pulse interval of 10 *ms*) to 143 *Hz* (pulse interval of 5 *ms*) for all train-offset times except -0.5 *ms* and 0.5 *ms*. This corresponds to the positive portion of the inhibitory biphasic pulse arriving half of a millisecond before and after the positive portion of the excitatory biphasic pulse. I observed the same trend for the standard FTSTS polarity. The general decrease in the efficacy of the FTSTS protocol going from a pulse interval of 10 *ms* to 5 *ms* was from the undesired forced spike-time difference between the two neuron populations counteracting the desired forced spike-time difference at the lower pulse interval. Two exceptions to this trend occurred

when the difference between desired and undesired forced spike-times of the two neuron populations was the greatest (-0.5 *ms* and 0.5 *ms*). The optimal pulse interval and train-offset time for the mirrored FTSTS polarity to increase the average synaptic weight was 5 *ms* (142 *Hz*) and 0.5 *ms*, respectively. Additionally, the optimal pulse interval and train-offset time to decrease the average synaptic weight was 10 *ms* (83 *Hz*) and -0.5 *ms*, respectively.

Finally, I considered the effect of frequency and train-offset time on the efficacy of the inverted mirrored FTSTS protocol. The effect of frequency and train-offset time on average synaptic weight rate change is shown in Figure 5.8D. The magnitude of the average synaptic weight rate change (efficacy) increased with the stimulation frequency up to a frequency of 83 *Hz*. I observed when the frequency was increased from 83 *Hz* to 142 *Hz* the efficacy decreased for all train-offset times. Similar to the other three polarities, this occurred due to the induced undesired forced spike-times counteracting the desired forced spike-time difference at the shorter pulse interval (higher frequency). For the inverted mirrored FTSTS protocol, the optimal pulse interval and train-offset time to increase the average synaptic weight was 10 *ms* (83 *Hz*) and 0.5 *ms*, respectively. Additionally, the optimal pulse interval and train-offset time to decrease the average synaptic weight was 10 *ms* (83 *Hz*) and -0.5 *ms*, respectively.

I examined the role frequency and train-offset time played in influencing the efficacy of the FTSTS protocol for all four polarities (see Figure 5.8). In general, an increase in the stimulation frequency increased the efficacy except at the highest frequencies. Additionally, at the highest frequency there were less deviations from this trend with the inverted polarities. Clearly, this established the best polarity of the excitatory population biphasic pulse as $a_E = -1$. A possible reason for this observation is that the negative polarity begins with the positive portion of the biphasic pulse. Therefore, the pulse can more quickly force the neurons in the excitatory population to fire, since it is not required to overcome any inhibition from the negative portion of the biphasic pulse. These results highlight the importance of the ability of FTSTS to force the neurons to fire during the positive portion of the biphasic pulse. Therefore, optimizing the remaining FTSTS parameter, pulse width, may further increase the efficacy of the protocol.

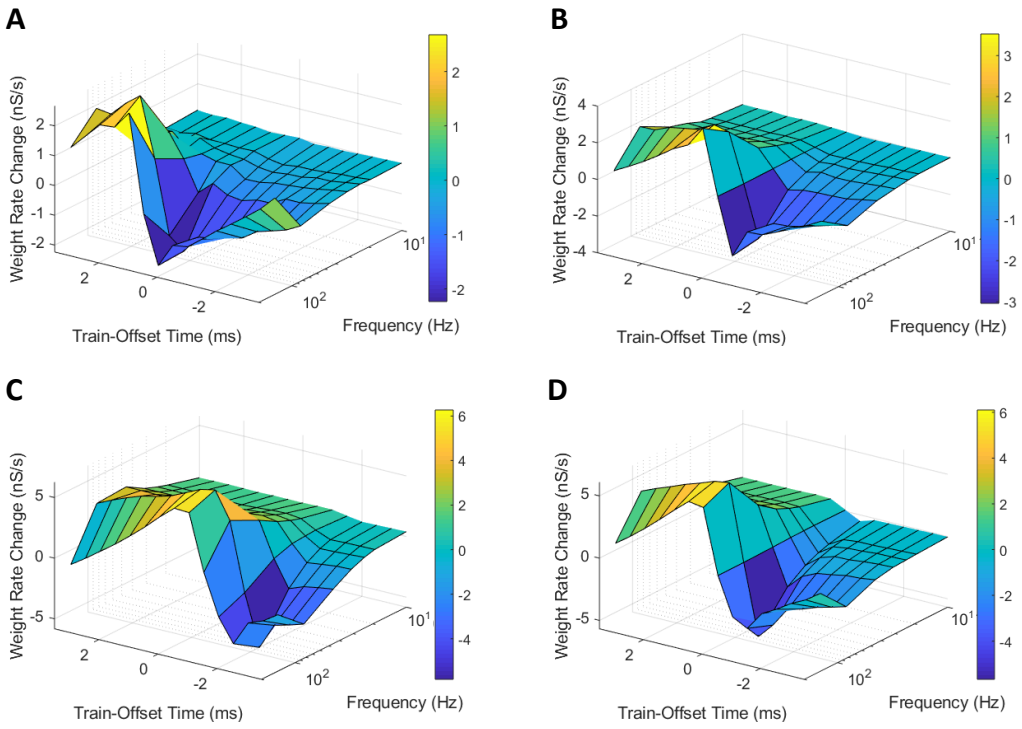

FIGURE 5.8: Efficacy of frequency and train-offset time on FTSTS. I measured the efficacy of the FTSTS protocol at different frequencies, train-offset times, and polarity pairs. The efficacy was measured as the rate of change in the average synaptic weight over the 5 second interval the FTSTS was applied for the **(A)** standard ($a_E = 1$ and $a_I = -1$), **(B)** mirrored ($a_E = 1$ and $a_I = 1$), **(C)** inverted standard ($a_E = -1$ and $a_I = 1$), and **(D)** inverted mirrored ($a_E = -1$ and $a_I = -1$) FTSTS protocols.

5.3.5 *Effect of Pulse Width on FTSTS Efficacy*

Finally, I examined the effect of the pulse width and train-offset time on the efficacy of the FTSTS protocol for all four FTSTS polarities. I applied the FTSTS protocol six seconds after the seizure initiating input ended for a duration of five seconds. I considered the pulse width values ranging from 1 ms to 5 ms and the train-offset times between -10 ms to 10 ms . The average excitatory-to-inhibitory synaptic weight at the start and end of the 5 second window were used to determine the synaptic weight rate change induced by the selected parameters. The synaptic weight rate change over the FTSTS application window was used to determine the efficacy of the chosen parameters, such that large magnitude synaptic weight changes indicated more efficient FTSTS parameters.

First, I analyzed the efficacy of the pulse width and train-offset time for the standard FTSTS protocol ($a_E = 1$ and $a_I = -1$). For each pulse width, Figure 5.9A shows a clear most effective train-offset time to increase or decrease the average synaptic weight. In general, the best train-offset time to increase the average synaptic weight occurred at $W + 1$ *ms*, where W is the pulse width. This timing attempted to force the excitatory neurons to fire 1 *ms* before the inhibitory neurons by delivering the positive portion of the biphasic pulse to the excitatory population 1 *ms* before the positive portion of the pulse delivered to the inhibitory population. The exception to this general train-offset timing pattern occurred at pulse widths greater than 3 *ms*. For pulse widths of 4 *ms* and 5 *ms*, the best train-offset time occurred at 8 *ms*. This resulted in a majority or all of the positive portion of the biphasic pulse delivered to the excitatory neurons arriving before the positive portion of the biphasic pulse delivered to the inhibitory population. Therefore, the excitatory neurons were forced to firing before the inhibitory neurons. The optimal pulse width to increase the synaptic weight was 2 *ms* with a train-offset time of 3 *ms*. I then considered the best parameters to decrease the average synaptic weight. There existed a clear optimal train-offset time for each pulse width to decrease the average synaptic weight. The best train-offset time was 0.5 *ms* for a pulse width of 1 *ms*, while all pulse widths greater than 1 *ms* had a train-offset time equal to the pulse width. For pulse widths greater than 1 *ms*, this resulted in the positive portion of the biphasic pulses delivered to both the excitatory and inhibitory populations arriving at the same time. Since the pulses delivered to each population had the opposite polarity, the negative portion arrived before the positive portion of the biphasic pulse delivered to the excitatory population, and the negative portion of the biphasic pulse delivered to the inhibitory population arrived after the positive portion. This resulted in the excitatory neurons responding slower to the excitatory portion of the pulse and the inhibitory neurons responding faster. It allowed the inhibitory neurons to fire before the excitatory neurons, while still forcing the excitatory neurons to fire after the inhibitory neurons with the additional inhibitory input. The optimal pulse width and train-offset time to decrease the average synaptic weight was 2 *ms* and 2 *ms*, respectively.

Then, I examined the efficacy of the pulse width and train-offset time of the inverted standard FTSTS polarity ($a_E = -1$ and $a_I = 1$). The best train-offset time at each pulse width to increase or decrease the average synaptic weight is shown in Figure 5.9C as the peak or trough, respectively. The efficiency of the inverted standard FTSTS protocol decreased with the pulse width for both increasing and decreasing the average synaptic weight. The trend of the best train-offset time for each pulse width to increase the average synaptic weight was $-W + 0.5\ ms$, where W is the pulse width. This resulted in the positive portion of the biphasic pulses delivered to the excitatory population arriving $0.5\ ms$ before the positive portion delivered to the inhibitory population. Due to the opposite polarities of the pulses delivered to each population, the negative portion of the biphasic pulse arrived before the positive portion of the pulse. This prevented the inhibitory neurons from firing before the excitatory neurons. Additionally, the negative portion of the biphasic pulse delivered to the excitatory population arrived mostly after the positive portion was delivered to the inhibitory population, which prevented the excitatory neurons from firing after the inhibitory neurons. The optimal train-offset time to decrease the synaptic weight followed a general trend of $-W - 1\ ms$ for pulse widths less than $4\ ms$ and a trend of $W - 1.5\ ms$ for pulse widths greater than or equal to $4\ ms$. For pulse widths less than $4\ ms$, the positive portion of the biphasic pulse delivered to the inhibitory population arrived $1\ ms$ prior to the positive portion delivered to the excitatory population. As the pulse width increased, the best train-offset time decreased to $-W - 1.5\ ms$. This may result from the increased inhibition of the inhibitory neurons by the negative portion of the biphasic pulse as the pulse width increased, which the positive portion of the biphasic must overcome to force the inhibitory neurons to fire. Therefore, the inhibitory neurons responded slower and required a larger gap between when the excitatory and inhibitory neurons are stimulated to ensure that most of the inhibitory neurons fire before the excitatory neurons.

Next, I determined the efficacy of the pulse width and train-offset time on the efficacy of the mirrored FTSTS polarity ($a_E = 1$ and $a_I = 1$). The symmetric polarities result in best train-offset times to increase or decrease the average synaptic weight that were the same across all pulse widths as shown in Figure 5.9B. The best train-offset

time to increase the synaptic weight for all pulse widths was 1 *ms*. This resulted in the positive portion of the biphasic pulse delivered to the excitatory neurons arriving 1 *ms* before the positive portion delivered to the inhibitory population. Due to the symmetry of the polarity, the neurons consistently responded to the positive portion of the pulse train in both of the neuron populations. The optimal pulse width and train-offset time to increase the average synaptic weight was 2 *ms* and 1 *ms*, respectively. Additionally, the best train-offset time for all pulse widths to decrease the synaptic weight was -0.5 *ms*. In this case, the positive portion of the biphasic pulse delivered to the inhibitory population arrived 0.5 *ms* before the portion delivered to the excitatory neurons. Again, the symmetry of the polarities ensured the neurons in both of the populations responded on the same timescale. The optimal pulse width and train-offset time to decrease the average syanptic weight of the network was 2 *ms* and -0.5 *ms*, respectively.

Finally, I analyzed how the pulse width and train-offset time parameters influenced the efficacy of the inverted-mirrored FTSTS protocol ($a_E = -1$ and $a_I = -1$). The surface plot of the change in average synaptic weight for the different parameter combinations of pulse width and train-offset time is shown in Figure 5.9D. The efficacy of the inverted FTSTS protocol decreased with the increase in the pulse width for both increasing and decreasing the synaptic weight. For pulse widths between 1 *ms* and 3 *ms*, the best train-offset time was 0.5 *ms*. The symmetric polarities results in the positive portion of the biphasic pulse delivered to the excitatory population arriving 0.5 *ms* before the positive portion delivered to the inhibitory population. Also, the negative portion following the positive portion of the biphasic pulse prevented unwanted neuron firing in both populations after forcing the neurons to fire. At the longer pulse widths considered, the train-offset times for a pulse width of 4 *ms* and 5 *ms* was 3.5 *ms* and 3 *ms*, respectively. These train-offset times result in a majority of the positive portion of the biphasic pulse delivered to the excitatory population arriving before the positive portion delivered to the inhibitory population. This may be due to the longer pulse width forcing unwanted firing when the positive portions of the the biphasic pulse overlapped, which occurred less at shorter pulse widths due to the 2 *ms* refractory period. The best train-offset times to

decrease the average synaptic weight was -0.5 *ms* for all pulse widths. This resulted in the positive portion of the biphasic pulse delivered to the inhibitory population arriving 0.5 *ms* before the positive portion delivered to the inhibitory population for all pulse widths. Due to the inhibitory input to the excitatory neurons resulting from the forcing the inhibitory neurons to fire, there was less unwanted firing when the positive portions of the biphasic pulses delivered to each population overlapped. Additionally, the negative portion of the biphasic pulse prevented unwanted firing in both populations, after forcing the neurons of the opposite population to fire. The optimal train-offset time and pulse width to decrease the average synaptic weight was -0.5 *ms* and 1 *ms*, respectively.

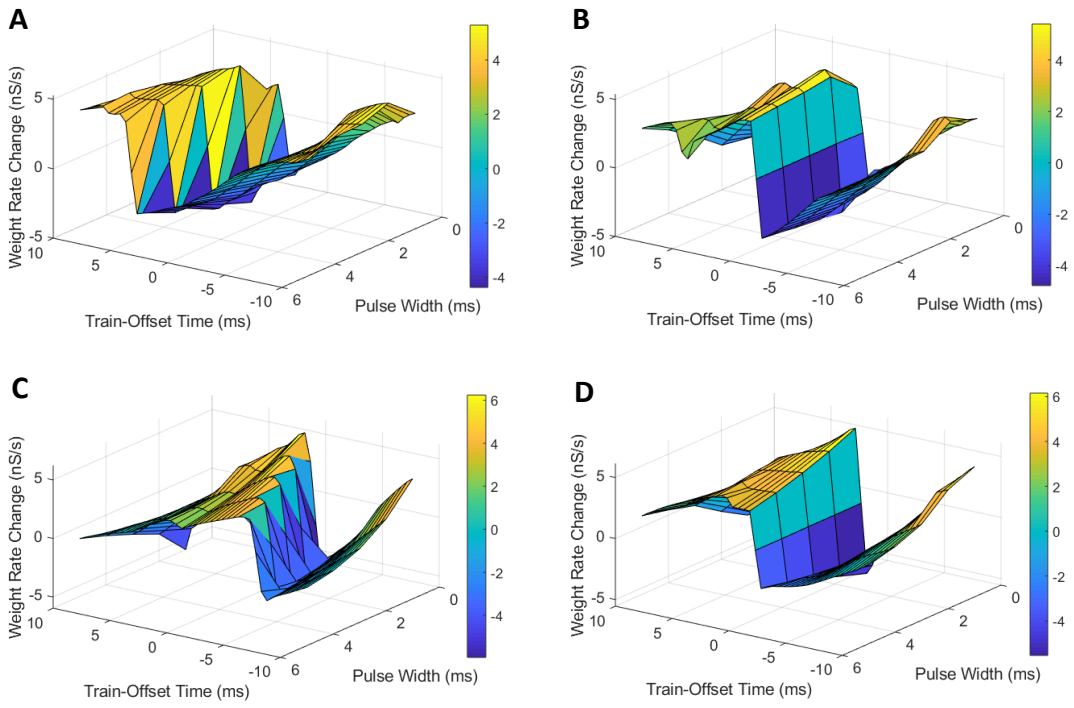

FIGURE 5.9: Efficacy of pulse width and train-offset time on FTSTS. I measured the efficacy of the FTSTS protocol at different pulse widths, train-offset times, and polarity pairs. The efficacy was measured as the rate of change in the average synaptic weight over the 5 second interval the FTSTS was applied for the **(A)** standard ($a_E = 1$ and $a_I = -1$), **(B)** mirrored ($a_E = 1$ and $a_I = 1$), **(C)** inverted standard ($a_E = -1$ and $a_I = 1$), and **(D)** inverted mirrored ($a_E = -1$ and $a_I = -1$) FTSTS protocols.

5.3.6 *Best FTSTS Parameters*

After examining the effect of amplitude, pulse interval and pulse width in combination with train-offset time on the efficacy of different polarities of FTSTS protocol, I determined the best FTSTS parameters. The optimal parameters to increase the average synaptic weight were a pulse interval of 10 ms, a pulse width of 1 ms, an inverted standard FTSTS polarity of ($a_E = -1$ and $a_I = 1$), and a train-offset time of -0.5 ms for an amplitude of 2 nA. While I could have chosen a higher amplitude, I chose 2 nA, since the rate of change in the average synaptic weight to increase the synaptic weight plateaued at higher amplitudes. Additionally, an amplitude of 2 nA induced a substantial decrease in the average synaptic weight when I applied the opposite polarity. Since the primary goal was to increase the synaptic weight to stop the neocortical seizure, I chose a pulse amplitude of 2 nA for the FTSTS protocol to increase and decrease the synaptic weight. The best parameters to decrease the average synaptic weight were a pulse interval of 10 ms, a pulse width of 1 ms, an inverted standard FTSTS polarity of ($a_E = -1$ and $a_I = 1$), and a train-offset time of -2 ms. I applied the FTSTS protocol to my biophysically constrained neocortical-onset seizure model with the best parameters to increase and decrease the average synaptic weight as shown in Figure 5.10. Both FTSTS protocol were applied at the 10 sec mark for 5 sec. Figure 5.10A shows after I applied the FTSTS protocol the initial seizure stopped and no further seizure activity was observed for the rest of the simulation. The FTSTS protocol increased the average synaptic weight while it was applied, which is shown in Figure 5.10B. I then applied the FTSTS protocol to decrease the average synaptic weight. Figure 5.10C shows the raster plot of the simulation where the FTSTS was applied and initially stopped the seizure. Shortly after the first seizure was prevented, very strong entire network seizures began to emerge. These full seizures continued to spontaneously occur for the rest of the simulation. The optimal FTSTS protocol decreased the average synaptic weight 30 nS over the 5 sec FTSTS duration (see Figure 5.10D).

5.3.7 *Integration of the FTSTS with Optogenetic Techniques*

One potential physical constraint of my FTSTS protocol is the requirement that the excitatory and inhibitory neuron populations are spatially separable and can be selectively stimulated, which may be difficult for the neocortical excitatory and inhibitory neurons. In order to address this physical constraint, I inserted two different optogenetic channelrhodopsins into the excitatory and inhibitory neurons. Then, I examined how the spatially selective optogenetic stimulation of the different neuron population could be integrated into my FTSTS protocol to control the average E-to-I synaptic weight and the seizure activity of the network. The two channelrhodopsins that I considered were Chronos and Chrimson, which were shown to selectively respond to blue (460 *nm*) and red (625 *nm*) light, respectively (Klapoetke *et al*., 2014). A schematic of the optogenetic set-up is shown in Figure 5.11A where the channelrhodopsin Chronos was inserted into the excitatory neurons and the channelrhodopsin Chrimson was inserted into the inhibitory neurons. Then, each neuron population was spatially and temporally stimulated with different light wavelengths turned on for 4 *ms*. After incorporating the optogenetic dynamics into each neuron population, I integrated the optical stimulation of the two neuron population with my FTSTS.

First, I integrated the optogenetic stimulation of the excitatory and inhibitory neurons with my FTSTS to increase the average E-to-I synaptic weight of the network and to decrease the prevalence of spontaneous neocortical seizures in the future. In order to incorporate my FTSTS with the optogenetic stimulation, I stimulated the excitatory neurons with a blue light applied 2 *ms* before stimulating the inhibitory neurons with the red light, which increased the average E-to-I synaptic weight. The red and blue lights were both turned on for a 2 ms duration. The blue and red light pulses were applied at a frequency of 5 Hz. Again, I initiated a seizure with a seizure initiating input applied for 3 *sec* shown as the red-square in Figure 5.11B. Then, I applied the optogenetic FTSTS protocol at 10 *sec* for a 10 *sec* duration. The optogenetic FTSTS was less efficient than direct stimulation with the biphasic electrical pulse trains so the protocol required a 10 *sec* stimulation duration to increase the average synaptic

weight by at least 15 *nS*, which is shown in Figure 5.11C. After the optogenetic FTSTS, I did not observe any spontaneous seizures for the rest of the simulation (see Figure 5.11B). Therefore, the integration of optogenetic techniques into my FTSTS protocol was able to overcome spatial constraints of the FTSTS protocol in the neocortex and to prevent the emergence of spontaneous seizures.

After showing that the integration of the optogenetic technique into my FTSTS protocol was able to increase the average synaptic E-to-I weight of the network, I examined whether the optogenetic FTSTS protocol would also be able to decrease the average E-to-I synaptic weight of the network and increase the prevalence of spontaneous seizures. Since the Chrimson channelrhodopsin dynamics were much slower than the Chronos channelrhodopsin dynamics, I swapped which channelrhodopsin was inserted into the excitatory and inhibitory neuron populations. In order to decrease the average synaptic, the Chronos channelrhodopsin was inserted into the inhibitory population and the Chrimson channelrhodopsin was inserted into the excitatory population. I was required to flip which channelrhodopsin was inserted into each population because the slower Chrimson dynamics caused unwanted neuron firing after optically stimulating the Chronos channelrhodopsin. Then, I initiated a seizure with a seizure initiating input (red-box) and applied the optogenetic FTSTS protocol at 10 *sec* for a 40 *sec* duration as shown in Figure 5.11D. The optogenetic FTSTS protocol stimulated the inhibitory neurons with blue (470 *nm*) light 2 *ms* before stimulating the excitatory neurons with red (625 *nm*) light. I applied the optogenetic FTSTS protocol for 40 *sec* to decrease the average synatpic weight by 15 *nS* as shown in Figure 5.11E. After the FTSTS protocol, very strong seizures across the entire neocortical network emerged for the rest of the simulation. This highlights the ability of the optogenetic FTSTS to spatially and temporally selectively stimulation the excitatory and inhibitory neurons to not only increase the synaptic weight but also decrease the average synaptic weight of the network.

5.4 SUMMARY

In this chapter, I determined the optimal parameters of my previously developed "Forced Temporal Spike-Time Stimulation" (FTSTS) protocol to control the average E-to-I synaptic weight of a biophysically constrained neocortical-onset seizure model. Previously, I showed that my FTSTS protocol was able to effectively control the average synaptic weight and as a consequence the synchronous state of a generic excitatory-inhibitory spiking neuron network (Schmalz and Kumar, 2019). Here, I showed my FTSTS protocol was able to control the average synaptic weight of the neocortical-onset seizure model in order to effectively stop seizures and prevent further spontaneous seizures (see Figure 5.5A). When I flipped the polarities of my FTSTS protocol, it increased the prevalence of spontaneous seizures (see Figure 5.5C). After showing that my FTSTS protocol was able to control the average excitatory-to-inhibitory synaptic weight in the neocortical model, I explored the effect of the FTSTS pulse parameters, such as amplitude, train-offset time, frequency, pulse width, and the pulse polarities, on the efficacy of the FTSTS protocol. I determined that the optimal FTSTS parameters to increase the average synaptic weight were a pulse interval of 10 ms, a pulse width of 1 ms, an inverted standard FTSTS polarity of ($a_E = -1$ and $a_I = 1$), and a train-offset time of -0.5 ms. Additionally, I found the optimal FTSTS parameters to decrease the average synaptic weight were a pulse interval of 10 ms, a pulse width of 1 ms, an inverted standard FTSTS polarity of ($a_E = -1$ and $a_I = 1$), and a train-offset time of -2 ms. Finally, I integrated two different channelrhodopsin Chronos and Chrimson into the excitatory and inhibitory neuron populations, respectively, in order to address physical spatial constraints of stimulating the excitatory and inhibitory neuron population separately. I showed that the optogenetic FTSTS protocol was able to effectively increase and decrease the average synaptic weight of the biophysically constrained neocortical model.

Throughout my investigation of the parameter space of my recently developed FTSTS protocol (Schmalz and Kumar, 2019), train-offset time induced the largest changes in the excitatory-to-inhibitory synaptic weights. As the train-offset time between the two pulses delivered to the excitatory and inhibitory neuron populations was shifted, the efficiency and outcome of the FTSTS protocol drastically changed.

For example in Figure 5.7A, when the train-offset time is shifted by 1.5 *ms* from 0.5 *ms* to 2 *ms*, the effect of the FTSTS protocol flipped from decreasing to increasing the excitatory-to-inhibitory average synaptic weight. Since the FTSTS protocol is based on controlling the spike-times of the two neuron populations, it follows that slightly shifting the off-set times between the two pulse trains will have a significant effect on the outcome of the stimulation protocol. This result has broader implications to already existing desynchronizing stimulation protocol, such as coordinated reset (Tass, 2003a,b) and deep brain stimulation (DBS) (Fisher *et al*., 2010; Zangiabadi *et al*., 2019; Krauss *et al*., 2020). While it was shown in (Schmalz and Kumar, 2019) that integration of the FTSTS protocol into coordinate reset could improve the desynchronization protocol, these results showed that off-setting stimulation trains of the different stimulating electrodes may further improve the efficacy of the desynchronization protocol by forcing spiking patterns in different neural population that result in the long-term desynchronization of the synchronous neural network. Additionally, if multiple high frequency stimulation (HFS) stimulating electrodes were inserted into separate neural populations for DBS, then offsetting the pulse trains of each electrode may improve neurostimulation therapies for already FDA approved diseases, such as epilepsy (Zangiabadi *et al*., 2019) and Parkinson's Disease(Krauss *et al*., 2020).

The investigation into the effect of the pulse interval (stimulation frequency) parameter on the efficacy of the FTSTS protocol highlighted how smaller pulse intervals (or higher stimulation frequencies) improved the efficacy of the protocol. One exception I observed to this trend occurred when the pulse interval was decreased from 10 *ms* (83 *Hz*) to 5 *ms* (142 *Hz*). Here, the efficacy generally decreased, since the lower pulse intervals (higher stimulation frequencies) produced an undesired spike-time pattern that counteracted the desired spike-time temporal pattern. While the optimal FTSTS protocol pulse interval was 10 *ms*, large pulse intervals (lower frequencies) were still able to control the excitatory-to-inhibitory synaptic weight. These lower frequencies might be more desirable in experiments or potentially in neurostimulation devices for epileptic patients, since lower frequencies may produce fewer side effects. Furthermore, if my protocol were used to stop and prevent seizures in *in vivo* experiments or in patients, the pulse interval

(stimulation frequency) parameter could be used in a closed-loop control protocol to oppose quickly or slowly changes synaptic weights with higher or lower frequencies, respectively.

Generally, I found that the parameters pulse amplitude and pulse width influenced the efficacy of the FTSTS protocol as expected. An increase in the pulse amplitude increased the efficacy of the FTSTS protocol, but the efficacy plateaued when the amplitude passed 2 nA. Additionally, I observed that smaller pulse widths favored a more productive FTSTS protocol. This results from the higher temporal specificity in the induced spike-times of each neuron population, which reduces extra unwanted induced spiking. Importantly, I showed that even with the extra spiking induced by longer pulse width the FTSTS protocol was able to control the average excitatory-to-inhibitory synaptic weight of the network. This is critical for implementation of the FTSTS into an experimental protocol where the stimulation pulse width may have a lower width limit.

In order to address spatial constraints of stimulating the excitatory and inhibitory populations separately, I integrated optogenetic stimulation dynamics into the FTSTS protocol. I inserted the Chronos channelrhodopsin into the excitatory population and the Chrimson channelrhodopsin into the inhibitory population. One of the major benefits promoted by the optogenetic community is the high spatial selectivity of optogenetic stimulation. Since the FTSTS protocol requires the selective stimulation of separate neuron populations, optogenetic stimulation would fill this requirement. Furthermore, I showed in Figure 3.20 that it is possible to integrate optogenetic dynamics into the FTSTS protocol to control the average synaptic weight. One experiment that would confirm my stimulation protocol would be to optogenetically stimulate excitatory neurons in layers 1-3 of the cortex and inhibitory neurons in layers 2/3 (Harris and Shepherd, 2015) and record the changes in dynamics of the excitatory and inhibitory neuron population in response to optogenetic FTSTS. If the FTSTS increased the weight between the excitatory and inhibitory neocortical neurons and the inhibitory population activity increases, this would suggest the FTSTS protocol is able to control the synaptic strength between the two populations.

Here, my goal was to determine the optimal FTSTS protocol parameters to control the excitatory-to-inhibitory synaptic weights and as a consequence the seizure state of the biophysical neocortical-onset seizure model. While I determined the optimal FTSTS parameters to control the synaptic weights, my protocol relies on the assumption that the excitatory and inhibitory neurons can be separately stimulated. I showed that this major limitation could be overcome by integrating the FTSTS protocol with an optogenetic stimulation protocol of the two neuron populations. Additionally, the biophysically constrained neocortical-onset seizure model I used (Liou *et al.*, 2020) only considered neocortical excitatory and inhibitory neurons and ignored any interconnectivity between neocortical neurons and neurons from other brain regions, such as the thalamus (Allendoerfer and Shatz, 1994; Harris and Shepherd, 2015). While I didn't consider internetwork connections with neurons of other brain regions, my protocol could be easily tested for this scenario. Also, the more separable the neuron population are from each other the more the efficacy and practicality of the FTSTS protocol would increase. In this work, I only considered an open-loop FTSTS protocol. One future direction of this project would be to close the loop and develop an optimal closed-loop framework to prevent the emergence of seizures to treat epilepsy. Finally, one of the ultimate goals of this project is to show in experiment that the FTSTS protocol is able to control the synaptic weight between two neuron populations and control the synchronous state of a pathological synchronous neuron network.

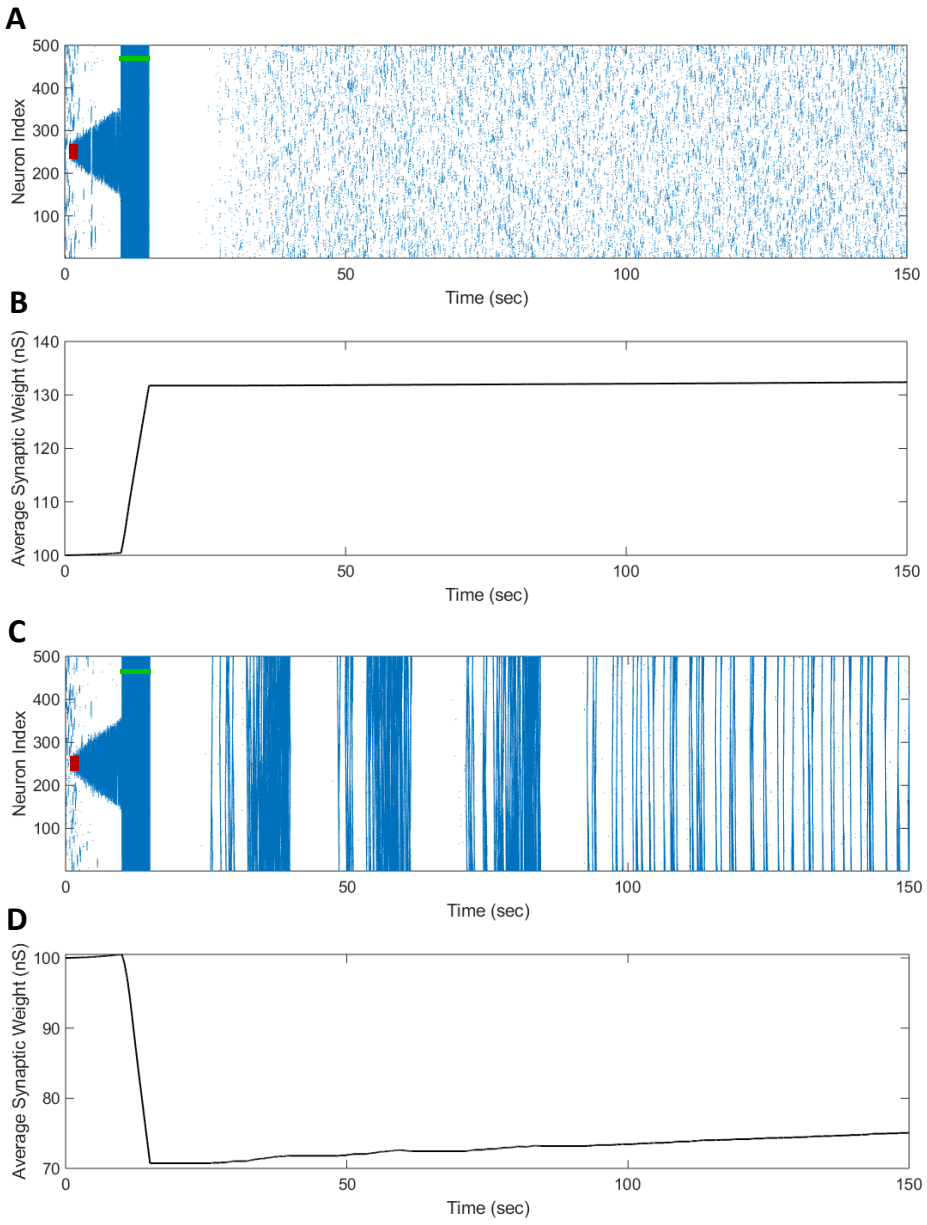

FIGURE 5.10: Optimal FTSTS Parameters to Control the Average Synaptic Weight. I applied my FTSTS protocol with a pulse amplitude of 2 nA, pulse interval of 10 ms, a pulse width of 1 ms, and an inverted standard polarity ($a_E = -1$ and $a_I = 1$). The initial seizure was induced by a seizure inducing input of 200 pA (red-bar). I applied a train-offset time of -0.5 m to increase the average synaptic weight in **(A)** in order to stop the initial seizure and prevent future seizures. **(B)** shows the increase in the average synaptic weight induced by FTSTS protocol (green-bar). I applied a train-offset time of -2 m to decrease the average synaptic weight in **(C)**, which initially stopped the first seizure but produced strong spontaneous seizure for the rest of the simulation. **(D)** shows the decrease in the average synaptic weight induced by FTSTS protocol (green-bar).

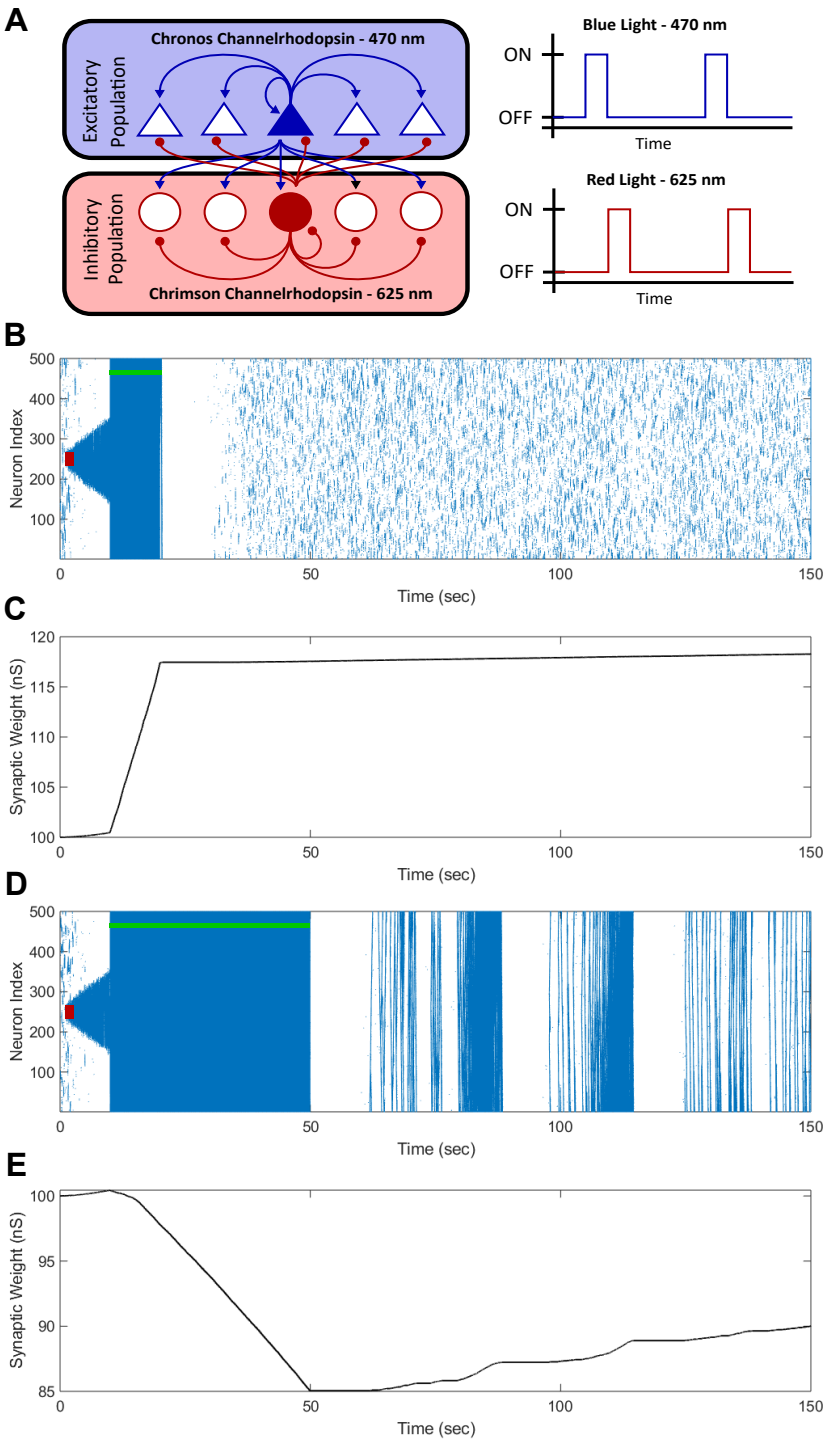
A
Chronos Channelrhodopsin - 470 nm
Excitatory Population
Inhibitory Population
Chrimson Channelrhodopsin - 625 nm
Blue Light - 470 nm
ON
OFF
Time
Red Light - 625 nm
ON
OFF
Time
B
Neuron Index
Time (sec)
C
Synaptic Weight (nS)
Time (sec)
D
Neuron Index
Time (sec)
E
Synaptic Weight (nS)
Time (sec)

FIGURE 5.11: Optogenetic FTSTS Control of the Average Synaptic Weight. I incorporated optogenetic stimulation techniques into my FTSTS protocol to spatially and temporally selectively stimulate the excitatory and inhibitory neurons with blue (470 nm) and red (625 nm) light as shown in **(A)**. A seizure was initiated with a seizure initiating input of 200 pA applied for 3 sec shown as the red-box. Then, I applied my optical FTSTS to control the average synaptic weight of the network (green-bar). In order to increase the average synaptic weight, the Chronos channelrhodopsin was inserted into the excitatory neurons and the Chrimson channelrhodopsin was inserted into the inhibitory neurons. The raster plot in **(B)** shows the forced firing by the optical stimulation and that no further seizure were observed after the optogenetic FTSTS protocol. **(C)** shows the decrease in the average synaptic weight by the optogenetic FTSTS protocol. In order to decrease the average synaptic weight of the network, the Chronos channelrhodopsin was inserted into the inhibitory neurons and the Chrimson channelrhodopsin was inserted into the excitatory neurons. **(D)** shows the raster-plot of the excitatory neocortical neurons and the increased prevalence of strong seizures after the optogenetic FTSTS protocol. **(E)** shows the decrease in the average synaptic weight induced by the optogenetic FTSTS protocol.

CHAPTER 6

Summary and Directions for Future Work

6.1 SUMMARY

In this dissertation, my focus was on developing neurostimulation strategies for controlling plasticity dynamics in the brain in order to fill in the gaps of my understanding of basic neuroscience questions and to develop novel therapies to treat neurological diseases, such as Parkinson's disease (PD) or epilepsy. In Chapters 2-3, I investigated how plasticity dynamics were modulated by the release of different neuromodulators, such as dopamine and acetylcholine, in the basal ganglia and the hippocampus. Based on these results, I suggested new therapies to treat PD, such as targeting the M4 receptors with a M4R antagonist, and new experiments that will shed light on the temporal dopaminergic modulation of the SC-CA1 synaptic plasticity in the hippocampus. In Chapters 4-5, I developed and optimized a novel stimulation strategy called "Forced Temporal Spike-Time Stimulation" (FTSTS) that is able to control the average synaptic weight of large excitatory-inhibitory neural networks and as a result the synchrony level of the networks. In contrast to other desynchronizing stimulation strategies, the FTSTS protocol could effectively drive the network between the synchronous and asynchronous states where the network would be in the driven state for a long-time without any further external input. I expanded upon this result in Chapter 5 where the FTSTS protocol was optimized on a biophysically constrained neocortical-onset seizure model.

In Chapter 2, I developed a biochemical computational model of corticostriatal plasticity in the direct medium spiny neuron in order to investigate how the loss of dopamine effects key plasticity proteins and how targeting the M4R can restore the levels of these key plasticity protein. Using this model, I showed how decreases in dopamine, which is associated with Parkinson's disease, reduced the profile of key corticostriatal plasticity signaling proteins. Additionally, I explored how the reduction of key plasticity proteins, due to dopamine depletion, could be restored by targeting

acetylcholine and calcium inputs. These results suggest that selectively targeting the M4R may represent a novel therapeutic tool to treat symptoms of Parkinson's Disease.

In Chapter 3, I developed a set of phenomenological models to describe the temporal dose-dependent effect of the dopamine D1/D5 receptors agonists SKF 38393, 6-bromo-APB, and dopamine, on the Schaffer-collateral CA1 (SC-CA1) pyramidal neuron synaptic plasticity using published electrophysiological data from hippocampal CA1 slice experiments on the % change in the field excitatory postsynaptic potential (fEPSP) slope. I investigated the biochemical effects with the electrical effects at the electrophysiological level in my model where I estimated the model parameters using a Bayesian framework with the existing electrophysiological data in the literature of diverse hippocampal CA1 slice experiments. I used my biophysical model to make quantitative predictions of the temporal dose-dependent modulation of the HFS/LFS induced LTP/LTD in SC-CA1 synapses by the various D1/D5 agonists. My model was capable of making quantitative predictions of the available experimental results under diverse HFS/LFS protocols. Furthermore, my model predictions showed a strong nonlinear dependency of the modulation of LTP/LTD by D1/D5 agonists that depended on the relative timing between the release of the D1/D5 agonists at various concentrations and the HFS/LFS protocol. Out of these modeled observation, I have suggested a set of experiments, such as

(1) the application of a high and low concentration of the D1/D5 agonist SKF 38393 immediately before a HFS or LFS protocol in order to verify my model predictions of a concentration dependent bifurcation of the action by the dopamine agonist on SC-CA1 synaptic plasticity, and

(2) the application of a high concentration of the dopamine agonist SKF 38393 immediately before two different LFS protocols that have been shown to induce the same level of LTD, but have dramatically different stimulation durations to validate my limited resources modeling hypothesis and support my model predictions.

In Chapter 4, I developed a novel stimulation strategy "Forced Temporal Spike-Time Stimulation (FTSTS)" that I showed, in simulation, was able to efficiently

desynchronize large excitatory-inhibitory (E-I) spiking neuron networks and keep the network desynchronized without any further input by harnessing the synaptic weight of the network. In contrast to other desynchronization stimulation strategies, my strategy focused on harnessing the underlying synaptic plasticity of the network to control the average network synaptic strength by forcing the spiking neurons to fire in specific temporal patterns, while the other stimulation strategies purely focus on suppressing the synchronous neural activity. Since my neurostimulation strategy focuses on controlling the temporal firing pattern, it provided complete control over the synchrony level of the network for a long period of time, not just desynchronization. Furthermore, I showed how combining FTSTS into already existing stimulation protocols, such as coordinate reset (CR), can enhance the overall performance of the CR stimulation strategy in desynchronizing large neural networks.

In Chapter 5, I explored the parameter space of the FTSTS protocol developed in Chapter 4 and determined the optimal parameters to efficiently control the average synaptic weight. I applied my strategy to a recently developed biophysically constrained neocortical-onset seizure model (Liou *et al.*, 2020) and showed my strategy was able to control the average synaptic weight and suppress the emergence of spontaneous seizures or induce more spontaneous seizures. Using this biophysically constrained model, I optimized parameters of the FTSTS protocol. Finally, I integrated the FTSTS into an optogenetic stimulation framework in order to show how optogenetic stimulation could be used to overcome spatial constraints of separately stimulating the excitatory and inhibitory neuron populations.

6.2 FUTURE DIRECTIONS

6.2.1 *Development of biochemical signaling model of D2R and A2aR*

In Chapter 2, I developed a biochemical kinetic model of the direct pathway MSN intracellular signaling pathways to study the effect of the loss of dopamine and the interaction of dopamine, acetylcholine, and calcium. I used the model to suggest potential new pharmaceutical neuromodulation strategies to treat the symptoms of PD. Here, I only considered the direct pathway MSN and ignored the indirect pathway

MSN. Therefore, a future direction of this work would be the development of a biochemical kinetic model of the intracellular pathways of the indirect pathway MSN in order to study the interaction of dopamine, adenosine, and calcium. This model could be used to study how the balance between the direct and indirect pathway pathways change as dopamine is depleted in the Parkinsonian state and develop novel strategies to restore the healthy dynamics.

6.2.2 *Biophysiologically 3D detailed modeling of the the hippocampus*

In Chapter 3, I developed a phenomenological model to describe the temporal dose-dependent dopaminergic modulation of high frequency stimulation (HFS) or low frequency stimulation (LFS) that modulated the induced long-term potentiation (LTP) or long-term depotentiation (LTD), respectively. I modeled the stimulation induced plasticity changes of the SC-CA1 synapse with a frequency dependent HFS/LFS model. In order to compare my model predictions to more experimental data on the dopaminergic modulation of the SC-CA1 synapse, a plasticity model that is able to account for other type of stimulation protocol induced plasticity changes, such as spike-timing dependent plasticity (STDP). Furthermore, a more biophysically representative model of the CA1 pyramidal neurons could help validate my model predictions. Since the different parts of the computational model of the temporal dose-dependent dopaminergic modulation of the SC-CA1 synapse could be easily swapped for better models as they become available, a more biophysically representative model of the CA1 neuron and plasticity could easily be incorporated in my previously developed model from Chapter 3. If these results support the model predictions from Chapter 3, it would validate my model predictions further.

The temporal dose-dependent dopaminergic modulation of SC-CA1 synaptic plasticity model could be expanded upon by replacing the CA1 pyramidal neuron with a morphologically and biophysically accurate single CA1 pyramidal neuron model. Previously, other researchers have developed morphologically and biophysically accurate models of CA1 pyramidal neurons (Migliore *et al.*, 2018) and reduced models that capture the same experimental variability as the more morphologically accurate models (Cutsuridis and Poirazi, 2015; Cutsuridis *et al.*,

2010; Turi *et al.*, 2019; Tomko *et al.*, 2021). The morphologically and biophysically accurate single compartment models of the CA1 pyramidal neuron reconstruct the experimentally determined neuron morphology and incorporate the intrinsic electrophysiological properties of the various ion channels of the CA1 pyramidal neuron. These electrophysiological models have been expanded by various groups to include intracellular biochemical signaling dynamics in order to capture the effect of neuromodulators, such as acetylcholine (Mergenthal *et al.*, 2020). Additional researchers have extend biophysical model developed by Migliore *et al.* (2018) to include facilitation and depression of post-synaptic potentials (Ecker *et al.*, 2020). Therefore, the more morphologically and biophysically accurate models of the CA1 pyramidal neuron could be incorporated into my model. Additionally, inclusion of the experimentally intracellular biochemical pathways similar to those used in the cholinergic model (Mergenthal *et al.*, 2020) could be incorporated into the morphologically accurate model of the CA1 pyramidal neuron (Migliore and Lansky, 1999) to examine how intracellular signaling pathways activated by stimulating the Schaffer-collateral interact with the biochemical signaling pathways activated by the dopamine agonist. These results would further support my model predictions.

6.2.3 *Closing the loop of FTSTS*

In Chapters 4 and 5, I developed a novel open-loop stimulation strategy called “Forced Temporal Spike-Time Stimulation" (FTSTS) where the parameters and the duration of the FTSTS protocol were determined prior to applying the protocol. A more efficient approach to controlling the synchrony of a spiking neural network would be a closed-loop control policy that responds to the changing dynamics. A future direction of the FTSTS strategy is to develop a close-loop control policy to control the state of a synchronous neural network. Towards this goal, the optimized FTSTS parameters determined in Chapter 5 could be used to inform the development of an optimal closed-loop FTSTS policy. The integration of a closed-loop control policy may produce a more robust neurostimulation strategy that would be capable of handling fluctuations in brain dynamics. Additionally, a close-loop FTSTS control policy will reduce the frequency of human hand-tuned modifications of the stimulation strategy.

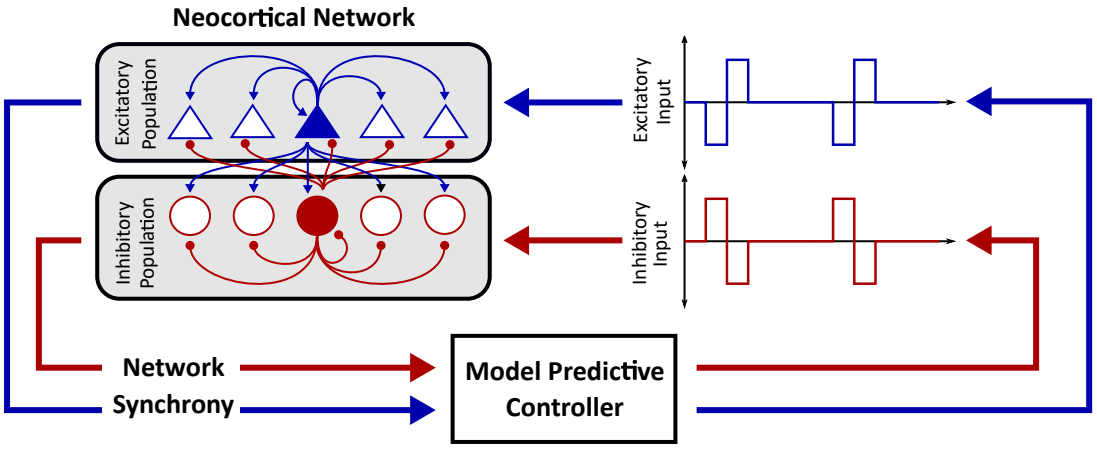

FIGURE 6.1: A schematic of the closed-loop optimal FTSTS design.

A successful implementation of a closed-loop FTSTS control policy would establish a proof-of-concept for controlling abnormally synchronized neuronal activity in a disease model

In order to develop the model-based predictive control (MPC) policy for controlling the synchrony of a spiking neuron network, the MPC policy could first be developed for a generic excitatory-inhibitory spiking neuron case described in Chapter 4, and then it could be extended to the biophysically constrained neocortical-onset seizure model. In the generic E-I neuron network case, the synchrony of the network measured by the Kuramoto order parameter could be used as a feedback signal to inform the MPC policy. Typically, the optimization problem formulation in the MPC framework involves minimizing a model predicted cost or reward (e.g., network synchrony) over a finite time horizon into the future while satisfying the input and output constraints (e.g., physiological bounds on the FTSTS amplitude, bounds on neuronal firing rates, etc.). In this case, one could formulate the reward function based on the E-I network synchrony, computed as the Kuramoto order parameter, although other reward functions, such as the average synaptic weight between the excitatory and inhibitory neurons computed based on the spiking data should be considered, as well. Upon developing a close-loop FTSTS protocol, the robustness of the closed-loop system to noise/perturbations would also need to be investigated by leveraging closed-loop analysis techniques embedded in MPC literature. Then, the MPC protocol could be extended to the neocortical-onset seizure

model. One potential hurdle to extending MPC to the neocortical model is an adequate synchrony or seizure state metric.

Bibliography

Abbott L.F. and Nelson S.B. 2000. Synaptic plasticity: taming the beast. Nature Neuroscience 3:1178.

Abrahamsson T., Lalanne T., Watt A.J., and Sjöström P.J. 2016. Long-term potentiation by theta-burst stimulation using extracellular field potential recordings in acute hippocampal slices. Cold Spring Harbor Protocols 2016:pdb–prot091298.

Alford S., Frenguelli B., Schofield J., and Collingridge G. 1993. Characterization of ca2+ signals induced in hippocampal ca1 neurones by the synaptic activation of nmda receptors. The Journal of physiology 469:693–716.

Allendoerfer K.L. and Shatz C.J. 1994. The subplate, a transient neocortical structure: its role in the development of connections between thalamus and cortex. Annual review of neuroscience 17:185–218.

Andreasen M., Lambert J., and Jensen M.S. 1989. Effects of new non-n-methyl-d-aspartate antagonists on synaptic transmission in the in vitro rat hippocampus. The Journal of physiology 414:317–336.

Aosaki T., Kimura M., and Graybiel A. 1995. Temporal and spatial characteristics of tonically active neurons of the primate's striatum. Journal of neurophysiology 73:1234–1252.

Aziz T.Z., Peggs D., Sambrook M., and Crossman A. 1991. Lesion of the subthalamic nucleus for the alleviation of 1-methyl-4-phenyl-1, 2, 3, 6-tetrahydropyridine (mptp)-induced parkinsonism in the primate. Movement disorders: official journal of the Movement Disorder Society 6:288–292.

Bacskai B.J., Hochner B., Mahaut-Smith M., Kaang B., Kandel E., Tsien R., *et al*. 1993. Spatially resolved dynamics of camp and protein kinase a subunits in aplysia sensory neurons. Science 260:222–226.

Bateup H.S., Svenningsson P., Kuroiwa M., Gong S., Nishi A., Heintz N., and Greengard P. 2008. Cell type–specific regulation of darpp-32 phosphorylation by psychostimulant and antipsychotic drugs. Nature neuroscience 11:932.

Bell C.C., Han V.Z., Sugawara Y., and Grant K. 1997. Synaptic plasticity in a cerebellum-like structure depends on temporal order. Nature 387:278.

Benabid A.L., Pollak P., Louveau A., Henry S., and De Rougemont J. 1987. Combined (thalamotomy and stimulation) stereotactic surgery of the vim thalamic nucleus for bilateral parkinson disease. Stereotactic and functional neurosurgery 50:344–346.

Bernard V., Normand E., and Bloch B. 1992. Phenotypical characterization of the rat striatal neurons expressing muscarinic receptor genes. Journal of Neuroscience 12:3591–3600.

Bhalla U.S. 2011. Multiscale interactions between chemical and electric signaling in ltp induction, ltp reversal and dendritic excitability. Neural Networks 24:943–949.

Bhalla U.S. 2014. Molecular computation in neurons: a modeling perspective. Current opinion in neurobiology 25:31–37.

Bhalla U.S. and Iyengar R. 1999. Emergent properties of networks of biological signaling pathways. Science 283:381–387.

Bi G.q. and Poo M.m. 1998. Synaptic modifications in cultured hippocampal neurons: dependence on spike timing, synaptic strength, and postsynaptic cell type. Journal of neuroscience 18:10464–10472.

Bibb J.A., Snyder G.L., Nishi A., Yan Z., Meijer L., Fienberg A.A., Tsai L.H., Kwon Y.T., Girault J.A., Czernik A.J., *et al*. 1999. Phosphorylation of darpp-32 by cdk5 modulates dopamine signalling in neurons. Nature 402:669–671.

Blackwell K. 2013. Approaches and tools for modeling signaling pathways and calcium dynamics in neurons. Journal of neuroscience methods 220:131–140.

Blackwell K.T. and Jedrzejewska-Szmek J. 2013. Molecular mechanisms underlying neuronal synaptic plasticity: systems biology meets computational neuroscience in the wilds of synaptic plasticity. Wiley Interdisciplinary Reviews: Systems Biology and Medicine 5:717–731.

Blackwell K.T. and Miningou N. 2020. Temporal pattern and synergy influence activity of erk signaling pathways during l-ltp induction. bioRxiv .

Blackwell K.T., Salinas A.G., Tewatia P., English B., Hellgren Kotaleski J., and Lovinger D.M. 2019. Molecular mechanisms underlying striatal synaptic plasticity: relevance to chronic alcohol consumption and seeking. European Journal of Neuroscience 49:768–783.

Blake J., Brown M., and Collingridge G. 1988. Cnqx blocks acidic amino acid induced depolarizations and synaptic components mediated by non-nmda receptors in rat hippocampal slices. Neuroscience letters 89:182–186.

Bliss T.V. and Collingridge G.L. 1993. A synaptic model of memory: long-term potentiation in the hippocampus. Nature 361:31–39.

Bliss T.V. and Lømo T. 1973. Long-lasting potentiation of synaptic transmission in the dentate area of the anaesthetized rabbit following stimulation of the perforant path. The Journal of physiology 232:331–356.

Blitzer R.D., Wong T., Nouranifar R., Iyengar R., and Landau E.M. 1995. Postsynaptic camp pathway gates early ltp in hippocampal ca1 region. Neuron 15:1403–1414.

Bolam J., Wainer B., and Smith A. 1984. Characterization of cholinergic neurons in the rat neostriatum. a combination of choline acetyltransferase immunocytochemistry, golgi-impregnation and electron microscopy. Neuroscience 12:711–718.

Brodie M., Barry S., Bamagous G., Norrie J., and Kwan P. 2012. Patterns of treatment response in newly diagnosed epilepsy. Neurology 78:1548–1554.

Brunel N. and Hansel D. 2006. How noise affects the synchronization properties of recurrent networks of inhibitory neurons. Neural Computation 18:1066–1110.

Brunel N. and Van Rossum M.C. 2007. Lapicque's 1907 paper: from frogs to integrate-and-fire. Biological cybernetics 97:337–339.

Brzosko Z., Zannone S., Schultz W., Clopath C., and Paulsen O. 2017. Sequential neuromodulation of hebbian plasticity offers mechanism for effective reward-based navigation. Elife 6:e27756.

Calabresi P., Di Filippo M., Ghiglieri V., Tambasco N., and Picconi B. 2010. Levodopa-induced dyskinesias in patients with parkinson's disease: filling the bench-to-bedside gap. The Lancet Neurology 9:1106–1117.

Calabresi P., Gubellini P., Centonze D., Picconi B., Bernardi G., Chergui K., Svenningsson P., Fienberg A.A., and Greengard P. 2000. Dopamine and camp-regulated phosphoprotein 32 kda controls both striatal long-term depression and long-term potentiation, opposing forms of synaptic plasticity. Journal of Neuroscience 20:8443–8451.

Calabresi P., Picconi B., Tozzi A., Ghiglieri V., and Di Filippo M. 2014. Direct and indirect pathways of basal ganglia: a critical reappraisal. Nature neuroscience 17:1022.

Caporaso G.L., Bibb J.A., Snyder G.L., Valle C., Rakhilin S., Fienberg A.A., Hemmings Jr H.C., Nairn A.C., and Greengard P. 2000. Drugs of abuse modulate the phosphorylation of arpp-21, a cyclic amp-regulated phosphoprotein enriched in the basal ganglia. Neuropharmacology 39:1637–1644.

Castro L.R., Brito M., Guiot E., Polito M., Korn C.W., Hervé D., Girault J.A., Paupardin-Tritsch D., and Vincent P. 2013. Striatal neurones have a specific ability to respond to phasic dopamine release. The Journal of physiology 591:3197–3214.

Cepeda C., Buchwald N., and Levine M. 1993. Neuromodulatory actions of dopamine in the neostriatum are dependent upon the excitatory amino acid receptor subtypes activated. Proceedings of the National Academy of Sciences 90:9576–9580.

Chen Z., Fujii S., Ito K.I., Kato H., Kaneko K., and Miyakawa H. 1995. Activation of dopamine d1 receptors enhances long-term depression of synaptic transmission induced by low frequency stimulation in rat hippocampal ca1 neurons. Neuroscience letters 188:195–198.

Christie J.M. and Jahr C.E. 2006. Multivesicular release at schaffer collateral–ca1 hippocampal synapses. Journal of Neuroscience 26:210–216.

Chuhma N., Mingote S., Moore H., and Rayport S. 2014. Dopamine neurons control striatal cholinergic neurons via regionally heterogeneous dopamine and glutamate signaling. Neuron 81:901–912.

Coffey R.J. 2009. Deep brain stimulation devices: a brief technical history and review. Artificial organs 33:208–220.

Collingridge G.L. 1985. Long term potentiation in the hippocampus: mechanisms of initiation and modulation by neurotransmitters. Trends in Pharmacological Sciences 6:407–411.

Collingridge G.L., Kehl S., and McLennan H.t. 1983. Excitatory amino acids in synaptic transmission in the schaffer collateral-commissural pathway of the rat hippocampus. The Journal of physiology 334:33–46.

Connolly B.S. and Lang A.E. 2014. Pharmacological treatment of parkinson disease: a review. Jama 311:1670–1683.

Cutsuridis V., Cobb S., and Graham B.P. 2010. Encoding and retrieval in a model of the hippocampal ca1 microcircuit. Hippocampus 20:423–446.

Cutsuridis V. and Poirazi P. 2015. A computational study on how theta modulated inhibition can account for the long temporal windows in the entorhinal–hippocampal loop. Neurobiology of learning and memory 120:69–83.

Daido H. 1992. Order function and macroscopic mutual entrainment in uniformly coupled limit-cycle oscillators. Progress of Theoretical Physics 88:1213–1218.

Damier P., Hirsch E., Agid Y., and Graybiel A. 1999. The substantia nigra of the human brain: Ii. patterns of loss of dopamine-containing neurons in parkinson's disease. Brain 122:1437–1448.

Daoudal G., Hanada Y., and Debanne D. 2002. Bidirectional plasticity of excitatory postsynaptic potential (epsp)-spike coupling in ca1 hippocampal pyramidal neurons. Proceedings of the National Academy of Sciences 99:14512–14517.

Dauer W. and Przedborski S. 2003. Parkinson's disease: mechanisms and models. neuron 39:889–909.

Davie C.A. 2008. A review of parkinson's disease. British medical bulletin 86:109–127.

Deuschl G., Schade-Brittinger C., Krack P., Volkmann J., Schäfer H., Bötzel K., Daniels C., Deutschländer A., Dillmann U., Eisner W., *et al*. 2006. A randomized trial of deep-brain stimulation for Parkinson's disease. New England Journal of Medicine 355:896–908.

Dong Y., Green T., Saal D., Marie H., Neve R., Nestler E.J., and Malenka R.C. 2006. Creb modulates excitability of nucleus accumbens neurons. Nature neuroscience 9:475–477.

Dudek S. and Bear M. 1992. Homosynaptic long-term depression in area ca1 of hippocampus and effects of n-methyl-d-aspartate receptor blockade. Proc Natl Acad Sci 89:4363–4367.

Ebert M., Hauptmann C., and Tass P.A. 2014. Coordinated Reset stimulation in a large-scale model of the STN-Gpe circuit. Frontiers in Computational Neuroscience 8:154.

Ecker A., Romani A., Sáray S., Káli S., Migliore M., Falck J., Lange S., Mercer A., Thomson A.M., Muller E., *et al*. 2020. Data-driven integration of hippocampal ca1 synaptic physiology in silico. Hippocampus 30:1129–1145.

Ferreira J., Katzenschlager R., Bloem B., Bonuccelli U., Burn D., Deuschl G., Dietrichs E., Fabbrini G., Friedman A., Kanovsky P., *et al*. 2013. Summary of the recommendations of the efns/mds-es review on therapeutic management of p arkinson's disease. European journal of neurology 20:5–15.

Fisher R., Salanova V., Witt T., Worth R., Henry T., Gross R., Oommen K., Osorio I., Nazzaro J., Labar D., *et al*. 2010. Electrical stimulation of the anterior nucleus of thalamus for treatment of refractory epilepsy. Epilepsia 51:899–908.

Foncelle A., Mendes A., Jedrzejewska-Szmek J., Valtcheva S., Berry H., Blackwell K.T., and Venance L. 2018. Modulation of spike-timing dependent plasticity: towards the inclusion of a third factor in computational models. Frontiers in Computational Neuroscience 12:49.

Fonseca R., Vabulas R.M., Hartl F.U., Bonhoeffer T., and Nägerl U.V. 2006. A balance of protein synthesis and proteasome-dependent degradation determines the maintenance of ltp. Neuron 52:239–245.

for Parkinson's Disease Study Group D.B.S. 2001. Deep-brain stimulation of the subthalamic nucleus or the pars interna of the globus pallidus in parkinson's disease. New England Journal of Medicine 345:956–963.

Forli A., Vecchia D., Binini N., Succol F., Bovetti S., Moretti C., Nespoli F., Mahn M., Baker C.A., Bolton M.M., *et al*. 2018. Two-photon bidirectional control and imaging of neuronal excitability with high spatial resolution in vivo. Cell Reports 22:3087–3098.

Frey U., Huang Y., and Kandel E. 1993. Effects of camp simulate a late stage of ltp in hippocampal ca1 neurons. Science 260:1661–1664.

Garcia-Munoz M., Young S.J., and Groves P.M. 1992. Presynaptic long-term changes in excitability of the corticostriatal pathway. NeuroReport 3:357–360.

Gerfen C.R. and Surmeier D.J. 2011. Modulation of striatal projection systems by dopamine. Annual review of neuroscience 34:441–466.

Gilman A.G. 1987. G proteins: transducers of receptor-generated signals. Annual review of biochemistry 56:615–649.

Girault J., Walaas S., Hemmings J.H., and Greengard P. 1990. Arpp-21, a camp-regulated phosphoprotein enriched in dopamine-innervated brain regions: tissue distribution and regulation of phosphorylation in rat brain. Neuroscience 37:317–325.

Glatt C.E. and Snyder S.H. 1993. Cloning and expression of an adenylyl cyclase localized to the corpus striatum. Nature 361:536.

Goldberg J.A. and Reynolds J. 2011. Spontaneous firing and evoked pauses in the tonically active cholinergic interneurons of the striatum. Neuroscience 198:27–43.

Golomb D., Yue C., and Yaari Y. 2006. Contribution of persistent na+ current and m-type k+ current to somatic bursting in ca1 pyramidal cells: combined experimental and modeling study. Journal of Neurophysiology 96:1912–1926.

Graham B.P. 2001. Pattern recognition in a compartmental model of a ca1 pyramidal neuron. Network: Computation in Neural Systems 12:473–492.

Handforth A., DeGiorgio C., Schachter S., Uthman B., Naritoku D., Tecoma E., Henry T., Collins S., Vaughn B., Gilmartin R., *et al*. 1998. Vagus nerve stimulation therapy for partial-onset seizures: a randomized active-control trial. Neurology 51:48–55.

Harris K.D. and Shepherd G.M. 2015. The neocortical circuit: themes and variations. Nature neuroscience 18:170–181.

Hauptmann C., Popovych O., and Tass P.A. 2005. Delayed feedback control of synchronization in locally coupled neuronal networks. Neurocomputing 65:759–767.

Hauptmann C. and Tass P. 2009. Cumulative and after-effects of short and weak coordinated reset stimulation: a modeling study. Journal of Neural Engineering 6:016004.

Heath R.G. 1963. Electrical self-stimulation of the brain in man. American Journal of Psychiatry 120:571–577.

Heath R.G. 1977. Modulation of emotion with a brain pacemaker: Treatment for intractable psychiatric illness. Journal of Nervous and Mental Disease .

Hebb D.O. 1949. The organization of behavior. Psychology Press.

Hegeman D.J., Hong E.S., Hernández V.M., and Chan C.S. 2016. The external globus pallidus: progress and perspectives. European Journal of Neuroscience 43:1239–1265.

Hernandez R.V., Navarro M.M., Rodriguez W.A., Martinez Jr J.L., and LeBaron R.G. 2005. Differences in the magnitude of long-term potentiation produced by theta burst and high frequency stimulation protocols matched in stimulus number. Brain research protocols 15:6–13.

Herron C.E., Lester R.A., Coan E.J., and Collingridge G.L. 1986. Frequency-dependent involvement of nmda receptors in the hippocampus: a novel synaptic mechanism. Nature 322:265–268.

Hersch S.M., Gutekunst C.A., Rees H., Heilman C.J., and Levey A.I. 1994. Distribution of m1-m4 muscarinic receptor proteins in the rat striatum: light and electron microscopic immunocytochemistry using subtype-specific antibodies. Journal of Neuroscience 14:3351–3363.

Heynen A.J., Abraham W.C., and Bear M.F. 1996. Bidirectional modification of ca1 synapses in the adult hippocampus in vivo. Nature 381:163–166.

Hodgkin A.L. and Huxley A.F. 1952. A quantitative description of membrane current and its application to conduction and excitation in nerve. The Journal of physiology 117:500.

Horne E.A. and Dell'Acqua M.L. 2007. Phospholipase c is required for changes in postsynaptic structure and function associated with nmda receptor-dependent long-term depression. Journal of Neuroscience 27:3523–3534.

Huang Y.Y. and Kandel E.R. 1995. D1/d5 receptor agonists induce a protein synthesis-dependent late potentiation in the ca1 region of the hippocampus. Proceedings of the National Academy of Sciences 92:2446–2450.

Huber K.M., Roder J.C., and Bear M.F. 2001. Chemical induction of mglur5- and protein synthesis–dependent long-term depression in hippocampal area ca1. Journal of neurophysiology 86:321–325.

Jedrzejewska-Szmek J., Luczak V., Abel T., and Blackwell K.T. 2017. β-adrenergic signaling broadly contributes to ltp induction. PLoS computational biology 13:e1005657.

Johnston M.V. 2004. Clinical disorders of brain plasticity. Brain and Development 26:73–80.

Kaczmarek L.K. and Levitan I.B. 1987. Neuromodulation: the biochemical control of neuronal excitability. Oxford University Press, USA.

Kandel E.R., Dudai Y., and Mayford M.R. 2014. The molecular and systems biology of memory. Cell 157:163–186.

Karpova A., Mikhaylova M., Thomas U., Knöpfel T., and Behnisch T. 2006. Involvement of protein synthesis and degradation in long-term potentiation of schaffer collateral ca1 synapses. Journal of Neuroscience 26:4949–4955.

Kasahara J., Fukunaga K., and Miyamoto E. 2001. Activation of calcium/calmodulin-dependent protein kinase iv in long term potentiation in the rat hippocampal ca1 region. Journal of Biological Chemistry 276:24044–24050.

KEMP J.M. and Powell T. 1970. The cortico-striate projection in the monkey. Brain 93:525–546.

Kemp J.M. and Powell T.P.S. 1971. The structure of the caudate nucleus of the cat: light and electron microscopy. Philosophical Transactions of the Royal Society of London. B, Biological Sciences 262:383–401.

Kim B., Hawes S.L., Gillani F., Wallace L.J., and Blackwell K.T. 2013. Signaling pathways involved in striatal synaptic plasticity are sensitive to temporal pattern and exhibit spatial specificity. PLoS Comput Biol 9:e1002953.

Kiss I.Z., Rusin C.G., Kori H., and Hudson J.L. 2007. Engineering complex dynamical structures: Sequential patterns and desynchronization. Science 316:1886–1889.

Klapoetke N.C., Murata Y., Kim S.S., Pulver S.R., Birdsey-Benson A., Cho Y.K., Morimoto T.K., Chuong A.S., Carpenter E.J., Tian Z., *et al*. 2014. Independent optical excitation of distinct neural populations. Nature methods 11:338–346.

Knight B.W. 1972. Dynamics of encoding in a population of neurons. The Journal of general physiology 59:734–766.

Kordower J.H., Olanow C.W., Dodiya H.B., Chu Y., Beach T.G., Adler C.H., Halliday G.M., and Bartus R.T. 2013. Disease duration and the integrity of the nigrostriatal system in parkinson's disease. Brain 136:2419–2431.

Kostenis E., Pfeil E.M., and Annala S. 2020. Heterotrimeric gq proteins as therapeutic targets? Journal of Biological Chemistry 295:5206–5215.

Kotaleski J.H. and Blackwell K.T. 2010. Modelling the molecular mechanisms of synaptic plasticity using systems biology approaches. Nature Reviews Neuroscience 11:239–251.

Krames E.S., Peckham P.H., Rezai A., and Aboelsaad F. 2009. What is neuromodulation? *In* Neuromodulation, pages 3–8, Elsevier.

Krauss J.K., Lipsman N., Aziz T., Boutet A., Brown P., Chang J.W., Davidson B., Grill W.M., Hariz M.I., Horn A., *et al*. 2020. Technology of deep brain stimulation: current status and future directions. Nature Reviews Neurology pages 1–13.

Kravitz A.V., Tye L.D., and Kreitzer A.C. 2012. Distinct roles for direct and indirect pathway striatal neurons in reinforcement. Nature neuroscience 15:816.

Kuramoto Y. 1984. Chemical oscillations, waves, and turbulence. Springer.

Kwan P. and Brodie M.J. 2000. Early identification of refractory epilepsy. New England Journal of Medicine 342:314–319.

Lanciego J.L., Luquin N., and Obeso J.A. 2012. Functional neuroanatomy of the basal ganglia. Cold Spring Harbor Perspectives in Medicine 2:a009621.

Lang A.E. and Lees A. 2002. Management of parkinson's disease: an evidence-based review. Mov disord 17:S1–S166.

Lemon N. and Manahan-Vaughan D. 2006. Dopamine d1/d5 receptors gate the acquisition of novel information through hippocampal long-term potentiation and long-term depression. Journal of Neuroscience 26:7723–7729.

Li C.j., Zhou M., Li H.g., Lv Q., Xu X.l., and Guo L.j. 2013. Clonidine suppresses the induction of long-term potentiation by inhibiting hcn channels at the schaffer collateral–ca1 synapse in anesthetized adult rats. Cellular and molecular neurobiology 33:1075–1086.

Lindroos R., Dorst M.C., Du K., Filipović M., Keller D., Ketzef M., Kozlov A.K., Kumar A., Lindahl M., Nair A.G., *et al*. 2018. Basal ganglia neuromodulation over multiple temporal and structural scales—simulations of direct pathway msns investigate the fast onset of dopaminergic effects and predict the role of kv4. 2. Frontiers in neural circuits 12:3.

Liou J.y., Smith E.H., Bateman L.M., Bruce S.L., McKhann G.M., Goodman R.R., Emerson R.G., Schevon C.A., and Abbott L. 2020. A model for focal seizure onset, propagation, evolution, and progression. Elife 9:e50927.

Lisman J., Yasuda R., and Raghavachari S. 2012. Mechanisms of camkii action in long-term potentiation. Nature reviews neuroscience 13:169–182.

Liu J., Wang W., Wang F., Cai F., Hu Z.L., Yang Y.J., Chen J., and Chen J.G. 2009. Phosphatidylinositol-linked novel d1 dopamine receptor facilitates long-term depression in rat hippocampal ca1 synapses. Neuropharmacology 57:164–171.

Lomo T. 1966. Frequency potentiation of excitatory synaptic activity in dentate area of hippocampal formation. *In* Acta Physiologica Scandinavica, page 128, Blackwell Science Ltd PO BOX 88, OSNEY MEAD, OXFORD OX2 0NE, OXON, ENGLAND.

Luczak V., Blackwell K.T., Abel T., Girault J.A., and Gervasi N. 2017. Dendritic diameter influences the rate and magnitude of hippocampal camp and pka transients during β-adrenergic receptor activation. Neurobiology of learning and memory 138:10–20.

Luz Y. and Shamir M. 2012. Balancing feed-forward excitation and inhibition via Hebbian inhibitory synaptic plasticity. PLoS Computational Biology 8:e1002334.

Mäki-Marttunen T., Iannella N., Edwards A.G., Einevoll G.T., and Blackwell K.T. 2020. A unified computational model for cortical post-synaptic plasticity. Elife 9:e55714.

Malinow R., Schulman H., and Tsien R.W. 1989. Inhibition of postsynaptic pkc or camkii blocks induction but not expression of ltp. Science 245:862–866.

Marcott P.F., Mamaligas A.A., and Ford C.P. 2014. Phasic dopamine release drives rapid activation of striatal d2-receptors. Neuron 84:164–176.

Martorell A.J., Paulson A.L., Suk H.J., Abdurrob F., Drummond G.T., Guan W., Young J.Z., Kim D.N.W., Kritskiy O., Barker S.J., *et al*. 2019. Multi-sensory gamma stimulation ameliorates alzheimer's-associated pathology and improves cognition. Cell 177:256–271.

Mathern G.W., Pretorius J.K., Leite J.P., Kornblum H.I., Mendoza D., Lozada A., and Bertram III E.H. 1998. Hippocampal AMPA and NMDA mRNA levels and subunit immunoreactivity in human temporal lobe epilepsy patients and a rodent model of chronic mesial limbic epilepsy. Epilepsy Research 32:154–171.

Matthies H. and Reymann K.G. 1993. Protein kinase a inhibitors prevent the maintenance of hippocampal long-term potentiation. Neuroreport 4:712–714.

Mattioni M. and Le Novère N. 2013. Integration of biochemical and electrical signaling-multiscale model of the medium spiny neuron of the striatum. PloS one 8:e66811.

Mauroy A., Rhoads B., Moehlis J., and Mezic I. 2014. Global isochrons and phase sensitivity of bursting neurons. SIAM Journal on Applied Dynamical Systems 13:306–338.

Megıas M., Emri Z., Freund T., and Gulyas A. 2001. Total number and distribution of inhibitory and excitatory synapses on hippocampal ca1 pyramidal cells. Neuroscience 102:527–540.

Mergenthal A., Bouteiller J.M.C., Yu G.J., and Berger T.W. 2020. A computational model of the cholinergic modulation of ca1 pyramidal cell activity. Frontiers in computational neuroscience 14:75.

Migliore M. and Lansky P. 1999. Long-term potentiation and depression induced by a stochastic conditioning of a model synapse. Biophysical journal 77:1234–1243.

Migliore R., Lupascu C.A., Bologna L.L., Romani A., Courcol J.D., Antonel S., Van Geit W.A., Thomson A.M., Mercer A., Lange S., *et al*. 2018. The physiological variability of channel density in hippocampal ca1 pyramidal cells and interneurons explored using a unified data-driven modeling workflow. PLoS computational biology 14:e1006423.

Mironov S., Skorova E., Taschenberger G., Hartelt N., Nikolaev V., Lohse M., and Kügler S. 2009. Imaging cytoplasmic camp in mouse brainstem neurons. BMC neuroscience 10:29.

Mitchell I., Clarke C., Boyce S., Robertson R., Peggs D., Sambrook M., and Crossman A. 1989. Neural mechanisms underlying parkinsonian symptoms based upon regional uptake of 2-deoxyglucose in monkeys exposed to 1-methyl-4-phenyl-1, 2, 3, 6-tetrahydropyridine. Neuroscience 32:213–226.

Mockett B.G., Brooks W.M., Tate W.P., and Abraham W.C. 2004. Dopamine d1/d5 receptor activation fails to initiate an activity-independent late-phase ltp in rat hippocampus. Brain research 1021:92–100.

Mockett B.G., Guévremont D., Williams J.M., and Abraham W.C. 2007. Dopamine d1/d5 receptor activation reverses nmda receptor-dependent long-term depression in rat hippocampus. Journal of Neuroscience 27:2918–2926.

Monga B., Froyland G., and Moehlis J. 2018. Synchronizing and desynchronizing neural populations through phase distribution control. *In* 2018 Annual American Control Conference (ACC), pages 2808–2813, IEEE.

Moshé S.L., Perucca E., Ryvlin P., and Tomson T. 2015. Epilepsy: new advances. The Lancet 385:884–898.

Mulkey R.M. and Malenka R.C. 1992. Mechanisms underlying induction of homosynaptic long-term depression in area ca1 of the hippocampus. Neuron 9:967–975.

Nabi A., Mirzadeh M., Gibou F., and Moehlis J. 2013a. Minimum energy desynchronizing control for coupled neurons. Journal of Computational Neuroscience 34:259–271.

Nabi A., Stigen T., Moehlis J., and Netoff T. 2013b. Minimum energy control for in vitro neurons. Journal of Neural Engineering 10:036005.

Nagai T., Yoshimoto J., Kannon T., Kuroda K., and Kaibuchi K. 2016. Phosphorylation signals in striatal medium spiny neurons. Trends in pharmacological sciences 37:858–871.

Nair A.G., Bhalla U.S., and Kotaleski J.H. 2016. Role of darpp-32 and arpp-21 in the emergence of temporal constraints on striatal calcium and dopamine integration. PLoS computational biology 12:e1005080.

Nair A.G., Castro L.R., El Khoury M., Gorgievski V., Giros B., Tzavara E.T., Hellgren-Kotaleski J., and Vincent P. 2019. The high efficacy of muscarinic m4 receptor in d1 medium spiny neurons reverses striatal hyperdopaminergia. Neuropharmacology 146:74–83.

Nair A.G., Gutierrez-Arenas O., Eriksson O., Jauhiainen A., Blackwell K.T., and Kotaleski J.H. 2014. Modeling intracellular signaling underlying striatal function in health and disease. *In* Progress in molecular biology and translational science, vol. 123, pages 277–304, Elsevier.

Nair A.G., Gutierrez-Arenas O., Eriksson O., Vincent P., and Kotaleski J.H. 2015. Sensing positive versus negative reward signals through adenylyl cyclase-coupled gpcrs in direct and indirect pathway striatal medium spiny neurons. Journal of Neuroscience 35:14017–14030.

Nakano T., Doi T., Yoshimoto J., and Doya K. 2010. A kinetic model of dopamine- and calcium-dependent striatal synaptic plasticity. PLoS computational biology 6:e1000670.

Navakkode S., Sajikumar S., Korte M., and Soong T.W. 2012. Dopamine induces ltp differentially in apical and basal dendrites through bdnf and voltage-dependent calcium channels. Learning & Memory 19:294–299.

Neves S.R., Ram P.T., and Iyengar R. 2002. G protein pathways. Science 296:1636–1639.

Neyman S. and Manahan-Vaughan D. 2008. Metabotropic glutamate receptor 1 (mglur1) and 5 (mglur5) regulate late phases of ltp and ltd in the hippocampal ca1 region in vitro. European journal of neuroscience 27:1345–1352.

Nishi A., Bibb J.A., Matsuyama S., Hamada M., Higashi H., Nairn A.C., and Greengard P. 2002. Regulation of darpp-32 dephosphorylation at pka-and cdk5-sites by nmda and ampa receptors: distinct roles of calcineurin and protein phosphatase-2a. Journal of neurochemistry 81:832–841.

Nishi A., Bibb J.A., Snyder G.L., Higashi H., Nairn A.C., and Greengard P. 2000. Amplification of dopaminergic signaling by a positive feedback loop. Proceedings of the National Academy of Sciences 97:12840–12845.

Nishi A., Kuroiwa M., Miller D.B., O'Callaghan J.P., Bateup H.S., Shuto T., Sotogaku N., Fukuda T., Heintz N., Greengard P., *et al*. 2008. Distinct roles of pde4 and pde10a in the regulation of camp/pka signaling in the striatum. Journal of Neuroscience 28:10460–10471.

Nishi A., Snyder G.L., and Greengard P. 1997. Bidirectional regulation of darpp-32 phosphorylation by dopamine. Journal of Neuroscience 17:8147–8155.

Nishi A., Watanabe Y., Higashi H., Tanaka M., Nairn A.C., and Greengard P. 2005. Glutamate regulation of darpp-32 phosphorylation in neostriatal neurons involves activation of multiple signaling cascades. Proceedings of the National Academy of Sciences 102:1199–1204.

Otmakhova N.A. and Lisman J.E. 1996. D1/d5 dopamine receptor activation increases the magnitude of early long-term potentiation at ca1 hippocampal synapses. Journal of Neuroscience 16:7478–7486.

Otmakhova N.A. and Lisman J.E. 1998. D1/d5 dopamine receptors inhibit depotentiation at ca1 synapses via camp-dependent mechanism. Journal of neuroscience 18:1270–1279.

Ouimet C., Hemmings H., and Greengard P. 1989. Arpp-21, a cyclic amp-regulated phosphoprotein enriched in dopamine-innervated brain regions. ii. immunocytochemical localization in rat brain. Journal of Neuroscience 9:865–875.

Panchalingam S. and Undie A.S. 2000. Optimized binding of [35s] gtpγs to gq-like proteins stimulated with dopamine d1-like receptor agonists. Neurochemical research 25:759–767.

Panchalingam S. and Undie A.S. 2005. Physicochemical modulation of agonist-induced [35s] gtpγs binding: Implications for coexistence of multiple functional conformations of dopamine d1-like receptors. Journal of Receptors and Signal Transduction 25:125–146.

Pandey S. and Srivanitchapoom P. 2017. Levodopa-induced dyskinesia: clinical features, pathophysiology, and medical management. Annals of Indian Academy of Neurology 20:190.

Papatheodoropoulos C. and Kostopoulos G. 2000. Decreased ability of rat temporal hippocampal ca1 region to produce long-term potentiation. Neuroscience letters 279:177–180.

Perucca E. 1998. Pharmacoresistance in epilepsy. CNS drugs 10:171–179.

Pfister J.P. and Tass P. 2010. STDP in oscillatory recurrent networks: theoretical conditions for desynchronization and applications to deep brain stimulation. Frontiers in Computational Neuroscience 4:22.

Pitcher J.A., Freedman N.J., and Lefkowitz R.J. 1998. G protein–coupled receptor kinases. Annual review of biochemistry 67:653–692.

Poewe W., Seppi K., Tanner C.M., Halliday G.M., Brundin P., Volkmann J., Schrag A.E., and Lang A.E. 2017. Parkinson disease. Nature reviews Disease primers 3:1–21.

Polito M., Klarenbeek J., Jalink K., Tritsch D., Vincent P., and Castro L.R. 2013. The no/cgmp pathway inhibits transient camp signals through the activation of pde2 in striatal neurons. Frontiers in cellular neuroscience 7:211.

Pollak P., Benabid A., Gross C., Gao D., Laurent A., Benazzouz A., Hoffmann D., Gentil M., and Perret J. 1993. Effects of the stimulation of the subthalamic nucleus in parkinson disease. Revue neurologique 149:175–176.

Popovych O.V., Hauptmann C., and Tass P.A. 2005. Effective desynchronization by nonlinear delayed feedback. Physical Review Letters 94:164102.

Popovych O.V., Lysyansky B., Rosenblum M., Pikovsky A., and Tass P.A. 2017. Pulsatile desynchronizing delayed feedback for closed-loop deep brain stimulation. PloS ONE 12:e0173363.

Popovych O.V. and Tass P.A. 2014. Control of abnormal synchronization in neurological disorders. Frontiers in Neurology 5:268.

Purves D., Augustine G.J., Fitzpatrick D., Hall W.C., LaMantia A.S., McNamara J.O., and White L.E. ???? Neuroscience. 6th. Oxford University Press, USA.

Rajput A., Sitte H., Rajput A., Fenton M., Pifl C., and Hornykiewicz O. 2008. Globus pallidus dopamine and parkinson motor subtypes: clinical and brain biochemical correlation. Neurology 70:1403–1410.

Rakhilin S., Olson P., Nishi A., Starkova N., Fienberg A., Nairn A., Surmeier D., and Greengard P. 2004. A network of control mediated by regulator of calcium/calmodulin-dependent signaling. Science 306:698–701.

Reyes-Harde M. and Stanton P.K. 1998. Postsynaptic phospholipase c activity is required for the induction of homosynaptic long-term depression in rat hippocampus. Neuroscience letters 252:155–158.

Reymann K.G., Bro R., Kase H., *et al*. 1988a. Inhibitors of calmodulin and protein kinase c block different phases of hippocampal long-term potentiation. Brain research 461:388–392.

Reymann K.G., Frey U., Jork R., and Matthies H. 1988b. Polymyxin b, an inhibitor of protein kinase c, prevents the maintenance of synaptic long-term potentiation in hippocampal ca1 neurons. Brain research 440:305–314.

Roberto M., Nelson T., Ur C., Brunelli M., Sanna P., and Gruol D. 2003. The transient depression of hippocampal ca1 ltp induced by chronic intermittent ethanol exposure is associated with an inhibition of the map kinase pathway. European Journal of Neuroscience 17:1646–1654.

Saftenku E.É. 2002. A simplified model of long-term plasticity in cerebellar mossy fiber–granule cell synapses. Neurophysiology 34:216–218.

Sajikumar S. and Frey J.U. 2004. Late-associativity, synaptic tagging, and the role of dopamine during ltp and ltd. Neurobiology of learning and memory 82:12–25.

Sajikumar S., Navakkode S., and Frey J.U. 2008. Distinct single but not necessarily repeated tetanization is required to induce hippocampal late-ltp in the rat ca1. Learning & Memory 15:46–49.

Schmalz J. and Kumar G. 2019. Controlling synchronization of spiking neuronal networks by harnessing synaptic plasticity. Frontiers in computational neuroscience 13:61.

Schultz W. 1998. Predictive reward signal of dopamine neurons. Journal of neurophysiology 80:1–27.

Schultz W. 1999. The reward signal of midbrain dopamine neurons. Physiology 14:249–255.

Schwiening C.J. 2012. A brief historical perspective: Hodgkin and huxley. The Journal of physiology 590:2571.

Selig D.K., Lee H.K., Bear M.F., and Malenka R.C. 1995. Reexamination of the effects of mcpg on hippocampal ltp, ltd, and depotentiation. Journal of Neurophysiology 74:1075–1082.

Sem-Jacobsen C. 1966. Depth-electrographic observations related to parkinson's disease. recording and electrical stimulation in the area around the third ventricle. Journal of neurosurgery 24:Suppl–388.

Shen W., Flajolet M., Greengard P., and Surmeier D.J. 2008. Dichotomous dopaminergic control of striatal synaptic plasticity. Science 321:848–851.

Shen W., Plotkin J.L., Francardo V., Ko W.K.D., Xie Z., Li Q., Fieblinger T., Wess J., Neubig R.R., Lindsley C.W., *et al*. 2015. M4 muscarinic receptor signaling ameliorates striatal plasticity deficits in models of l-dopa-induced dyskinesia. Neuron 88:762–773.

Shetty M.S. and Sajikumar S. 2017. Differential involvement of ca2+/calmodulin-dependent protein kinases and mitogen-activated protein kinases in the dopamine d1/d5 receptor-mediated potentiation in hippocampal ca1 pyramidal neurons. Neurobiology of learning and memory 138:111–120.

Shewcraft R.A., Dean H.L., Fabiszak M.M., Hagan M.A., Wong Y.T., and Pesaran B. 2020. Excitatory/inhibitory responses shape coherent neuronal dynamics driven by optogenetic stimulation in the primate brain. Journal of Neuroscience 40:2056–2068.

Shivarama Shetty M., Gopinadhan S., and Sajikumar S. 2016. Dopamine d1/d5 receptor signaling regulates synaptic cooperation and competition in hippocampal ca 1 pyramidal neurons via sustained erk 1/2 activation. Hippocampus 26:137–150.

Siegfried J. and Lippitz B. 1994. Bilateral chronic electrostimulation of ventroposterolateral pallidum: a new therapeutic approach for alleviating all parkinsonian symptoms. Neurosurgery 35:1126–1130.

Singer A.C., Martorell A.J., Douglas J.M., Abdurrob F., Attokaren M.K., Tipton J., Mathys H., Adaikkan C., and Tsai L.H. 2018. Noninvasive 40-hz light flicker to recruit microglia and reduce amyloid beta load. Nature protocols 13:1850–1868.

Smith Y., Raju D.V., Pare J.F., and Sidibe M. 2004. The thalamostriatal system: a highly specific network of the basal ganglia circuitry. Trends in neurosciences 27:520–527.

Song S., Miller K.D., and Abbott L.F. 2000. Competitive hebbian learning through spike-timing-dependent synaptic plasticity. Nature Neuroscience 3:919.

Stefan H., Kreiselmeyer G., Kerling F., Kurzbuch K., Rauch C., Heers M., Kasper B.S., Hammen T., Rzonsa M., Pauli E., *et al*. 2012. Transcutaneous vagus nerve stimulation (t-vns) in pharmacoresistant epilepsies: A proof of concept trial. Epilepsia 53:e115–e118.

Stemmer P.M. and Klee C.B. 1994. Dual calcium ion regulation of calcineurin by calmodulin and calcineurin b. Biochemistry 33:6859–6866.

Stramiello M. and Wagner J.J. 2008. D1/5 receptor-mediated enhancement of ltp requires pka, src family kinases, and nr2b-containing nmdars. Neuropharmacology 55:871–877.

Stramiello M. and Wagner J.J. 2010. Cocaine enhancement of long-term potentiation in the ca1 region of rat hippocampus: Lamina-specific mechanisms of action. Synapse 64:644–648.

Surmeier D.J., Bargas J., Hemmings Jr H.C., Nairn A.C., and Greengard P. 1995. Modulation of calcium currents by a d1 dopaminergic protein kinase/phosphatase cascade in rat neostriatal neurons. Neuron 14:385–397.

Tanimura A., Pancani T., Lim S.A.O., Tubert C., Melendez A.E., Shen W., and Surmeier D.J. 2018. Striatal cholinergic interneurons and parkinson's disease. European Journal of Neuroscience 47:1148–1158.

Tass P. and Hauptmann C. 2009. Anti-kindling achieved by stimulation targeting slow synaptic dynamics. Restorative Neurology and Neuroscience 27:591–611.

Tass P.A. 2003a. Desynchronization by means of a coordinated reset of neural subpopulations: A novel technique for demand-controlled deep brain stimulation. Progress of Theoretical Physics Supplement 150:281–296.

Tass P.A. 2003b. A model of desynchronizing deep brain stimulation with a demand-controlled coordinated reset of neural subpopulations. Biological Cybernetics 89:81–88.

Tass P.A. 2007. Phase resetting in medicine and biology: stochastic modelling and data analysis. Springer Science & Business Media.

Tass P.A. and Hauptmann C. 2007. Therapeutic modulation of synaptic connectivity with desynchronizing brain stimulation. International Journal of Psychophysiology 64:53–61.

Tass P.A. and Majtanik M. 2006. Long-term anti-kindling effects of desynchronizing brain stimulation: a theoretical study. Biological Cybernetics 94:58–66.

Temperli P., Ghika J., Villemure J.G., Burkhard P., Bogousslavsky J., and Vingerhoets F. 2003. How do Parkinsonian signs return after discontinuation of subthalamic DBS? Neurology 60:78–81.

Thurman D.J., Beghi E., Begley C.E., Berg A.T., Buchhalter J.R., Ding D., Hesdorffer D.C., Hauser W.A., Kazis L., Kobau R., *et al*. 2011. Standards for epidemiologic studies and surveillance of epilepsy. Epilepsia 52:2–26.

Tomko M., Benuskova L., and Jedlicka P. 2021. A new reduced-morphology model for ca1 pyramidal cells and its validation and comparison with other models using hippounit. Scientific reports 11:1–16.

Toni T., Welch D., Strelkowa N., Ipsen A., and Stumpf M.P. 2008. Approximate bayesian computation scheme for parameter inference and model selection in dynamical systems. Journal of the Royal Society Interface 6:187–202.

Triesch J., Vo A.D., and Hafner A.S. 2018. Competition for synaptic building blocks shapes synaptic plasticity. Elife 7:e37836.

Turi G.F., Li W.K., Chavlis S., Pandi I., O'Hare J., Priestley J.B., Grosmark A.D., Liao Z., Ladow M., Zhang J.F., *et al*. 2019. Vasoactive intestinal polypeptide-expressing interneurons in the hippocampus support goal-oriented spatial learning. Neuron 101:1150–1165.

Undieh A.S. 2010. Pharmacology of signaling induced by dopamine d1-like receptor activation. Pharmacology & therapeutics 128:37–60.

Utter A.A. and Basso M.A. 2008. The basal ganglia: an overview of circuits and function. Neuroscience & Biobehavioral Reviews 32:333–342.

Vlachos I., Deniz T., Aertsen A., and Kumar A. 2016. Recovery of dynamics and function in spiking neural networks with closed-loop control. PLoS Computational Biology 12:e1004720.

Wigström H., Gustafsson B., Huang Y.Y., and Abraham W. 1986. Hippocampal long-term potentiation is induced by pairing single afferent volleys with intracellularˆ injected depolarizing current pulses. Acta Physiologica Scandinavica 126:317–319.

Wilson D. and Moehlis J. 2014. Optimal chaotic desynchronization for neural populations. SIAM Journal on Applied Dynamical Systems 13:276.

Witt A., Palmigiano A., Neef A., El Hady A., Wolf F., and Battaglia D. 2013. Controlling the oscillation phase through precisely timed closed-loop optogenetic stimulation: a computational study. Frontiers in neural circuits 7:49.

Yagishita S., Hayashi-Takagi A., Ellis-Davies G.C., Urakubo H., Ishii S., and Kasai H. 2014. A critical time window for dopamine actions on the structural plasticity of dendritic spines. Science 345:1616–1620.

Yapo C., Nair A.G., Clement L., Castro L.R., Kotaleski J.H., and Vincent P. 2017. Detection of phasic dopamine by d1 and d2 striatal medium spiny neurons. The Journal of physiology 595:7451–7475.

Yapo C., Nair A.G., Kotaleski J.H., Vincent P., and Castro L.R. 2018. Switch-like pka responses in the nucleus of striatal neurons. J Cell Sci 131:jcs216556.

Zangiabadi N., Ladino L.D., Sina F., Orozco-Hernández J.P., Carter A., and Téllez-Zenteno J.F. 2019. Deep brain stimulation and drug-resistant epilepsy: a review of the literature. Frontiers in neurology 10:601.

Zeitler M. and Tass P.A. 2015. Augmented brain function by coordinated reset stimulation with slowly varying sequences. Frontiers in Systems Neuroscience 9:49.

Zhang X.l., Sullivan J.A., Moskal J.R., and Stanton P.K. 2008. A nmda receptor glycine site partial agonist, glyx-13, simultaneously enhances ltp and reduces ltd at schaffer collateral–ca1 synapses in hippocampus. Neuropharmacology 55:1238–1250.

Ztaou S., Maurice N., Camon J., Guiraudie-Capraz G., Kerkerian-Le Goff L., Beurrier C., Liberge M., and Amalric M. 2016. Involvement of striatal cholinergic interneurons and m1 and m4 muscarinic receptors in motor symptoms of parkinson's disease. Journal of Neuroscience 36:9161–9172.